LANTHANIDE-CONTAINING NANOMATERIALS AND COMPLEXES: UTILIZING LANTHANIDE LUMINESCENCE FOR A BROAD RANGE OF APPLICATION

by

Chad M. Shade

B.S. in Chemistry, University of Pittsburgh, 2005

Submitted to the Graduate Faculty of

Chemistry in partial fulfillment

of the requirements for the degree of

Doctor of Philosophy

University of Pittsburgh

2011

UNIVERSITY OF PITTSBURGH

GRADUATE SCHOOL OF ARTS AND SCIENCES

This dissertation was presented

by

Chad M. Shade

It was defended on

February 23, 2011

and approved by

Dr. Marcel P. Bruchez, Associate Professor, Department of Chemistry,

Carnegie Mellon University

Dr. Alexander Star, Assistant Professor, Department of Chemistry

Dr. David H. Waldeck, Professor, Department of Chemistry

Dissertation Advisor: Dr. Stéphane Petoud, Adjunct Professor, Department of Chemistry

LANTHANIDE-CONTAINING NANOMATERIALS AND COMPLEXES: UTILYZING LANTHANIDE LUMINESCENCE FOR A BROAD RANGE OF APPLICATION

Chad M. Shade, Ph.D.

University of Pittsburgh, 2011

Combining materials on the nanoscale (1 – 1000 nanometers) with luminescent lanthanide cations has far-reaching implications for exploring the size regime where fundamental biological interactions take place. Nanomaterials such as nanocrystals (NCs), dendrimers, metal-organic frameworks (MOFs) and micelles are uniquely suited for locating lanthanide cations and lanthanide sensitizers in close proximity of one another to stimulate the so-called antenna effect. This approach is necessary to take advantage of the numerous and complementary photophysical properties of luminescent lanthanide cations because lanthanide luminescence is inherently difficult to stimulate and observe for practical applications. A secondary yet equally important feature of nanomaterials is the ability to maximize the number of lanthanide cations and sensitizers per unit volume to increase the overall number of emitted photons and hence sensitivity of the detection platform.

State-of-the art spectroscopic techniques have been employed to characterize the properties of lanthanide-containing nanomaterials towards the development of biological reporters and sensors. In particular, a combination of luminescence intensity and lifetime measurements provide sensitive and real-time information on the local environment experienced by the detection platform. This information provides valuable insight for researchers interested in

the understanding of diseases and diagnostitians interested in making early and accurate assessments of disease.

Using the above-mentioned techniques, we have demonstrated the usefulness of lanthanide luminescence in biological applications and for sensing biologically relevant species such as molecular oxygen. Moreover, our polymetallic nanomaterial approach has allowed us to develop strategies that the lanthanide chemistry community can use to quickly identify lanthanide sensitizers that are adaptable to their respective lines of research. The lanthanide-containing nanomaterial systems have potential applications in the field of chemical sensors and biological imaging, and a fundamental understanding of the energy transfer processes may lead to better sensors and imaging agents.

TABLE OF CONTENTS

LIST OF TABLES

LIST OF FIGURES

LIST OF EQUATIONS

PREFACE

I would like to thank all of my laboratory co-workers and collaborators who have participated in research projects, discussed results and ideas, or provided me with advice over the years. I single out my research advisor, Professor Stéphane Petoud, and express my sincerest gratitude for nurturing my growth as a scientist and helping me to navigate through the graduate school process. I must also thank my parents for without them I would not be here – not in the cliché biological sense – for instilling in me a deep appreciation for math and medical science and for serving as towering examples of the hard-working people Berks County, PA is famous for producing. I would like to thank all of my friends, but especially Dr. Douglas R. Kauffman and Dr. Kristi Kauffman (née O'Neal), who have provided me with an unending supply of comfort food and comfortable surroundings. Last, but certainly not least, I thank my girlfriend Ms. Alicia Salvadeo for her selfless offering of support during the long months of writing and preparing research proposals and doctoral dissertations.

1.0 INTRODUCTION

Analytical methods based on fluorescence are among the most sensitive detection techniques available. Fluorescence detection is a flexible method and does not require expensive instrumentation or large amounts of reagents. Various fields of scientific research that currently employ fluorescence detection to locate and identify biological events, whether *in vivo* or *in vitro*, rely mostly on organic fluorescent reporters and, to a lesser extent, luminescent semiconductor nanocrystals ("quantum dots") that have been developed for application more recently. The fluorescence signals of organic dyes are often difficult to discriminate from those arising from the biological matrix itself ("autofluorescence") because most organic fluorophores have similar photophysical properties: i) luminescence lifetimes (pico- to nanoseconds) and ii) spectral topography. These limitations in resolving the signal from autofluorescence typically result in an overall decrease in detection sensitivity. An additional limitation of organic fluorophores that affects detection sensitivity is the overlap between absorption and emission spectra, leading to the re-absorption phenomenon. Another limitation of organic fluorophores that prevents long or repeated experiments is their tendency to photobleach rapidly.

1.1 LUMINESCENT LANTHANIDE CATIONS

Trivalent lanthanide cations possess several luminescent properties that complement and/or supersede those of organic fluorophores and quantum dots for bioanalytical applications. More specifically, sharp emission bands, whose wavelengths are not affected by experimental conditions, and long luminescence lifetimes,[1] taken together allow spectral and temporal discrimination of the lanthanide signal from autofluorescence, thus maximizing the signal-to-noise ratio and hence detection sensitivity. Their emission of sharp bands that do not overlap is a unique advantage for the development of multiplex assays. In addition, most lanthanide complexes do not photobleach.

The traditional approach to obtain sufficient emission signal from lanthanide complexes in solution requires the cations to be sensitized by an appropriate "antenna",[2] which is classically an organic chromophoric group. At the present time, the most efficient lanthanide emitters for applications in solution are based on lanthanide complexes synthesized from small molecules. Several of these lanthanide complexes have demonstrated advantages for specific analytical applications, such as inhomogeneous and homogeneous time-resolved assays on well-plates, but none possess the versatility required for working across a broader range of bioanalytical applications, such as biologic imaging through fluorescence microscopy.[1] In addition, most of the current lanthanide complexes are hindered by low quantum yield values and limited molar absorptivities. As a result, they do not emit a sufficient number of photons to compete for the detection sensitivity obtained with organic fluorophores, further limiting their potential for applications.

The luminescence sensitivity depends on the signal-to-noise ratio. The number of photons emitted by each discrete luminescent species (the signal) is therefore a crucial parameter and

depends on four independent parameters: 1) the overall absorption of the complex, 2) the number of lanthanide cations present in the complex, 3) the efficiency of the sensitizer to transfer energy to the lanthanide, and 4) the protection of the lanthanide against non-radiative deactivations. As described previously, the typical limitation for lanthanide complexes lies in their low quantum yields, which depend on parameters 3 and 4. This limitation is particularly important for complexes emitting in the NIR domain since the smaller energy gap between ground and excited states results in a greater probability of non-radiative deactivations.[2] We propose to overcome this limitation by creating lanthanide complexes that emit a large number of photons by promoting parameters 1 and 2. This goal will be achieved by forming polymetallic (several lanthanide emitters) species with large extinction coefficients. We take advantage of numerous host matrices, including nanocrystals (NCs), metal-organic frameworks (MOFs), poly(amidoamine) (PAMAM) dendrimers, and micelles to address all of these requirements (see Figure 1-1).

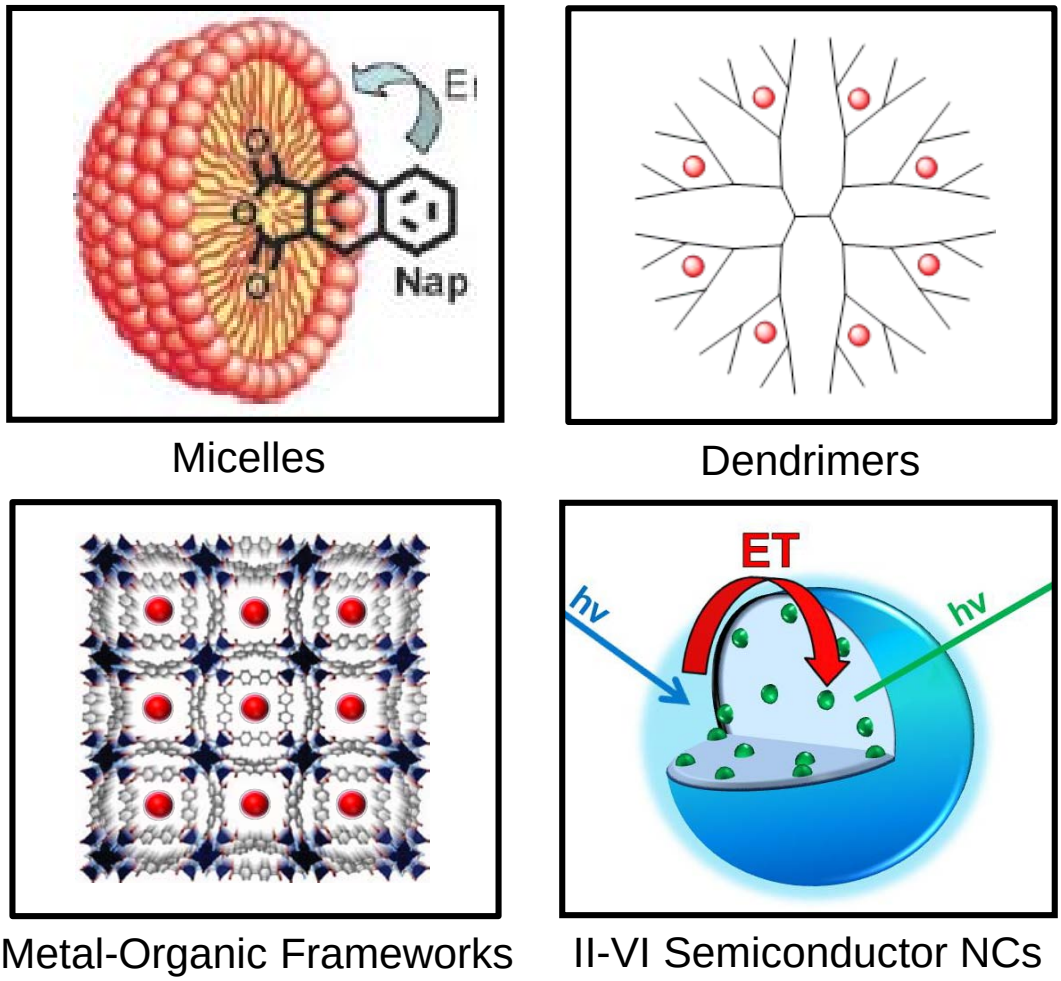

Figure 1-1. Nanomaterials described in this doctoral dissertation which use the polymetallic lanthanide strategy. These nanomaterials include type II-VI semiconductor nanocrystals (NCs), metal-organic frameworks (MOFs), poly(amidoamine) (PAMAM) dendrimers and micelles.

1.2 ADVANTAGES OF LUMINESCENT LANTHANIDE COMPLEXES FOR BIOANALYTICAL APPLICATIONS

Lanthanide cations (Ln^{3+}) possess unique luminescence spectral signatures which appear as sharp bands across the visible[3] and near-infrared (NIR)[4] domains (Figure 1-2), enabling efficient spectral discrimination between their signals from biological background fluorescence (autofluorescence).[5]

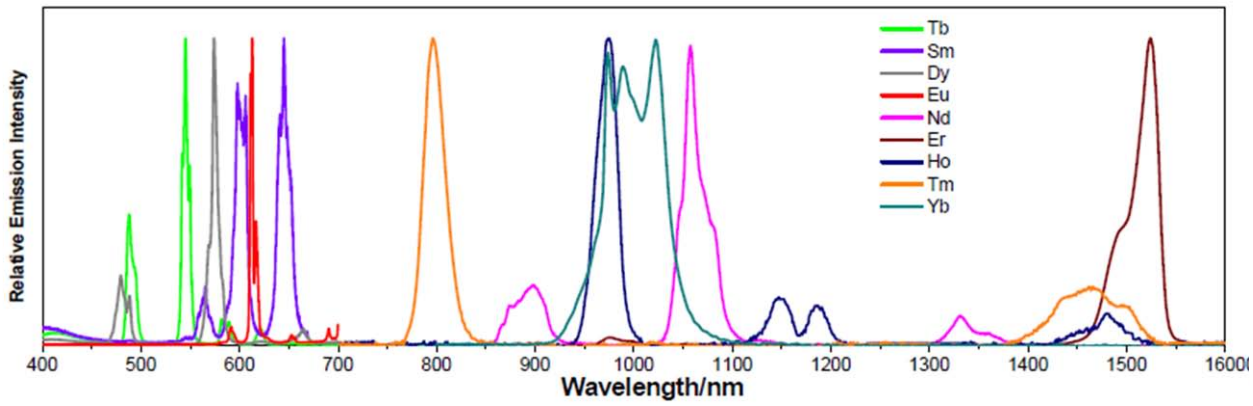

Figure 1-2. Normalized emission spectra of luminescent lanthanide complexes in solution, illustrating the sharp bands and minimal overlap of lanthanide luminescence.[3,4]

Owing to the forbidden nature of the electronic transitions that are the basis for these bands (Laporte rule)[6] and the filling of the f-block by the different lanthanide cations, several unique photophysical properties emerge that are beneficial for more sensitive luminescence analysis in

biological conditions for several reasons. 1) Interactions between Ln^{3+} and organic ligands are predominantly electrostatic,[7] hence emission from complexed lanthanides also appears as sharp, atom-like emission bands.[3,4] Additionally, the energy positions of these bands are insensitive to changes in experimental conditions such as temperature, pressure, pH, solvent or biological environment (hydrophilic – hydrophobic interactions). As depicted in Figure 1-2, these bandwidths are significantly narrower than either of those typically observed for organic fluorophores and luminescent semiconductor nanocrystals ("quantum dots")[8,9]. 2) The minimal overlap between the emission bands of the different lanthanide cations allows for the detection of individual signals of several different lanthanide emitters simultaneously with a common experimental setup (including common excitation wavelength). This unique advantage ensures that the luminescence bands of lanthanides are the most promising for *multiplex assays.* 3) Lanthanide complexes also have large energy gaps between their absorption and emission bands, limiting any re-absorption phenomena. 4) Lanthanide cations have luminescence lifetimes within the range of micro- to milli-seconds,[10-12] much longer than the pico- to nano-second lifetimes reported for fluorescent organic molecules and proteins. For biological imaging applications, the long luminescence lifetimes allow simple and accurate discrimination of the lanthanide complex signal from autofluorescence through time-resolved measurements, a detection technology widely used for homogeneous bioassays *in vitro*.[5,6] Time-resolved detection is a standard feature present in most modern fluorimeters and fluorescence plate readers. Fluorescence microscopes suitable for timeresolved measurements have been described.[13] 5) Due to the shielding of the 4f orbitals by the 5s and 5p, the lanthanide cations of the series have similar reactivities. Their sizes are fairly similar, the apparent radii[14] of the trivalent lanthanides being all within approximately

2% from the beginning to the end of the series. This allows for easy replacement of one lanthanide cation by another in a ligand.

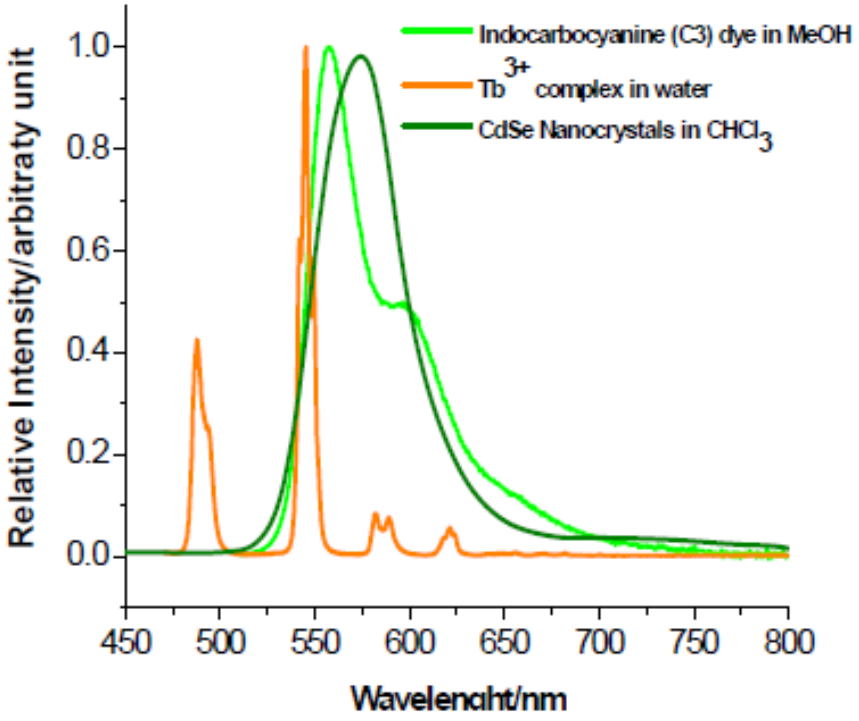

Figure 1-2. Comparison of the normalized emission spectra of a luminescent lanthanide complex $(Tb^{3+})^3$ in water, of a semi-conductor nanocrystals (CdSe – "quantum dots") and of a Cy3 organic fluorophore in solution.

Lanthanide complexes are photostable. Most described lanthanide complexes do not photobleach.[5,13,15-17] Trivalent electron-deficient lanthanide cations stabilize the excited states of organic ligands, preventing deleterious and irreversible photoreactions when the complex is irradiated (Figure 1-3). Increased resistance to photobleaching would allow for longer shelf lives,

easier handling, extended experiment times and/or repetitive observation within the same experiment. Even the most resistant organic fluorophores currently available are susceptible to rapid photobleaching when exposed to a strong excitation signal. The luminescence decay occurs even more rapidly for organic molecules emitting in the near-infrared domain.

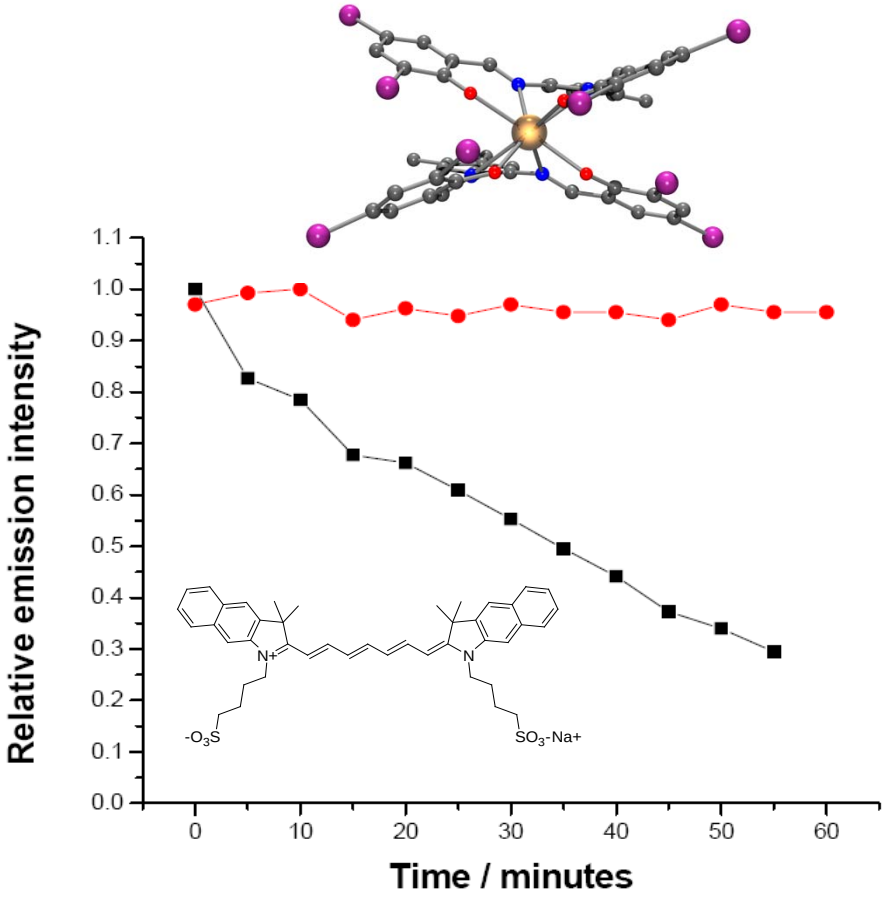

Figure 1-3. Photostability of an Nd^{3+} complex (red curve) compared to an organic Indocyanine green chromophore (black curve).[18]

As mentioned previously, several lanthanide cations emit in the NIR domain, an area of the electromagnetic spectrum which has several advantages for biological imaging: 1) Biologic tissues do not have significant native autofluorescence in the NIR range,[19] therefore use of NIR photons eliminates background fluorescence, one of the most important issues for fluorescence-based biologic imaging and bioanalytical measurements. 2) NIR photons can cross deeply into tissues (several centimeters) without causing damage or significant loss of intensity due to the low absorption of NIR photons in such media.[20,21] 3) The use of NIR light is also one of the best strategies to maximize the resolution of biologic images, since NIR photons scatter less than visible light.[22] Currently, organic molecules are the most used NIR fluorophores, but their use is limited because most undergo rapid photodecomposition (photobleaching). For these reasons, NIR-luminescent lanthanide complexes are among the most promising candidates for NIR reagents, along with semiconductor nanocrystals[23,24] and modified carbon nanotubes.[25] Lanthanide complexes can be excited in the NIR domain by multiphoton techniques.[26,27] Modern fluorescence microscopes designed for biologic imaging are often equipped with lasers able to perform such two-photon excitation.

1.3 STRATEGIES FOR USING LUMINESCENT LANTHANIDE CATIONS

Luminescent lanthanide cations must be sensitized with a suitable “antenna”. Since f→f transitions are forbidden by the Laporte rule,[7,28] free lanthanide cations cannot be directly excited with reasonable efficiency. This limitation can be overcome by placing the lanthanide cations in close proximity to a suitable sensitizer, which is able to absorb as much light as possible in the

UV/visible range and efficiently convert the resulting energy to the lanthanide cations ("*antenna effect*").[3,29-31] For most lanthanide complexes reported in literature, coordination bonds are formed directly between the chromophoric center and the lanthanide cation which limits the choice of sensitizer. A second requirement to obtain good luminescence intensity from lanthanide cations is to sufficiently shield them from interactions with external quenchers, such as solvent molecules, that will create non-radiative deactivation of the excited states, decreasing the luminescence intensity. Protection can be achieved through complete coordination of the lanthanide cation (coordination numbers between 8 and 10 in solution)[32,33] and/or by designing ligands that sterically prohibit access to the metal cation.[10,11,32-37] The last major requirement is that the lanthanide complexes are thermodynamically stable or kinetically inert to prevent their dissociation in solution in order to maintain their luminescence properties and to prevent the release of toxic lanthanide cations.[38]

2.0 INCORPORATING LANTHANIDE CATIONS WITH CADMIUM SELENIDE NANOCRYSTALS: A STRATEGY TO SENSITIZE AND PROTECT TERBIUM(III)

2.1 CHAPTER PREFACE

The aim of this work was to investigate the energy transfer efficiency between semiconductor nanocrystals (SCNCs) and luminescent lanthanide cations. Specifically, we explored the sensitization of Tb^{3+} luminescence by CdSe nanocrystals as a function of growth time and measured the protection provided by this crystalline nanomaterial against nonradiative deactivations. The material contained in this chapter was published as a communication in *The Journal of the American Chemical Society*; the figures in this chapter have been reproduced with permission from *J. Am. Chem. Soc.* **2005**, *127(48)*, 16752. Copyright 2005 American Chemical Society; the full citation is listed as Reference 39 in the bibliography section.[39]

List of authors: Demetra A. Chengelis, Adrienne M. Yingling, Paul D. Badger, Chad M. Shade, Stéphane Petoud

Author contribution: The author of this dissertation was responsible as an undergraduate researcher for reproducing much of the nanoparticle synthesis and photophysical

characterization, including Tb^{3+}-centered quantum yields and luminescence lifetimes, and contributing to the preparation of the published manuscript.

2.2 INTRODUCTION

As biological assays based on luminescence become more prevalent, the demand increases for reporters with properties such as strong resistance to photobleaching and a signal which can be discriminated from background fluorescence (autofluorescence). The narrow, well-defined emission bands and long luminescence lifetimes of lanthanide cations make them more desirable than organic fluorophores as reporters.[4-6,40,41] To exploit the luminescent properties of lanthanide cations, they need to be sensitized by a suitable "antenna".[29,30] Sensitization has typically been accomplished by coordinating organic ligands having high molar absorptivities to luminescent lanthanide cations. One of the inherent limitations of this approach is that organic ligands possess high frequency vibrations that often deactivate the excited states of the lanthanide cations, or provide poor protection from solvent vibrations, decreasing luminescence intensity.[36,42] We tested a novel strategy to remove these limitations by using luminescent semiconductor CdSe nanocrystals as an antenna to sensitize and protect Tb^{3+}. This work demonstrates that combining Tb^{3+} with CdSe semiconductor nanocrystals (**SCNC**s) creates an advantageous new type of lanthanide-based luminescent material.

In recent developments, nanoparticles have shown that they can play an important role as biological reporters.[8,22,43-47] **SCNC**s have unique photophysical properties arising from their quantum confinement effects. For example, the emission band maximum is dependent on

nanocrystal size and displays a bathochromic shift as the nanocrystal radius increases.[48] **SCNC**s also display a broad continuum of absorbance wavelengths with large epsilon values, which provides a wide excitation range.[8] In addition, they are highly photostable,[47] can be used in highly dilute solutions, and have a long shelf life. **SCNC**s have been used in a variety of biological applications, such as imagery, replacing traditional organic fluorophores.[8,22,46] Although the emission bands of CdSe **SCNC**s are more narrow than typical organic fluorophores, they are still broader than those of lanthanide cations.

Lanthanide cations have three main advantages for biological applications: long luminescence lifetimes (micro- to millisecond), which allows autofluorescence removal through time-resolved measurements,[5] sharp emission bands,[4,40] and insensitivity to photobleaching. Since transitions within the f-orbitals are Laporte forbidden, free lanthanide cations have extremely low extinction coefficients. To overcome this limitation, a sensitizer (antenna) is attached to the lanthanide cation, which harvests light and transfers energy to excite the metal ion.

2.3 EXPERIMENTAL

Chemicals. Trioctylphosphine [TOP] (90%) was purchased from Fluka. Trioctylphosphine oxide [TOPO] (99%), Cadmium Oxide (99.99% puratrem), n-tetradecylphosphonic acid [TDPA] (98%), 1-Hexadecylamine [HDA] (98%), and Terbium Nitrate (99.998%) were purchased from Sigma- Aldrich. Selenium Powder (99.99%) was purchased from Strem Chemicals Inc. Toluene, THF, and methanol were purchased from Fischer Scientific, and chloroform was purchased from

EMD Chemicals Inc. Argon gas was purchased from Valley National Gases Inc. All chemicals were used as purchased without purification except toluene, which was distilled over sodium under nitrogen.

Instrumentation. Absorption spectra were recorded on a Perkin-Elmer Lambda 9 Spectrometer controlled by a personal computer using software supplied by Perkin-Elmer. Time-resolved and steady-state emission and excitation spectra were recorded with a Cary Eclipse fluorimeter controlled by a personal computer using software supplied by Varian. Additionally, some spectra, both steady state and time-resolved were recorded with a modified JY Horiba Fluorolog-3 Spectrofluorimeter equipped with a phosphorimeter module. Steady state luminescence quantum yields were measured using quinine sulfate reference solutions (Φ=0.546).[49] Time-resolved luminescence quantum yields were measured using [Tb(H_{22}IAM)] reference solutions (Φ=0.59).[3] Excitation and emission spectra were corrected for the instrumental function. The quantum yields were calculated using Equation 2-1:

$$\Phi_x/\Phi_r = [A_r(\lambda_r)/A_x(\lambda_x)][I(\lambda_r)/I(\lambda_x)][\eta_x^2/\eta_r^2][D_x/D_r]$$

Equation 2-1

where subscript r stands for the reference and x for the sample; A is the absorbance at the excitation wavelength, I is the intensity of the excitation light at the same wavelength, η is the refractive index (η = 1.333 in H_2O, η = 1.4458 in chloroform) and D is the measured integrated luminescence intensity.

The Tb^{3+} luminescence lifetime measurements were performed by excitation of solutions in 1 cm quartz cells (NSG Precision Cells, Inc.) using either a Perkin-Elmer xenon flash lamp or a Nd:YAG Continuum Powerlite 8010 laser (354nm, third harmonic) as the excitation source. Emission was collected at a right angle to the excitation beam, and wavelengths were selected by means of the Spex FL1005 double monochromator or a Spectral Products CM 110 1/8 meter monochromator. The signal was monitored by a Hamamatsu R928 photomultiplier coupled to a 500 MHz bandpass digital oscilloscope (Tektronix TDS 620B). Signals from > 500 flashes were collected and averaged. Reported lifetimes were averages of at least three independent experiments on samples from several different batches. Luminescence decay curves were treated with Origin 7.0 software. The experimental decay curves were fitted to single, double, and triple exponential models. Of these models, the one which provided the best fit of the data was selected.

TEM images were obtained with a JEOL 2000-FX Scanning Transmission Electron Microscope. Samples were prepared by spraying onto a Ted Pella, Inc. Carbon Type-B substrate film attached to a 200 mesh copper grid. The acceleration voltage was 200kV and the magnifications were up to 850,000x. Images were obtained in TEM mode using a Gatan CCD camera and software.

Energy Dispersive X-Ray Fluorescence spectra (EDS) were obtained by qualitative energy dispersive X-Ray analysis using an Oxford Instruments X-Ray detector and pulse height analyzer connected to an EMISPEC analysis system.

Synthesis of CdSe:Tb. 1.0 mmol of selenium powder was dissolved in 4 mL of trioctylphosphine (TOP) and 0.10 mL of anhydrous toluene through vigorous stirring. Excess air

was removed through Schlenk de-gassing techniques under nitrogen and the solution was stored under nitrogen until used.

In the following procedure, trioctylphosphine oxide (TOPO) was used as the solvent, cadmium oxide (CdO) and terbium nitrate ($Tb(NO_3)_3 \bullet 5H_2O$) were used as precursors (doping levels between 10-18%), and hexadecylamine (HDA) or N-tetradecyl phosphonic acid (TDPA) were used as a ligand for the Cd^{2+} and Tb^{3+}. Nucleation occurred upon injection of the Se stock solution into the heated reaction mixture.

10 mmol TOPO, 0.33-0.36 mmol CdO, 0.04-0.07 mmol $Tb(NO_3)_3$, and 0.80 mmol HDA or TDPA were placed in a three neck 50 mL round bottom flask. The flask necks were fitted with water condensers. To control the temperature, the reaction vessel was fitted with a thermocouple temperature controller connected to a heating mantle. Contents were placed under argon, stirred magnetically, and heated to 300°C. Selenium stock solution was injected at 300°C, and the temperature was then reduced to 250°C for the duration of growth. Alternatively, for slower growth, the selenium stock solution was injected at 250°C and nanocrystals were grown at 230°C. (For injection and growth at the higher temperatures, typical growth times of 15 to 30 seconds have been found to be optimal for maximizing Tb^{3+} centered emission. At the lower temperatures, growth times of 30 seconds to 1 minute were best for terbium sensitization.) Aliquots were removed at a variety of times ranging from seconds to hours after injection using a syringe. Samples were then dissolved in chloroform. The resulting products were suspended in chloroform, and purified by precipitation with methanol and centrifugation (14 000 rpm) followed by redissolution of the nanocrystals in the desired solvent (usually chloroform, hexane, or toluene) for spectroscopic analysis.

Synthesis of CdSe. For comparison purposes, CdSe nanocrystals were synthesized following the same method as described for CdSe:Tb nanocrystals, with the following exception: 0.40 mmol of CdO was used, and all lanthanide was omitted.

2.4 RESULTS AND DISCUSSION

A new class of reporters with synergistic properties is synthesized by using the **SCNC** structure to sensitize and protect lanthanide cations. The **SCNC**s' energy levels can be tuned, enabling efficient matching to the various accepting levels of different lanthanide cations. As antennae, nanocrystals can minimize luminescence quenching by isolating the lanthanide cation from high frequency vibrations. Unlike organic molecules,[36,42] **SCNC**s possess only low energy lattice vibrations that are less efficient in deactivating the lanthanide cations' excited states. The CdSe:Tb **SCNC**s were synthesized following procedures inspired by Peng et al.[50,51] and Strouse et al.[52] The detailed procedure is described in the Supporting Information. Growth times of the nanocrystals have been chosen in order to maximize the luminescence intensity of Tb^{3+}; 30 s was found to be optimal for the experimental conditions. The synthesized CdSe:Tb nanocrystals were visualized with transmission electron microscopy (TEM); see Figure 2-1a. Purified and isolated samples dissolved in hexane were aerated onto carbon-coated copper grids for imaging. The sample used for the TEM image was also analyzed by energy dispersive X-ray spectroscopy (EDS). The data reported in Figure 2-1 indicate the nanocrystals are comprised of Cd, Se, and the dopant[52] Tb.

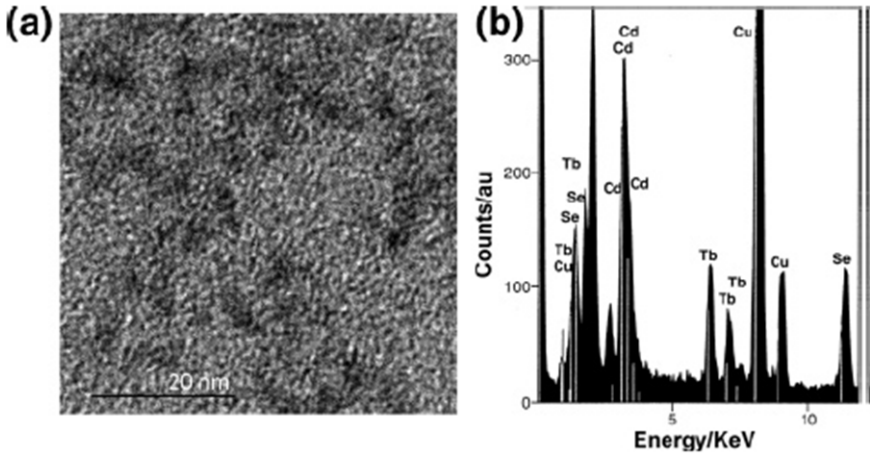

Figure 2-1. Physical characterization of CdSe:Tb. (a) TEM image of the CdSe:Tb nanocrystals, taken at a magnification of 850 K. The size bar represents 20 nm. (b) Energy dispersive X-ray spectroscopy (EDS) analysis of these nanocrystals. The Cu peaks are generated from the copper grid support used for imaging.

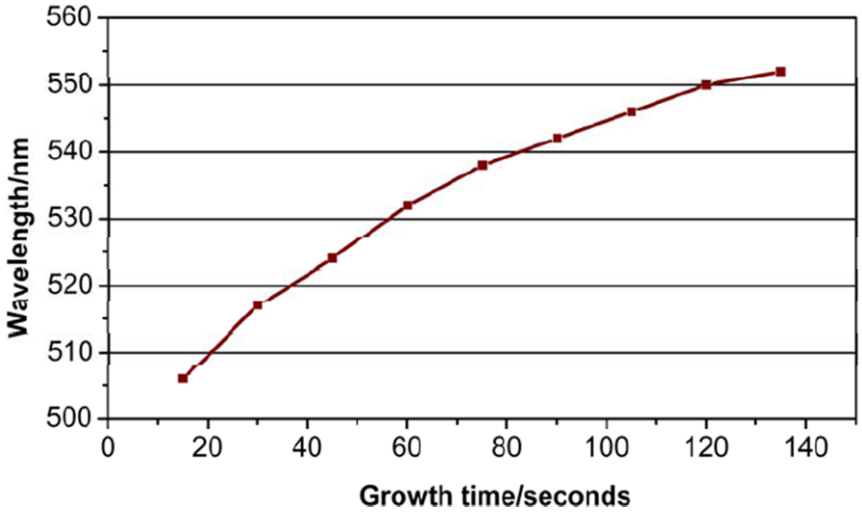

Figure 2-2. Growth time versus the wavelength of the fluorescence emission maximum for CdSe:Tb SCNC. This graph demonstrates the ability to control the size and photophysical properties of the doped nanocrystals through the synthesis.

The CdSe:Tb **SCNC**s of different growth times display a bathochromic shift (Figure 2-2), which demonstrates that doping does not interfere with the quantum confinement properties. Steady-state and time-resolved emission and excitation spectra were collected for the CdSe:Tb nanocrystal aliquots. The emission arising from the lanthanide cation can be discriminated from the nanocrystal luminescence through time-resolved measurements using a typical delay after flash of 200 μs. The total emission of the nanocrystals as well as the Tb^{3+} specific emission was quantified and analyzed for different samples, leading to several interesting findings. In steady-state mode, the total emission of the CdSe:Tb **SCNC**s appears as a relatively broad band (orange, Figure 2-3). This can be explained by the short material growth time of samples used for this photophysical investigation, leading to a polydisperse size distribution of nanocrystals. Longer growth times and alternative synthetic methods should lead to less dispersity and thus sharper

emission bands. Nevertheless, the Tb^{3+} emission appears as narrow, atom-like luminescence. The corresponding excitation spectrum (black, Figure 2-3) displays a sharp maximum around 300 nm and appears as an asymmetrical band. The time-resolved emission spectrum revealed the four main observable Tb^{3+} transitions ($^5D_4 \rightarrow {}^7F_J$, J = 6, 5, 4, 3 by decreasing order of energy, green in Figure 2-3). The time-resolved excitation spectrum (magenta, Figure 2-3) monitoring the Tb^{3+} $^5D_4 \rightarrow {}^7F_5$ transition (λ_{em} = 545 nm) revealed a profile that resembles the steady-state excitation spectrum and differs from the excitation profile of the lanthanide salt $Tb(NO_3)_3$ (see Figure 2-4). These findings confirm that the nanocrystal structure is acting as an antenna for Tb^{3+}; that is, Tb^{3+} emission is sensitized through the electronic structure of the **SCNC**s.

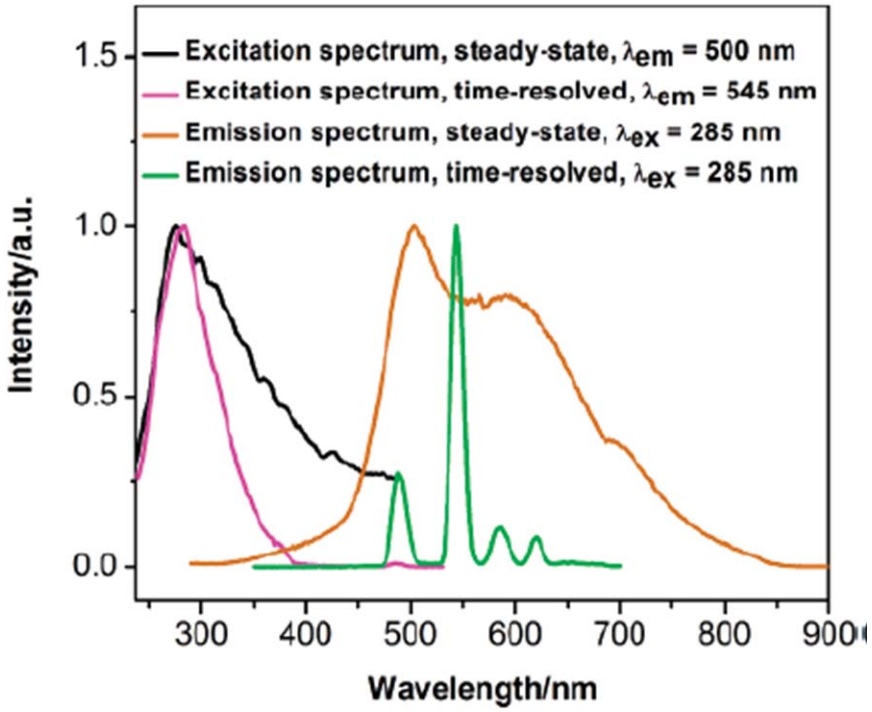

Figure 2-3. Normalized steady-state and time-resolved excitation and emission spectra of CdSe:Tb SCNCs (in chloroform). The Tb^{3+} emission is in the same range as the nanocrystal emission; however, it is easily distinguished through time-resolved measurements.

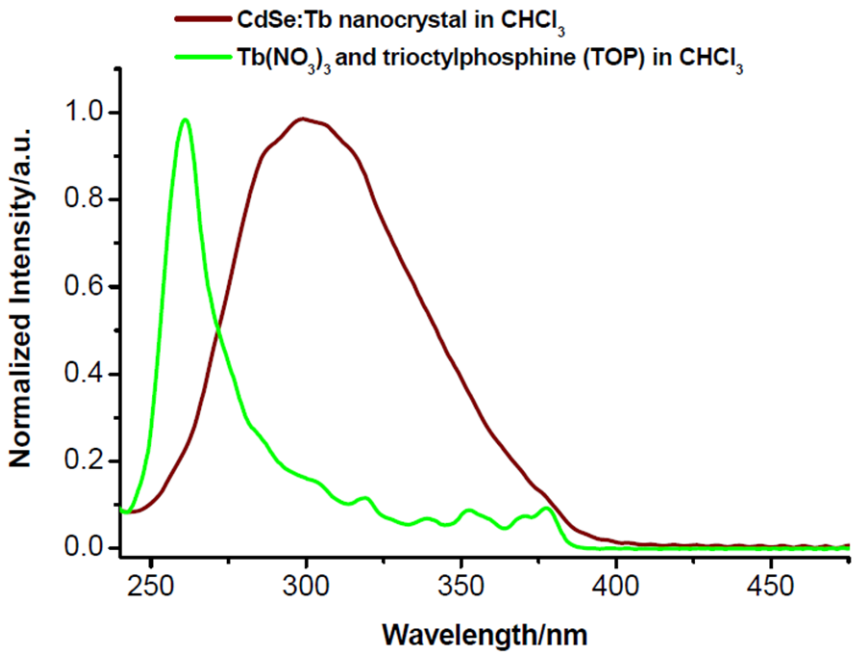

Figure 2-4. Normalized time-resolved excitation spectra of CdSe:Tb nanocrystals in $CHCl_3$ (magenta) and of a solution of TOP, $Tb(NO_3)_3$ in $CHCl_3$ (green); λ_{em} = 545nm, room temperature. CdSe:Tb nanocrystals used for this experiment have been collected 30 seconds after injection of Se.

To quantify the overall luminescence efficiencies of the nanocrystals and the Tb^{3+} metal ion, quantum yields were recorded in steady-state and time-resolved modes. The average overall quantum yield at room temperature for the nanocrystals upon excitation at 300, 305, and 310 nm was determined to be 2.5(±0.1) x 10^{-2}. The quantum yield for the Tb^{3+}-centered emission was determined to be 3(±1) x 10^{-4}. These relatively low quantum yield values are compensated by the high extinction coefficient of **SCNC**s and the large number of lanthanide emitters. We expect that coating the nanocrystals will increase both quantum yields. Two different types of energy transfer mechanisms can be postulated to explain sensitization of the Tb^{3+} cations: (1) Förster[53]-type of energy transfer (dipole-dipole interaction) and (2) Dexter[54]-type of energy transfer

(energy transfer via electron exchange). At present, we do not have sufficient data to quantify the relative contribution of these two mechanisms to the overall energy transfer. Additional experiments are currently being done to address this question.

The time profile of Tb^{3+} luminescence was measured at room temperature. Excitation of CdSe:Tb at 354 nm in a 60/40 mixture of toluene/THF (containing 6000 ppm water, which is efficient at quenching Tb^{3+} luminescence)[36,42] shows a dual exponential decay law, with time constants of 4.7 ± 0.2 and 2.02 ± 0.06 ms. These two lifetime values are tentatively attributed to Tb^{3+} located in the interior and at the surface of the nanocrystals, respectively. As a comparison, the Tb^{3+} luminescence lifetime of a solution of $Tb(NO_3)_3$ in the presence of undoped CdSe nanocrystals has a monoexponential decay with a time constant of 1.81 ± 0.01 ms. The longest Tb^{3+} luminescence lifetime recorded for CdSe:Tb **SCNC**s is more than double this value. These results indicate that some of the Tb^{3+} cations are well protected by the **SCNC** from water quenchers and suggest that the Tb^{3+} is a dopant of the nanocrystal (surface and/or core).[52] These lifetimes are long in comparison to luminescence lifetimes commonly observed for lanthanide complexes containing organic ligands in solution.[42]

2.5 CONCLUSIONS

This work suggests that incorporating lanthanide cations into **SCNC**s could lead to a new family of luminescent reporters with improved photophysical properties. These preliminary results validate the proposed approach to synthesizing CdSe:Tb **SCNC**s, with the electronic structure of the nanocrystals serving as an antenna for the lanthanide cation. The long lanthanide

luminescence lifetimes observed support the hypothesis that the Tb^{3+} cations are well protected from non-radiative deactivation by the **SCNC**. Since both Tb^{3+} and nanocrystal emission can be detected simultaneously, and the Tb^{3+} signal is easily discriminated through time-resolved measurements, this species has a double luminescence signature. This feature is important for biodetection agents, where a doubly verified signal helps identify false results, either negative or positive.

Acknowledgements

We would like to thank Cole VanOrmer (Department of Engineering, University of Pittsburgh) for the TEM and EDS work, Professor David H. Waldeck for his help and advice, and the Electronic, Machine, and Glass shops of the University of Pittsburgh Chemistry Department.

3.0 LANTHANIDE SENSITIZATION IN II-VI SEMICONDUCTOR MATERIALS: A CASE STUDY WITH TERBIUM (III) AND EUROPIUM (III) IN ZINC SULFIDE NANOPARTICLES

3.1 CHAPTER PREFACE

The aim of this work was a more thorough investigation into the energy transfer mechanisms between semiconductor nanoparticles and luminescent lanthanide cations. Here we intended to expand the strategies describeded in Chapter 2.0 to include other types of band gap nanomaterials. Specifically, we chose to focus on ZnS as a more biologically and environmentally relevant alternative to CdSe. In addition to our synthetic experimental work, we engaged in a collaboration with physical chemists to elucidate the energy transfer mechanisms. The material contained in this chapter has been accepted for publication as a full paper in *The Journal of Physical Chemistry*; the figures and tables in this chapter have been reproduced with permission from *J. Phys. Chem. A.* DOI: 10.1021/jp109786w. Copyright 2010 American Chemical Society; the full citation is listed as Reference 55 in the bibliography section.[55]

List of authors: Prasun Mukherjee, Chad M. Shade, Adrienne M. Yingling, Daniel N. Lamont, David H. Waldeck, Stéphane Petoud

Author contribution: The author of this dissertation was responsible for approximately half of the nanoparticle syntheses reported in this chapter in addition to collecting the HRTEM images and some of the photophysical characterization including Ln^{3+}-centered luminescence lifetimes, providing interpretation of the results and contributing to the overall conception of the project and preparation of the published manuscript.

3.2 ABSTRACT

This work explores the sensitization of luminescent lanthanide Tb^{3+} and Eu^{3+} cations by the electronic structure of zinc sulfide (ZnS) semiconductor nanoparticles. Excitation spectra collected, while monitoring the lanthanide emission bands, reveals that the ZnS nanoparticles act as an antenna for the sensitization of Tb^{3+} and Eu^{3+}. The mechanism of lanthanide ion luminescence sensitization is rationalized in terms of an energy and charge transfer between trap sites and is based on a semi-empirical model, proposed by Dorenbos and coworkers,[56-61] to describe the energy level scheme. This model implies that the mechanisms of luminescence sensitization of Tb^{3+} and Eu^{3+} in ZnS nanoparticles are different; namely Tb^{3+} acts as a hole trap, while Eu^{3+} acts as an electron trap. Further testing of this model is made by extending the studies from ZnS nanoparticles to other II-VI semiconductor materials; namely, CdSe, CdS, and ZnSe.

3.3 INTRODUCTION

Historically, luminescent lanthanides have been extensively used as phosphors, and more recently they have attracted interest as a new class of luminescent probes and sensors for biological applications.[62-69] Lanthanides have a number of luminescence properties that make them an attractive alternative to organic fluorophores in bioanalytical applications and biological imaging. Whereas typical organic fluorophores are prone to photobleaching mechanisms, lanthanide luminescence is highly resistant to photobleaching and hence allows longer experiment times or their repetition. The sharp atom-like lanthanide emission bands and the negligible overlap between the bands of different lanthanide ions makes them promising candidates for multiplex biological assays through spectral discrimination or for barcode types of applications.[70] Moreover, the long lanthanide luminescence lifetimes (millisecond time range for lanthanide emitting in the visible) allows their signal to be distinguished from the background autofluorescence of biological media (nanosecond time range) through temporal discrimination for improved detection sensitivity.

A major requirement for the use of lanthanides as biological imaging agents is the detection sensitivity they can provide which includes the emission of a sufficient number of photons in order to obtain good detection sensitivity. The direct excitation of lanthanides is inefficient because most of the interesting f-f transitions are Laporte forbidden.[28,71] As a consequence, the molar extinction coefficients of lanthanide ions are very low[72] ($\leq 10\ M^{-1}cm^{-1}$ as opposed to 10^4-$10^5\ M^{-1}cm^{-1}$ for typical organic fluorophores). The low number of absorbed photons will result in a low number of emitted photons. To overcome this limitation, the concept of sensitization through an antenna effect has been established.[68,73-83] In this process, photons

from the excitation light are absorbed by a chromophore with high extinction coefficient that transfers the energy to the accepting levels of the lanthanide ions, thus creating a high population of electronically excited lanthanide ions and enhancing the amount of luminescent photons. In addition to efficient energy pumping by this antenna effect, it is also important to prevent the quenching of lanthanide ion excited states by nonradiative energy transfer to the overtones of high frequency vibrational modes such as –OH, –NH and –CH.[10] For applications under biological conditions, it is especially important to protect the lanthanide ions from water molecules.

Semiconductor nanoparticles that contain lanthanide ions are advantageous for biological applications over the undoped nanoparticles because the sharp emission signal corresponding to each lanthanide ion has a unique spectroscopic signature for spectral identification and unambiguous identification. Depending on the lanthanide cations, there is a broad choice of emission wavelength throughout the entire visible and near-IR spectral regions. The near-IR luminescence of lanthanide cations is of special benefit for biological applications because i) the absence of native autofluorescence of tissues in the near-IR region; therefore, a good signal-to-noise ratio is obtained for more sensitive detection, and ii) near-IR photons can cross significant depths of tissues for potential non-invasive investigation. Recently Chengelis et. al. reported on the incorporation of terbium ions (Tb^{3+}) in CdSe nanoparticles.[39] Although Tb^{3+} luminescence sensitization was observed for the CdSe/Tb^{3+} system, its emission was obscured by the more intense CdSe bandgap emission in steady-state mode and a time-gated method was required to specifically identify the Tb^{3+} luminescence. From the excitation spectrum, collected upon monitoring the 545 nm centered Tb^{3+} emission signal, it is evident that part of the excitation energy is transferred from the CdSe nanoparticle states to the accepting energy levels of Tb^{3+}

ions demonstrating that the electronic structure of the nanoparticle can act as an antenna. While the CdSe/Tb^{3+} system demonstrates the use of the nanoparticles as an antenna, it has intrinsic limitations, namely, the efficiency of CdSe in sensitizing Tb^{3+} luminescence was low, and the Cd and Se components of the nanoparticles are toxic, thus limiting their applicability for studying biological systems and for diagnostic purposes. To overcome these two drawbacks, we have created a ZnS/Tb^{3+} nanoparticle system, in which the individual constituents are non-toxic or less toxic and more environmentally friendly. Moreover, as the bulk band gap of ZnS is larger than that of CdSe (3.6 eV as opposed to 1.7 eV),[84] the electronic structure of ZnS is expected to sensitize lanthanides more efficiently than CdSe because it ensures a more favorable match of lanthanide acceptor energy levels with respect to the nanoparticle donating energy levels.[61] This work reports results on ZnS nanoparticles containing three different lanthanides: two visible-emitting lanthanides, Tb^{3+} and Eu^{3+} in ZnS nanoparticles, and corresponding control experiments with Gd^{3+} (which does not have accepting electronic levels in the relevant energy range). ZnS nanoparticle systems without lanthanides were also studied for comparison. Both steady-state and time-resolved luminescence measurements demonstrate that ZnS acts as an efficient antenna to sensitize Tb^{3+} and Eu^{3+} luminescence. A comparison with other II-VI materials; (namely, Tb^{3+} incorporated in CdSe, CdS and ZnSe), is made in order to elucidate the energy transfer mechanism between the lanthanide and the nanoparticle host.

Understanding the mechanism of lanthanide luminescence sensitization is of main importance for controlling the performance and properties of novel optical materials. Because lanthanide ions behave as hard acids, they bind strongly to hard bases, following the preference order O>N>S. Various researchers have devoted considerable effort to understanding and exploiting the mechanisms for the luminescence sensitization of lanthanide ions in

semiconductor materials. Some of the discussed mechanisms are based on a defect related Auger transition model,[85-87] a resonant energy transfer model,[88] bound exciton models[79,89] and shallow donor (or acceptor) models.[90] It is generally believed that exciton recombination plays a key role in the luminescence sensitization of lanthanide cations. Although a number of researchers have discussed lanthanide luminescence in bulk semiconductors[91-101] and semiconductor nanoparticles,[102-114] the mechanism of lanthanide luminescence sensitization is still not fully elucidated and does not allow the synthesis of lanthanide-based nanomaterials with predictable properties. The mechanism of Tb^{3+} luminescence sensitization in bulk ZnS has attracted considerable attention. For example, Anderson[73] finds that the process includes (a) a donor level related to Tb^{3+} [$6s^2 5d^1$] that lies 0.4 eV below the conduction band; the $4f^8$ levels were assumed to be located somewhere below the valence band, (b) a hole trap that lies 1.02 eV above the valence band (assumed to be a copper-related site),[115,116] and (c) that the excitation of the $4f^8$ electronic system occurs during recombination of the electron-hole pair in these traps. While these efforts provide a useful framework for the current studies, the luminescence sensitization of Tb^{3+} and Eu^{3+} in ZnS nanoparticles is not well understood. Previous studies have been limited by an inability to identify the location of lanthanide ground and excited states with respect to the valence and conduction bands of the semiconductor materials. In this work, the nature of sensitization in the ZnS nanoparticles is discussed in light of the model proposed by Dorenbos,[56-61] for the relative energetics of the lanthanide ions in the host semiconductor.

3.4 EXPERIMENTAL

Chemicals. Trioctylphosphine [TOP] (90%), zinc stearate (tech.), octadecene (90% tech.), and tetracosane (99%) were purchased from Sigma-Aldrich-Fluka. Chloroform was purchased from J. T. Baker. Sulfur, toluene, and methanol were purchased from Fisher Scientific. Terbium (III) nitrate (99.9%) was purchased from Strem, europium (III) nitrate (99.99%) was purchased from Aldrich, and gadolinium (III) nitrate (99.99%) was purchased from Alfa Aesar. In all cases, hydrated lanthanide salts were used. n-Hexane and 1-octanol were purchased from Acros, and ethyl acetate was purchased from EMD. Argon gas was purchased from Valley National. All chemicals were used as purchased without purification, except toluene, which was distilled over sodium under nitrogen.

Nanoparticle Synthesis. All ZnS nanoparticle systems were synthesized using a non-coordinating solvent system consisting of octadecene and tetracosane. Zinc stearate and lanthanide nitrate salts were used as cation precursors and elemental sulfur served as the anion precursor. Tetracosane (4.0 g), octadecene (3.0 mL), and 0.68 mmol of zinc stearate were loaded into a three neck round bottom flask and heated to 350 °C while stirring under nitrogen. The lanthanide stock solution (0.12 mmol lanthanide nitrate dissolved in a combination of octadecene and trioctylphosphine oxide) was injected after approximately two hours of heating and allowed to stir within the reaction mixture for at least 30 minutes. The sulfur stock solution (sulfur powder dissolved in octadecene) was injected approximately 1 hour after the lanthanide stock solution. The reaction temperature was then decreased to a value between 270 °C and 300 °C for the duration of nanocrystal growth. Aliquots of sample were removed at varying growth times.

The resulting nanoparticles were then redispersed in an appropriate solvent for spectroscopic analysis.

ZnS nanoparticles without lanthanides incorporated were prepared using the methods described above, however the zinc stearate precursor was increased to 0.80 mmol and the lanthanide stock solution preparation was omitted.

Procedure for Chemical Purification of Nanoparticles. Solid nanoparticle samples were dissolved in approximately 5 mL of butanol with sonication. Methanol was then added to precipitate the nanoparticle, followed by 30 minutes of centrifugation. The precipitate was then re-dissolved in butanol, and the nanoparticles were subsequently precipitated with methanol and then centrifuged. The precipitate was then dissolved in approximately 2 mL of octanol to remove the insoluble reaction side products. The samples were then centrifuged for 30 minutes and methanol and 1 mL of ethyl acetate were added to the decantant. This was then followed by 30 minutes of centrifugation, discarding the decantant, and drying the precipitate under flowing nitrogen.

Steady-state Optical Measurements. Steady-state absorption spectra were obtained on an Agilent 8453 UV-visible spectrophotometer with 1-nm resolution. Steady-state excitation and emission spectra were recorded using a Jobin Yvon Horiba Fluorolog-322 with a 5-nm bandpass; spectra were corrected for excitation and emission (lamp, detector and monochromator). A 1-cm pathlength quartz cuvette was used for the measurements. All measurements were performed at room temperature.

Quantum Yields. Absorption spectra were recorded on either a Perkin-Elmer Lambda 9 Spectrometer coupled to a personal computer using software supplied by Perkin-Elmer or on an Agilent 8453 UV-visible spectrophotometer. Quantum yields were recorded by the relative method using references. Steady-state luminescence quantum yields were measured using quinine sulfate reference solution (solvent H_2SO_4 1N, Φ=0.546).[49] Time-gated luminescence quantum yields were measured using [Tb(H_{22}IAM)] reference solution (solvent water, Φ=0.59).[40] Spectra were corrected for the instrumental response. The quantum yields were calculated using Equation 3-1:

$$\frac{\Phi_x}{\Phi_r} = \frac{A_r(\lambda_r)\cdot I(\lambda_r)\cdot \eta_x^2 \cdot D_x}{A_x(\lambda_x)\cdot I(\lambda_x)\cdot \eta_r^2 \cdot D_r}$$

Equation 3-1

where subscript r stands for the reference and x for the sample; A is the absorbance at the excitation wavelength, I is the intensity of the excitation light at the same wavelength, η is the refractive index (η = 1.333 in water, η = 1.496 in toluene, η = 1.446 in chloroform) and D is the measured integrated luminescence intensity. ZnS systems (λ_{ex} = 315, 320 and 325 nm) were measured in chloroform whereas ZnSe (λ_{ex} = 315, 320 and 325 nm) and CdSe (λ_{ex} = 300, 305 and 310 nm) systems were measured in toluene.

Lanthanide-centered quantum yields for ZnSe/Ln^{3+} and CdSe/Ln^{3+} were collected with the fluorimeter in time-gated mode whereas the contribution from lanthanide-centered emission was discriminated spectrally from the overall quantum yield. For the ZnS/Ln^{3+} systems

calculations were performed by integrating the narrow emission bands arising from the lanthanide cations in steady-state mode.

Time-Gated Measurements. Time-gated excitation and emission spectra were collected with a Varian Cary Eclipse fluorescence spectrophotometer with 10 nm and 20 nm bandpass for Tb and Eu samples respectively**.** The spectra were acquired with a delay time and a gate time of 0.2 ms and 5 ms, respectively. Using such a delay time, only lanthanide sharp bands are expected to appear in the spectra without any contribution from shorter lived nanoparticle bandgap emission. Both excitation and emission filters were set in auto mode in the software. All measurements were performed at room temperature.

Time-Resolved Measurements. The time-resolved luminescence decay kinetics was measured using the time-correlated single-photon counting (TCSPC) technique. Samples were excited with the frequency doubled output (centered at ~300 nm) of a synchronously pumped cavity dumped dye laser (Coherent Model 599) using rhodamine 6G as the gain medium; emission from the sample was collected at different wavelengths using a monochromator. The instrument response function had a full-width–at-half-maximum (FWHM) of ~40 ps. A 1-cm pathlength quartz cuvette was used for all the time-resolved measurements. All measurements were performed at room temperature. Experiments were done with a 1 MHz laser repetition rate. Lifetime values were found to be similar with 125 kHz (for ZnS/Tb) and 300 kHz (for ZnS/Gd and ZnS) repetition rate; these measurements were done at selected wavelengths. Lifetime decay traces were fitted by an iterative reconvolution method with IBH DAS 6 decay analysis software.

The Tb^{3+} and Eu^{3+} luminescence lifetime measurements were performed by excitation of solutions in 1 mm quartz cells (NSG Precision Cells, Inc.) using either a Xenon flash lamp or a Nd-YAG Continuum Powerlite 8100 laser (354 nm, third harmonic) as the excitation source. Emission was collected at a right angle to the excitation beam, and wavelengths were selected by means of the Spex FL1005 double monochromator or a Spectral Products CM 110 1/8 meter monochromator. The signal was monitored by a Hamamatsu R928 photomultiplier tube coupled to a 500 MHz bandpass digital oscilloscope (Tektronix TDS 620B). Signals from > 500 flashes were collected and averaged. Luminescence lifetimes were averaged using samples from several different batches. Luminescence decay curves were imported into Origin 7.0, and analyzed using the Advanced Fitting Tool.

Table 3-1. Luminescence Lifetime Parameters for Different Systems Studied.[a]

System	Growth time (min)	λ_{em} (nm)	a_1	τ_1 (ns)	a_2	τ_2 (ns)	a_3	τ_3 (ns)	$\langle\tau\rangle^b$ (ns)	χ^2
ZnS/Tb	1	400	0.64	0.26	0.31	2.0	0.05	7.9	1.2	1.28
ZnS/Tb	1	490	0.52	0.51	0.39	3.2	0.09	11.7	2.6	1.21
ZnS/Tb	1	520	0.48	0.53	0.41	3.3	0.11	11.8	2.9	1.13
ZnS/Tb	1	545	0.46	0.54	0.41	3.3	0.13	11.5	3.1	1.14
ZnS/Tb	20	390	0.67	0.21	0.28	1.6	0.05	7.1	0.94	1.46
ZnS/Tb	20	420	0.63	0.37	0.31	2.3	0.06	8.5	1.5	1.40
ZnS/Tb	20	450	0.60	0.45	0.33	2.6	0.07	9.6	1.8	1.34
ZnS/Tb	20	490	0.57	0.52	0.35	3.0	0.08	10.7	2.2	1.23
ZnS/Tb	20	515	0.55	0.55	0.36	3.2	0.09	11.0	2.4	1.14
ZnS/Tb	20	545	0.54	0.62	0.36	3.4	0.10	11.2	2.7	1.13
ZnS/Eu	1	500	0.35	0.35	0.49	3.3	0.15	9.8	3.2	1.47
ZnS/Eu	1	615	0.34	0.39	0.47	3.4	0.19	9.4	3.5	1.42
ZnS/Eu	1	618	0.39	0.30	0.43	3.1	0.18	9.1	3.1	1.26
ZnS/Eu	1	630	0.40	0.33	0.42	3.2	0.17	9.2	3.0	1.49
ZnS/Eu	1	660	0.43	0.31	0.40	2.9	0.17	8.7	2.8	1.33
ZnS/Eu	1	700	0.48	0.27	0.36	2.5	0.16	8.0	2.3	1.24
ZnS/Eu	24	400	0.49	0.30	0.41	2.3	0.10	8.3	1.9	1.48
ZnS/Eu	24	615	0.34	0.37	0.47	3.4	0.19	9.8	3.6	1.41
ZnS/Gd	1	390	0.74	0.14	0.23	1.4	0.03	7.1	0.64	1.74
ZnS/Gd	1	430	0.67	0.25	0.28	2.0	0.04	8.6	1.1	1.67
ZnS/Gd	1	470	0.62	0.37	0.33	2.7	0.05	10.5	1.6	1.62
ZnS/Gd	1	510	0.57	0.42	0.36	3.0	0.07	11.5	2.1	1.57
ZnS/Gd	1	550	0.55	0.45	0.37	3.2	0.08	11.9	2.4	1.52
ZnS/Gd	20	390	0.72	0.18	0.24	1.6	0.04	7.5	0.81	1.62
ZnS/Gd	20	430	0.65	0.30	0.30	2.1	0.05	8.8	1.3	1.49
ZnS/Gd	20	470	0.60	0.40	0.34	2.6	0.06	10.3	1.7	1.37
ZnS/Gd	20	510	0.54	0.47	0.37	3.0	0.09	11.2	2.4	1.31
ZnS/Gd	20	550	0.52	0.49	0.38	3.2	0.10	11.4	2.6	1.24
ZnS	1	390	0.73	0.12	0.24	0.96	0.03	4.9	0.47	1.34
ZnS	1	430	0.70	0.25	0.26	1.3	0.04	6.0	0.75	1.31

Table 3-1 (continued).										
ZnS	1	470	0.65	0.33	0.30	2.1	0.05	8.1	1.2	1.48
ZnS	1	510	0.57	0.34	0.36	2.4	0.07	9.1	1.7	1.32
ZnS	1	550	0.54	0.36	0.38	2.6	0.08	9.6	2.0	1.21
ZnS	20	390	0.75	0.26	0.22	2.1	0.03	19.0	1.2	1.58
ZnS	20	430	0.71	0.33	0.26	2.4	0.03	16.4	1.4	1.49
ZnS	20	470	0.65	0.35	0.31	2.5	0.04	12.7	1.5	1.39
ZnS	20	510	0.60	0.37	0.34	2.6	0.06	11.3	1.8	1.38
ZnS	20	550	0.58	0.38	0.35	2.8	0.07	11.0	2.0	1.22

[a] $\lambda_{ex} \approx 300$ nm. [b] $\langle \tau \rangle = \sum a_i \tau_i$

Table 3-2. Luminescence Lifetime Parameters for Different Systems Studied.[a]

System	**Growth time (min)**	**λ_{em} (nm)**	**a_1**	**τ_1 (ns)**	**a_2**	**τ_2 (ns)**	**a_3**	**τ_3 (ns)**	**$\langle\tau\rangle^b$ (ns)**	**χ^2**
ZnS/Tb	1	400	0.67	0.4	0.30	2.5	0.03	10	1.3	1.41
ZnS/Tb	1	490	0.46	0.4	0.41	2.5	0.13	10	2.5	1.31
ZnS/Tb	1	520	0.41	0.4	0.43	2.5	0.16	10	2.8	1.23
ZnS/Tb	1	545	0.38	0.4	0.44	2.5	0.18	10	3.1	1.23
ZnS/Tb	20	390	0.73	0.4	0.25	2.5	0.02	10	1.1	1.85
ZnS/Tb	20	420	0.65	0.4	0.31	2.5	0.04	10	1.4	1.54
ZnS/Tb	20	450	0.58	0.4	0.36	2.5	0.06	10	1.7	1.42
ZnS/Tb	20	490	0.52	0.4	0.39	2.5	0.09	10	2.1	1.32
ZnS/Tb	20	515	0.48	0.4	0.40	2.5	0.12	10	2.4	1.27
ZnS/Tb	20	545	0.45	0.4	0.42	2.5	0.13	10	2.5	1.17
ZnS/Eu	1	500	0.37	0.4	0.49	3.5	0.14	10	3.3	1.54
ZnS/Eu	1	615	0.34	0.4	0.49	3.5	0.17	10	3.6	1.47
ZnS/Eu	1	618	0.39	0.4	0.46	3.5	0.15	10	3.3	1.34
ZnS/Eu	1	630	0.41	0.4	0.45	3.5	0.14	10	3.1	1.56
ZnS/Eu	1	660	0.45	0.4	0.43	3.5	0.12	10	2.9	1.45
ZnS/Eu	1	700	0.52	0.4	0.39	3.5	0.09	10	2.5	1.40

Table 3-2 (continued).										
ZnS/Eu	24	400	0.57	0.4	0.37	3.0	0.06	10	1.9	1.80
ZnS/Eu	24	615	0.34	0.4	0.48	3.5	0.18	10	3.6	1.42
ZnS/Gd	1	390	0.77	0.4	0.21	2.5	0.02	10	1.0	2.48
ZnS/Gd	1	430	0.69	0.4	0.27	2.5	0.04	10	1.4	1.88
ZnS/Gd	1	470	0.59	0.4	0.34	2.5	0.07	10	1.8	1.69
ZnS/Gd	1	510	0.59	0.4	0.31	2.5	0.10	10	2.0	1.77
ZnS/Gd	1	550	0.48	0.4	0.40	2.5	0.12	10	2.4	1.79
ZnS/Gd	20	390	0.78	0.4	0.20	2.5	0.02	10	1.0	2.18
ZnS/Gd	20	430	0.68	0.4	0.28	2.5	0.04	10	1.4	1.56
ZnS/Gd	20	470	0.57	0.4	0.36	2.5	0.07	10	1.8	1.38
ZnS/Gd	20	510	0.49	0.4	0.40	2.5	0.11	10	2.3	1.42
ZnS/Gd	20	550	0.45	0.4	0.41	2.5	0.14	10	2.6	1.40
ZnS	1	390	0.86	0.4	0.13	2.5	0.01	10	0.77	1.88
ZnS	1	430	0.82	0.4	0.17	2.5	0.01	10	0.85	1.52
ZnS	1	470	0.68	0.4	0.29	2.5	0.03	10	1.3	1.59
ZnS	1	510	0.55	0.4	0.39	2.5	0.06	10	1.8	1.41
ZnS	1	550	0.51	0.4	0.41	2.5	0.08	10	2.0	1.29
ZnS	20	390	0.79	0.4	0.17	2.5	0.04	15	1.3	1.92
ZnS	20	430	0.72	0.4	0.25	2.5	0.03	15	1.4	1.45
ZnS	20	470	0.68	0.4	0.29	2.5	0.03	15	1.4	1.45
ZnS	20	510	0.59	0.4	0.33	2.5	0.08	10	1.9	1.47
ZnS	20	550	0.55	0.4	0.36	2.5	0.09	10	2.0	1.25

[a] $\lambda_{ex} \approx 300$ nm. Lifetime parameters kept fixed at 0.4 ns, 2.5 ns and 10 ns in fitting, lifetime values were changed in the cases where the χ^2 value was high. [b] $< \tau >= \sum a_i \tau_i$

Calculation of Förster Energy Transfer. The rate of the nonradiative energy transfer k_{ET} in a Förster energy transfer mechanism is given by Equation 3-2.[117,118]

$$k_{ET} = \frac{1}{\tau_F}\left(\frac{R_0}{R}\right)^6$$

Equation 3-2

$$R_0^{\,6} = \frac{9000(\ln 10)\Phi_D}{128\pi^5 n^4 N}\,\frac{2}{3}\,\frac{\int_0^{\infty} F_D(\bar{\nu})\,\varepsilon_A(\bar{\nu})\,\bar{\nu}^{-4}\,d\bar{\nu}}{\int_0^{\infty} F_D(\bar{\nu})\,d\bar{\nu}}$$

Equation 3-3

In this expression τ_F is the average lifetime of the donor (assumed as 1 ns for ZnS nanoparticle, see Table 3-1 and Table 3-2), R is the distance between the donor and acceptor, R_0 is the critical distance at which the rate of energy transfer is equal to the inverse of fluorescence lifetime of the donor and described by Equation 3-3, n is the refractive index of the medium (considered as 2.4 for ZnS, 2.5 for CdS, 2.5 for ZnSe and 2.5 for CdSe),[119,120] N is Avogadro's number, Φ_D is the fluorescence quantum yield of the nanoparticle donor (assumed arbitrarily as 0.20), $F_D(\bar{\nu})$ is the nanoparticle donor emission spectrum in absence of acceptor lanthanide ions on a wavenumber scale, and $\varepsilon_A(\bar{\nu})$ is the molar extinction coefficient of the lanthanide ions (in $M^{-1}cm^{-1}$) on a wavenumber scale. The $\varepsilon_A(\bar{\nu})$ values considered in the calculation were the corresponding values in dilute acid.[72] The calculated J_F and R_0 values for various nanoparticles with 1 minute growth time and lanthanide ions are summarized in Table 3-3, corresponding calculations for the longer growth time samples yielded similar results.

Calculation of Dexter Energy Transfer. The rate of energy transfer in a Dexter energy transfer mechanism is given by Equation 3-4.[118]

$$k_{ET} = \frac{2\pi}{\hbar} K J_D \exp\left(-\frac{2R}{L}\right)$$

Equation 3-4

$$J_D = \frac{\int_0^\infty F_D(\bar{\nu})\varepsilon_A(\bar{\nu})d\bar{\nu}}{\int_0^\infty F_D(\bar{\nu})d\bar{\nu}\int_0^\infty \varepsilon_A(\bar{\nu})d\bar{\nu}}$$

Equation 3-5

In this expression $F_D(\bar{\nu})$ is the nanoparticle donor emission spectrum in absence of acceptor lanthanide ions on a wavenumber scale and $\varepsilon_A(\bar{\nu})$ is the molar extinction coefficient of the lanthanide ions (in $M^{-1}cm^{-1}$) on a wavenumber scale, K is a parameter that is related to the electronic coupling parameter between the donor and acceptor and has no direct analog to measured experimental parameters, R is the distance between the donor and acceptor, and L is the average van der Waals radius between the initial and final molecular orbital of the donor and acceptor. The $\varepsilon_A(\bar{\nu})$ values considered in the calculation were the corresponding values in dilute acid.[72] The calculated J_D values (described by Equation 3-5) for various nanoparticles with 1 minute growth time and lanthanide ions are summarized in Table 3-3, corresponding calculations for the longer growth time samples yielded similar results.

Table 3-3. Comparison of the relevant parameters under Förster and Dexter energy transfer mechanisms in different systems studied.[a]

Donor Emission Spectrum	**Acceptor Absorption Spectrum**	**J_F ($M^{-1}cm^3$)**	**R_0 (Å)**	**J_D (cm)**
ZnS	Tb^{3+}	6.9×10^{-20}	2.5	6.8×10^{-5}
ZnS	Eu^{3+}	2.0×10^{-19}	3.0	1.1×10^{-4}
ZnS/Tb	Tb^{3+}	8.0×10^{-20}	2.6	8.4×10^{-5}
ZnSe	Tb^{3+}	6.4×10^{-20}	2.4	6.5×10^{-5}
ZnSe/Tb	Tb^{3+}	5.8×10^{-20}	2.4	5.7×10^{-5}
CdS/Tb	Tb^{3+}	9.3×10^{-20}	2.5	1.0×10^{-4}
CdSe/Tb	Tb^{3+}	9.6×10^{-20}	2.6	1.0×10^{-4}

[a] In cases where the Tb^{3+} incorporated spectrum were used for the donor emission, Tb^{3+} luminescence contribution was removed before the calculation of the overlap integral.

Table 3-4. Comparison of Ln^{3+} luminescence intensities from time-gated measurements [λ_{em} (Tb^{3+}) = 545 nm, λ_{em} (Eu^{3+}) = 616 nm] with different excitation wavelength.[a]

System	I_{em} [λ_{ex} = 300 nm] : I_{em} [λ_{ex} = 375 nm] : I_{em} [λ_{ex} = 440 nm]
ZnS/Tb	1 : 0.04 ± 0.01 : 0.00013 ± 0.00005
ZnS/Eu	1 : 0.23 ± 0.08 : 0.02 ± 0.01

[a] Values in the table represent the average and standard deviation from multiple measurements using different solutions.

3.5 RESULTS AND DISCUSSION

HRTEM Imaging. High resolution Transmission Electron Microscopy (HRTEM) images were obtained using a JEOL-2100 CF instrument operating between 120 kV and 200 kV. A representative TEM image is shown in Figure 3-1. The size distribution of ZnS:Tb nanoparticles was calculated using Image J software and found to be 3.3 ± 0.4 nm in average diameter. Both the stoichiometry (lanthanide to zinc ratio) and the location of the lanthanides in the nanoparticles are not yet fully quantified. These data will be reported in a more comprehensive future study that will address the stoichiometry and the relative importance of the lanthanide locations – on the surface or in the bulk of the nanoparticles.

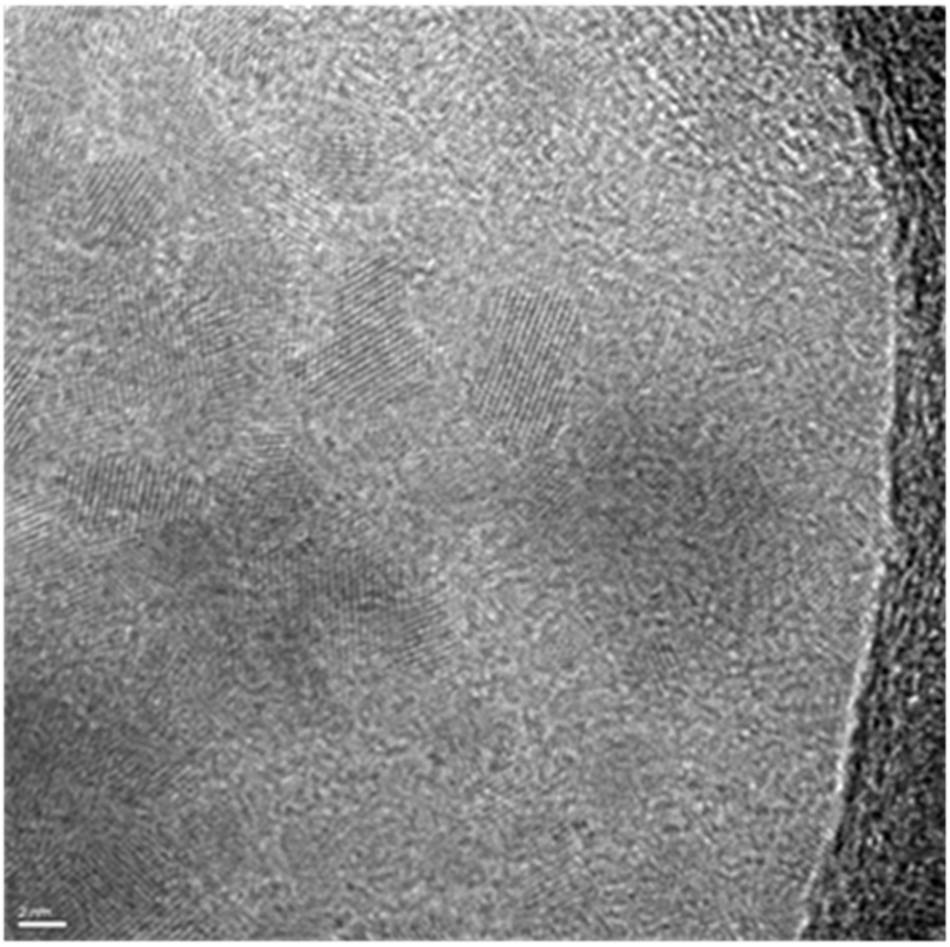

Figure 3-1. Representative HRTEM image of synthesized ZnS/Tb nanoparticles. A 2 nm scale bar is shown on the bottom left of the image.

Absorption Spectra. Representative absorption spectra of ZnS nanoparticles dissolved in chloroform are shown in Figure 3-2 for two different growth times. The absorption spectra reveal characteristic bands centered at ~290 nm and ~360 nm. The band with an apparent maximum at ~290 nm shows a small dependence on growth time and is attributed to the lowest energy exciton band of the nanoparticle. The ~360 nm band is probably associated with a transition involving a

trap state. The assignment of the ~290 nm band is corroborated by a simple estimation of the nanoparticle band gap, using a method proposed by Brus[121] (Equation 3-6), and found to be ~4.2 eV, corresponding to a ~290 nm band gap transition. In this model the change in bandgap with nanoparticle size is given by Equation 3-6:

$$E_g(\text{nano}) \approx E_g(\text{bulk}) + \frac{\hbar^2\pi^2}{2R^2}\left[\frac{1}{m_e} + \frac{1}{m_h}\right] - \frac{1.8e^2}{\varepsilon R}$$

Equation 3-6

Assuming E_g(bulk) = 3.6 eV, R = 1.65 nm (see above), $m_e = 0.25m_0$, $m_h = 0.59\ m_0$, ε = 8.3, E_g(nano) = 4.2 eV. The effective mass and dielectric constant values were adopted from the work by Murphy and coworkers.[122] We assign the long wavelength tail to the contribution from various surface states of the nanoparticles *(vide infra)*.

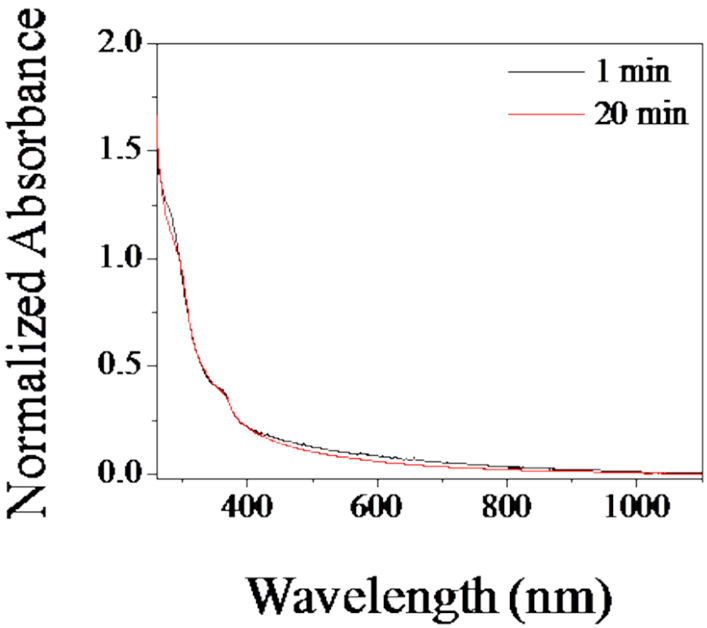

Figure 3-2. Representative normalized absorption spectra of a ZnS nanoparticle sample dissolved in chloroform obtained with growth times of 1 minute and 20 minutes. Spectra were normalized arbitrarily at 295 nm. The band at ~290 nm is associated with the band gap transition.

Luminescence Spectra. Figure 3-3 shows steady-state luminescence excitation and emission spectra for the lanthanide incorporated ZnS nanoparticles and for undoped ZnS nanoparticles (NP) without lanthanide ions, in $CHCl_3$. The spectra correspond to ~20 minutes NP growth time; the spectra corresponding to the analysis of the samples obtained after 1 minute growth times are similar.

ZnS/Tb Spectra. Figure 3-3B shows emission spectra for ZnS/Tb. For λ_{ex} = 300 nm, λ_{em} bands were identified at ~ 410 nm (ZnS band), 490 nm, 545 nm, 585 nm, and 620 nm (Tb^{3+} sharp bands); for λ_{ex} = 375 nm, λ_{em} bands were assigned at ~ 455 nm (ZnS band), 490 nm (weak

Tb^{3+} band), and 545 nm (Tb^{3+} band); and for λ_{ex} = 440 nm, a λ_{em} band was assigned at ~ 510 nm (ZnS band). An excitation wavelength dependence (red edge effect) is observed, i.e., with increase in λ_{ex} the emission band position shifts towards the red.

The excitation spectra (Figure 3-3A) also depend on λ_{em}. For λ_{em} = 410 nm (ZnS emission), the λ_{ex} bands were identified at ~ 260 nm and 350 nm; for λ_{em} = 450 nm (ZnS emission), the λ_{ex} bands were assigned at ~ 270 nm and 375 nm; and for λ_{em} = 545 nm (Tb^{3+} emission), a broad λ_{ex} feature appeared. To examine whether this wavelength dependence reflects size heterogeneity of the sample, efforts were made to improve the sample's size distribution. Thus centrifugation was performed at 20,000 rpm for 2 hours, a chemical purification by solvent precipitation method (see Experimental) was used, and the nanoparticle samples were dialyzed. None of these three methods yielded any noticeable change in the excitation wavelength dependent behavior. Based on these studies, the excitation wavelength dependent emission spectra are taken to reflect the energy distribution of surface states on the nanoparticles.

Sensitization of the lanthanide emission is evident in the steady-state emission spectra. Interestingly, the lanthanide emission intensity displays a wavelength dependence; when exciting the sample at 300 nm, terbium (Tb^{3+}) bands at ~490 nm and ~545 nm are clearly identifiable; whereas a 375 nm excitation results only in a weak Tb^{3+} emission. Excitation with 440 nm light results in no observable Tb^{3+} sensitization in the steady-state mode, however a weak Tb^{3+} sensitization can be observed in time-gated mode. This dependence on excitation energy correlates with the energy level mismatch between the donating excited states of ZnS nanoparticles and the accepting levels of Tb^{3+} ions (*vide infra*).

The broad excitation spectrum, with an absence of any atom-like band upon monitoring the Tb^{3+} emission, clearly indicates that the electronic structure of ZnS nanoparticles act as an antenna for the Tb^{3+} sensitization (and not from direct excitation of the lanthanide cations). Additional evidence for this interpretation has been obtained from the time-gated spectrum (*vide infra*).

The broad nature of the nanoparticle emission band indicates that the spectrum consists primarily of surface states or results from the combined emission of core states of variously sized nanoparticles. Peng and coworkers[123] have reported that the bandgap photoluminescence of ZnS nanoparticles is often mixed with a deep trap tail; namely a bandgap photoluminescence at ~310 nm (FWHM of 10-12 nm) and a broad band ~380 nm deep trap emission. A similar broad emission from ZnS nanoparticle surface states was also reported by Chen and coworkers.[124] Also Murphy and coworkers[122] reported a broad emission band centered at ~435 nm upon excitation of 5 nm ZnS nanoparticles at 270 nm, and have attributed that emission to sulfur vacancies, more generally to shallow electron traps. Although the band maximum is somewhat shifted, this reported blue emission is qualitatively similar to that observed in this study while exciting the sample at ~300 nm. While the chemical nature of the surface states remains unclear, it seems evident that they play a significant role in broadening the emission spectrum. The observation that 1 minute and 20 minutes growth time samples have identical emission spectra indicates that the surface state distribution does not change with the growth time for the synthetic parameters that were utilized here.

ZnS/Eu Spectra. Figure 3-3D shows the steady-state emission spectra for ZnS/Eu^{3+}. For λ_{ex} = 300 nm, a λ_{em} band was assigned at ~ 460 nm (ZnS band); for λ_{ex} = 375 nm, a λ_{em} band was found at ~ 455 nm (ZnS band); and for λ_{ex} = 440 nm, a λ_{em} band was found at ~ 510 nm

(ZnS band). These materials also display a red edge effect. Although this observation is qualitatively similar to the spectral change observed for the ZnS/Tb samples, some differences are evident; in particular, the emission spectrum for λ_{ex} = 300 nm has a similar emission band maximum as that for the spectrum with λ_{ex} = 375 nm. The absence of broad emission with band maximum centered at ~520 nm upon exciting the sample at ~300 nm indicates that the samples under investigation in the present work do not have significant emission from Eu^{2+}. While working on an extensive tabulation of charge transfer energies to Eu^{3+} in different inorganic materials, Dorenbos could not find any literature information of this data in sulfides.[58] In a previous study, Blasse et al. concluded that for systems in which E_{CT} (Eu^{3+}) < 2.5 eV, Eu^{3+} is not the stable valence state.[125] The unavailability of this parameter value was taken to be an indication of Eu^{2+} being the stable valence state for Eu compounds where $E_{CT} < E_F$, E_F being the Fermi energy level.[58] However, Dorenbos did not exclude the possibility of the existence of Eu^{3+} state in sulfides exclusively.[58] The luminescence from Eu^{3+} ions in sulfide systems is known.[106,107,109,111-114] The absence of broad emission with band maximum centered at ~520 nm upon exciting the sample at ~300 nm indicates that the samples under investigation in the present work do not have evident spectral contribution from Eu^{2+}. With λ_{ex} = 260 nm Chen and coworkers have reported a broad emission of Eu^{2+} in ZnS/Eu^{2+} nanoparticles with the band maximum located at ~530 nm and assigned it to the allowed $4f^6 5d$-$4f^7$ transition.[126] Similar broad Eu^{2+} emission was also observed by Shu-Man and coworkers in Eu doped ZnS nanoparticles with band maximum located at ~520 nm.[127]

Figure 3-3C shows the excitation spectra for ZnS/Eu^{3+}. For λ_{em} = 410 nm (ZnS emission), λ_{ex} bands were identified at approximately 255 nm, 270 nm, and 350 nm; for λ_{em} = 450 nm (ZnS emission), λ_{ex} bands were assigned at approximately 260 nm, and 370 nm; and for

λ_{em} = 620 nm (attributed to Eu^{3+} emission), a λ_{ex} band appeared at approximately 360 nm, with a broad excitation band centered at approximately 510 nm (assigned to a charge transfer transition from anion valence band to Eu^{3+} ions, *vide infra*).

The luminescence signal from the Eu^{3+} is not clearly evident in the steady-state spectra; however, it becomes prominent in time-gated mode (*vide infra*). Qualitatively, the less intense Eu^{3+} emission indicates that the ZnS nanoparticles are less efficient in sensitizing Eu^{3+}, as compared to the corresponding Tb^{3+} system. The broad band located on the emission spectrum probably reflects the contribution from surface states, as was discussed previously for ZnS/Tb samples. Similar to the observation found in ZnS/Tb system, no shift in band positions was observed in the emission spectra for 1 minute and 24 minutes growth time samples, suggesting that the surface states play an important role.

ZnS/Gd Spectra. Figure 3-3E and F show the excitation and emission spectra of ZnS/Gd. Other than the lack of Tb^{3+} emission bands, the nanoparticle spectra recorded on ZnS/Gd samples (exclusive of the ions 4f emission bands) were found to be very similar to those recorded for the ZnS/Tb samples in terms of band positions, excitation wavelength dependence and broadness of the spectra, indicating that luminescence sensitization of Tb^{3+} has a negligible impact on the nanoparticle emission in ZnS/Tb samples.

ZnS Spectra. Figures 3G and H show the excitation and emission spectra of ZnS. These spectra show an excitation wavelength dependence (red edge effect) that is similar to that observed for the ZnS/Tb and ZnS/Gd samples, indicating that the red edge effect arises from an intrinsic property of the ZnS nanoparticles and is not caused by the lanthanide ion. The broad nature of nanoparticle emission indicates that the spectrum is strongly influenced by the surface states, as are the samples where lanthanide ions are incorporated in the nanoparticle.

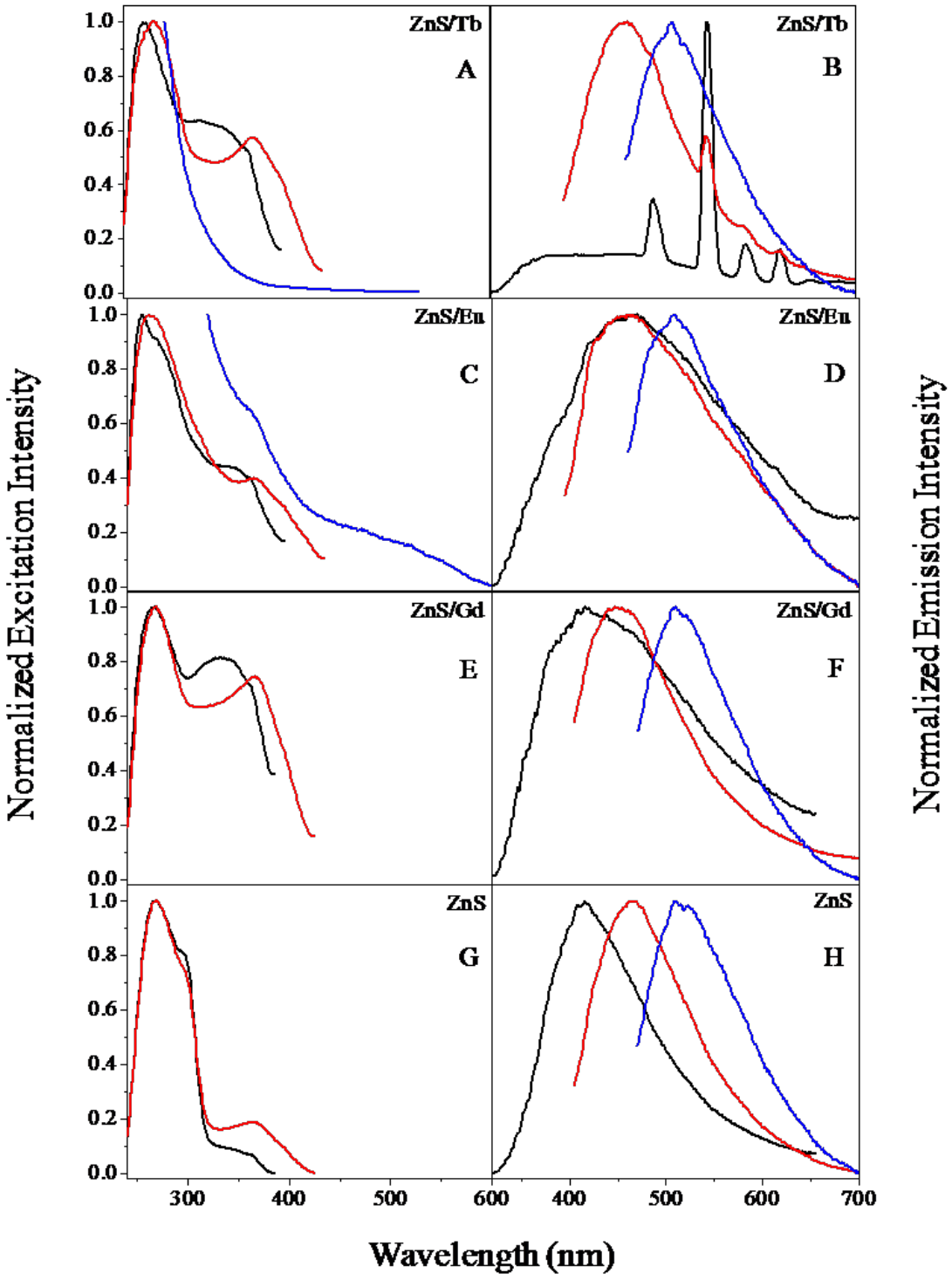

Figure 3-3. Left Panel: Normalized excitation spectra for λ_{em} = 410 nm (black), 450 nm (red), and 545 nm (blue) (only for ZnS/Tb); and 620 nm (blue) (only for ZnS/Eu). Right Panel: Normalized emission spectra for λ_{ex} = 300 nm (black), 375 nm (red), and 440 nm (blue). All of the spectra are taken in chloroform.

Time-gated Excitation and Emission Spectra. Representative time-gated excitation and emission spectra of ZnS/Tb (1 minute growth time) and ZnS/Eu (24 minutes growth time) nanoparticle samples in $CHCl_3$ are shown in Figure 3-4. The attempt to collect spectra for the ZnS/Gd and the ZnS nanoparticles under the same conditions only showed the background signal.

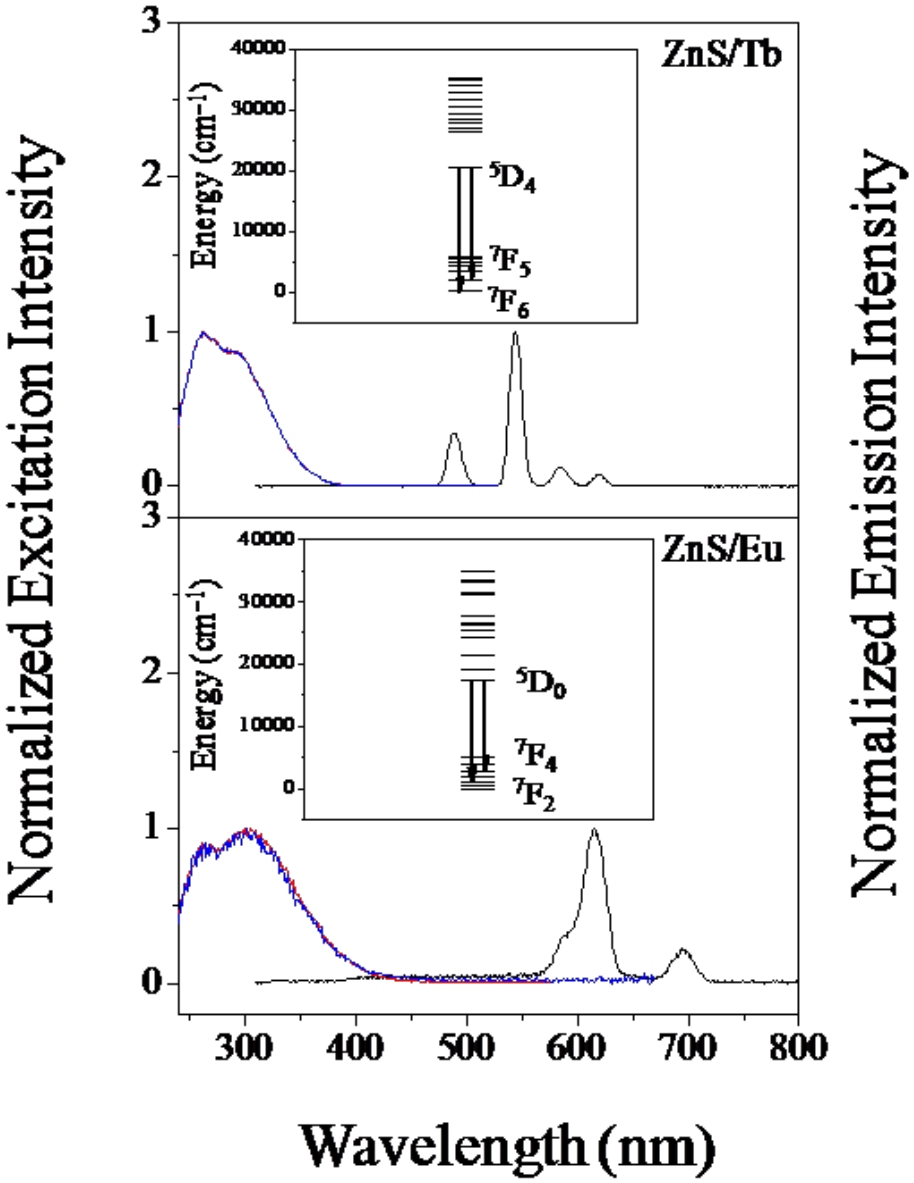

Figure 3-4. Normalized time-gated excitation and emission spectra of ZnS/Tb [λ_{ex} = 300 nm (black), λ_{em} = 490 nm (red), λ_{em} = 545 nm (blue)] (upper panel) and ZnS/Eu [λ_{ex} = 300 nm (black), λ_{em} = 616 nm (red), λ_{em} = 696 nm (blue)] (lower panel) nanoparticle samples in chloroform. Inset shows the electronic transitions associated with the 490 nm and 545 nm bands for ZnS/Tb, 616 nm and 696 nm bands for ZnS/Eu.

These spectra reveal that the electronic levels of ZnS nanoparticles can be used to sensitize the Tb^{3+} and Eu^{3+} emission. Sharp lanthanide emission bands were clearly visible for both the ZnS/Tb and the ZnS/Eu samples. For the ZnS/Tb sample, the bands with apparent maxima at 490 nm, 545 nm, 585 nm, and 620 nm were assigned to transitions from $^5D_4$ to $^7F_6$, $^7F_5$, $^7F_4$, $^7F_3$ respectively. For the ZnS/Eu sample, the bands at 590 nm, 616 nm, and 696 nm were assigned to transitions from $^5D_0$ to $^7F_1$, $^7F_2$, $^7F_4$ respectively.

The excitation spectra, recorded upon monitoring the lanthanide emission, reveal a broad excitation spectrum that is similar to the one recorded for the ZnS nanoparticles, upon monitoring their emission at either 410 nm or 450 nm. These results imply that the same energy route is used to sensitize emission of the ZnS and lanthanide emission, proceeding by energy transfer from the electronic states of the ZnS to the accepting levels of Tb^{3+} or Eu^{3+}. This conclusion is confirmed by the absence of sharp intra-configurational f-f bands in the excitation spectra, which would indicate direct excitation of lanthanide ions. It is important to note that the energy transfer from the 4f-5d excitation band of Tb^{3+}, and the charge transfer band of Eu^{3+}, are broad excitation bands and may contribute to the excitation spectrum. The 4f-5d excitation band in Tb^{3+} arises at ~4.8 eV,[57] and for Eu^{3+} (in sulfide compounds) the charge transfer band from the anion valence band to Eu^{3+} occurs at ~2.2 eV.[60] Although excitation at higher energies cannot rule out the possibility of some partial energy transfer from Tb^{3+} 4f-5d excitation band, the strongest Tb^{3+} and Eu^{3+} luminescence arises from exciting the sample in the 280 nm to 350 nm window and argues in favor of the ZnS bandgap excitation being the dominant excitation pathway. However, the luminescence of Tb^{3+} decreases more sharply with increasing wavelength than does that of Eu^{3+} (*vide infra*, see Figure 3-7 and Table 3-4), suggesting that the charge transfer excitation from the anion valence band to Eu^{3+} can also play a role in the Eu^{3+}

sensitization. It is important to appreciate that the charge transfer band in Eu^{3+} is weak and its contribution alone cannot account for the sensitization; in particular, that arising from exciting the sample at higher energies.

ZnS Luminescence Lifetime Measurements. Luminescence lifetime parameters for the different systems studied are summarized in Table 3-1. Table 3-1 shows values for all parameters in a sum of three exponentials varied in the fitting procedure. To see any obvious trend in the individual lifetime components, the decay data were also fit to a sum of exponentials with lifetime components fixed and varying only the amplitudes (Table 3-2). This procedure gives rise to somewhat lesser quality fits, as judged by the relative χ^2 value being higher; however they are adequate and reveal a clear relationship between lifetime components in the different systems. Note that the average lifetime remains relatively unchanged while varying all parameters versus fixing the lifetime components in the fitting procedure. Some representative luminescence decays for 1 minute growth time samples are shown in Figure 3-5.

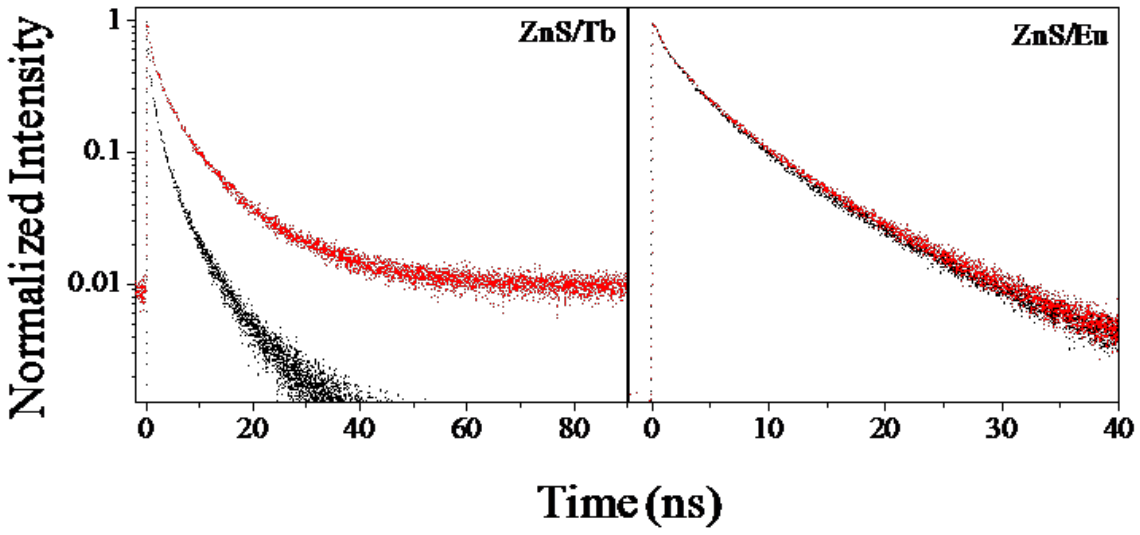

Figure 3-5. Representative luminescence decay plots shown for different nanoparticle systems studied in chloroform. For ZnS/Tb the black curve is at λ_{em} = 400 nm (no Tb^{3+} emission) and the red curve is at λ_{em} = 545 nm. For ZnS/Eu the black curve is λ_{em} = 500 nm (no Eu^{3+} emission) and the red curve is λ_{em} = 618 nm. Luminescence decay parameters are summarized in Table 3-1 and Table 3-2. The traces that have been recorded with a time windows that can only give information on nanoparticle electronic structure decay kinetics as they have shorter emission lifetimes.

ZnS/Tb Samples. The samples obtained with 1 minute and 20 minutes growth time behave similarly in terms of the decay kinetics. The experimental lifetime decays were typically fitted with the sum of three decaying exponentials, with a subnanosecond component which comprises ~60% of the emission, a 2-3 ns component with ~30% contribution, and the longest time component (~10 ns) with an amplitude of ≤~10%. The average lifetime increases continuously with increasing λ_{em}, which indicates that the emission band shifts with time. Attempts were made to monitor the Tb^{3+} emission by lowering the repetition rate to ~100 kHz

and increasing the full time window to 5 microseconds; in all cases only the ZnS emission was significant and no longer time component, which might be related to the Tb^{3+} emission, was observed. At all wavelengths, only the ZnS emission is important. Long lived Tb^{3+} emission appears as a baseline as shown in the left panel in Figure 3-5 at 545 nm.

ZnS/Eu Samples. ZnS/Eu behaves differently compared to all other systems. Namely, the longer lifetimes are more dominant in this sample and the amplitude of the subnanosecond component is much lower. This result suggests that a different energy transfer mechanism may take place. Balandin and coworkers[128] used a theoretical investigation of ZnO quantum dots to predict an increase in radiative lifetime for surface bound ionized acceptor-exciton complex, as compared to the lifetimes of confined excitons and surface bound ionized donor-exciton complexes. Such a type of complex would give rise to an increase in quantum yield. A comparison of the overall quantum yield of ZnS/Eu^{3+} (0.27 ± 0.02) to that of ZnS/Tb^{3+} (0.12 ± 0.03) corroborates this conclusion. The lack of a long-lived baseline in the ZnS/Eu sample, as compared to the ZnS/Tb sample, reflects the decreased luminescence of the Eu^{3+} bands in the steady-state spectra (Figure 3-3D).

ZnS/Gd Samples. Because of an energy level mismatch between the donating energy levels of the nanoparticles and the Gd^{3+} accepting levels no Gd^{3+} luminescence is observed. The fact that the ZnS/Gd^{3+} sample's nanoparticle emission is very similar to the ZnS emission of the ZnS/Tb^{3+} shows that the ZnS properties are not sensitive to the presence and nature of the lanthanide cations.

ZnS Samples. The average lifetime of the ZnS sample is comparable to that of the corresponding value in the presence of Tb^{3+} and Gd^{3+}. The ZnS sample's emission lifetime depends on λ_{em} in a fashion which is similar to that found for the lanthanide containing

nanoparticles. Thus the emission wavelength dependence appears to be an intrinsic property of the nanoparticles and is not associated with the presence of lanthanide ions (Tb^{3+}, Eu^{3+} and Gd^{3+}) in the system. The origin of the shift might be caused by decays from different donor-acceptor pairs that vary in distance, that is, close pairs emit with faster lifetime at higher energy and the distant pairs emit at lower energy.[129]

Lanthanide Ion Luminescence Lifetime Measurements. The luminescence lifetimes of the lanthanide cations were recorded using a low repetition rate Nd-YAG laser based setup. Experimental luminescence signals were fitted best by a biexponential decay for Tb^{3+} and Eu^{3+}. For ZnS/Tb^{3+}, the luminescence lifetime values were found to be 0.92 ± 0.01 ms and 2.50 ± 0.06 ms, whereas, for ZnS/Eu^{3+}, the corresponding values were 2.0 ± 0.01 ms and 3.6 ± 0.2 ms. The lifetimes for the Tb^{3+} emission band are similar to those observed for CdSe/Tb^{3+} in a previous study.[39] Two components could arise from different locations of the lanthanide ions in the nanoparticles; e.g. Tb^{3+} in the core of the ZnS nanoparticles may be better protected and have a longer luminescence lifetime, whereas the shorter lifetime component may originate from the surface located Tb^{3+} which experiences more solvent quenching. Examples of lifetime values for molecular complexes with well protected Tb^{3+} and Eu^{3+} cation coordination sites are 1.3 ms and 0.78 ms respectively.[130] The longer lifetime values recorded in the nanoparticle samples suggest that the lanthanide ions are better protected from quenching through vibrations located in solvent (and in the organic sensitizer for molecular complexes) when in the nanoparticles, as was reported previously by Chengelis et. al. for CdSe/Tb^{3+}.[39]

A Mechanism for Sensitization of Lanthanide Luminescence. This section considers the possibility of Förster (dipole-dipole interaction) and Dexter (exchange interaction) electronic energy transfer mechanisms in the studied systems, but argues that a different mechanism operates.

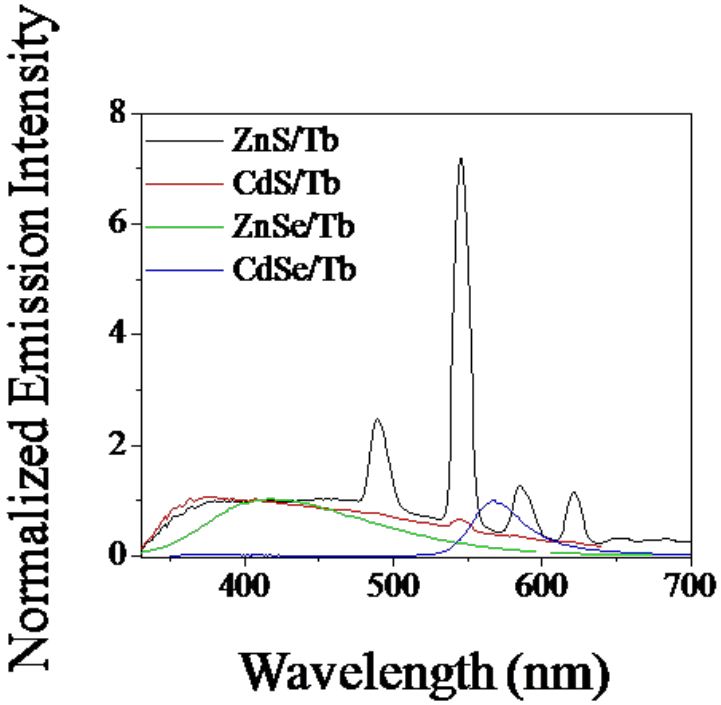

Figure 3-6. Emission spectra of different systems studied with $\lambda_{ex} \approx 300$ nm. The ZnS/Tb (black), CdS/Tb (red) and ZnSe/Tb (green) spectra are normalized to unity at 410 nm and the CdSe/Tb spectrum (blue) is normalized to unity at the band position. These spectra clearly put in evidence the difference in Tb^{3+} luminescence sensitization efficiency by different types of nanoparticles. The ZnSe/Tb spectrum is broken at ~600 nm to eliminate the second order band from the excitation light.

The rate of energy transfer under the Förster formulation depends on (a) the spectral overlap of donor and acceptor (J_F), (b) the donor luminescence quantum yield, (c) the donor luminescence lifetime, (d) the relative orientation of donor and acceptor transition dipoles, and (e) the distance between donor and acceptor. Most of the lanthanide transitions (dipolar electric) are formally forbidden and thus have a low oscillator strength and a low energy transfer rate by the Förster mechanism. The Förster overlap integral is $J_F \sim 10^{-19}$-10^{-20} $M^{-1}cm^3$ for the systems studied here, whereas the typical value of J_F for organic fluorophores is on the order of 10^{-13}-10^{-15} $M^{-1}cm^3$.[117] Assuming a $\Phi_D = 0.2$, one calculates an R_0 of ~ 2.5 Å for a lanthanide, which should be compared to a value of R_0 = 25 Å for a typical organic fluorophore. The ratio of the rate of energy transfer for organic fluoropohores in comparison with the ZnS/Tb^{3+} nanoparticle samples is ~ 10^6. Based on this estimate, we conclude that the Förster mechanism is less likely to play a significant role in the energy transfer process for the systems investigated in the present study. More straightforward evidence against the operation of the Förster energy transfer mechanism can be established from a comparison of J_F and R_0 values in the different systems studied (see Table 3-3). The Förster model predicts that the Eu^{3+} sensitization should be larger than Tb^{3+} in ZnS nanoparticles for a given distance, by ~ 3 times; in contrast, the experiments show that Tb^{3+} is at least two-fold more luminescent than Eu^{3+} (*vide infra*). In addition, a comparison of the host nanoparticles (ZnS, ZnSe, CdS, CdSe) indicates that the rate of energy transfer to Tb^{3+} should be very similar in ZnS and CdS; however, experiments demonstrate that ZnS is more efficient than CdS in sensitizing Tb^{3+} luminescence (Figure 3-6). This comparison assumes that both nanoparticles have similar luminescence lifetime in absence of acceptors and Tb^{3+} resides at almost equal distance from the nanoparticle sensitizing center.

The rate of energy transfer for the Dexter formulation depends on (a) the spectral overlap of donor emission and acceptor absorption (J_D) and (b) the electronic coupling factor. The Dexter mechanism can account for energy transfer involving forbidden transitions. The fact that the calculated J_D values are very similar in the different systems indicates that the experimental trend in energy transfer rates among the different nanoparticles can only be explained by a concomitant change in the electronic coupling parameter. While this possibility cannot be excluded, it seems unlikely. Thus, it seems that both the Förster and Dexter energy transfer mechanisms play a negligible role in the energy transfer mechanism of the studied systems.

A number of other plausible mechanisms for luminescence sensitization in lanthanide cations in semiconductors have been proposed. For example, Klik et al., in the context of InP/Yb^{3+},[78] rationalized Yb^{3+} sensitization in InP by the mechanism: (a) excitation of the semiconductor from the valence band to conduction band, (b) capturing of a free electron at a Yb^{3+} related trap, (c) generation of an electron-hole pair on the trap, and (d) non-radiative recombination of electron-hole pair to excite the Yb^{3+}, thus generating the Yb^{3+} emission. This model was based on earlier studies by Palm et al.,[79] Takahei and coworkers,[131,132] Thonke et. al.[133] and Needels et. al.[134] In molecular systems, Lazarides et al. has discussed a redox-based energy transfer mechanism in the context of molecular d-f complexes.[135] Mechanisms of this type require a detailed knowledge of the dopant energy levels in the host semiconductor.

Although much has been discussed about the lanthanide sensitization in semiconductor materials, considerably less is known about the energy level positions of lanthanide ions in the host material.[136-140] The location of dopant ion energy levels with respect to the valence and conduction bands of the host lattice is of extreme importance, because it is useful for predicting the luminescence properties, and the charge trapping and de-trapping kinetics. Recently,

Dorenbos[56-61] has addressed the problem of locating lanthanide impurity levels in a host crystal semi-empirically and developed a model that relies on three host dependent parameters: (a) the charge transfer energy from the anion valence band to Eu^{3+}, (b) the redshift of the first 4f to 5d transition in appropriate lanthanide ions, and (c) the band gap of the semiconductor material. The fundamental assumptions in this method are that the binding energies of the 4f electrons follow a universal trend and that the charge transfer energy between the anion valence band and Eu^{3+} is equal to the energy gap between the valence band of the host material and the ground state of Eu^{2+}. Once the Eu^{2+} ground state energy level is assigned, all other energy levels can be predicted according to the trend in binding energies. The energy diagram in Figure 3-7 uses this method to predict the energy levels of lanthanide ions in bulk II-VI semiconductor materials. In this diagram the charge transfer energy was obtained by using Jörgensen's relationship between the charge transfer energy and the Pauling electronegativity of the anions.[141] For sulfides, selenides and tellurides, we have assumed the charge transfer energy values of 2.17, 2.06 and 0.34 eV respectively. The value (2.17 eV) for sulfide compounds is in good agreement with the assignment of the charge transfer band (~2.43 eV) in the ZnS/Eu system (vide infra). The parameter values in this scheme were obtained from the work of Dorenbos and coworkers[59] and the ground state energies of lanthanides were placed in accordance to the systematic trend of 4f electron binding energies of trivalent lanthanide ions in narrower band gap materials. The energy difference between the 4f ground states of Eu^{3+} and Eu^{2+} was assumed to be 5.70 eV.[60] The higher lying energy levels of Tb^{3+} and Eu^{3+} were placed from the tabulation of Carnall and coworkers for trivalent lanthanide aquo ions.[142,143] The values of the energy levels estimated with this calculation approach compare well to existing data. Wen-lian and coworkers[108] have shown that the Tb^{3+} ground and excited energy levels in ZnS nanoparticles are located at 0.9 eV above

the valence band and 0.5 eV below the conduction band, respectively. In a separate study, Chen and coworkers[126] have placed the ground state of Eu^{2+} at 1.6 eV above the valence band of bulk ZnS. Although these values do not match exactly with the values reported in this work, they show sufficiently good qualitative agreement. Considering the typical error of ± 0.5 eV, estimated by Dorenbos, the agreement with the available literature is reasonable. It has to be noted that as long as any systematic error in assigning these energy level values is relatively constant, it should not change the conclusions discussed here.

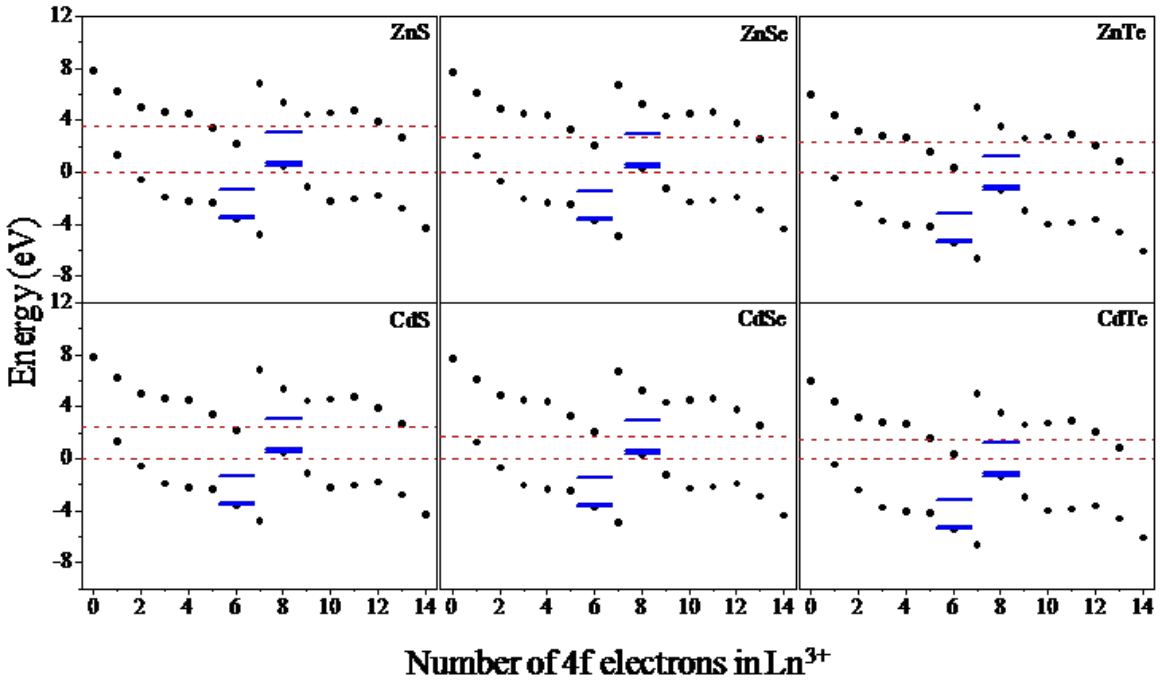

Figure 3-7. Energy level diagram of lanthanide (III) ions in different II-VI semiconductor materials based on the method proposed by Dorenbos.[56-61] At each abscissa value, the lower and higher solid circles are the ground state energy of lanthanide (III) and lanthanide (II) ions respectively. The blue solid horizontal lines at x = 6 and 8 represents the ground and excited states of Eu^{3+} and Tb^{3+} ions. The red dashed lines represent the bulk band gap values; the valence band energy is arbitrarily set at zero. It is worth noting that Tb^{3+} is a potential hole trap in II-VI sulfide and selenide compounds and Eu^{3+} can potentially act as an electron trap in these compounds.

To determine the charge transfer energy from the anion valence band to Eu^{3+}, the excitation spectra of ZnS/Tb and ZnS/Eu were compared (see Figure 3-8). The band at ~510 nm is assigned to a charge transfer band of Eu^{3+} in the ZnS/Eu system. Note that the red shifted emission spectrum for ZnS/Eu systems with λ_{ex} = 300 nm could arise from its charge transfer nature. Circumstantial evidence for this assignment in the ZnS/Eu system comes from a

comparison of Tb^{3+} and Eu^{3+} emission intensities with different excitation wavelengths (see Table 3-4). While the intensity of the Tb^{3+} luminescence decreases sharply when exciting the sample with lower energy than the bandgap of the ZnS nanoparticles, the situation is different for the ZnS/Eu system. Considerable luminescence intensity was observed from Eu^{3+} in ZnS nanoparticles even while exciting the sample at longer wavelength values. Although this observation does not directly prove the existence of a charge transfer band in the ZnS/Eu system, it strongly suggests that some energy level located lower than the bandgap of ZnS nanoparticles exists, and it is involved in the sensitization of Eu^{3+} in the ZnS doped nanoaparticles.

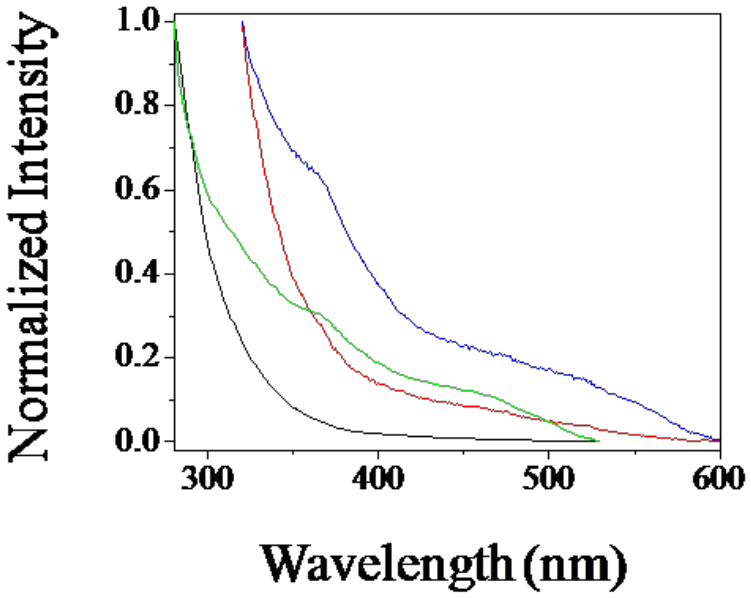

Figure 3-8. Normalized steady-state excitation spectra of ZnS/Tb nanoparticles with λ_{em} = 545 nm (black) and 620 nm (red). The green and blue curves are the corresponding spectra for ZnS/Eu nanoparticles. Spectra are normalized arbitrarily to the maximum intensity.

Several features of the energy level diagram in Figure 3-7 are noteworthy.

1. Both the ground and excited states of Tb^{3+} lie within the band gap of bulk ZnS, an effect which should be more pronounced in nanoparticles because of the quantum confinement and hence a higher band gap (~ 4.2 eV as opposed to 3.6 eV for bulk material). This indicates that the Tb^{3+} can potentially act as a hole trap in ZnS. Moreover, it suggests that the excited electron in the $^5D_4$ level of Tb^{3+} does not undergo ready autoionization. These two conditions result in the enhancement of the Tb^{3+} luminescence in ZnS. It is generally believed that the luminescence efficiency of lanthanide ions is increased when their 3+ levels act as trap states.[131]
2. The $^5D_4$ level of Tb^{3+} lies above the conduction band of CdSe so that autoionization of the Tb^{3+*} should be efficient, thereby decreasing its luminescence efficiency. Experimentally, the ZnS/Tb^{3+} emission is much stronger than the CdSe/Tb^{3+} emission, for which the overall quantum yields of ZnS/Tb^{3+} and CdSe/Tb^{3+} are 0.12 ± 0.03 and 0.025 ± 0.001 respectively, whereas the Tb^{3+} contribution to the overall quantum yield were found to be 0.05 ± 0.01 and 0.000015 ± 0.000003. It should also be noted that the time-gated mode is required to observe the Tb^{3+} emission in CdSe/Tb^{3+},[39] whereas they were readily observable in steady-state mode for ZnS/Tb^{3+} luminescence.
3. The energy level locations of Eu^{3+} are qualitatively different from Tb^{3+} in ZnS, as both the ground and excited states of Eu^{3+} lie below the valence band of ZnS. It is important to note that the ground state of Eu^{2+} lies within the band gap of ZnS, which makes the system a potential electron trap. Based on these considerations, Eu^{3+} can be brought to the excited state by two possible pathways: (1) a bandgap transition of the ZnS host and

(2) a ZnS valence band to Eu^{2+} ground state transition. Our observations are consistent with either of these mechanisms.

4. ZnS should be more efficient than ZnSe in sensitizing Tb^{3+} luminescence, because as the excited energy level of Tb^{3+} lies close to the conduction band of ZnSe, the excited electrons face a competitive nonradiative path of autoionization. To test this hypothesis ZnSe/Tb nanoparticles were prepared. The measured Tb^{3+} lanthanide-centered quantum yield value for ZnSe/Tb is 0.00018 ± 0.00007 as compared to 0.05 ± 0.01 for ZnS/Tb system, validating this prediction.
5. Based on the energy level diagrams, CdS should be more efficient in sensitizing Tb^{3+} luminescence than is CdSe, but similar or less efficient than ZnS. To check this prediction, experiments with the CdS/Tb system were undertaken. Results from these experiments are shown in Figure 3-9. Sharp Tb^{3+} bands are clearly visible at 490 nm and 545 nm. Interestingly, a band shift in the time-gated excitation spectra with the growth time of nanoparticles is evident and attributed to the effect of quantum confinement. This shift unequivocally points toward the presence of an antennae effect for the Tb^{3+} sensitization. Moreover, based on the ratio of bandgaps and Tb^{3+} emission intensities, it is apparent that the ZnS is more efficient than CdS in sensitizing Tb^{3+} luminescence, which is consistent with the prediction based on the energy level diagrams. The ratio of ZnS bandgap emission to the Tb^{3+} luminescence at ~545 nm in ZnS and CdS was found to be 1:10:1.4.

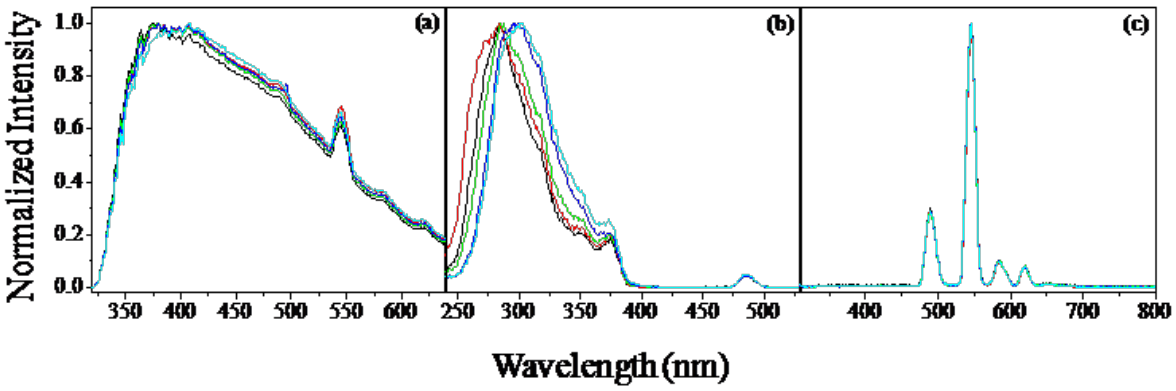

Figure 3-9. Normalized (a) steady-state emission with λ_{ex} = 300 nm, (b) time-gated excitation with λ_{em} = 545 nm and (c) time-gated emission with λ_{ex} = 300 nm of CdS nanoparticles in chloroform with 1 minute (black), 2 minutes (red), 5 minutes (green), 10 minutes (blue) and 20 minutes (cyan) growth times. Intensities of the excitation and emission spectra are normalized to the highest intensity of the respective spectra. Sharp Tb^{3+} bands are clearly visible in the steady-state mode. We observe a band shift in the excitation spectra monitoring the Tb^{3+} emission band, which undoubtedly confirms the presence of the antennae effect between the electronic structure of the nanoparticle and Tb^{3+}.

3.6 CONCLUSIONS

An efficient and less toxic luminescent lanthanide system, comprised of ZnS nanoparticles with incorporated lanthanide ions, has been established. Efficient sensitization was observed for both the ZnS/Tb^{3+} and the ZnS/Eu^{3+} systems. The ZnS/Tb^{3+} nanoparticles appear to be more efficient lanthanide-based emitters, with lanthanide-centered quantum yield values for ZnS/Tb^{3+} and

ZnS/Eu^{3+} being 0.05 ± 0.01 and 0.00013 ± 0.00004 respectively. Excitation spectra, while monitoring the lanthanide emission, clearly reveal that ZnS nanoparticles act as an antenna to sensitize the lanthanide luminescence in these systems. Moreover, the absence of observable sharp bands in the excitation spectra indicate that direct excitation of lanthanides has a negligible contribution to the overall sensitization mechanism. These systems represent a significant improvement over the originally proposed system $CdSe/Tb^{3+}$, in their efficiency for lanthanide luminescence sensitization.

The mechanism of lanthanide luminescence sensitization in II-VI semiconductor materials can be rationalized by a semi-empirical method proposed by Dorenbos and coworkers.[56-61] Energy level diagrams indicate that in ZnS, Tb^{3+} can act as a potential hole trap and provide a dramatic increase in sensitization efficiency because its energy levels lie between the nanoparticle band edges. The mechanism of Eu^{3+} luminescence sensitization, on the other hand, follows a different type of mechanism. In ZnS, Eu^{3+} can act as a potential electron trap; hence the sensitization can be achieved either by direct bandgap excitation or by a valence band to Eu^{2+} transition. Either mechanism can explain the experimental observations in the ZnS/Eu system. A comparison of lanthanide efficiency in ZnS nanoparticles is made with respect to other II-VI materials. Emphasis is given to Tb^{3+} doped ZnSe and CdS nanoparticles; both being less efficient than the ZnS nanoparticles in sensitizing the Tb^{3+} luminescence, which is consistent with the predictions based on the energy level positions.

Acknowledgements

We thank Dr. Pieter Dorenbos for useful comments.

4.0 GRAPHITIC NANOCAPSULES

4.1 CHAPTER PREFACE

The aim of this work was to build upon concepts presented in Chapters 2.0 and 3.0 and continue the pursuit of biological compatibility by exploring a novel delivery strategy. Specifically, we provided experimental evidence that Tb^{3+}-doped ZnS nanoparticles can be encapsulated within the hollow cavities of nitrogen-doped carbon nanotube cups (NCNCs). We found that the luminescence of Tb^{3+} would serve as a useful indicator of nanoparticle incorporation within the NCNCs. In addition to our experimental work, we engaged in a collaboration with other material chemists to further our mutual trajectory towards biological applications. The material contained in this chapter was published as a communication in the journal *Advanced Materials*; the figures in this chapter have been reproduced with permission from *Adv. Mater.* **2009**, *21(46)*, 4692. Copyright 2009 Wiley-VCH Verlag GmbH & Co. KGaA; the full citation is listed as Reference 144 in the bibliography section.[144]

List of authors: Brett L. Allen, Chad M. Shade, Adrienne M. Yingling, Stéphane Petoud, Alexander Star

Author contribution: The author of this dissertation was responsible for collecting the photophysical characterization including time-resolved spectroscopic measurements and providing interpretation of the results and contributing to the preparation of the published manuscript.

4.2 ABSTRACT

Carbon nanomaterials have made vast strides in a variety of fields including biological and materials sciences.[145] Synthesis of hollow carbon nanomaterials, such as fullerenes[146] and carbon nanotubes (CNTs),[147] are particularly useful for their inherent capacity to contain materials. This containment has been demonstrated by encapsulation of metal nanoparticles and C_{60} within the hollow interior of CNTs,[148] alluding to applications in drug delivery, which are typically dominated by the field of polymer nanocapsules.[149,150] Although the wetting and the capillarity of CNTs is an active area of research,[151,152] such encapsulation into hollow carbon nanomaterials is typically performed at high temperatures during their synthesis[153] or by their opening under oxidative conditions,[154] limiting the ability to encapsulate a wide range of organic molecules. Here, we demonstrate the crosslinkage of nitrogen-doped carbon nanotube cups (NCNCs) via incubation in 4% glutaraldehyde for the formation of graphitic nanocapsules with hollow interiors. We found that the use of basal nitrogen functionalities on adjacent NCNCs leads to a crosslinkage through this common fixing agent. Moreover, we demonstrate the encapsulation of gold nanoparticles (GNPs) or lanthanide-containing ZnS:Tb nanoparticles into NCNCs, where they are subsequently trapped through the linkage process. In addition to being chemically inert,

this system affords a facile encapsulation process with the capacity to hold varying cargo within the interior cavity. We anticipate our encapsulation method to be the starting point of more sophisticated drug-delivery or storage systems.

4.3 INTRODUCTION

The desire for creating hollow nanostructures and utilizing inherent cavities is becoming more predominant as applications in drug delivery and medical diagnostics become increasingly popular.[155,156] For instance, it has been demonstrated that CNTs can be filled with a chemotherapeutic agent that inhibits the growth of tumor cells.[157] Furthermore, it has been shown that such hollow nanomaterials may encapsulate fluorescent molecules for potential application in diagnostic imaging.[158] In the realm of energy applications, hollow nanomaterials have found use primarily as storage media for lithium and hydrogen.[159,160] While these applications demonstrate novelty and practicality, facilitating such work is difficult. In our study, we utilize synthesized NCNCs for the encapsulation of commercially available GNPs as well as ZnS:Tb nanoparticles through simple glutaraldehyde crosslinking, thus taking advantage of inherent nitrogen functionalities on the basal rim of these structures.

4.4 EXPERIMENTAL

Crosslinkage of NCNCs. Approximately 0.1mg of NCNC powder[161] was suspended in pure ethanol (EtOH; 10 mL) through ultrasonication for 5 min. Following the appearance of a stable suspension, 4% glutaraldehyde in EtOH (500µL) was added to the suspension and allowed to incubate for 24 h before characterization.

Synthesis of ZnS:Tb Nanoparticles. A reaction mixture of zinc stearate (0.4801 g), tetracosane (4.1180 g), and octadecene (5 mL) was heated to 360 ^{o}C for 2 h, while stirring under nitrogen. After dissolution of the cation precursor within the reaction mixture, the dopant lanthanide (Tb) mixture consisting of $Tb(NO_3)_3$ (0.0601 g), toluene (0.5 mL), octadecene (2.5 mL), and trioctylphosphine (TOP)(2 mL) was injected rapidly and left to stir for 1 h at a reduced temperature of 300 ^{o}C. Subsequently, a solution consisting of sulfur (0.0090 g), toluene (0.5 mL), and octadecene (2.5 mL) was injected to initiate the nucleation of nanoparticles. Aliquots were withdrawn at various times (1–120 min), and particle sizes of ~2–4nm further purified by dissolution in butanol followed by precipitation in methanol. Precipitated nanocrystals were re-dissolved in octanol to remove excess solvent (octadecene/tetracosane), and precipitated once more with methanol.

Encapsulation of GNPs or ZnS:Tb Nanoparticles into NCNCs. Similarly to crosslinkage, approximately 0.1mg of NCNC powder was suspended in EtOH through ultrasonication for 5 min. Concurrently, commercially available GNPs (Sigma–Aldrich) were diluted in pure EtOH at a 16:1 ratio (EtOH to stock solution). Following the appearance of a stable suspension of NCNCs, the diluted GNPs (or ZnS:Tb) were added at a volume of 500µL. This suspension was

then re-sonicated for another 5 min before 4% glutaraldehyde (500μL) was added and incubated for 24 h.

TEM. Low-resolution TEM images were obtained with a Philips/FEI Morgagni microscope. The electron-beam accelerating voltage of the TEM was held constant at 80 keV for all imaging. All samples were suspended in EtOH, dropcasted onto a lacey-carbon TEM grid (Pacific Grid-Tech), and allowed for the solvent to evaporate completely.

AFM. Characterization was carried out on a Multimode scanning-probe microscope (Veeco). Samples were prepared by spin-coating NCNCs and their variations (suspended in EtOH) onto a freshly cleaved sheet of mica. After 45 min of drying in ambient conditions, the images were taken. Tapping-mode experiments using supersharp tips (AppNano ACL-SS) (~2 nm) allowed for the intricate characterization of all samples.

Time-Resolved Spectroscopy. Time-resolved emission and excitation spectra were collected on a Varian Cary Eclipse fluorimeter, coupled to a personal computer with software supplied by Varian. Scans were collected with 10 flashes, a 5.0ms gate time, a 0.5 ms delay time (if no other value is stated), and a 20.0 ms total decay time. Excitation and emission slits of 20nm were used. An automated filter set was used for all excitation and emission scans. Samples were placed in 1-mm quartz fluorescence cells purchased from NSG Precision Cells, Inc. (Farmingdale NY). Spectra were smoothed using OriginPro (Version 7.0).

4.5 RESULTS AND DISCUSSION

NCNCs were prepared as mentioned previously.[161] Figure 4-1 shows a schematic representation of the initial synthesis process. Thermal decomposition of hydrocarbons over the in situ generated catalyst perpetuates the growth of graphitic fibers. These fibers, typically 1–4 mm in length and 12–40 nm in diameter, appear as stacked, conical segments in transmission electron microscopy (TEM) images (Figure 4-1, right). In addition to the induction of multiple nitrogen functionalities, unique to this hybrid material is the nitrogen doping within the graphitic lattice that forces the lattice walls to run in parallel, diagonally outward from the main long axis, thus isolating each segment from its nearest neighbor.[161] Mechanical grinding of stacked NCNCs with a mortar and pestle breaks the van der Waals attraction between them and exposes various possible nitrogen functionalities on the open basal plane. With this methodology, individualized NCNCs are removed from their ‘‘stacked’’ conformation and are further opened to subsequent manipulation by crosslinkage with 4% glutaraldehyde in EtOH.

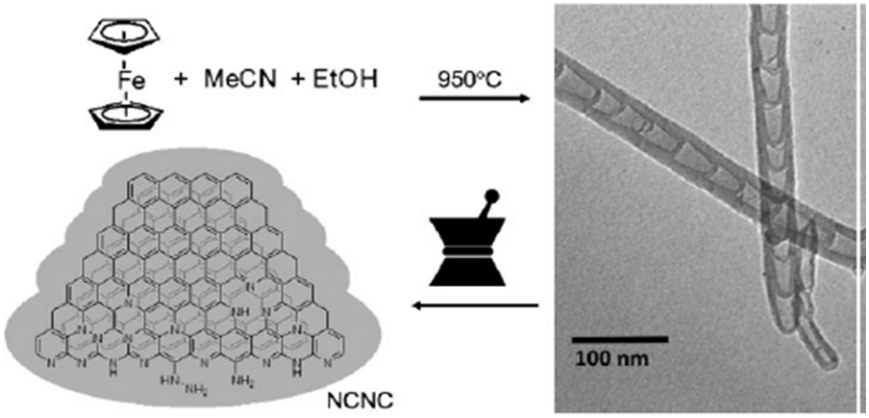

Figure 4-1. Schematic representation of the preparation of NCNCs. Chemical vapor deposition (CVD) from ferrocene, acetonitrile (MeCN), and ethanol (EtOH) creates stacked NCNCs. Mechanical separation with a mortar and pestle separates the stacks into isolated structures with varying plausible nitrogen functionalities including aniline- and hydrazine-type functionalities that can react with glutaraldehyde to form aromatic hemiaminal, imine, and hydrazone compounds. The rightmost image displays the TEM image of the stacked-cup formation of NCNCs.

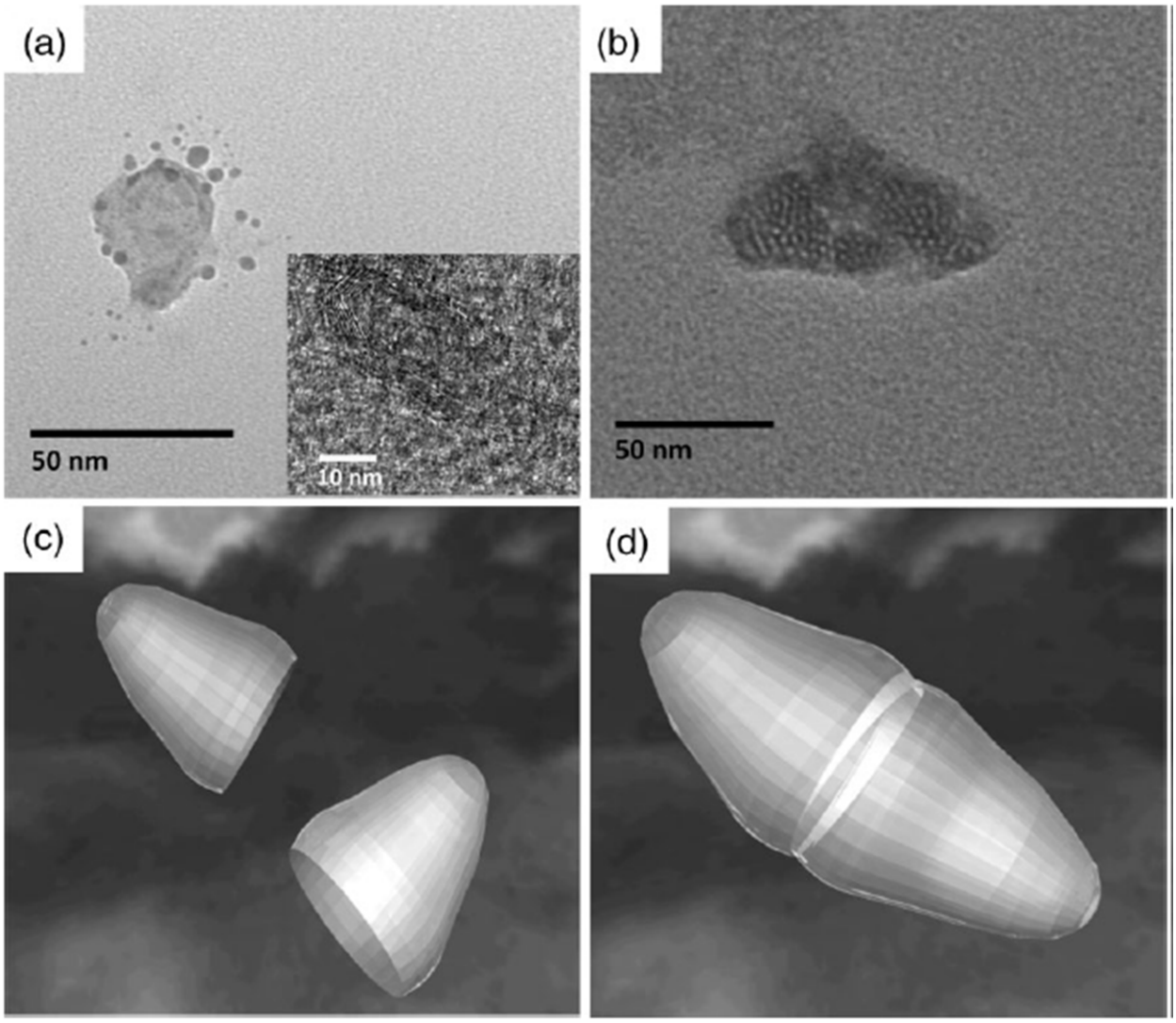

Figure 4-2. a) TEM image of a single separated NCNC. The graphitic lattice structure is clear from the high-resolution TEM image (inset). b) Cartoon illustration depicting adjacent, separated NCNCs. c) TEM image of crosslinked NCNCs. d) Cartoon illustration depicting the crosslinkage of NCNCs.

Figure 4-2a shows the TEM image of a single, separated NCNC. As can be seen, the single NCNC is approximately 40nm in length with an ‘‘open’’ end and a curved cap as reported previously.[161] High-resolution TEM imaging (inset) shows that these cuplike structures consist of multiple walls (~10 walls shown). A cartoon image, as shown in Figure 4-2b, further illustrates the separated NCNCs. Due to the presence of nitrogen functionalities on the basal ‘‘open’’ plane of these structures, we are able to crosslink two neighboring NCNCs of similar diameter, as will be explained further. Figure 4-2c shows the TEM image of such crosslinked NCNCs. The linked structure is approximately 80nm in length and exhibits a ‘‘capsule’’ shape, in contrast to the separated structures. A cartoon image shown in Figure 4-2d further illustrates the crosslinking between proximal structures. Presumably, the reaction of the nitrogen groups on the base of NCNCs with glutaraldehyde leads to the formation of covalent bonding between the ‘‘linker’’ molecules and the NCNCs.

Progressing further with the utilization of this system, it is desirable to establish the capability for encapsulation during the crosslinkage process as a step towards functional nanocapsules. Thus, we investigated the capture of commercially available GNPs of an approximately 5-nm (mean) diameter. The basal openings of NCNCs are 20–30 nm in diameter, accommodating for such small particles to penetrate the inner cavity. As such, the addition of GNPs in solution to a suspension of NCNCs prior to the addition of 4% glutaraldehyde should allow for the encapsulation of particles within the inner cavities of the crosslinked structure.

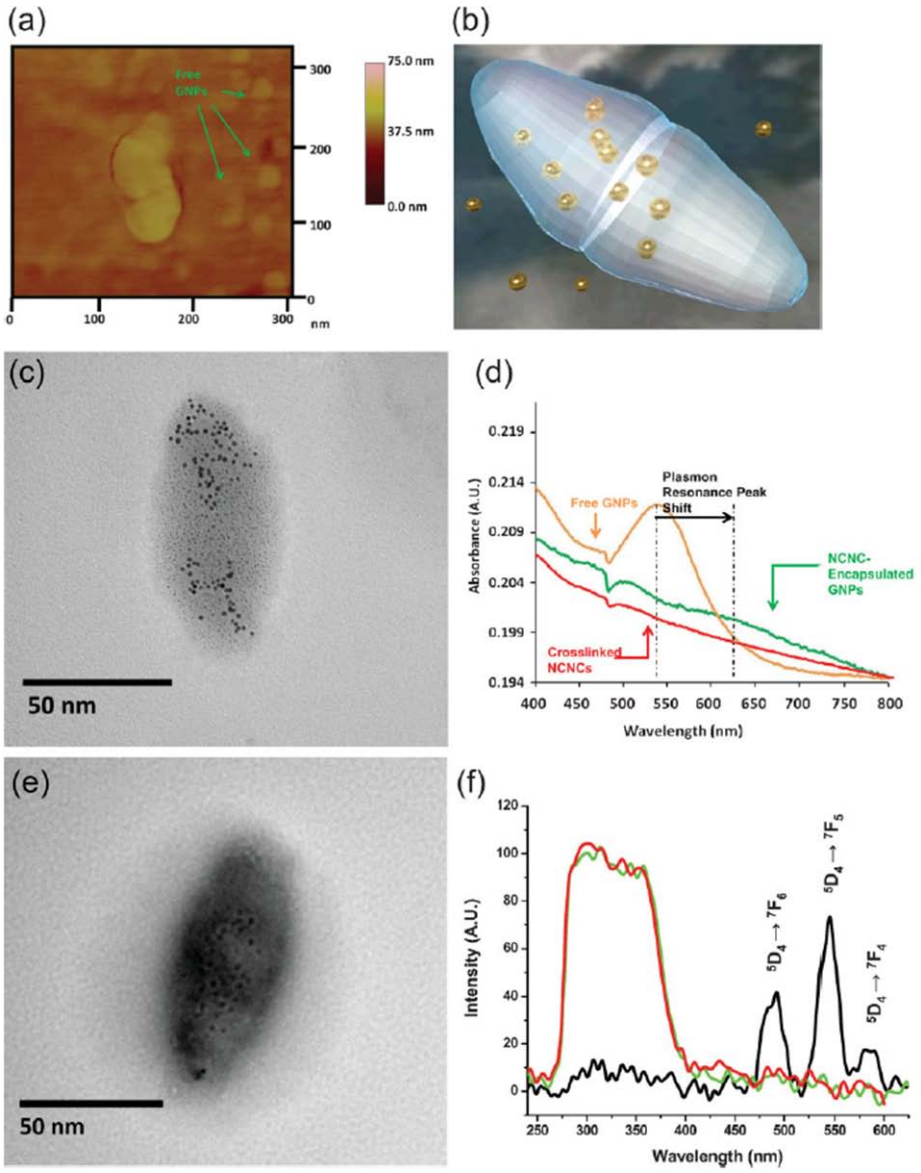

Figure 4-3. a) AFM image of crosslinked NCNCs with GNPs. Free GNPs are seen sporadically in the field of view as indicated. b) Cartoon illustration of the crosslinkage of adjoining NCNCs with interior confinement of GNPs. c) TEM image of crosslinked NCNCs encapsulating GNPs (5 nm in diameter) in the interior cavities. d) UV/Vis spectra of free GNPs, vacant crosslinked NCNCs, and GNPs after encapsulation in crosslinked NCNCs. All spectra are taken in EtOH. e) TEM image of ZnS:Tb nanoparticles encapsulated in crosslinked NCNCs. Encapsulation was performed under identical conditions as GNP encapsulation. f) Time-resolved emission spectrum at an excitation wavelength of λ_{ex} = 225 nm with a 0.5 ms delay of ZnS:Tb (black), crosslinked NCNCs (red), and ZnS:Tb encapsulated in NCNCs (green).

Figure 4-3a depicts an atomic force microscopy (AFM) image of the resultant incubation. Initial observations from a height image captured in tapping mode demonstrate the successful linkage of two adjacent NCNCs, with free GNPs positioned sporadically in the surrounding field. It is worth mentioning here that minute size distortions are common in tapping-mode imaging. Therefore, NCNC and GNP sizes were confirmed by section analysis. No predominant features confirm exterior adsorption; however, because of the method of imaging, AFM did not elucidate the interior confinement of GNPs. Figure 4-3b further illustrates the results of such GNP encapsulation. TEM was utilized to prove spatial interior confinement. The GNPs appear to be confined to the interior cavity of the crosslinked NCNCs, as illustrated in Figure 4-3c. In majority, this confinement of GNPs is centralized within two specific areas of the crosslinked structures. Both distributions appear at the topmost conical portion of each structure. Additionally, the lack of sporadic distribution of GNPs alludes to interior confinement, as opposed to exterior adsorption.

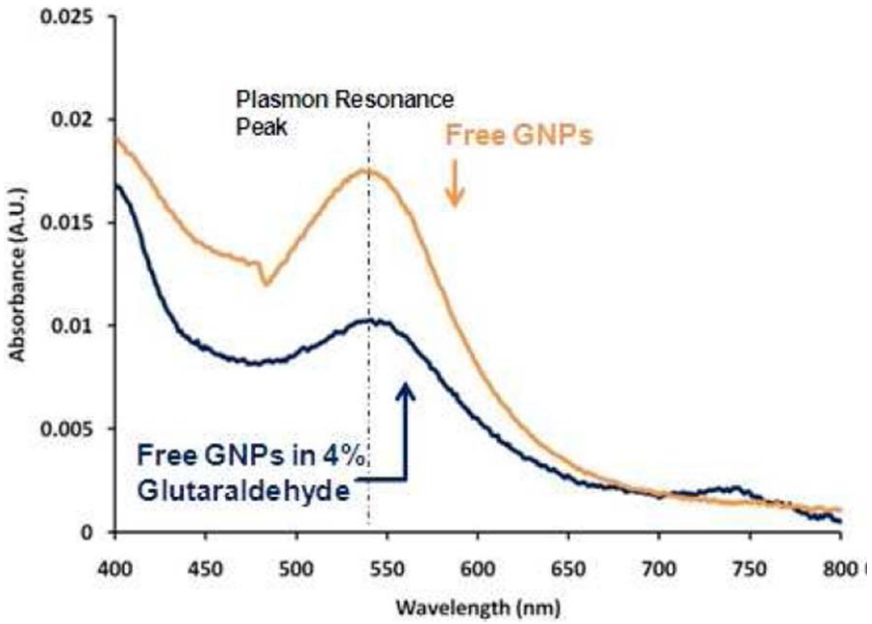

Figure 4-4. UV-Vis spectra of free GNPs and GNPs added to 4% glutaraldehyde in EtOH.

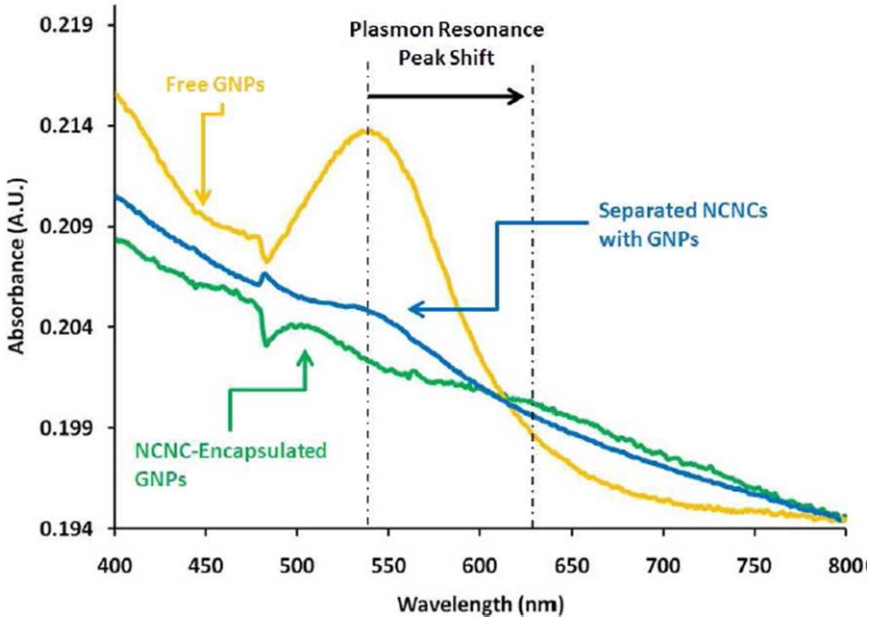

Figure 4-5. UV-Vis spectroscopic comparison of free GNPs, separated NCNCs incubated with GNPs prior to cross-linkage, and GNPs encapsulated by NCNCs after 4% glutaraldehyde addition. It is important to note that only the encapsulated GNPs demonstrate a Plasmon resonance shift, due to spatial confinement of the particles. This is not the case for unlinked-NCNCs allowing movement within the hollow cavity and back out.

We investigated optical properties of the resulting functional system using UV/Vis spectroscopy (Figure 4-3d). At approximately 540 nm, the surface-plasmon resonance band for free GNPs (with a mean diameter of 5 nm) is evident.[162] After incubation with NCNCs during crosslinking, the band for GNPs is greatly suppressed and appears at approximately 625 nm, significantly red shifted, as is expected according to the literature for GNP aggregation.[163] These spectra are different from those of separated NCNCs and crosslinked NCNCs without GNPs. In addition, control experiments, where NCNCs were crosslinked prior to the addition of GNPs,

demonstrate a majority of vacant NCNCs, with rare cases of exterior adsorption of GNPs as indicated by TEM and AFM imaging. No shift of the surface-plasmon resonance band was observed by UV/Vis spectroscopy. Furthermore, control experiments with 4% glutaraldehyde and GNPs incubated in EtOH show no shift of the surface-plasmon resonance band.

In addition to ease of facilitation, this encapsulation system exhibits interesting mechanistic components, resulting in larger linkage success rates. Because the linkage of two adjacent structures occurs on the open basal planes of NCNCs, there is an intrinsic diameter compatibility between them. We have observed that only NCNCs with similar diameters will participate in the successful crosslinkage with glutaraldehyde to make a nanocapsule. Essentially, it is thought that crosslinkage of smaller-diameter NCNCs to larger-diameter NCNCs will be less stable due to incomplete crosslinkage of the nitrogen functionalities. To satisfy this bonding scheme, structures with similar diameter must be in close proximity for capsule formation to occur. Incompatible-diameter species have been observed but are a rarity (~2%).

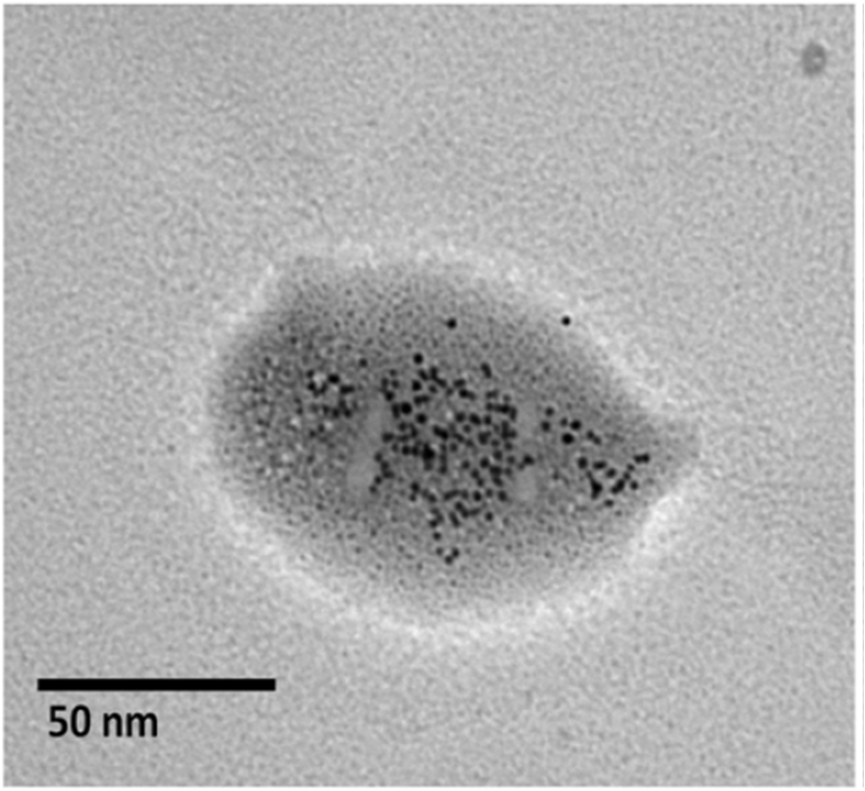

Figure 4-6. TEM image of another NCNC nanocapsule encapsulating GNPs, demonstrating migration within the interior cavity.

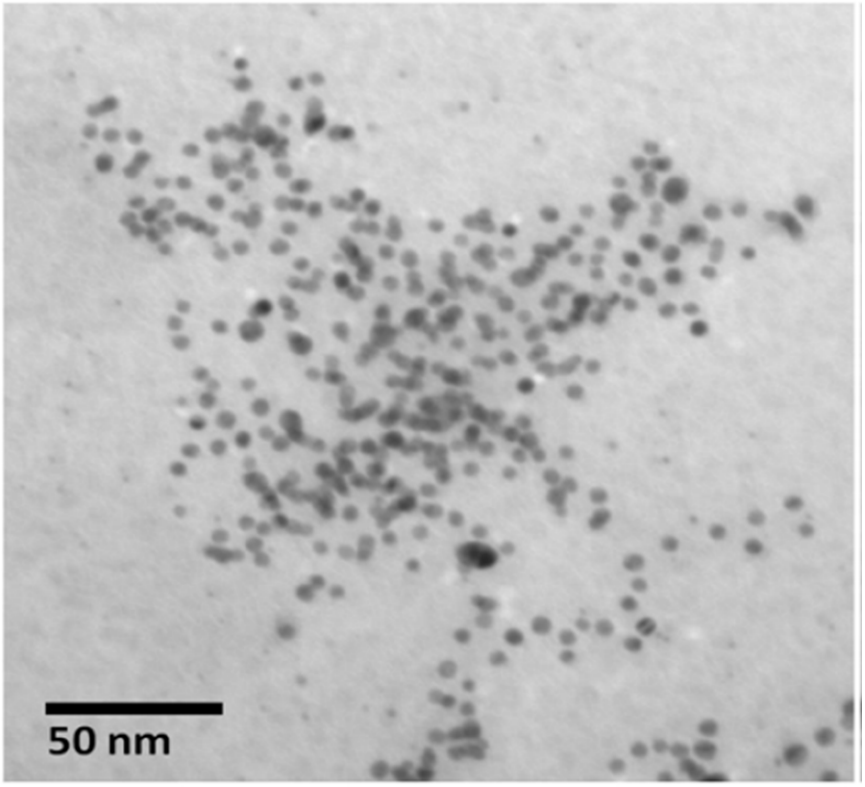

Figure 4-7. TEM image of non-encapsulated GNPs on the same TEM grid as in Figure 4-6.

Presumably due to capillary action, GNPs are taken into the interior cavity of NCNCs. NCNCs are comparable to CNTs in graphitic composition and their hollow interior and, previously, it has been observed that CNTs exhibit capillary forces, resulting in entrapped species.[164] Furthermore, GNPs are able to migrate through the confines of the joint interior cavity within adjoining NCNCs. Because of this simplistic uptake mechanism, other nanoparticles or molecular species should be encapsulated without significantly manipulating external conditions. Additionally, once encapsulation occurs, aggregation may ensue due to a change in the chemical environment. Commercially available GNPs are initially suspended in aqueous solution by

electrostatic stabilization[165] with a variety of salts. Upon encapsulation, GNPs are surrounded by a hydrophobic shell, possibly without the presence of stabilizing salts. However, we cannot completely rule out the possibility of aggregation due to spatial confinement. In either case, such aggregation is responsible for the red shift of the Plasmon resonance band discussed above and in accordance with the literature.[166]

For confirmation of capillary uptake and for a demonstration of the general applicability of this system, a control sample of ZnS nanoparticles doped with Tb^{3+} (ZnS:Tb)[39,123] (~2–4nm in size) was used in an identical procedure. ZnS:Tb nanoparticles are encapsulated within crosslinked NCNCs as viewed by TEM imaging in Figure 4-3e. Because of the presence of luminescent lanthanide cations within the ZnS shell, it is also possible to track the luminescence emission related to the Tb^{3+} species. Free ZnS:Tb nanoparticles (in ethanol) are shown in a time-resolved emission spectrum (recorded with a 0.5 ms delay), as demonstrated in Figure 4-3f. Three narrow emission bands are present corresponding to the slow relaxation from the $^5D_4$ state to ^7F_J levels of Tb^{3+}. More importantly, once encapsulated by NCNCs through the same crosslinkage procedure ascribed for GNPs, a major change in the optical properties is observed and the Tb^{3+} luminescence is strongly suppressed, as demonstrated in Figure 4-3f. Such encapsulation and change in the luminescence properties further demonstrates the broad applicability of this system, including the design of photonic materials.

It is also worth mentioning here that it should be possible to tailor specific interior volumes based upon the control of the growth process of NCNCs. Previous theoretical studies have demonstrated growth dependence on the presence of the nitrogen abundance from the stock precursor.[167] The current synthesis affords NCNCs with 2–7% N-doping of the graphitic lattice.[161] However, increasing this doping effect directly by increasing the relative abundance in

the liquid precursor will tailor shorter NCNCs and, thus, smaller interior cavities. Furthermore, precise control over diameter distributions of catalytic particles should allow for a direct determination of the diameter distributions of NCNCs.

4.6 CONCLUSIONS

In conclusion, by imparting NCNCs with basal nitrogen functionalities, we were able to utilize a common fixing agent, glutaraldehyde, for the crosslinkage of two adjacent structures, creating a ‘‘nanocapsule’’. Further to this process, we have demonstrated a capillary-uptake encapsulation method for the confinement of nanoparticles within the interior cavities of adjoining NCNCs. The results allude to applications in drug delivery and energy storage. Through utilization of the hollow cavities for drugs or chemotherapeutic agents, followed by this crosslinkage for encapsulation, it may be possible to perpetuate a delivery platform, where simple bond cleavage releases the cargo, while leaving the carbon shell open for functionalization, thus directing the NCNCs to specific areas of the body. Moreover, it may be possible to use the interior of these structures for catalysis or storage. Further investigations of encapsulation and subsequent ‘‘releasing’’ mechanisms will increase the potential applicability for such materials.

5.0 A STRATEGY TO PROTECT AND SENSITIZE NEAR-INFRARED LUMINESCENT NEODYMIUM(III) AND YTERBIUM(III): ORGANIC TROPOLONATE LIGANDS FOR THE SENSITIZATION OF LANTHANIDE(III)-DOPED NANOCRYSTALS

5.1 CHAPTER PREFACE

The aim of this work was to combine aspects of our previously established nanocrystal approach with more traditional organic sensitizers as well as advantages from both techniques. Specifically, we used $NaYF_4$ nanocrystals to protect the excited states of near-infrared emitting lanthanides from nonradiative deactivation and sensitized their luminescence by decorating the surface of the nanocrystals with tropolonate chromophoric ligands. We gained practical insight into improving the overall brightness of classic lanthanide sensitization strategies. The material contained in this chapter was published as a communication in *The Journal of the American Chemical Society*; the figures in this chapter have been reproduced with permission from *J. Am. Chem. Soc.* **2007**, *129(48)*, 14834. Copyright 2007 American Chemical Society; the full citation is listed as Reference 168 in the bibliography section.[168]

List of authors: Jian Zhang, Chad M. Shade, Demetra A. Chengelis, Stéphane Petoud

Author contribution: The author of this dissertation was equally responsible for the nanocrystal synthesis reported in this chapter in addition to collecting physical characterization of the nanoscrystals including TEM images and XRD patterns, photophysical characterization including steady-state excitation and emission profiles and Ln^{3+}-centered luminescence lifetimes, and providing interpretation of the results and contributing to overall conception of the project and the preparation of the published manuscript.

5.2 INTRODUCTION

Lanthanide-based near-infrared (NIR) emitters have a great potential to serve as bioanalytical reporters for several reasons: (i) NIR photons scatter less than visible photons, improving image resolution.[22] (ii) Biological systems have low native autofluorescence in the NIR energy domain,[169] resulting in higher detection sensitivity due to improved signal-to-noise ratio. (iii) Most luminescent lanthanide complexes are not susceptible to photodecomposition, allowing long or repeated experiments and simplifying sample storage and preparation procedures. Since f-f transitions are Laporte forbidden,[28] free Ln^{3+} have low extinction coefficients resulting in low luminescence intensity. Therefore, it is necessary to sensitize these cations through a suitable chromophore ("antenna effect"),[30] an area of research that has been highly active in recent years.[34,170-175] However, this approach has intrinsic limitations because lanthanide luminescence is easily quenched through nonradiative routes when the cations are in close proximity to the vibrational overtones of -OH, -NH, and -CH groups present in the sensitizing ligand and/or solvent.[42] This effect is particularly dramatic for NIR emitting Ln^{3+} because of relatively small

energy gaps between ground and excited electronic states.[42] To alleviate this limitation, Ln^{3+} have been incorporated into inorganic matrices, such as LnF_3,[176] Ln_2O_3,[177] $LnPO_4$,[178] $LnVO_4$,[179] TiO_2,[180] and Zeolites.[181] These materials protect lanthanide cations from sources of nonradiative deactivation; however, they have either limited (e.g., $LnVO_4$) or no absorbance in the UV range. Thus, these inorganic materials are not able to sensitize lanthanide luminescence with the efficiency of organic sensitizers.

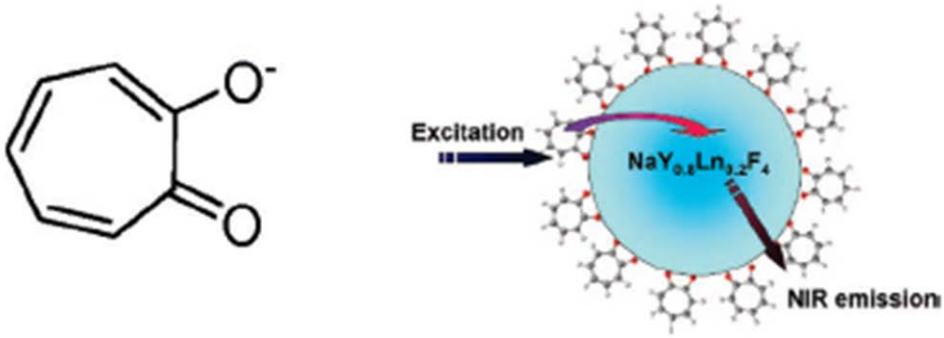

Figure 5-1. Molecular Structure of Tropolonate and Schematic Illustration of Tropolonate Capped Nd^{3+}- or Yb^{3+}-Doped $NaYF_4$ Nanocrystals and the Energy Transfer Process.

Here we introduce a strategy to overcome the limited lanthanide sensitization by binding organic tropolonate chromophoric groups to the surface of $NaYF_4$ nanocrystals (NCs), doped with NIR emitting Nd^{3+} or Yb^{3+} (Figure 5-1). Tropolonate ($Trop^-$) was chosen as a capping ligand since it has been previously demonstrated to be a suitable sensitizer for several lanthanide

cations emitting in the NIR range when coordinated in $KLn(Trop)_4$ complexes.[4,182] These novel systems use the $NaYF_4$ matrix to protect Ln^{3+} from nonradiative deactivations, while a chromophoric coating sensitizes their luminescence.

5.3 EXPERIMENTAL

Chemicals. Tropolone, KOH standard solution in methanol (0.100 N), Y_2O_3, Nd_2O_3,Yb_2O_3, oleic acid (90%), oleylamine (>80%), 1-octadecene (>90%), trifluoroacetic acid (99%), $NaCF_3COO$ (>97%) were purchased from Aldrich. The synthesis was carried out using standard oxygen-free procedures. All the solvents, absolute ethanol and chloroform, were used as received. $Y(CF_3COO)_3$ $Nd(CF_3COO)_3$ and $Yb(CF_3COO)_3$ were prepared according to literature method[22].

Synthesis of Nd^{3+} or Yb^{3+}-Doped $NaYF_4$ Nanocrystals[28,169]. Sodium trifluoroacetate (0.136g, 1.0mmol),$Y(CF_3COO)_3$ (0.386g, 0.8 mmol) and $Nd(CF_3COO)_3$ (0.107g, 0.2 mmol) or $Yb(CF_3COO)_3$ (0.113g, 0.2 mmol) were then added to the reaction vessel with octadecene (5.05 g, 20 mmol), oleic acid (2.82g, 10 mmol) and oleylamine (2.68 g, 10 mmol). The mixture was heated to 100 °C under vacuum and stirred for 30 min to remove the residual water and oxygen. The solution was then heated to 325 °C under argon and maintained at this temperature for 40 min. Subsequently, the mixture was allowed to cool to room temperature, and the resulting NCs were precipitated by addition of ethanol and isolated via centrifugation. The resulting solid was then washed twice with ethanol and dried under vacuum for 24 h.

Methods. UV-vis absorption spectra were recorded on a Perkin-Elmer Lambda 19 spectrophotometer. FT-IR spectra were recorded on a Perkin-Elmer Spectrum BX FT-IR instrument.

Lanthanide luminescence emission and excitation spectra were measured using a Jobin Yvon-Horiba Fluorolog-322 spectrofluorometer (detector for NIR domain: DSS-IGA020L, Electro-Optical Systems, Inc.).

The luminescence lifetime measurements were performed by excitation of solutions in 1 cm quartz cells using a Nd:YAG Continuum Powerlite 8010 Laser (354 nm, 3rd harmonic) as the excitation source. Emission was collected at a right angle to the excitation beam and emission wavelengths were selected using a Spectral Products CM 110 1/8 meter monochromator. The signal was monitored by a cooled photomultiplier (Hamamatsu R316-2) coupled to a 500 MHz bandpass digital oscilloscope (Tektronix TDS 754D). The signals (15,000 points each trace) from at least 500 flashes were collected and averaged. Luminescence decay curves were imported into Origin 7.0 scientific data analysis software. The decay curves were analyzed using the Advanced Fitting Tool module and fitted with mono-, bi- and tri-exponential modes. Of the three modes, the lifetime value was chosen based on the best fit of the decay curve on the criteria of the minimum χ^2 statistical parameter. Lifetimes are averages of at least three independent determinations.

Powder X-ray diffraction (XRD) patterns of the dried powders were recorded on a Philips X'pert diffractometer (PW3710) with a slit of 1/2° at a scanning rate of 3° min^{-1}, using Cu Kα radiation, λ=1.5406 Å). Samples were evaporated or pressed onto glass microscope slides.

TEM Method. A small drop of solution containing the sample was placed on a carbon coated copper grid. After several seconds, the drop was removed by blotting with filter paper. The sample that remained on the grid was allowed to dry before inserting the grid into the microscope. The grids were viewed on a transmission electron microscope (Hitachi H-7100 TEM, Hitachi High Technologies America, 5100 Franklin Drive, Pleasanton, CA, 94588) operating at 75 kV. Digital images were obtained using an AMT Advantage 10 CCD Camera System (Advanced Microscopy Techniques Corporation, 3 Electronics Ave., Danvers, MA, 01923) and NIH Image software. Particle diameter was measured using a negatively stained catalase crystal as a calibration standard.

5.4 RESULTS AND DISCUSSION

A synthetic method to prepare Nd^{3+} or Yb^{3+} doped $NaYF_4$ NCs was developed on the basis of a recently reported synthesis of $NaYF_4$ NCs (see Experimental).[183,184] The $Trop^-$ capped NCs were synthesized using the following procedure. Tropolone was dissolved in methanol, then deprotonated with an equimolar amount of KOH in methanol. Chloroform was added to obtain a 1/1 (v/v) $MeOH/CHCl_3$ solvent mixture. This solution was added to a purified solution of NCs dispersed in chloroform. The resulting mixture was sonicated for 2 h, and the solvent was removed under vacuum. The resulting solid was washed with ethanol and DMSO and dried under vacuum for 24 h. The binding of the $Trop^-$ groups to the surface of nanocrystals was monitored through FT-IR spectroscopy (Figure 5-2). Upon reaction, the absorption bands assigned to the original capping ligands of the NCs (oleic acid, oleylamine, and octadecene)

present at 2924 and 2854 cm^{-1} disappear and are replaced by the characteristic absorption bands of Trop- at 1595 and 1510 cm^{-1}.

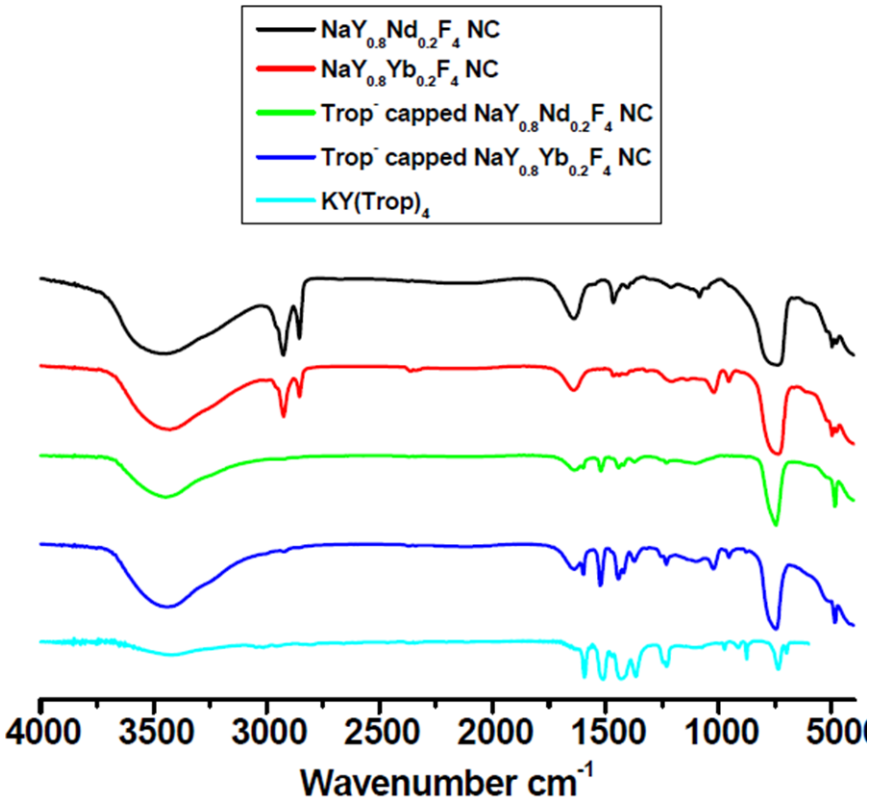

Figure 5-2. FT-IR spectra of $NaY_{0.8}Nd_{0.2}F_4$ NCs, $NaY_{0.8}Yb_{0.2}F_4$ NCs, $Trop^-$ capped $NaY_{0.8}Nd_{0.2}F_4$ NCs, and $Trop^-$ capped $NaY_{0.8}Yb_{0.2}F_4$ NCs. For comparison, the FT-IR spectra of $KY(Trop)_4$ is also depicted.

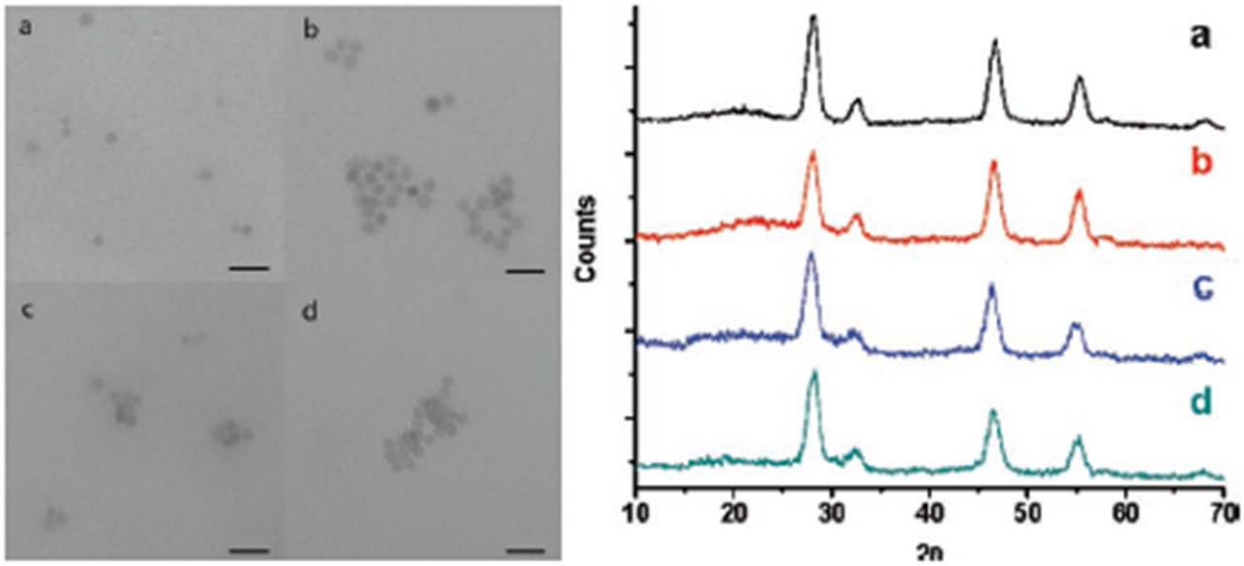

Figure 5-3. TEM and XRD characterization of NCs. Transmission electron microscopy images (left, scale bar: 20 nm) and the X-ray diffraction patterns (right) of uncapped and capped NCs. (a) $NaY_{0.8}Yb_{0.2}F_4$ NCs, (b) $Trop^-$ capped $NaY_{0.8}Yb_{0.2}F_4$ NCs, (c) $NaY_{0.8}Nd_{0.2}F_4$ NCs, (d) $Trop^-$ capped $NaY_{0.8}Nd_{0.2}F_4$ NCs.

The XRD patterns (Figure 5-3, right) of the uncapped and capped $NaY_{0.8}Ln_{0.2}F_4$ NCs (Ln: Nd or Yb) reveal the formation of cubic R-$NaYF_4$ (space group: *Fm*3*m*). All diffraction peak positions and intensities agree well with calculated values.[185] Transmission electron microscopy (TEM) images (Figure 5-3, left) of both uncapped and capped NC samples also indicate that the obtained nanocrystals are of single-crystalline nature with high crystalline size uniformity. They are relatively monodisperse with roughly spherical shape. The average sizes are 6.1 ± 0.6 nm, 6.0 ± 0.6 nm, 5.3 ± 0.7 nm, and 5.3 ± 0.6 nm for $NaY_{0.8}Yb_{0.2}F_4$ NCs, $Trop^-$ capped $NaY_{0.8}Yb_{0.2}F_4$ NCs, $NaY_{0.8}Nd_{0.2}F_4$ NCs, and Trop- $NaY_{0.8}Yb_{0.2}F_4$ NCs, respectively (Figure 5-4). Such relatively small sizes are compatible for use in many bioanalytical applications.

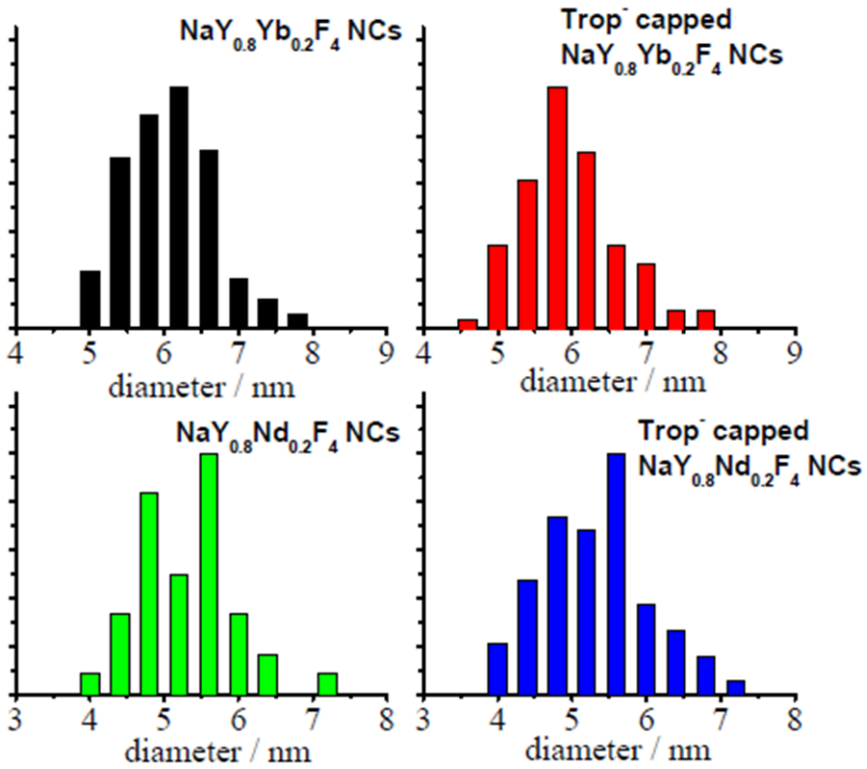

Figure 5-4. Histogram of the nanocrystal size distribution derived from the TEM images.

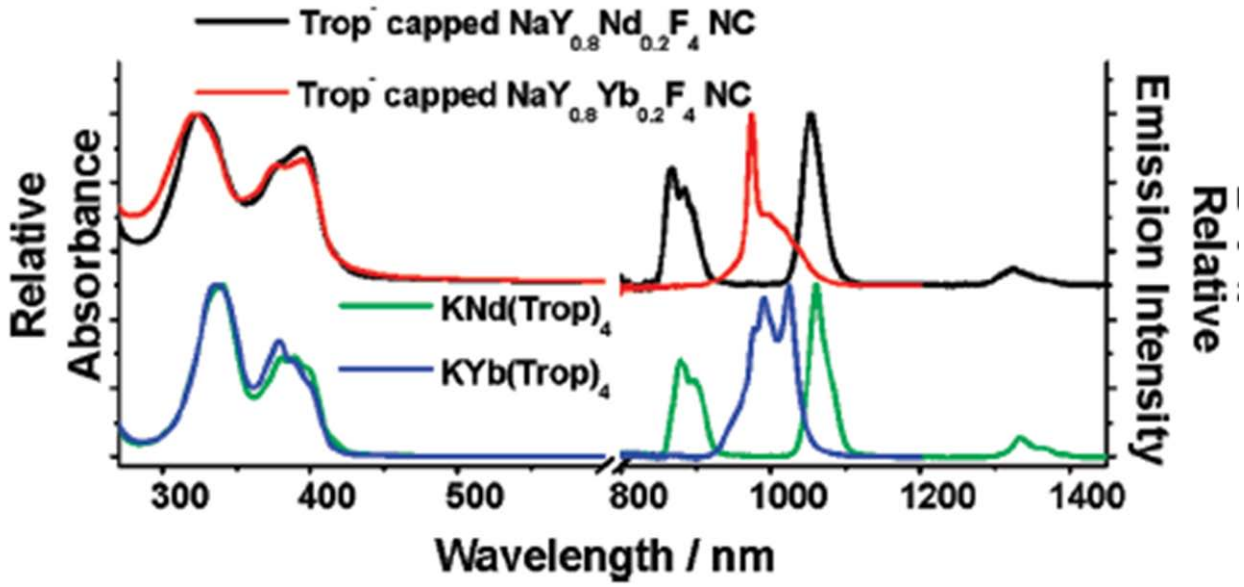

Figure 5-5. Photophysical characterization of Trop$^-$-capped NCs and corresponding complexes. Normalized UV-vis absorption (left) and NIR luminescence emission spectra (right) of the complex (bottom) (λ_{ex}=340 nm, 10^{-4} M) and Trop$^-$-capped NCs (ca. 1 g L^{-1}) in DMSO (top).

The UV-vis absorption spectra (Figure 5-5) of Trop- capped NCs in DMSO reveal the presence of two bands with apparent maxima centered around 323 and 384 nm, similar to those observed for $[Ln(Trop)_4]^-$ confirming the presence of Trop$^-$ on the surface of NCs. Upon excitation at 340 nm, the characteristic sharp NIR emission bands arising from Nd^{3+} or Yb^{3+} were observed (Figure 5-5). The excitation profiles of lanthanide luminescence in both Nd^{3+} and Yb^{3+} doped NCs are similar (Figure 5-6), demonstrating that the lanthanide cations are sensitized through the same source: the electronic structure of the Trop$^-$ ligand. For Yb^{3+}, there is a significant energy gap between the energy donating levels of Trop and its accepting levels.

Energy transfer over this large gap could be explained by phonon-assisted or electron-transfer mechanisms.[186,187]

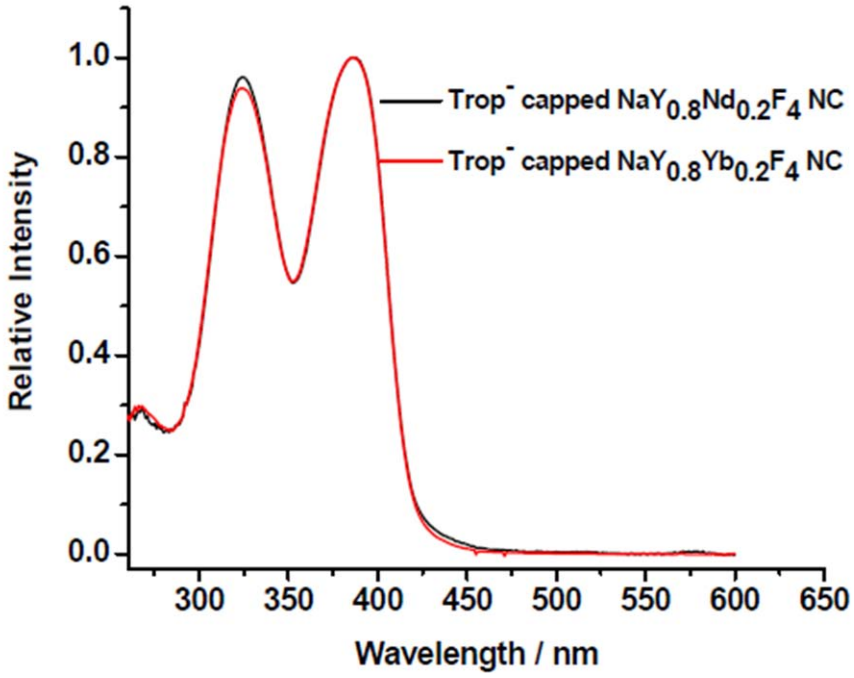

Figure 5-6. Normalized NIR luminescence excitation spectra of the complex $Trop^-$ capped NCs (ca. 1 g L^{-1}) in DMSO. (Emission wavelength were set as 1055 nm and 975 nm for $Trop^-$ capped $NaY_{0.8}Nd_{0.2}F_4$ NC and $Trop^-$ capped $NaY_{0.8}Yb_{0.2}F_4$ NC respectively.

The lifetimes of the luminescence arising from Nd^{3+} and Yb^{3+} in Trop-capped NCs and in $[Ln(Trop)_4]^-$ complexes were determined in DMSO and are reported in Table 5-1. It is important to note that the Nd^{3+} and Yb^{3+} luminescence decays in $[Ln(Trop)_4]^-$ complexes are best fit as

monoexponential decays, indicating a unique coordination environment around the central Ln^{3+}.[4,182] Since there should be more than one coordination environment for Ln^{3+} in the NCs (i.e., core and surface), multiexponential decay profiles are expected. The experimental results reflect this hypothesis. For Yb^{3+} in the NCs, the experimental decay was best fitted as a biexponential function. The longest component is attributed to the luminescence decay from cations in the NC core and is the major contribution to the overall intensity. The second component is significantly shorter and can be attributed to Yb^{3+} with a lower level of protection from nonradiative deactivation, likely located at the surface of the nanocrystals. The experimental decay recorded for Nd^{3+} in the NCs is best fit with a triple exponential decay. Similar to Yb^{3+}, there is a long component which corresponds to luminescence decay from Nd^{3+} in the nanocrystal matrix. The two shorter components are assigned to Nd^{3+} at or near the NCs surface in different coordination environments. Since Nd^{3+}, unlike Yb^{3+}, has a large number of excited states, and thus additional routes for nonradiative deactivations, it may be more sensitive to coordinating ligands than Yb^{3+} resulting in additional lifetime components.

Table 5-1. Luminescence Lifetimes (μs) of the Complexes and $Trop^-$-Capped NCs and Contribution to Luminescence Intensity in Brackets. λ_{ex} = 354 nm.

Ln^{3+}	**$NaY_{0.8}Ln_{0.2}F_4$ NC**	**$KLn(Trop)_4$**
Yb^{3+}	68(3), [80(2)%]	12.43(9)
	4.1(4), [20(2)%]	
Nd^{3+}	12.6(9), [22(1)%]	1.10(4)
	3.7(2), [63(6)%]	
	1.1(2), [15(6)%]	

Globally, significantly longer luminescence lifetimes were observed for the $Trop^-$ capped Yb^{3+}/Nd^{3+} doped NCs than for the corresponding molecular complex $[Ln(Trop)_4]^-$. The longest components among the luminescence lifetimes were more than 5 times longer for Yb^{3+} and more than 11 times longer for Nd^{3+}. These values prove that our strategy to increase protection around the lanthanide cations through their incorporation in NCs is successful.

5.5 CONCLUSIONS

In conclusion, we have demonstrated the success of an innovative strategy to protect and sensitize NIR emitting Nd^{3+} and Yb^{3+} cations via doping in $NaYF_4$ NCs coated with sensitizing tropolonate chromophores. The NC matrix protects the Ln^{3+} from nonradiative deactivation via high-energy vibrations of solvent molecules and/or of organic ligands, as proven by the longer luminescence lifetimes. Through this work, we have established proof that it is possible to combine the antenna effect provided by organic chromophores with the protection from an inorganic matrix, thereby reducing the usual limitations of NIR lanthanide luminescence in coordination complexes. This is a general strategy that can be expanded for application to different combinations of organic chromophores, lanthanide cations, and inorganic matrices. The NCs have a relatively small size, and combined with the proper choice of ligand system(s) to give the capped NCs water solubility, it will be possible to extend this methodology for bioanalytical applications.

Acknowledgements

We thank Joseph P. Suhan, (Dept. of Biological Science, Carnegie Mellon University) for help in acquiring the TEM images. We also thank Prof. Richard A. Butera (Dept. of Chemistry, University of Pittsburgh) for his insight in the interpretation of XRD data.

6.0 ZINC-ADENINATE METAL-ORGANIC FRAMEWORK FOR AQUEOUS ENCAPSULATION AND SENSITIZATION OF NEAR-INFRARED AND VISIBLE EMITTING LANTHANIDE CATIONS

6.1 CHAPTER PREFACE

The aim of this work was to propose the use of a metal-organic framework (MOF) as a lanthanide-containing nanomaterial for luminescent biological applications. Specifically, the facile incorporation of lanthanide cations within the architecture of **bio-MOF-1** through cation exchange was demonstrated as well as the sensitization of lanthanide luminescence by the organic constituents. Preliminary experiments were also undertaken which highlight the combination of MOFs and lanthanide cations as a possible sensor array for biologically relevant molecules, specifically molecular oxygen. In addition to our experimental work, we engaged in a collaboration with other material chemists to further our collective goals of biological applications. The material contained in this chapter is currently in the revision stage of publication as a research communication in *The Journal of the American Chemical Society*, and the figures and tables have been reproduced with permission by *J. Am. Chem. Soc.* **2011**, *133(5),* 1220. Copyright 2011 American Chemical Society; Copyright 2011 American Chemical Society; the full citation is listed as Reference 188 in the bibliography section.[188]

List of authors: Jihyun An, Chad M. Shade, Demetra A. Chengelis-Czegan, Stéphane Petoud, Nathaniel L. Rosi

Author contribution: The author of this dissertation was responsible for contributing to the design of the experiments including the photophysical characterization of the Ln^{3+}-containing MOFs through steady-state excitation and emission profiles, O_2 detection experiments, Ln^{3+}-centered luminescence lifetimes and q-value analysis, providing interpretation of the results and contributing to the preparation of the published manuscript.

6.2 ABSTRACT

Luminescent MOFs, **Ln^{3+}@bio-MOF-1**, were synthesized via a post-synthetic cation exchange of **bio-MOF-1** with Tb^{3+}, Sm^{3+}, Eu^{3+}, or Yb^{3+} and their photophysical properties were studied. We demonstrate that **bio-MOF-1** encapsulates and sensitizes visible and near-infrared emitting lanthanide cations in aqueous solution.

6.3 INTRODUCTION

Luminescent lanthanide cations, in particular those emitting in the near-infrared (NIR) domain, have several emissive properties that are highly desirable for biomedical analysis.[1,62,67,68,189]

However, their luminescence intensities are often limited in aqueous media. This is typically due to the low quantum yields and therefore the relatively low number of photons emitted by each discrete molecular complex. Furthermore, the stability in water and hence biocompatibility of lanthanide molecular complexes often limit their use in biological applications. For such applications, it is critical that these complexes do not dissociate at low concentration which would result in the loss of lanthanide sensitization and/or the release of free lanthanide cations.

Metal-organic frameworks (MOFs)[190,191] have several advantages that render them useful for sensitizing lanthanide cations.[192-195] First, MOFs have well-defined structures in which a large number of chromophoric sensitizers and lanthanide cations can be incorporated. This fundamental aspect of MOFs results in a large number of photons emitted per unit volume, an important advantage that enhances detection sensitivity. Second, MOF structures can be tailored to modulate and optimize the photoluminescence properties of lanthanide cations.[194,196] Third, MOFs provide a rigid scaffold that can serve to protect lanthanide cations from solvent quenching. To date, most lanthanide MOFs consist of a lanthanide cation and an organic linker/sensitizer, and therefore the lanthanide cation is an important structural component of the MOF.[190]

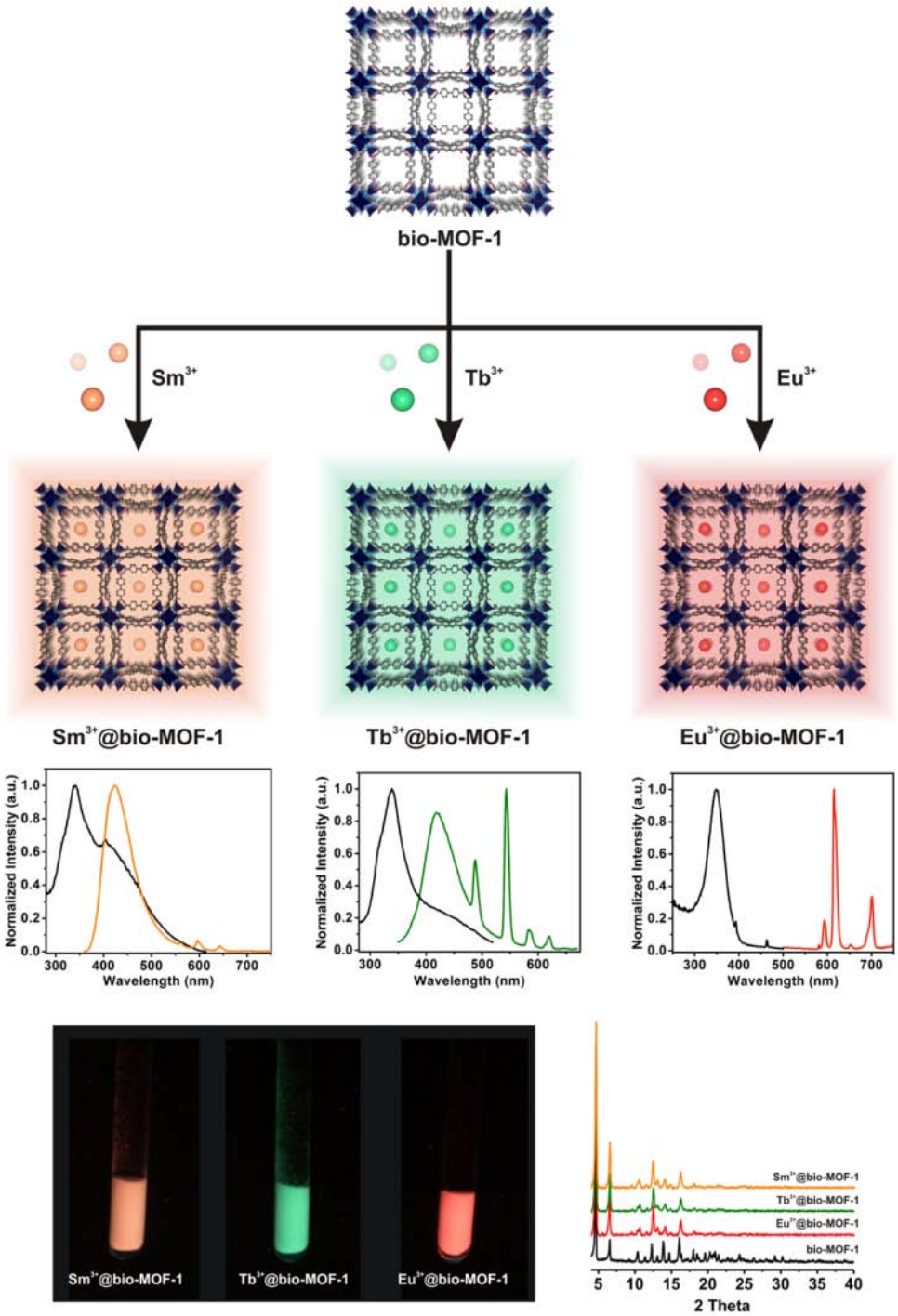

Figure 6-1. **Bio-MOF-1** encapsulation and sensitization of lanthanide cations. (A) Schematic illustration of Ln^{3+} incorporation into bio-MOF-1and subsequent Ln^{3+} sensitization by the framework. (B) Excitation and emission spectra of **Sm^{3+}@bio-MOF-1** (i), **Tb^{3+}@bio-MOF-1** (ii), and **Eu^{3+}@bio-MOF-1** (iii). (C) Samples of **Ln^{3+}@bio-MOF-1** illuminated with 365 nm UV light. (lamp spectrum is depicted in Figure 6-2) (D) XRPD patterns of **Ln^{3+}@bio-MOF-1.**

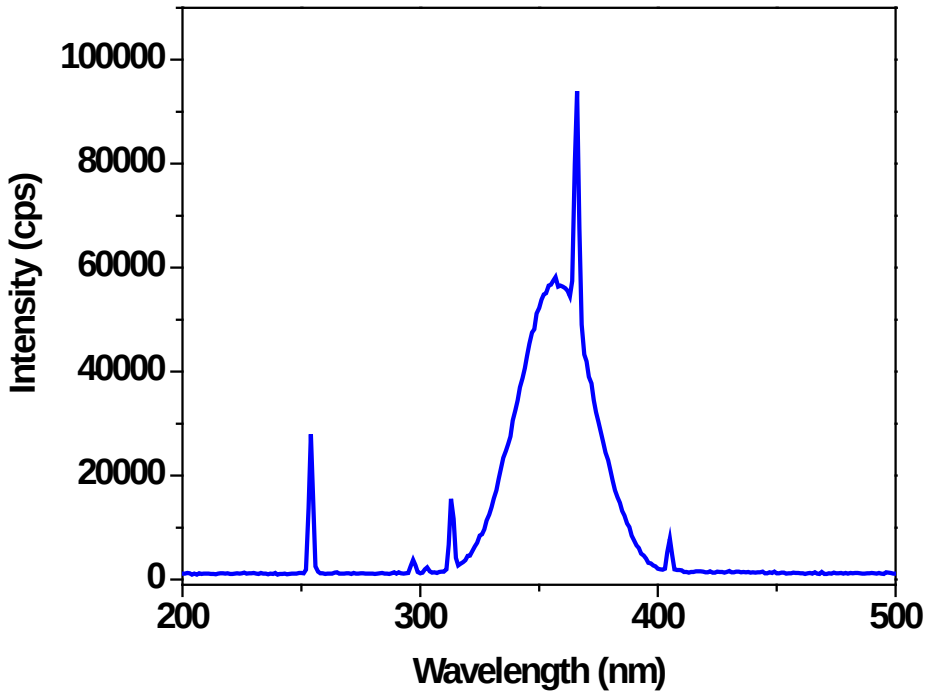

Figure 6-2. Emission profile of the handheld UV lamp used to collect the picture depicted in Figure 6-1C.

In this communication, we present a versatile strategy for generating luminescent lanthanide MOFs that are compatible for applications in aqueous solutions. Specifically, we show that a MOF can serve as both a host and an antenna for protecting and sensitizing extra-framework lanthanide cations emitting in the visible and NIR that are encapsulated within the MOF pores. We have developed a new class of porous metal-adeninate materials termed 'bio-MOFs.[197-200] In this study, we use **bio-MOF-1**[198] $[Zn_8(ad)_4(BPDC)_6O\bullet 2Me_2NH_2,8DMF,11H_2O]$ (ad = adeninate; BPDC = biphenyldicarboxylate; DMF = dimethylformamide), a rigid, permanently porous (~1700 m^2/g) structure as a scaffold for hosting and sensitizing several

visible and NIR-emitting lanthanide cations. **Bio-MOF-1** is anionic and organic cations or cationic drug molecules via straightforward dimethylammonium (DMA) cations reside in its 1-D pores. We have shown that the DMA cations can be exchanged with other cation exchange experiments.[198,200] We therefore reasoned that we could replace the DMA cations with specific lanthanide cations in a similar post-synthetic fashion.[201] Thus, we could load lanthanide cations into the pores of **bio-MOF-1** and analyze the luminescence properties of the resulting host-guest material (Figure 6-1). Ideally, the MOF would serve as a 'lantern' for protecting the lanthanide cations and enhancing their luminescence.[202]

6.4 EXPERIMENTAL

General Procedures. Unless otherwise noted, all chemicals were purchased from Aldrich Chemical Co. N,N'-dimethylformamide (DMF) were purchased from Fisher Scientific. All purchased starting materials were used without further purification. The elemental microanalyses (EA) were performed by Galbraith Laboratories. INC. using a Perkin-Elmer 240 Elemental Analyzer and by the University of Illinois, Department of Chemistry Microanalytical Laboratory using an Exeter Analytical CE440. Thermogravimetric analysis (TGA) was performed using a TGA Q500 thermal analysis system. All TGA experiments were performed under a N_2 atmosphere from 25-600 °C at a rate of 1 °C /min. Data were analyzed using the TA Universal Analysis software package. X-Ray powder diffraction (XRPD) patterns were collected using a Bruker AXS D_8 Discover powder diffractometer at 40 kV, 40 mA for Cu Kα, (λ = 1.5406 Å) with a scan speed of 0.20 sec/step and a step size of .02018 º. The data were analyzed for d-

spacing measurements using the EVA program from the Bruker Powder Analysis Software package. The simulated powder patterns were calculated using Mercury 2.0. The purity and homogeneity of the bulk products were determined by comparison of the simulated and experimental XRPD patterns. Nanopure (NP) water (18 MΩ) was produced using a water purification system from Barnstead Nanopure. Energy-disperse X-Ray spectroscopy analysis (EDS) was measured on a Philips XL 30 SEM equipped with an EDAX CDU leap detector.

Preparation of Ln^{3+}@bio-MOF-1. Bio-MOF-1 was synthesized according to our previously reported procedure.[198] The lanthanide cation loading was performed by cation exchange. Ln^{3+} nitrates ($Eu(NO_3)_3 \cdot 6H_2O$ 99.99% and $Tb(NO_3)_3 \cdot 5H_2O$ 99.9% from Aldrich ; $Yb(NO_3)_3 \cdot 5H_2O$ 99.9% and $Sm(NO_3)_3 \cdot 6H_2O$ 99.9% from Strem) were used as purchased. A solution of Ln^{3+} nitrate in DMF (0.1 M) was prepared. Ln^{3+} cation exchange was performed as follows: a) the as-synthesized material was rinsed with DMF (3X); b) the material was soaked in the Ln^{3+} nitrate solution (10 min) followed by solution removal; c) the material was again soaked in the Ln^{3+} nitrate solution (10 min) followed by solution removal; d) the material was soaked in the Ln^{3+} nitrate solution (24 h) followed by solution removal. Step d) was repeated every 24 h for 21 days. After cation exchange was completed, the materials were thoroughly washed with nanopure water and thereafter soaked in nanopure water (at least 24 h). After completion of this procedure, XRPD patterns were collected for each cation-exchanged material (Figure 6-1D and Figure 6-19B).

Composition of Ln^{3+} Exchanged Materials. We calculated the number of cations per **Ln^{3+}@bio-MOF-1** sample by analyzing data collected from EA, TGA and EDS. From these data, we determined that after cation exchange, there were 0.43-0.91 cations per unit material ($Zn_8(Ad)_4(BPDC)_6O$).

Table 6-1. Energy-disperse X-Ray spectroscopy analysis (EDS) data.

	Yb^{3+}@bioMOF-1	**Eu^{3+}@bioMOF-1**	**Tb^{3+}@bioMOF-1**	**Sm^{3+}@bioMOF-1**
Ln^{3+} %	10.2 (± 0.2) %	7 (± 1.0) %	5.1 (± 0.7) %	7 (± 1.0) %
Zn^{2+} %	89.8 (± 0.2) %	93 (± 1.0) %	94.9 (± 0.7) %	93 (± 1.0) %

Elemental Analysis:

Yb^{3+}@bio-MOF-1. $C_{104}H_{86}N_{20.72}O_{38.16}Zn_8Yb_{0.908}$ = $Zn_8(Ad)_4(BPDC)_6O \cdot 0.908Yb^{3+}$, $0.72NO_3^-$, $11H_2O$. Calcd.: C, 42.83; H, 2.97; N, 9.95. Found: C, 42.93; H, 2.87; N, 10.09

Eu^{3+}@bio-MOF-1. $C_{104}H_{106}N_{20}O_{46}Zn_8Eu_{0.6668}$ = $Zn_8(Ad)_4(BPDC)_6O \cdot 0.6668Eu^{3+}$, $21H_2O$ Calcd.: C, 41.69; H, 3.57; N, 9.35. Found: C, 41.84; H, 2.64; N, 9.33

Tb^{3+}@bio-MOF-1. $C_{105.43}H_{145.73}N_{20.72}O_{63}Zn_8Tb_{0.428}$ = $Zn_8(Ad)_4(BPDC)_6O \cdot 0.428Tb^{3+}$, 0.716DMA, $38H_2O$ Calcd.: C, 38.35; H, 4.45; N, 8.79. Found: C, 38.38; H, 3.09; N, 8.98

Sm^{3+}@bio-MOF-1. $C_{104}H_{146}N_{20}O_{66}Zn_8Sm_{0.6668}$ = $Zn_8(Ad)_4(BPDC)_6O \cdot 0.6668Sm^{3+}$, $41H_2O$ Calcd.: C, 37.22; H, 4.39; N, 8.35. Found: C, 37.09; H, 3.22; N, 8.65

Thermogravimetric Analysis. The EA data and the TGA data can be roughly correlated. There are two discernible weight loss steps in the TGA plots of **Ln^{3+}@bio-MOF-1** (Figure 6-3): **Yb^{3+}@bio-MOF-1**, 7.93 % weight loss (rt to 50 °C) corresponds to loss of 8 H_2O (calcd. 5.0 %) and 5.8 % weight loss (50 to 250 °C) corresponds to loss of 3 H_2O and 0.72 NO_3 (calcd. 3.4 %). **Eu^{3+}@bio-MOF-1**: 11.5 % weight loss (rt to 50 °C) corresponds to loss of 18 H_2O (calcd. 10.8 %) and 3.2 % weight loss (50 to 250 °C) corresponds to loss of 3 H_2O (calcd. 1.8 %). **Sm^{3+}@bio-MOF-1**: 18.4 % weight loss (rt to 50 °C) corresponds to loss of 34 H_2O (calcd. 18.2 %) and 3.9 % weight loss (50 to 250 °C) corresponds to loss of 7 H_2O) (calcd. 3.8 %). **Tb^{3+}@bio-MOF-1:** 17.7 % weight loss (rt to 50 °C) corresponds to loss of 33 H_2O (calcd. 18.0 %) and 3.6 % weight loss (50 to 250 °C) corresponds to loss of 5 H_2O and 0.716 DMA (calcd. 3.7 %).

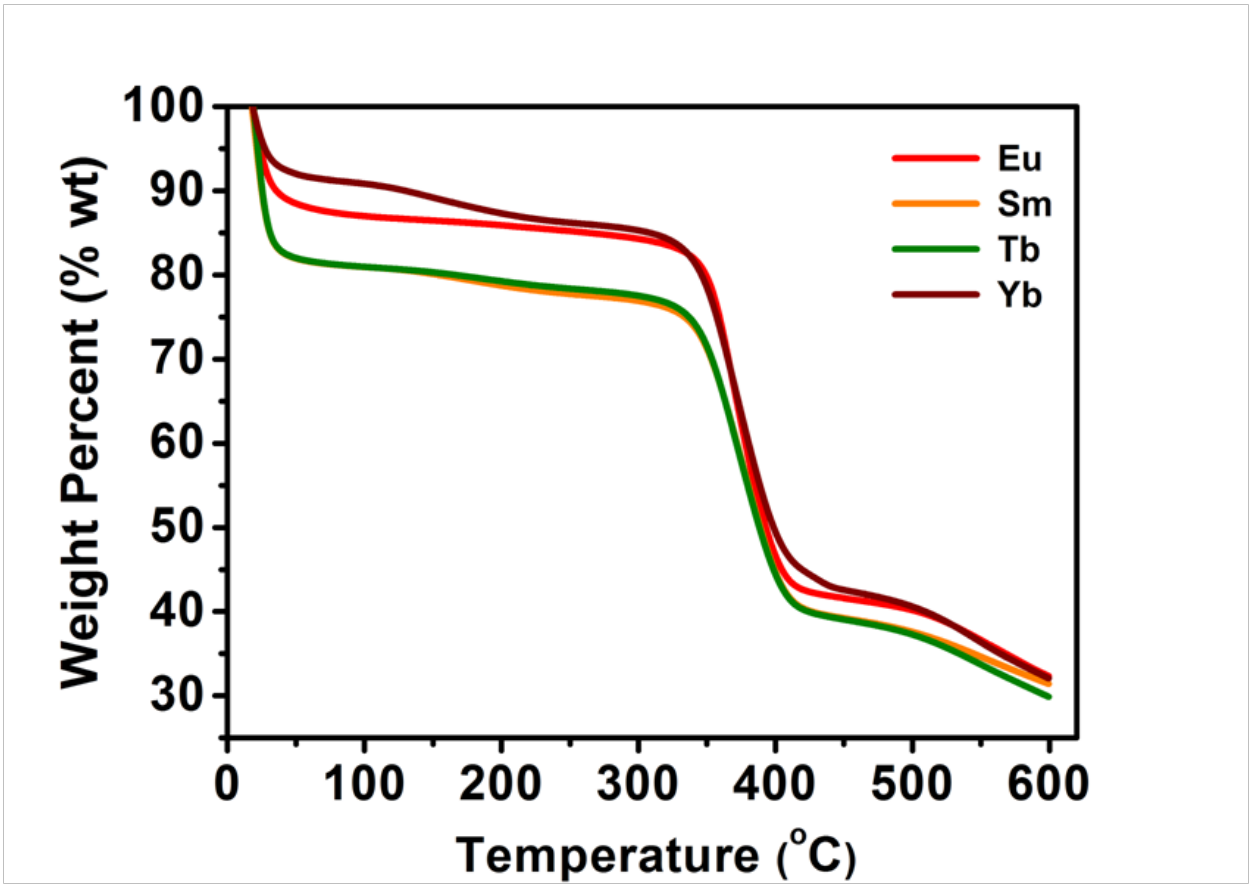

Figure 6-3. Thermogravimetric analyses of **Ln^{3+}@bio-MOF-1**.

Gas Adsorption Measurements. A N_2 adsorption isotherm for **Yb^{3+}@bio-MOF-1** was collected volumetrically as a function of relative pressure using an Autosorb 1 by Quantachrome. Samples of chloroform-exchanged **Yb^{3+}@bio-MOF-1** were weighed using an AB54-S/FACT (Mettler Toledo) electrogravimetric balance (sensitivity 0.1 mg). A 9 mm large bulb cell (from Quantachrome) of known weight was loaded with ~60 mg of sample for the gas adsorption experiment. The sample was degassed at 200 °C for 22-24 hours on a degassing station until the outgas rate was no more than 3.5 mTorr/min. The degassed sample and sample cell were weighed precisely and then transferred back to the analyzer. The temperature of the sample was controlled by a refrigerated bath of liquid nitrogen (77 K). The N_2 adsorbate was of UHP grade.

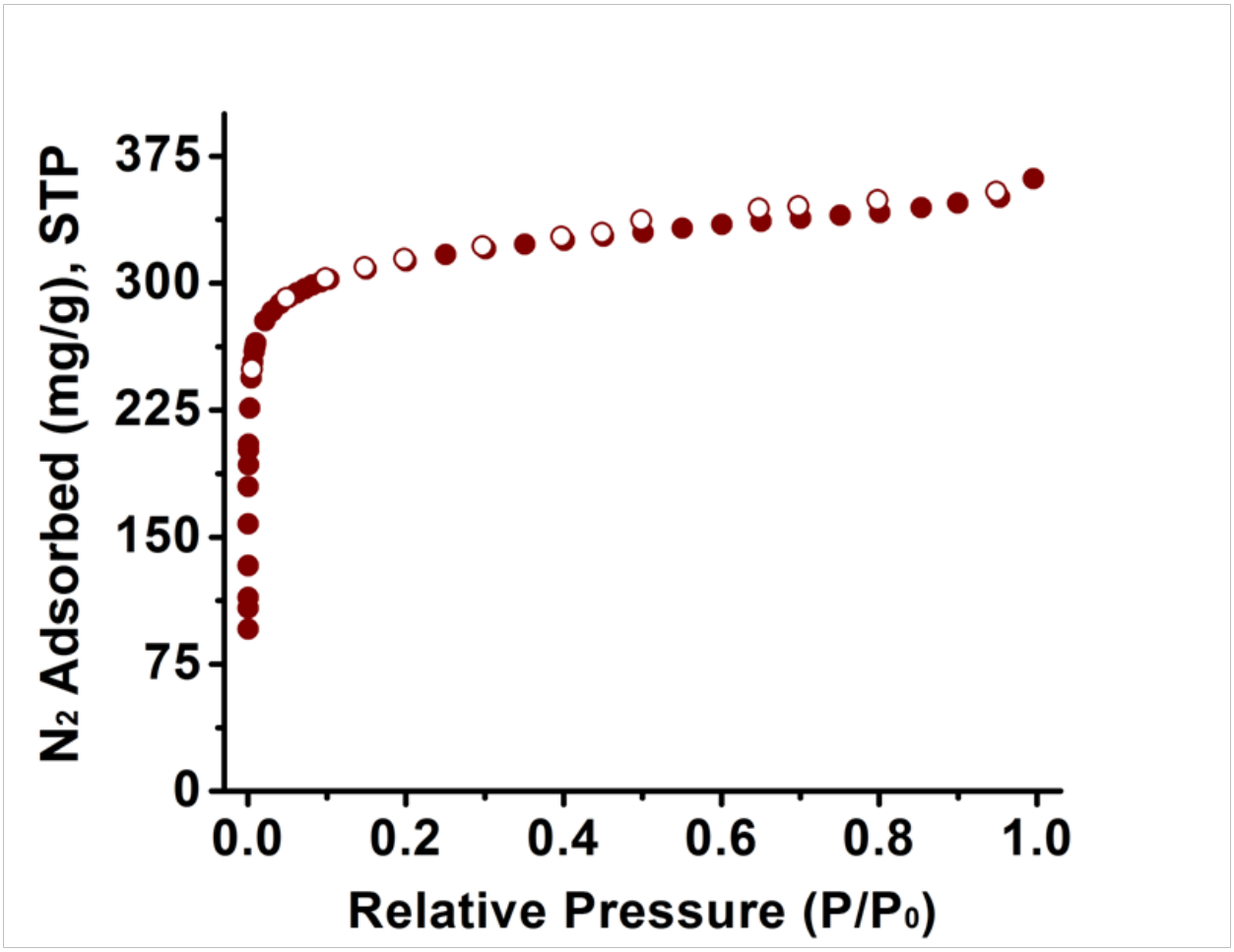

Figure 6-4. N_2 adsorption isotherm for **Yb^{3+}@bio-MOF-1** (filled, adsorption; empty, desorption). The BET Surface area is ~960 m^2/g.

Luminescence Measurements. Absorption spectra were recorded on a Perkin-Elmer Lambda 9 Spectrometer coupled with a personal computer using software supplied by Perkin-Elmer. Spectra were collected after instrumental zeroing with two quartz cuvettes of solvent.

Luminescence spectra in the visible and near infrared range (NIR) were measured using a Jobin Yvon–Horiba Fluorolog-322 spectrofluorimeter equipped with an Electro-Optical Systems,

Inc. DSS-IGA020L detector for the NIR domain fitted with an integration sphere developed by Frédéric Gumy and Jean-Claude G. Bünzli (Laboratory of Lanthanide Supramolecular Chemistry, École Polytechnique Féderale de Lausanne (EPFL), BCH 1402, CH- 1015 Lausanne, Switzerland) as an accessory to the Fluorolog FL3-22 spectrometer (Patent pending). Quartz tube sample holders were employed.[203] Quantum yield measurements of the solid state samples were measured with the integration sphere, using ytterbium tropolonate[4], $[Yb(trop)_4]^-$ (λ_{ex} = 340 nm) as the reference for the NIR range and TbH_2IAM[3] (λ_{ex} = 340 nm) as the reference for the visible range.

Lanthanide luminescence lifetimes in the NIR were measured using a Nd:YAG Continuum Powerlite 8010 laser (354 nm, third harmonic) as the excitation source. Emission was collected at a right angle to the excitation beam, and wavelengths were selected by a Spectral Products CM 110 1/8 meter monochromator. The signal was monitored with a HamamatsuR316-02 photomultiplier tube for the NIR range. The signal was collected on a 500 MHz band pass digital oscilloscope (Tektronix TDS 754D). For each flash, the experimental decay was recorded with a resolution of 50,000 points. To minimize experimental contribution, signals from >1000 flashes were collected and averaged. Luminescence lifetimes in the visible range were measured using the flash lamp and R928 Hamamatsu photomultiplier tube detector of a Jobin Yvon–Horiba Fluorolog-322 spectrofluorimeter. The signal was monitored with the Tektronix TDS 754D oscilloscope. Luminescence decay curves were analyzed with Origin 7.0 software using exponential fitting models. Three independent decay curves were collected on each sample, and reported lifetimes are an average of at least two independent measurements.

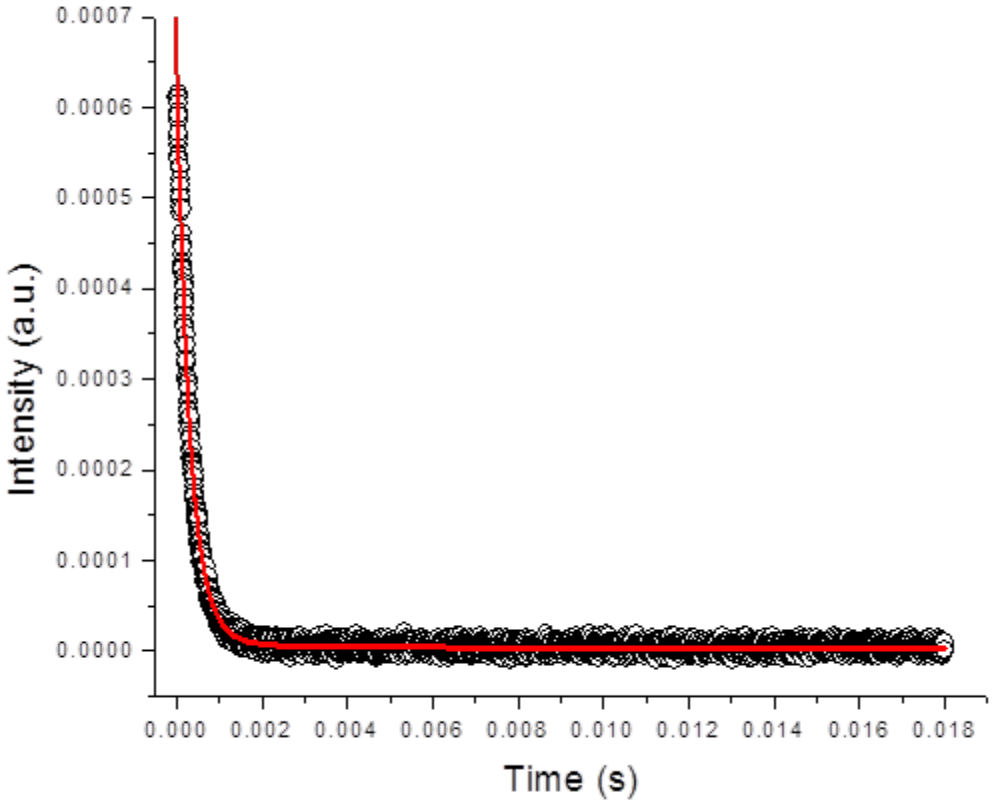

Figure 6-5. Luminescence lifetime decay curve for Eu^{3+}@bio-MOF-1 in H_2O with overlay of bi-exponential fitting function (red line).

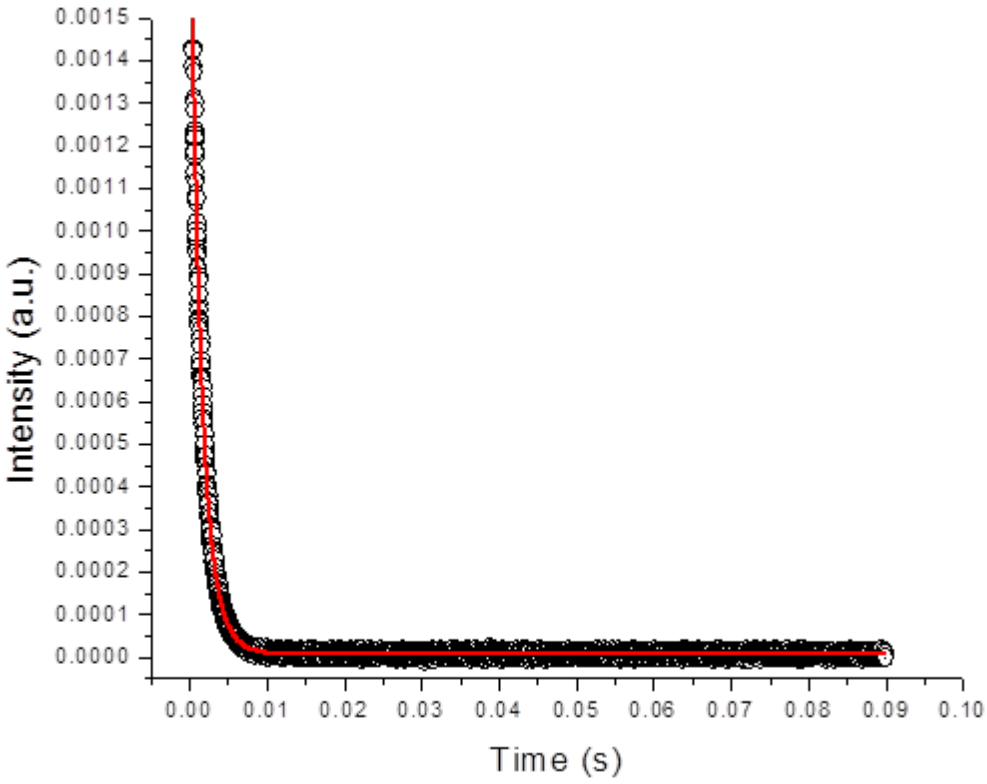

Figure 6-6. Luminescence lifetime decay curve for Eu^{3+}@bio-MOF-1 in D_2O with overlay of bi-exponential fitting function (red line).

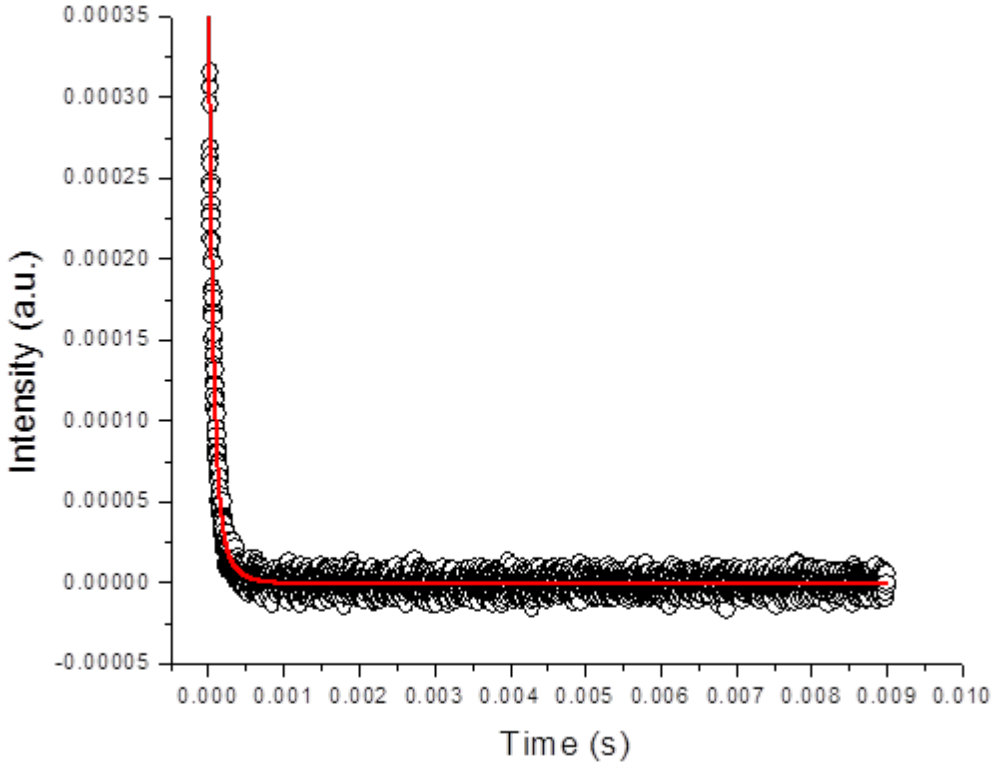

Figure 6-7. Luminescence lifetime decay curve for Tb^{3+}@bio-MOF-1 in H_2O with overlay of bi-exponential fitting function (red line).

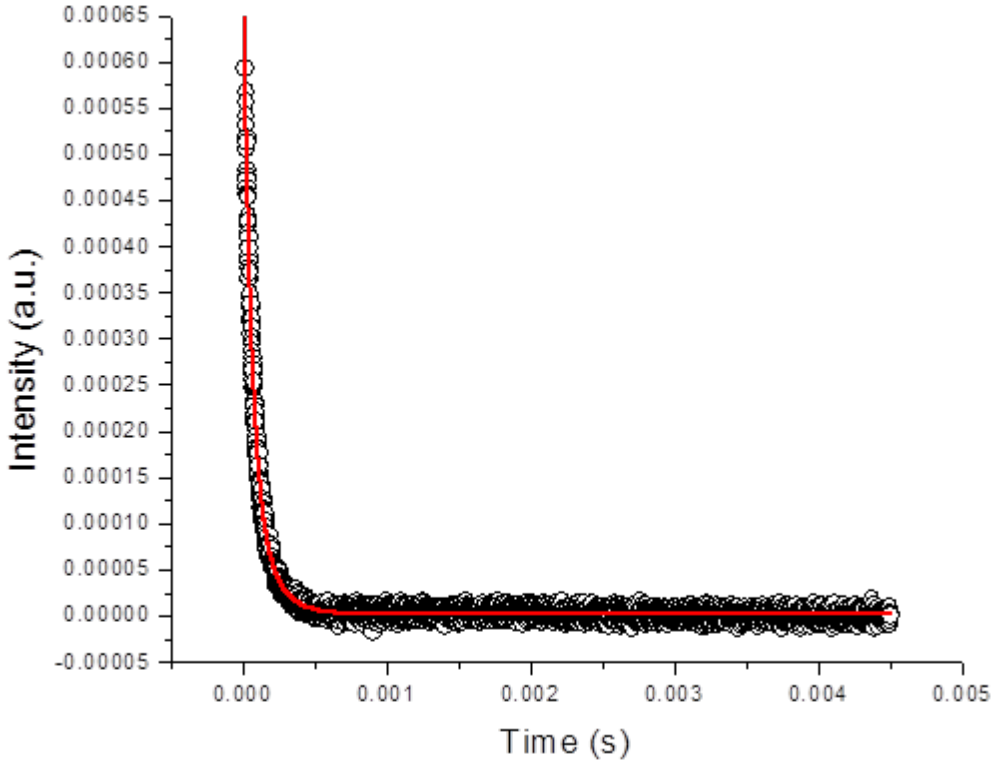

Figure 6-8. Luminescence lifetime decay curve for Tb^{3+}@bio-MOF-1 in D_2O with overlay of bi-exponential fitting function (red line).

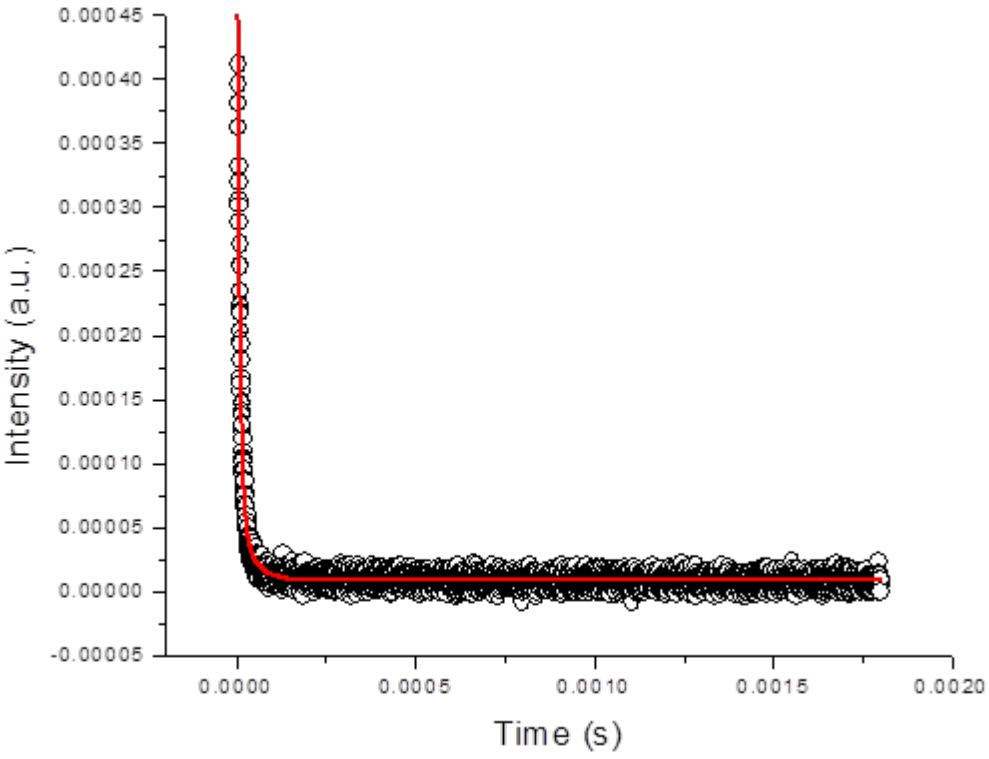

Figure 6-9. Luminescence lifetime decay curve for Sm^{3+}@bio-MOF-1 in H_2O with overlay of bi-exponential fitting function (red line).

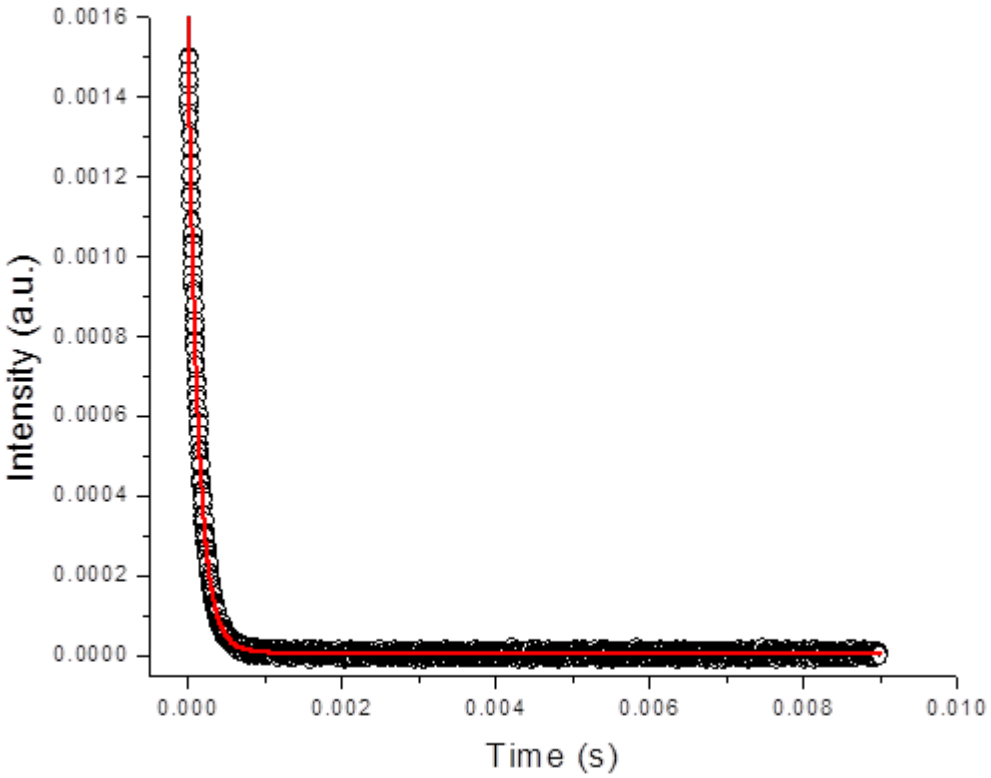

Figure 6-10. Luminescence lifetime decay curve for Sm^{3+}@bio-MOF-1 in D_2O with overlay of bi-exponential fitting function (red line).

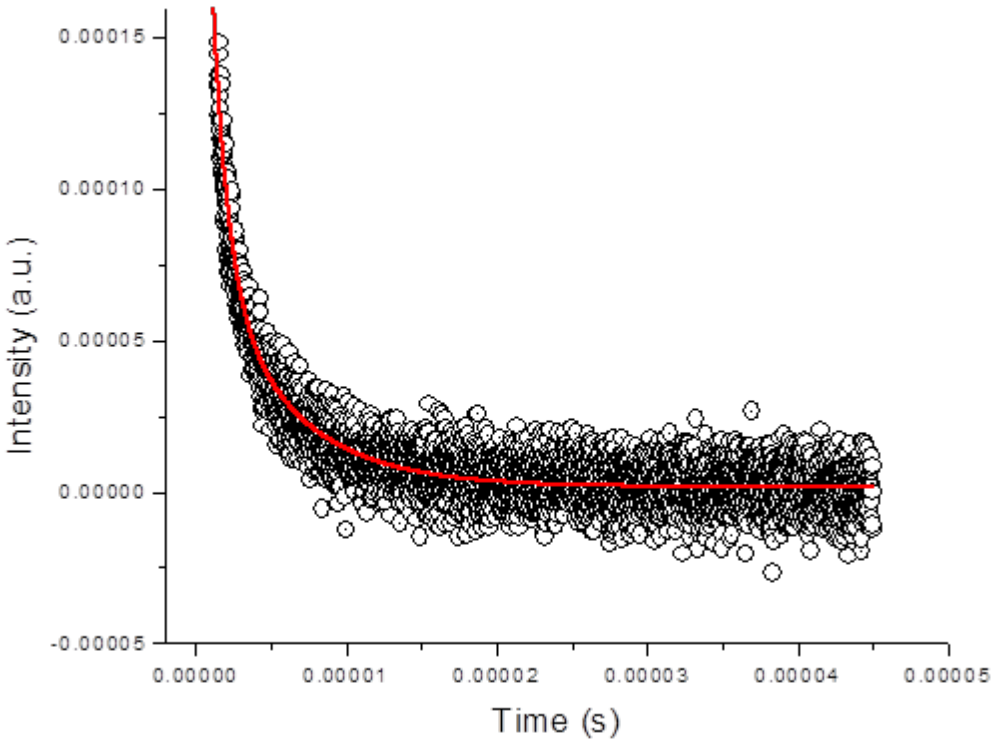

Figure 6-11. Luminescence lifetime decay curve for Yb^{3+}@bio-MOF-1 in H_2O with overlay of bi-exponential fitting function (red line).

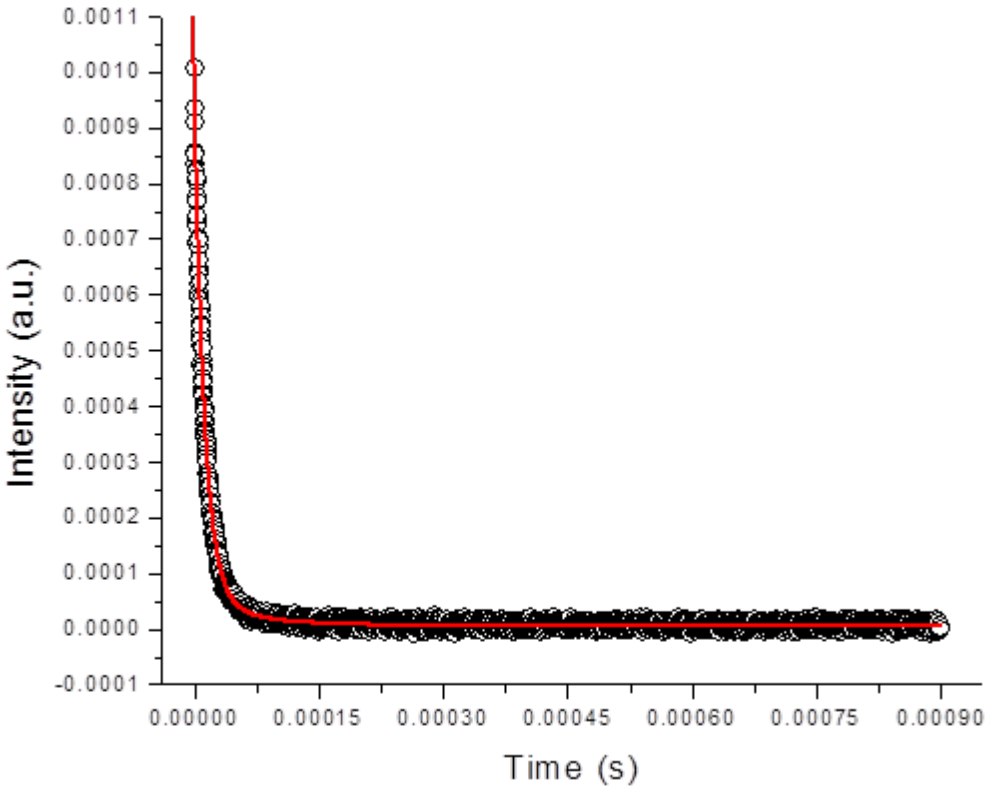

Figure 6-12. Luminescence lifetime decay curve for Yb^{3+}@bio-MOF-1 in D_2O with overlay of bi-exponential fitting function (red line).

q-value calculation for Eu@bio-MOF-1.[10] Each component of the bi-exponential luminescence decay curve fitted for **Eu^{3+}@bio-MOF-1** in H_2O was paired with a corresponding value in D_2O. Specifically, we coupled the two shortest components and the two longest components of the lifetimes generated from the iterative fitting process and then substituted these into the empirical formula developed by Beeby et al

The resulting q-values carry an intrinsic error of ±0.5 water molecules coordinating to each trivalent europium cation.

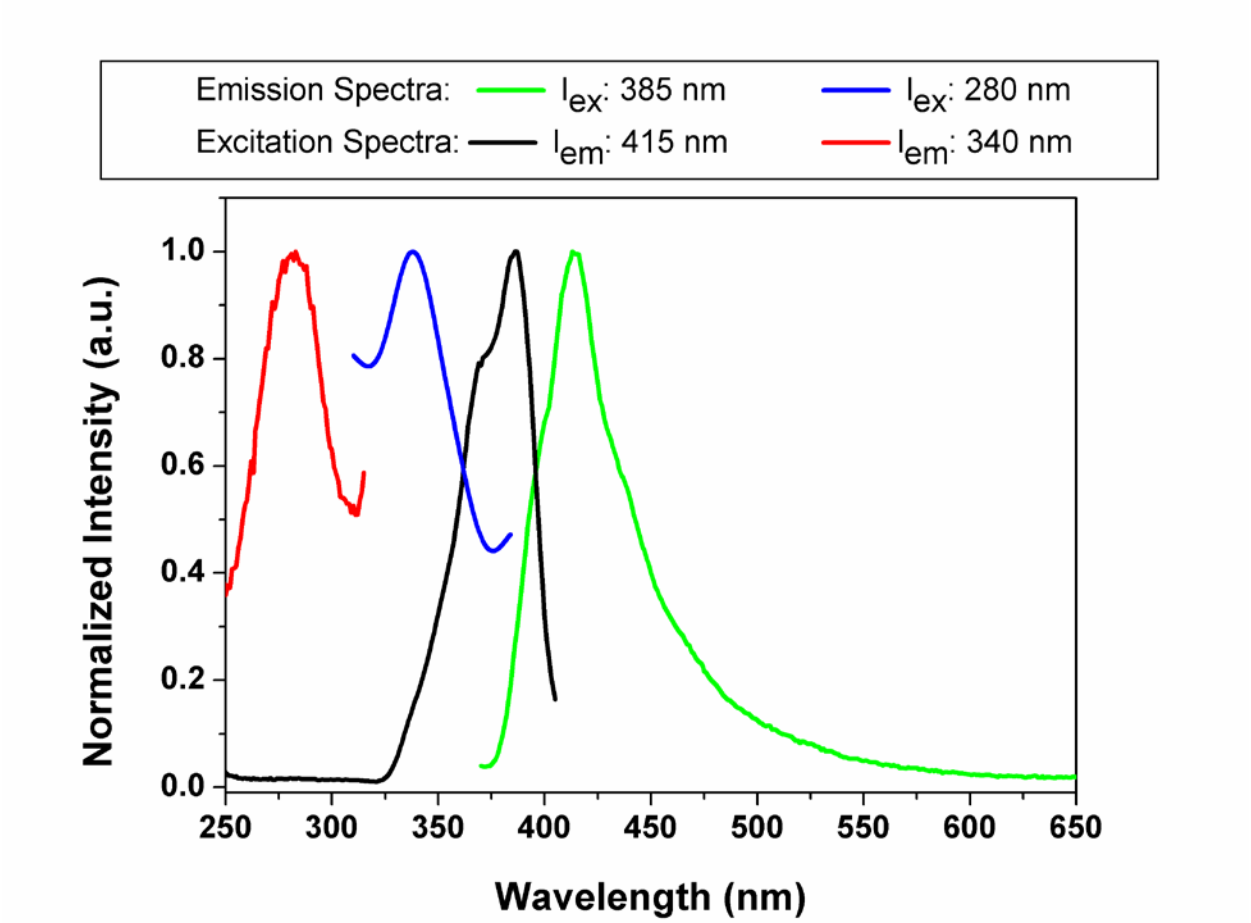

Figure 6-13. Fluorescence emission and excitation spectra. Emission spectra collected upon λ_{ex} = 280 nm (blue) and λ_{ex} = 385 nm (green) of **bio-MOF-1** in DMF and corresponding excitation spectra collected upon λ_{em} = 340 nm (red) and λ_{em} = 415 nm (black) of the band maxima.

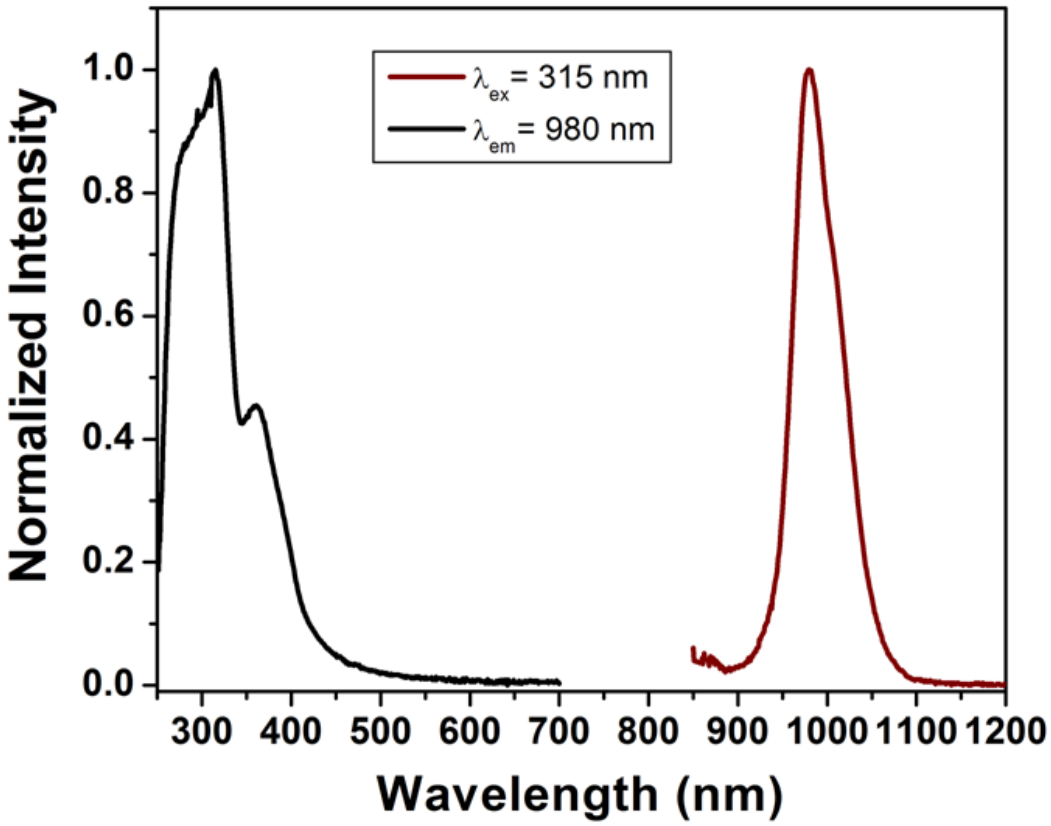

Figure 6-14. Excitation spectrum of ytterbium luminescence at 980 nm (black) and the NIR emission spectrum (wine) with λ_{ex} = 315 nm in DMF.

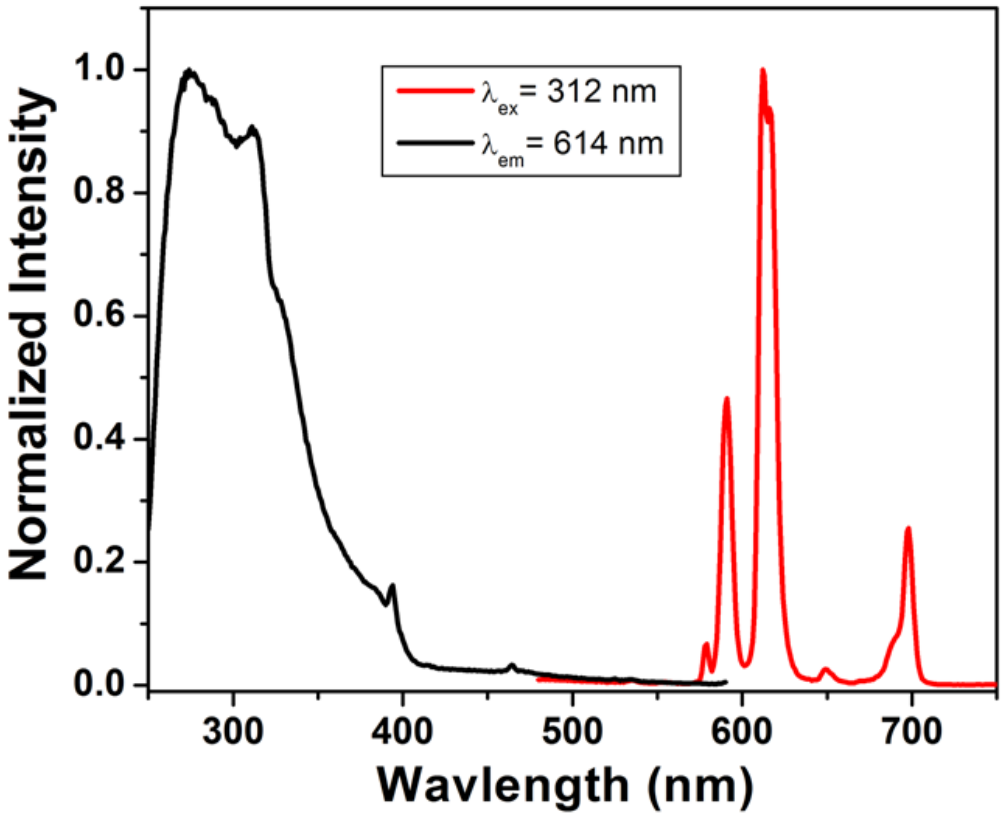

Figure 6-15. Excitation spectrum of europium luminescence at 614 nm (black) and the visible emission spectrum (red) with λ_{ex} = 312 nm in DMF.

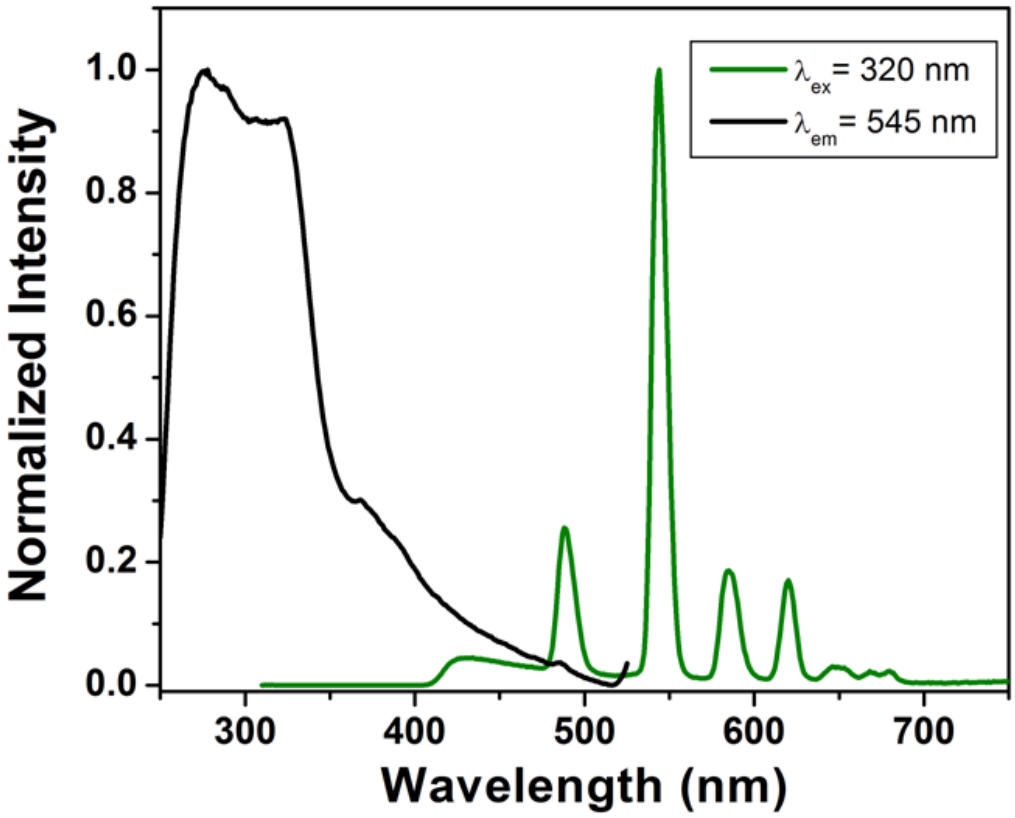

Figure 6-16. Excitation spectrum of terbium luminescence at 545 nm (black) and the visible emission spectrum (green) with λ_{ex} = 320 nm in DMF.

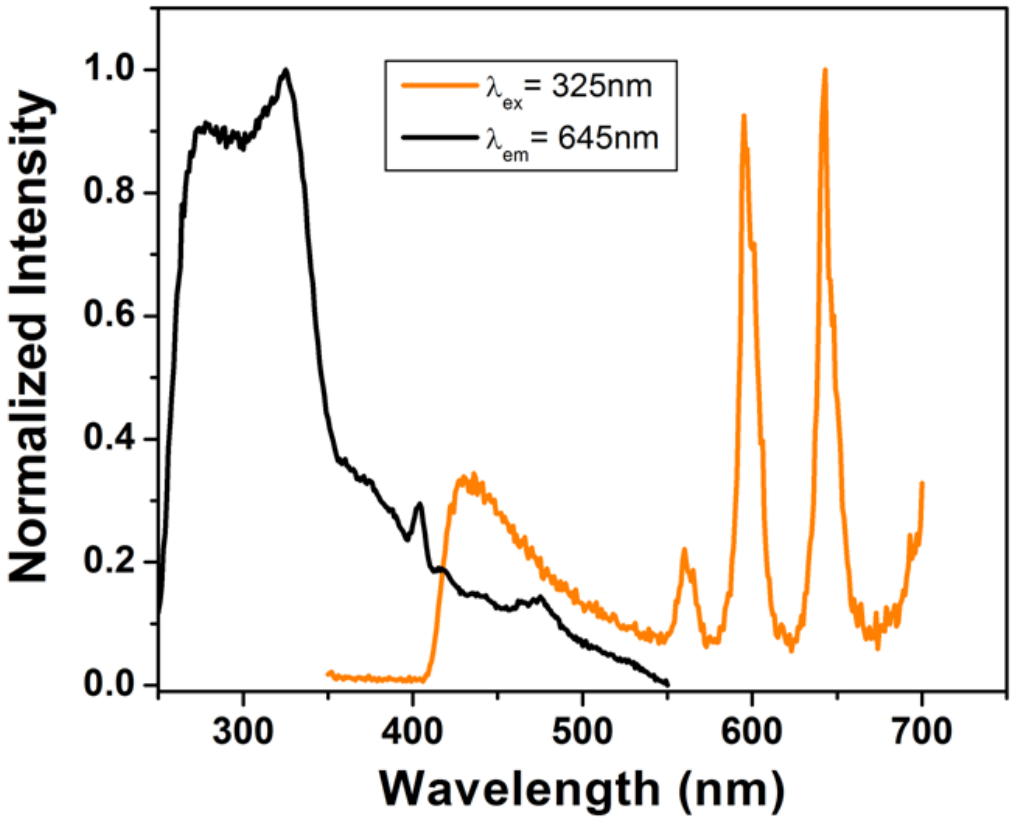

Figure 6-17. Excitation spectrum of samarium luminescence at 645 nm (black) and the visible emission spectrum (orange) with λ_{ex} = 325 nm in DMF.

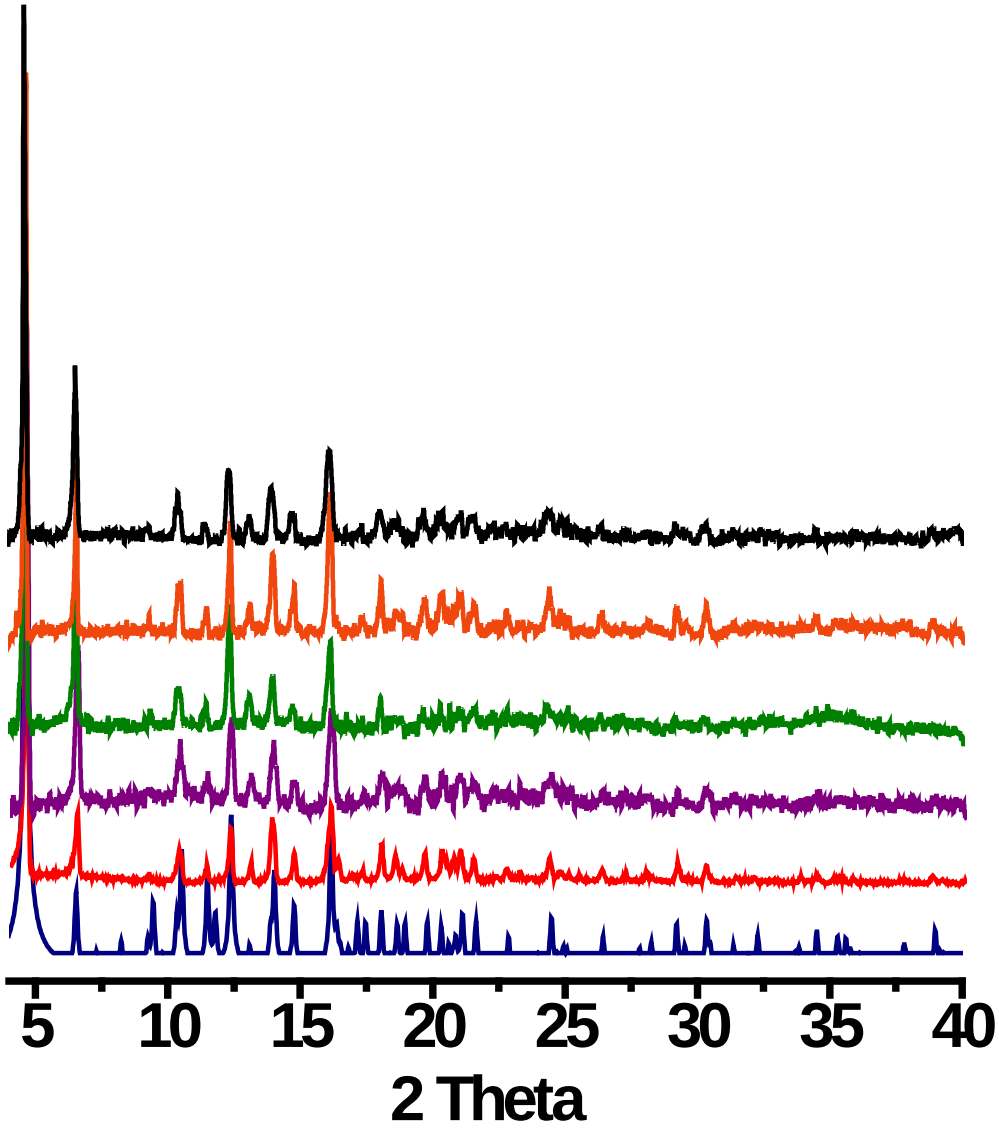

Figure 6-18. XRPD data of **Ln^{3+}@bio-MOF-1** samples after luminescence experiments. These data are compared to data collected for as-synthesized **bio-MOF-1** and data simulated from single-crystal diffraction data of **bio-MOF-1**

Oxygen Detection Experiments. A custom-built gas-delivery chamber[204], housed within a modified JY Horiba Fluorolog-322 spectrofluorimeter coupled to an Electro-Optical Systems, Inc. DSS-IGA020L detector, was used to collect steady-state emission spectra for the gas-sensitivity measurements. A 715 nm long-pass filter was used, and spectra were corrected for non-linearities in the lamp and detector.

6.5 RESULTS AND DISCUSSION

To introduce lanthanide ions into the pores of **bio-MOF-1**, samples of the material were soaked in DMF solutions of nitrate salts of either Tb^{3+}, Sm^{3+}, Eu^{3+}, or Yb^{3+} (Figure 6-1A).[205] Energy-dispersive X-Ray spectroscopy (EDS) and elemental analysis (EA) data of the Ln^{3+}-exchanged materials revealed successful lanthanide cation incorporation into the material to yield **Tb^{3+}@bio-MOF-1**, **Sm^{3+}@bio-MOF-1**, **Eu^{3+}@bio-MOF-1**, and **Yb^{3+}@bio-MOF-1** (see experimental for detailed formulation). Ln^{3+} loading does not impact the crystalline integrity of **bio-MOF-**1, as confirmed using X-Ray powder diffraction (XRPD) (Figure 6-1D and Figure 6-19B).

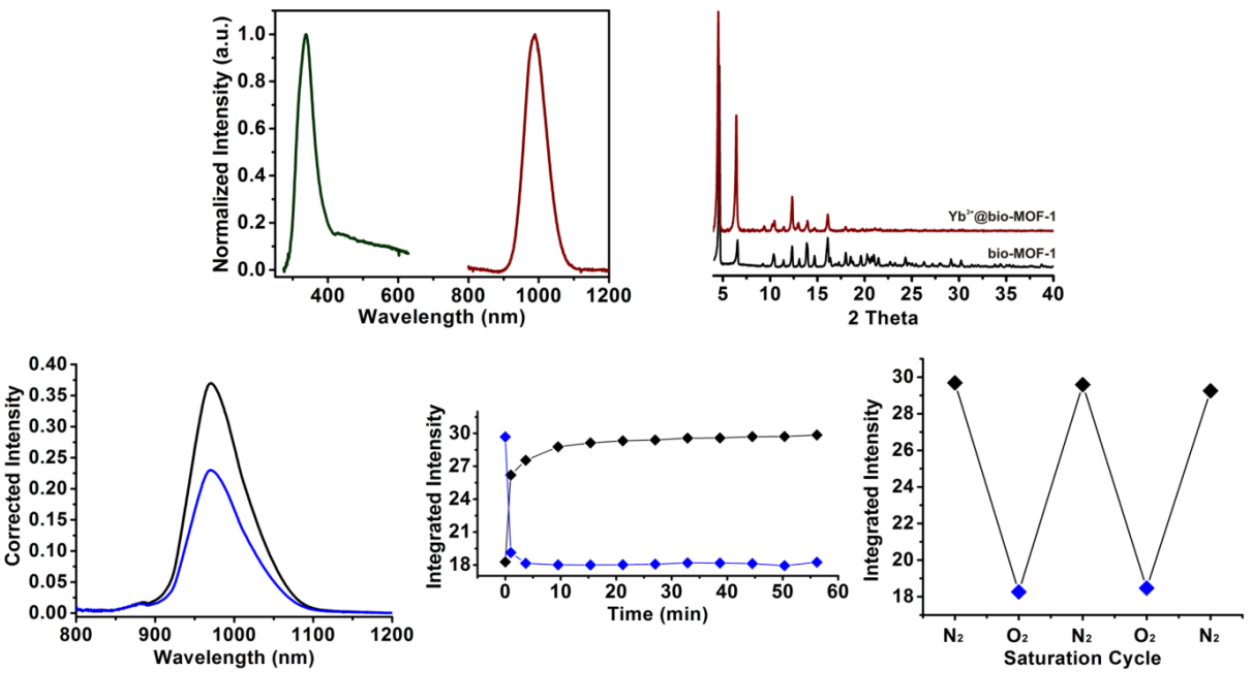

Figure 6-19. Yb^{3+} sensitization and O_2 detection studies. (A) NIR excitation and emission spectra of **Yb^{3+}@bio-MOF-1**. (B) XRPD of **Yb^{3+}@bio-MOF-1**. (C) Yb^{3+} emission profile under N_2 (black) and O_2 (blue). (D) Decrease in Yb^{3+} signal over time after exposure to O_2 (blue) and revival of Yb^{3+} signal over time upon exposure to N_2 (black). (E) Integrated intensities of Yb^{3+} emission over multiple cycles of exposure to N_2 (black) and O_2 (blue).

Initial spectroscopic studies (Figure 6-13) of **Tb^{3+}@bio-MOF-1** (Figure 6-16)**, Sm^{3+}@bio-MOF-1** (Figure 6-17), **Eu^{3+}@bio-MOF-1** (Figure 6-15) and **Yb^{3+}@bio-MOF-1** (Figure 6-14) in DMF indicated that **bio-MOF-1** sensitizes several visible and NIR emitting lanthanide cations in an organic solvent. Encouraged by these results, we proceeded to study the luminescence properties of these materials in aqueous environments. Each **Ln^{3+}@bio-MOF-1** sample was soaked in nanopure water (18 MΩ resistivity) to completely remove the DMF solvent molecules, and XRPD of the water-exchanged samples confirmed retention of crystalline

integrity (Figure 6-1D and Figure 6-19B). When excited with a standard laboratory UV lamp (365 nm), the samarium, europium, and terbium samples emitted their distinctive colors (Eu^{3+}, red; Tb^{3+}, green; Sm^{3+}, orange-pink), which were readily observed with the naked eye as a qualitative indication of lanthanide senstitization (Figure 6-1C). Lanthanide-centered excitation spectra recorded for **Tb^{3+}@bio-MOF-1 (**λ_{em} = 545 nm**)**, **Sm^{3+}@bio-MOF-1** (λ_{em} = 640 nm**), Eu^{3+}@bio-MOF-1 (**λ_{em} = 614 nm**)** and **Yb^{3+}@bio-MOF-1** (λ_{em} = 970 nm) all indicate the presence of a main band with an apparent maximum located at 340 nm, an indication that energy migrates through the same electronic levels located in the MOF chromophoric structure for all four compounds. The individual samples were then each irradiated with 340 nm light and the characteristic sharp emission bands corresponding to the respective encapsulated lanthanide cations were detected (Figure 6-1B and Figure 6-19A).

Despite the strong ability of water to quench the emission of NIR emitting lanthanides, the Yb^{3+} signal is easily detected (Figure 6-19A). These data demonstrate that the MOF scaffold, can effectively serve as an antenna for sensitizing three different visible-emitting lanthanide cations and one NIR-emitting lanthanide cation in an aqueous environment. It is worth noting that Yb^{3+} is a special lanthanide cation with respect to energy transfer as it has only one accepting electronic level. The hypothesis for energy transfer for this cation involves one of the following two mechanisms: 1) a phonon-assisted mechanism from either the triplet state or a metal-to-ligand charge transfer state of the sensitizer or 2) an internal double-electron transfer mechanism.[187,206] Importantly, after all the measurements in water, the materials still retained their crystallinity, as evidenced by their XRPD patterns (Figure 6-18). These results indicate that these luminescent materials are therefore compatible with aqueous conditions and are photo-stable. Our ability to easily detect lanthanide luminescence in the presence of water provided an

indication that the MOF was able to not only sensitize but also provide sufficient protection to the lanthanide.

To quantify the level of protection provided by **bio-MOF-1** and to more completely understand the environment of the encapsulated lanthanide cations, we measured the lanthanide-centered luminescence lifetimes in water (Table 6-2). The best fit for each of the **Ln^{3+}@bio-MOF-1** samples was systematically bi-exponential, suggesting the presence of two distinct lanthanide environments within the MOF architecture. The **Tb^{3+}@bio-MOF-1** lifetimes, 62±1 μs and 224±9 μs, were surprisingly much shorter than Tb^{3+} lifetimes recorded for molecular complexes that are typically in the range of 1000 to 2000 μs.[207] It is probable that back-energy-transfer from Tb^{3+} to **bio-MOF-1** is occurring, as evidenced by a marked increase in luminescence lifetimes at 77K to 1970±80 μs (data not shown).[208] Despite this limitation, the Tb^{3+} luminescence can be easily detected and observed with the naked eye, which further illustrates the benefits of having a large number of lanthanides and sensitizers in a small volume.

Table 6-2. Ln^{3+} luminescence lifetimes (μs) and quantum yields of **Ln^{3+}@bio-MOF-1**.

Ln^{3+}	**τ_1 (H_2O)[a]**	**τ_2 (H_2O) [b]**	**τ_1 (D_2O)[a]**	**τ_2 (D_2O)[a]**	**$\Phi(Ln^{3+})$ [b]**
Tb^{3+}	62(1)	224(9)	54.2(9)	142(9)	1.7(0.1) x 10^{-2}
Sm^{3+}	7.4(3)	35(5)	131.1(7)	539(41)	2.8(0.2) x 10^{-3}
Eu^{3+}	299.9(5)	986(48)	1163(6)	1886(7)	8.4(0.1) x 10^{-2}
Yb^{3+}	1.1(1)	5.5(4)	12.1(2)	55.9(5)	2.5(0.2) x 10^{-4}

[a] λ_{ex} = 354 nm ; λ_{em} = 545 nm (Tb^{3+}), 640 nm (Sm^{3+}), 614 nm (Eu^{3+}), 970 nm (Yb^{3+}). [b] λ_{ex} = 340 nm; in H_2O

Luminescence lifetimes were also collected in deuterated water (Table 6-2) to determine q-values, the calculated number of water molecules coordinating to each lanthanide cation (see Table 6-1).[10] Very short luminescence lifetimes were observed once again for **Tb^{3+}@bio-MOF-1** in D_2O, a further indication that the Tb^{3+} excited state is quenched by contributions other than solvent vibrations. Due to this special consideration, q-values could not be calculated for the **Tb^{3+}@bio-MOF-1** system. **Eu^{3+}@bio-MOF-1** displays the longest luminescence lifetimes in both solvents; it displays a calculated q-value of 2.7 for the shorter set of lifetime values, which suggests that the MOF provides limited protection from water in one pore environment. A q-value of 0.3 calculated from the set of the two longest luminescence lifetimes indicates that a second environment within **bio-MOF-1** provides a higher level of protection to the lanthanide cations. These calculated q-values indicate that two different numbers of water molecules are

bound to the lanthanide cations in the MOF pores. This result is consistent with TGA data, which reveal two different types of water loss (Figure 6-3).

The lanthanide-centered quantum yields of **Ln^{3+}@bio-MOF-1** in water were measured (Table 6-2). The quantum yields are all reasonably high considering the aqueous environment, providing an indication that the lanthanide cations are protected to a significant extent within the pores, and the energy transfer from the sensitizer embedded in the MOF to the lanthanide cations is efficient. Since **bio-MOF-1** encapsulates a large number of lanthanide cations within a defined space, the luminescence intensity of **Ln^{3+}@bio-MOF-1** is quite high.

Effectively, **bio-MOF-1** serves as a high surface area scaffold (Figure 6-4) for sensitizing lanthanide cations and arranging and exposing them in 3-D space. We therefore reasoned that **Ln^{3+}@bio-MOF-1** materials could potentially serve as sensors for small molecules. To evaluate this possibility, we performed preliminary O_2 detection experiments using **Yb^{3+}@bio-MOF-1** in solid-state conditions.[209] While several visible emitting complexes have been tested for oxygen sensing,[204,210-212] we note that NIR luminescence has the advantage to allow for more sensitive detection in complex media such as biological samples which have very low native NIR fluorescence (favorable to signal to noise ratio). Samples of **Yb^{3+}@bio-MOF-1** were dried for 15 hours at 200 ^{o}C and mounted on quartz slides in a gas chamber within our fluorimeter. **Yb^{3+}@bio-MOF-1** responds to the presence of O_2 gas, as evidenced by monitoring the Yb^{3+} luminescence signal upon excitation with 340 nm light. An approximate 40% signal decrease was observed within the first five minutes of introducing O_2 gas to a purged chamber under ambient pressure (Figure 6-19C). After five minutes, the system reached equilibrium and the signal maintained its intensity for the duration of exposure, approximately one hour (Figure 6-19D). Purging the chamber once more with N_2 resulted in the restoration of the Yb^{3+} signal to

its original intensity. Importantly, this experiment is reversible, and we demonstrated that the Yb^{3+} signal maintains its original intensity after several cycles of exposure to O_2 and N_2 (Figure 6-19E). These are important advantages that merit consideration when designing a photostable O_2 sensor.

6.6 CONCLUSIONS

In conclusion, we have shown that porous anionic **bio-MOF-1** can incorporate lanthanide cations via a simple cation exchange process and sensitize multiple lanthanide cations, thus allowing for the facile preparation of multiple different luminescent materials. Further, we showed that bio-MOF-1 protects and sensitizes visible and NIR-emitting lanthanides in water. To our knowledge, this is the first example of a MOF that sensitizes NIR emitting lanthanide cations in water. These results are particularly exciting as water is a highly quenching solvent, and materials which protect lanthanides from water are necessary for enabling the use of NIR-emitting lanthanides in biological environments. Finally, we have demonstrated that **Ln^{3+}@bio-MOF-1** materials can potentially be used as versatile high surface area sensors for small molecules, including dioxygen. We believe this versatile strategy for generating new luminescent lanthanide materials will be useful for preparing new sensors and reporters for biological systems.

7.0 FORMATION OF POLYMETALLIC COMPLEXES AND SCAFFOLDING THE ANTENNA EFFECT FOR MORE LUMINESCENT LANTHANIDE REPORTERS: A DENDRIMER-2,3-NAPHTHALIMIDE LIGAND THAT SENSITIZES SEVERAL DIFFERENT LANTHANIDE CATIONS EMITTING IN THE VISIBLE AND IN THE NEAR-INFRARED: PR3+, ND3+, SM3+, EU3+, TB3+, DY3+, HO3+, ER3+, TM3+ AND YB3+

7.1 CHAPTER PREFACE

The aim of this work was to build upon our polymetallic strategy as a means of increasing the overall number of emitted photons per discrete molecule for taking advantage of lanthanide luminescence. Specifically, we used poly(amidoamine) (PAMAM) dendrimers to scaffold the antenna effect between several lanthanide cations contained within the internal cavities and 2,3-naphthalimide organic chromophores substituted along the surface. With this system and this strategy, we have been able for the first time to report the sensitization of ten different lanthanide cations emitting in the visible and near-infrared with a unique chromophoric ligand. Ultimately we pursued this strategy in subsequent chapters with 1,8-naphthalimide for biological applications due to the ease of further synthetic modification to this sensitizer unit, however, the work presented in this chapter was an important advance for our research in luminescent

lanthanide chemistry. The material contained in this chapter is currently being organized as a full research paper.

List of authors: Chad M. Shade, Grzegorz P. Filipczyk, Hyounsoo Uh, Sebastian Blanck, Matthias Bischoff, Benedikt Huber

Author contribution: The author of this dissertation was responsible for some of the dendrimer synthesis and much of the photophysical characterization, including Ln^{3+}-centered quantum yields and luminescence lifetimes, absorption and fluorescence/phosphorescence excitation and emission profiles, providing interpretation of the results and contributing to the preparation of the manuscript.

7.2 ABSTRACT

This article describes the results of a strategy to overcome the limited luminescence intensities of lanthanide complexes by using a polymetallic strategy and to investigate the suitability of the chosen 2,3-naphthalimide to sensitize various visible- and NIR-emitting lanthanide cations. In this approach, the number of photons emitted by each discrete lanthanide complex is maximized by incorporating several lanthanide cations into each dendrimer and by attaching a large number of chromophoric sensitizers at the branch termini of dendrimers to maximize the absorption of the polymetallic complex. Because the sensitizing groups do not need to be bound directly to the

metal ion, a broad choice of chromophoric groups is possible, an additional advantage of this strategy. Polyamidoamine (PAMAM) dendrimers will be used as the basis for this work: the oxygen atoms that are located in their arms will be used for the coordination of the luminescent lanthanide cations.

7.3 INTRODUCTION

The field of polymer chemistry has enabled the development of dendrimer nanotechnology. Through the iterative coupling of dendrons (the monomer of dendrimers), versatile "carrier devices" on the nanometer scale are made. Dendrimers are built from successive layers, or generations, so the diameters grow linearly while the number of coordinating groups grows geometrically. Among the types of dendrimers that have been discovered, the polyamidoamine (PAMAM)[213-215] family of dendrimers are known to have low biological toxicity, to be stable *in vivo*, and to have been employed in a broad variety of biomedical applications such as MRI contrast agents, biosensors, and molecular "sponges" for toxic metals.[213,216-218] Used as MRI contrast agents, PAMAM dendrimers have shown good biocompatibility; *in vivo* deliverability without significant degradation for the time of the measurement, considering the efficiency of these contrast agents depends on the structural integrity of the molecule.[219] The PAMAM structure possesses oxygen atoms in the amide groups of their internal branches. Oxygen atoms are hard Lewis bases, suitable for forming strong coordination bonds with lanthanide cations.[28] By coordinating the lanthanide cations in these internal branches, one protects the metal ion by minimizing its interaction with the solution or surrounding environment. For these reasons, we

have hypothesized that the internal branches of the PAMAM dendrimer should be useful for binding and protecting several lanthanide cations.

The branch termini of the PAMAM family of dendrimers contain chemical groups such as terminal primary amines, alcohol or carboxylic groups, enabling the dendrimers to be functionalized with suitable groups to serve as chromophores, signal antenna, or targeting molecules. To improve detection sensitivity by sensitizing lanthanide cations with an antenna effect, we terminated the end branches of the dendrimer with 2,3-naphthalimide chromophores (Figure 7-1). Certain naphthalimide groups can be further modified to permit the attachment of groups for specific biological targeting, such as peptides, proteins, antibodies or oligonucleotides. The naphthalimide groups could also potentially be modified to control the solubility properties, photophysical properties and the reporter's ability to act as a sensor.

In summary, the dendrimer structure must achieve three primary functions: 1) coordinating several lanthanide cations in an organized manner (formation of the polymetallic complex), 2) protecting the lanthanide cations from non-radiative pathways from the environment, and 3) offering an attachment point for chromophoric groups. The PAMAM dendrimer starting materials are readily (commercially) available as aqueous or methanolic solutions with the end branches terminated by $–NH_2$, -OH or –COOH groups, allowing synthetic flexibility. In addition, these dendrimers are available in different generations from Dendritech, Michigan, (from 0 to 10 for PAMAM-NH2 dendrimers, and 0.5 to 7.5 for the PAMAM-COOH dendrimers).

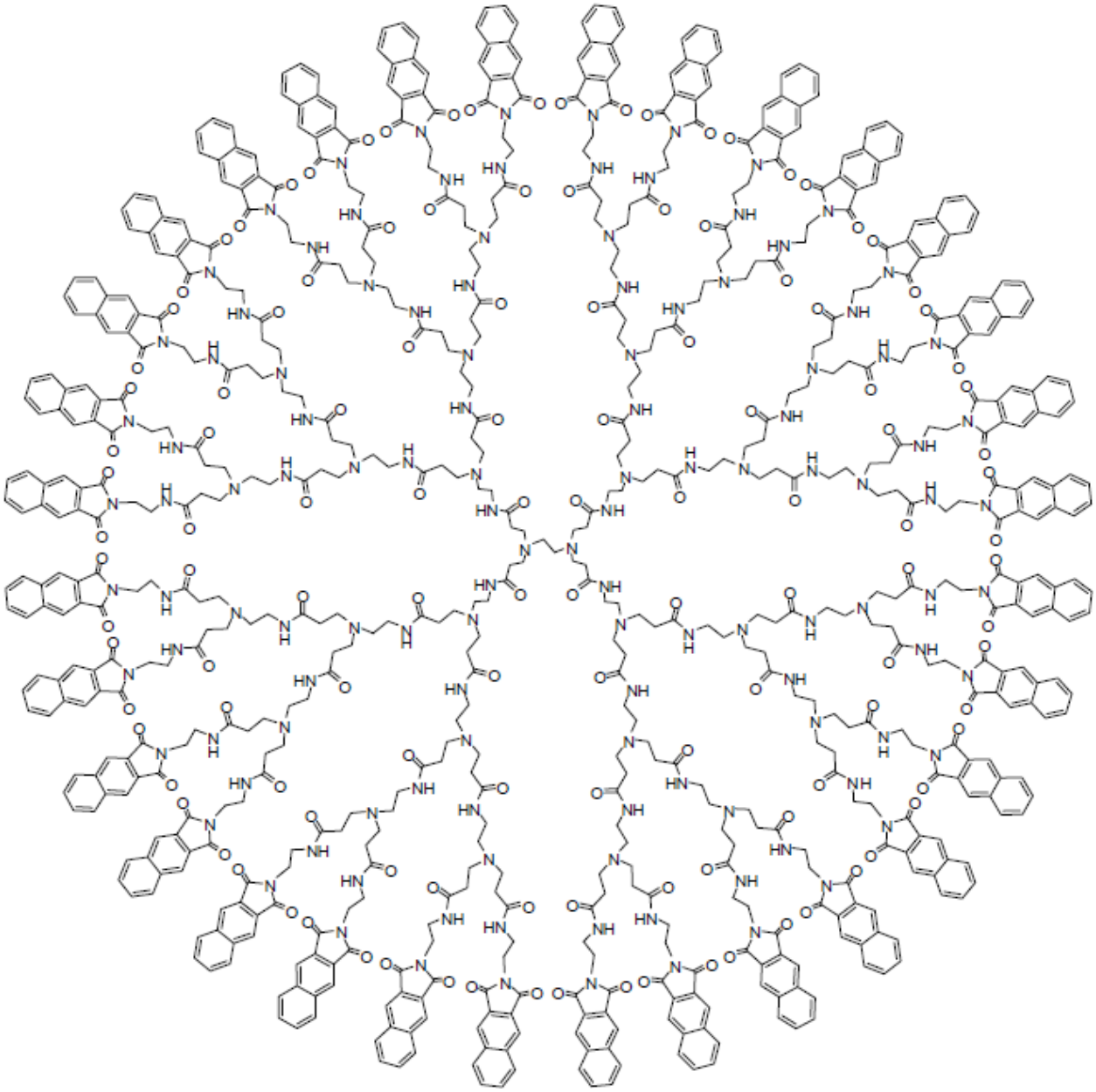

Figure 7-1. Molecular structure of G3-PAMAM-(2,3-naphthalimide)$_{32}$.

A derivative of the naphthalimide group, 2,3-naphthalimide (Figure 7-1), has been chosen as the lanthanide sensitizer in this project for several complementary reasons: 1) It possess highly populated triplet states,[220] an advantage for the sensitization of luminescent lanthanides since it is hypothesized[28] that in most cases the energy transfer occurs mostly from the ligand triplet state to the lanthanide accepting levels. Therefore, highly populated triplet states are expected to have a positive impact on the efficiency of the intramolecular ligand-to-lanthanide energy transfer.[29,221,222] 2) The 2,3-naphthalimide group can be easily modified to tune the photophysical properties of the resulting lanthanide complex, to provide sensing functionality (response of the luminescent reporter to a molecule or ion of biological relevance, for example) or for the attachment to a targeting agent such as a peptide, protein, antibody, or oligonucleotide. The substitution chemistry of naphthalimide groups is described in the literature.[223-230] Only one research group has reported the use of a naphthalimide group (1,8-naphthalimide) for sensitizing the visible emitting Eu^{3+} lanthanide cation. Their ligand design is different from ours, the complex being monometallic and the lanthanide cation being directly bound to the oxygen groups of the carbonyl of the naphthalimide groups.[231] This binding mode can only provide a limited coordination number to the lanthanide cations, limiting the protection of the cation and the overall stability of the complex.

A limited amount of work has been dedicated to the synthesis of polymetallic lanthanide complexes that are stable in solution (many polymetallic lanthanide complexes have been developed as solid state materials, but most of these dissociate in solution). Bünzli, Piguet and co-workers have developed di- and tri metallic tri-helical lanthanide complexes.[232,233] The synthesis of the ligands used to form these rigid complexes involves many steps and is time-consuming. An increase in the number of metal ions incorporated would require the development

of larger ligands with higher structutal complexity, which would be further synthetically challenging. Kawa and Fréchet have used dendrimers as antennae for Eu^{3+}, Tb^{3+} and Er^{3+} in monometallic dendrimers, where the solitary lanthanide cation is located at the center of each dendrimer, a design that does not allow incorporation of more than one metal ion per discrete molecule.[234] Balzani, Vögtle and coworkers have used dendrimer ligands for the development of polynuclear lanthanide complexes with cations emitting in the visible and in the near-infrared.[235] The lanthanide cations are also incorporated in the dendrimer ligand, but the dendrimer in their approach is structurally different from those of interest for our work, which leads to different properties. Their dendritic ligands incorporate dansyl-type chromophores that are substituted in the branches of the dendrimer.[175] Fewer amide groups are available for the coordination of lanthanide cations (typically 18 oxygen atoms from amide groups for their dendrimer, in comparison to at least 60 oxygens from a generation-3 dendrimer in our approach) **5**). Extension of the type of ligand proposed by Balzani, Vögtle *et al.* would require significant additional work and the overall generation of the dendrimer may be limited by the steric hindrance generated by the relatively bulky dansyl chromophoric groups present in the core of the dendrimer. There is a greater possibility for expansion with our polyamidoamine types of dendrimers, leading to a larger number of incorporated lanthanide cations for maximizing the luminescence intensity. In addition, the hypothesized distance between chromophore groups and lanthanide cations should be sufficient to rule out any possibility of energy transfer other than the dipole-dipole type of interaction (exclusion of Dexter mechanism)[54], a desirable characteristic for studying ligand-to-lanthanide energy transfer. Dendrimer ligands have also been used for the design of polymetallic Gd^{3+} complexes for the development of medical resonance imaging (MRI) contrast agents. The design of such ligands is different (the lanthanide cations are bound to a preorganized

coordinating group in the end branches of the dendrimer) and is not suitable for the development of luminescent lanthanide complexes due to the lack of chromophoric groups.[236]

i.) Create highly luminescent lanthanide compounds by synthesizing polymetallic lanthanide complexes coordinated in 2,3-naphthalimide dendrimer ligands that possess high absorbance

ii.) Sensitize several lanthanide cations emitting in the visible and in the NIR using a common 2,3-naphthalimide sensitizer (and therefore a common excitation, an advantage for many practical applications)

We have chosen the structure of a generation-3 poly(amidoamine) PAMAM dendrimer as the candidate to achieve these goals, (Figure 7-1), because these macromolecules possess many oxygen atoms, located on internal amide arms, that are suitable for coordinating several lanthanide cations. The 60 oxygen atoms located in the generation-3 PAMAM dendrimer are hypothesized to bind a number of lanthanides comprised between seven and eight per dendrimer, taking into account a coordination number of eight. Due to the thirty-two arms of the generation-3 dendrimer, multiple 2,3-naphthalimide groups can be attached, maximizing the molar absorptivity of the resulting compound. The globular nature of the dendrimer has been hypothesized to allow for formation of lanthanide complexes that are kinetically inert and thus dissociate slowly. In addition, the dendrimer structure is expected to protect coordinated lanthanide cations from nonradiative deactivation. We shall make use of the following short-hand notation to make all future references to dendrimer-lanthanide complexes in this paper, Gx-$(Ny)_n$:mLn^{3+}, with 'x' indicating the generation of the poly(amidoamine) dendrimer, a parameter

'y' designating the family of naphthalimide derivative covalently attached to the termini of the dendrimer, the subscript 'n' denoting the number of naphthalimide groups, a coefficient 'm' referring to the number of lanthanide cations coordinated in the dendrimer. 'Ln^{3+}' is the symbol that stands for any of the lanthanide cations. For example, the ligand depicted in Figure 7-1 will be named G3-$(N23)_{32}$, with "N23" for "2,3-napthalimide". Both 'n' and 'm' depend upon the generation of the dendrimer. For example, generation-3 has thirty-two branch termini and can thus be functionalized with thirty-two 2,3-naphthalimide sensitizers.

Preliminary results for the G3-$(N23)_{32}$:$8Eu^{3+}$ have been reported in the *Journal of the American Chemical Society*.[237] It has been demonstrated that this dendrimer ligand is able to incorporate an average of 7.5 lanthanide cations in solution. Monoexponential luminescence lifetimes of the Eu^{3+} cations recorded at room temperature (1.10 ms) and 77 K (1.16 ms) indicate that each lanthanide cation in the dendrimer is well protected from non-radiative deactivation by the dendritic structure. Despite the low efficiency of energy transfer between the chromophore and lanthanide cation (quantum yield of 0.06%), the Eu^{3+} centered emission is still visible with the naked eye when irradiated with a regular laboratory UV lamp (λ_{ex} = 354 nm) due to the large number of conjugated chromophoric groups (high absorbance) and luminescent cations. In this work, we have extended our study to other luminescent lanthanides. We have investigated the suitability of the G3-$(N23)_{32}$ for the coordination and as a sensitizer for other visible- and NIR-emitting lanthanides.

7.4 EXPERIMENTAL

Reagents. The PAMAM generation 3 dendrimer dissolved in anhydrous methanol (26.03% by weight) was purchased from Dendritech (Michigan). 2,3-naphthalic anhydride, was purchased from TCI America (New York). Methylsulfoxide extra dry with molecular sieves and N,N-Dimethylformamide, extra dry with molecular sieves, were purchased from Acros Organics. $Ln(NO_3)_3 \cdot nH_2O$ (Ln = Tb, Er and Yb, 99.9% or 99.99%, n = 5 or 6), were purchased from Aldrich. $Ln(NO_3)_3 \cdot 6H_2O$ (Ln = Eu, Nd Gd and La, 99.9% or 99.99%) and $LnCl_3 \cdot 6H_2O$ (Ln = Pr, Sm, Dy, Ho and Tm, 99.9% or 99,99%) were bought from Strem Chemicals. Quinine sulfate (99.0%) was purchased from Fluka. All deuterated NMR solvents were purchased from Cambridge Isotope Labs and used as received.

Instruments. ^{1}H-NMR (300 MHz) and ^{13}C-NMR (75 MHz) spectra were recorded with a Bruker AC300 spectrometer. DMSO-D_6, CD_3OD and CDC_{l3} were used as solvents unless otherwise stated. δ values are quoted in ppm; coupling constants are given in Hz. Elemental analyses were performed by Atlantic Microlab, Inc. MS-ESI were measured on a Micromass Autospec and Agilent HP 1100 series LC-MSD. Thin layer chromatography was carried out on 0.25 mm GF60A silica plates. Column and Flash Chromatography were performed using silica gel (60-200 Mesh). Solvent ratios refer to volume prior to mixing. Ultrafree-15 Centrifugal Filter Units with 10,000 Dalton cut off filter were used for centrifugal separation and purification. Solvent removal and compound drying were completed using a rotary evaporator and vacuum oven (35 mmHg, 40 Celsius degree unless otherwise stated).

UV/VIS absorption spectra were recorded on a Perkin-Elmer Lambda 19 spectrophotometer coupled with personal computer using software supplied by Perkin-Elmer in 1

cm quartz cells manufactured by NSG Precision Cells, Inc. Absorbencies were converted into molar extinction coefficients by means of Equation 7-1. Results were collected as a plot of extinction coefficients versus wavelength.

$$A = \varepsilon bc$$

Equation 7-1

Where: ε is the molar extinction coefficient, *b* is cell thickness and *c* is the molar concentration. Luminescence and phosphorescence excitation and emission spectra were collected using a Cary Eclipse coupled to a personal computer with software supplied by Varian or a modified Jobin Yvon – Spex Fluorolog-322 spectrofluorimeter equipped with cell holders for both room temperature and 77K measurements. This instrument enables measurement of radiation in both visible and NIR. Spectra were corrected for the instrumental function (excitation and emission). All measurements were taken with samples in 1 mm or 1cm quartz cells manufactured by NSG Precision Cells, Inc.

Batch Spectrophotometric Titration. A batch spectrophotometric titration was performed with G3-$(N23)_{32}$:nLn^{3+} solutions in DMSO or water at 10^{-6} M, with Ln = Eu^{3+}, Tb^{3+}, Nd^{3+} or Yb^{3+} . Solutions were prepared by diluting previously prepared stock solutions of these complexes. The following M:L ratios were used, keeping the dendrimer concentration constant and increasing 'n' 1:2, 1:4, 1:6, 1:7, 1:7.5, 1:8, 1:8.5, 1:9, 1:10, 1:12, 1:14, unless otherwise stated. The metal-centered visible emission was measured using phosphorescence mode with appropriate delay time to eliminate any remaining ligand-centered emission. The metal-centered NIR emission was collected using a 715 nm cut-off filter to block any ligand second-order emission. Each spectrum

was baselined, zeroed, and corrected for instrument function. The titrations were repeated over several days to assess the formation time of the complexes. Emission intensities measured each day were compared to a control reference solution of quinine sulfate and corrected accordingly. Three batches of solution were prepared and used for measuring each G3-$(N23)_{32}$:nLn^{3+} complex. The corrected emission bands were integrated using either Origin software (version 7.0) or Spex software. Plots of integrated intensity of emission versus G3-$(N23)_{32}$:nLn^{3+} ratio and of integrated intensity divided by the Ln^{3+} concentration versus the G3-$(N23)_{32}$:nLn^{3+} Ln:PAMAM ratio were drawn.

Determination of the Energy Position of the Ligand Centered Triplet State. Samples of the G3-$(N23)_{32}$:8Gd^{3+} complex in anhydrous DMSO were placed in a quartz tube, which was then put into a quartz cryostat filled with liquid nitrogen. Once the sample was frozen at 77K, the cryostat sample holder was placed in the instrument, and the tube was aligned in the excitation light beam. Measurements were conducted with a Varian Cary Eclipse fluorimeter. The excitation and emission spectra were collected, with increasing delay times until the phosphorescence band was the only unchanged remaining signal observed on a spectrum. For the 3D phosphorescence scan, a total decay time of 20.0 ms, a delay time of 1.0 ms, and a 5.0 ms gate time were used. A single flash and automated excitation and emission filters were used. For the kinetic transmetallation experiment, where a $Eu(NO_3)_3$ DMSO solution was added to a G3-$(N23)_{32}$:8Eu^{3+} DMSO solution, a delay time of 0.2 ms was used.

Measurement of the Triplet State Luminescence Lifetime. Luminescence lifetime measurements of the triplet state for complexes with G3-$(N23)_{32}$:8Gd^{3+} were performed by excitation of solutions in a quartz tube using a Nitrogen laser as a source of excitation (Oriel model 79110, wavelength 337.1 nm, pulse width at half-height 15ns) with an external trigger allowing repetition of the laser pulse every 10-20 seconds to assure complete decay of the phosphorescence after each excitation pulse. Emission was collected at a right angle to the excitation beam, and wavelengths were selected by means of the Jobin-Yvon Spex Fluorolog-322 FL1005 double monochromator. The signal was monitored by a Hamamatsu R928 photomultiplier coupled to a 500 MHz bandpass digital oscilloscope (Tektronix TDS 620B). The signal from > 500 flashes was collected and averaged. Background signals were similarly collected and subtracted from sample signals. Luminescence lifetimes were averaged from at least three independent measurements.

Steady State Luminescence Quantum Yield Measurements. Metal luminescence quantum yields for visible emitting lanthanides were measured using a quinine sulfate reference (Φ = 0.546).[238] Two pairs of solutions with different absorbancies for each pair were prepared of both the unknown and the reference. Emission spectra were collected using a Jobin-Yvon Spex Fluorolog-322 Spectrofluorimeter and spectra were corrected for the instrumental function. For each sample/reference pair, the total integrated emission was measured using the same spectral parameters for each pair. The quantum yields for visible emitting lanthanides were calculated using Equation 7-2. The refractive index value (η) are as follows: η = 1.333 in 0.05 M H_2SO_4, η = 1.479 in DMSO. Metal luminescence quantum yields for NIR emitting lanthanides were measured using a erbium (III) tropolonate reference ($\Phi=1.7x10^{-4}$).[4] Three pairs of solutions with

different absorbancies for each pair were prepared of both the unknown and the reference. For each sample/reference pair, the total integrated emission upon excitation at four different wavelengths was measured using the same experimental parameters for each pair. Plots of the total integrated emissions (E) against absorbencies (A) yielded straight lines with slopes E/A. The quantum yields (Φ_x) were calculated from the following Equation 7-2:[239]

$$\Phi_x = \Phi_r [slop_x/slop_r] (\eta_x/\eta_r)^2$$

Equation 7-2

Where subscript *r* stands for the reference and *x* for the sample.

Measurement of the Kinetic of Complex Formation. Measurements of the kinetic of complex formation were performed using a Varian Cary Eclipse coupled to a personal computer with software supplied by Varian. The instrument was equipped with a home built thermostated cell holder and stirrer. The cuvette containing a solution of the dendrimer in anhydrous DMSO was placed in the cell holder, $Eu(NO_3)_3$ solution (in DMSO) was added and the measurement was started. Intensity of emission at the wavelength 614 nm was recorded once every hour for three weeks. Plots of emission intensity versus time were recorded.

7.5 RESULTS AND DISCUSSION

The G3-$(N23)_{32}$ ligand has been synthesized according to a protocol previously established in our group.[237] The ligand was purified using a different method by transferring the cooled reaction to a dialysis membrane which was kept in a beaker of anhydrous DMSO for four days, the DMSO solution being changed once a day for of the first three days. The purified product was dried in a vacuum oven for two days and the product was collected. The final compound was characterized using NMR. ^{1}H-NMR (300 MHz, DMSO-d_6, δ): 8.35 (br s, 64H, Ar H), 8.13 (br s, 64H, Ar H), 8.02 (br s, 32H, –N*H*), 7.68 (br s, 92H, Ar H and –N*H*), 3.62 (br s, 64H, –$N(CO)_2C\mathit{H}_2$–), 3.15–3.45 (br s, 64H, –NHCH_2–), 3.01 (br s, 56H, –NHCH_2–), 2.35–2.65 (br s, 60H, –NCH_2CH_2NH–), 2.25–2.35 (m, 120H, –NCH_2CH_2CO–), 2.00–2.20 (m, 120H, –COCH_2–).

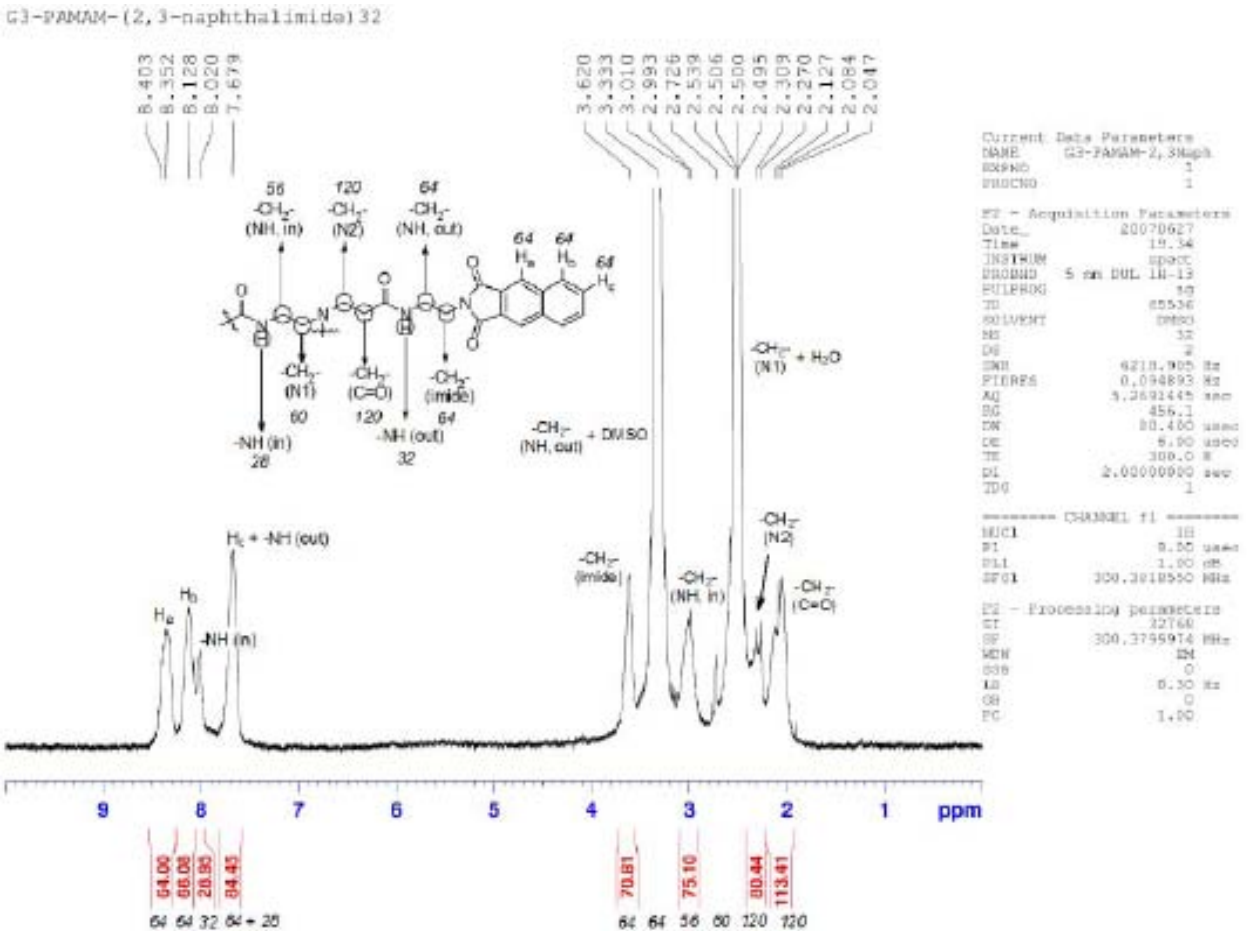

Figure 7-2. ^{1}H NMR spectrum of an arm of a G3-PAMAM-(2,3-naphthalimide)$_{32}$.

Synthesis and Physical Characterization of the G3-(N23)$_{32}$:8Eu^{3+} Lanthanide Complex. Lanthanide complexes were synthesized using the protocol that we have previously described for Eu^{3+}.[237] Previously published experiments have shown that G3-(N23)$_{32}$ forms complexes with Eu^{3+} ions in the average ratio of 7.5 (M:L).[237] By virtue of how the f-block is filled, the dendritic ligand G3-(N23)$_{32}$ will form complexes with other lanthanides in the same ratio since the different lanthanides have similar chemical reactivities, the 4f orbitals being shielded by the 5s and 5p. Nevertheless, there is a difference in size of the Ln^{3+} ions along the lanthanide series. To

verify our hypothesis, we have chosen Nd^{3+} ions for another spectrophotometric titration. Europium(III) and Neodymium(III) with CN=8 differ in ionic radii (Nd^{3+}: 1.109 Å and Eu^{3+}: 1.066 Å).[14] Two batches of Nd^{3+} complexes in different ratios to G3-$(N23)_{32}$ were prepared for a batch spectroscopic titration as described in the experimental section. The results confirmed that G3-$(N23)_{32}$ forms complexes with $Nd(NO_3)_3 \cdot 6H_2O$ with an average ratio of 7.5 (M:L). Graphs illustrating these results are depicted in Figure 7-3.

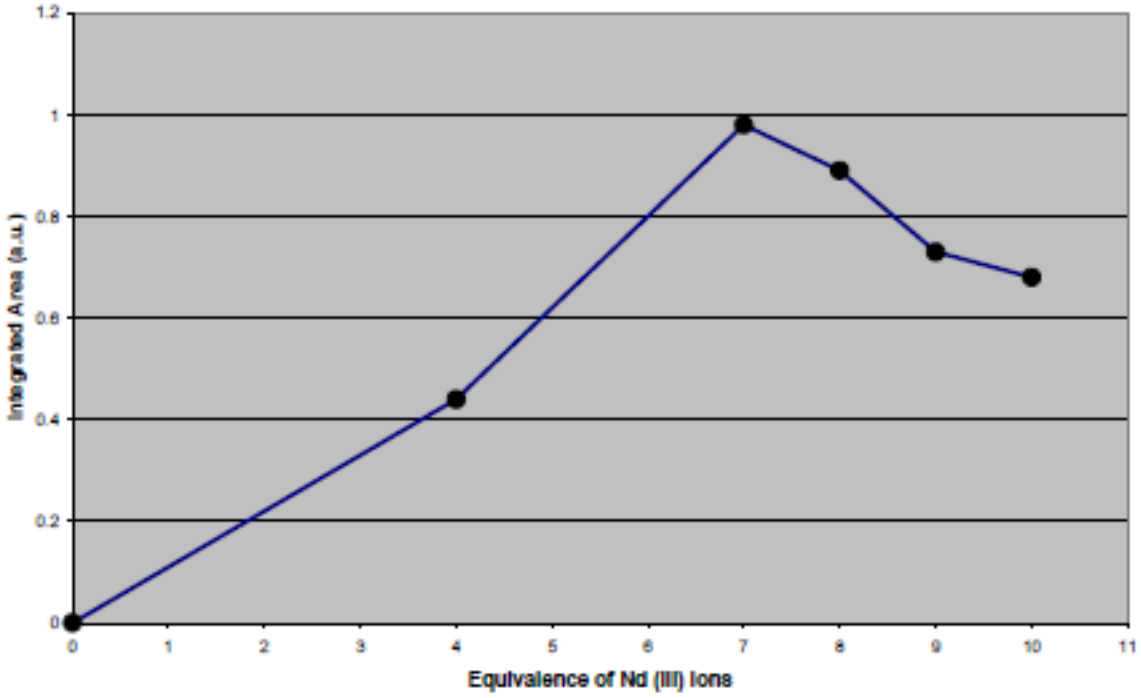

Figure 7-3. Plot of integrated intensity of Nd^{3+} emission versus the metal-to-ligand ratio.

As mentioned previously, Ln^{3+} ions can accommodate coordination numbers between 8 and 12. Since the G3-$(N23)_{32}$ dendrimer ligand possesses 60 oxygen atoms, one could bind 7 ions with coordination number 8, which would use 56 and leave 4 oxygen atoms not coordinated (or 8 ions with coordination number 7). Another possible arrangement would be 8 bonded ions, with a coordination number of 9 for lanthanides. However, in this case lanthanide ions would bind not only to amide's oxygen atoms but also to the nitrogen atoms of the tertiary amines, as in the case of complexes with EDTA or DTPA, to saturate the coordination environment of the Ln^{3+} ions to number 9. For all the additional physical and photophysical characterization of the complexes formed with the different lanthanide cations, the solutions described in the Table 7-1 have been prepared.

Table 7-1. Amounts of solutions used for all the physical and spectroscopic characterization. All solutions in DMSO.

Lanthanide Salt	Lanthanide Solution (M)	Volume Added (μL)	G3-$(N23)_{32}$ Stock Solution (M)	Volume Added (μL)	Final Volume (μL)	G3-$(N23)_{32}$:8Ln^{3+} Solution (M)
$Pr(NO_3)_3$	5.55E-03	596	4.13E-04	1000	1596	2.59E-04
$Nd(NO_3)_3$	5.53E-03	598	4.13E-04	1000	1598	2.59E-04
$Sm(NO_3)_3$	5.59E-03	592	4.13E-04	1000	1592	2.60E-04
$Eu(NO_3)_3$	5.30E-03	624	4.13E-04	1000	1624	2.55E-04
$Gd(NO_3)_3$	5.17E-03	640	4.13E-04	1000	1640	2.52E-04
$Tb(NO_3)_3$	5.47E-03	524	1.79E-04	2000	2524	1.42E-04
$Dy(NO_3)_3$	7.15E-03	401	1.79E-04	2000	2401	1.49E-04
$Ho(NO_3)_3$	5.25E-03	631	4.13E-04	1000	1631	2.54E-04
$Er(NO_3)_3$	5.30E-03	624	4.13E-04	1000	1624	2.55E-04
$Tm(NO_3)_3$	5.46E-03	606	4.13E-04	1000	1606	2.57E-04
$Yb(NO_3)_3$	5.14E-03	644	4.13E-04	1000	1644	2.51E-04

Kinetic Formation of the Complex. For the previously described batch luminescence titrations, the emission spectra of solutions containing different lanthanide:metal ratios were monitored over several days. The results revealed changes of the emission intensities with time with a stabilization of the observed emission spectra intensity after seven days (after which time, no changes were observed anymore). The dendrimer is hypothesized to require an extended period

of time to adopt a final conformation. To quantify the time required for the complex to reach its most stable form, a preliminary experiment was designed in which a solution with a M:L ratio of 8:1 was prepared and the emission signal arising from Eu^{3+} was monitored (upon excitation of the 2,3-naphtahlimide groups) during a three week period from the initial mixing of the reagents. The Eu^{3+} cation was chosen for these experiments because of the intermediate ionic radius within the lanthanide series, therefore Eu^{3+} is a more representative choice of lanthanide cation. This independent experiment (Figure 7-4) confirmed that the complex is fully formed after approximately seven days, as determined from the batch titration experiment previously described. A limited, steady decrease in Eu^{3+} emission intensity was observed after the first seven days. Approximately 5% signal intensity decreased during the second week.

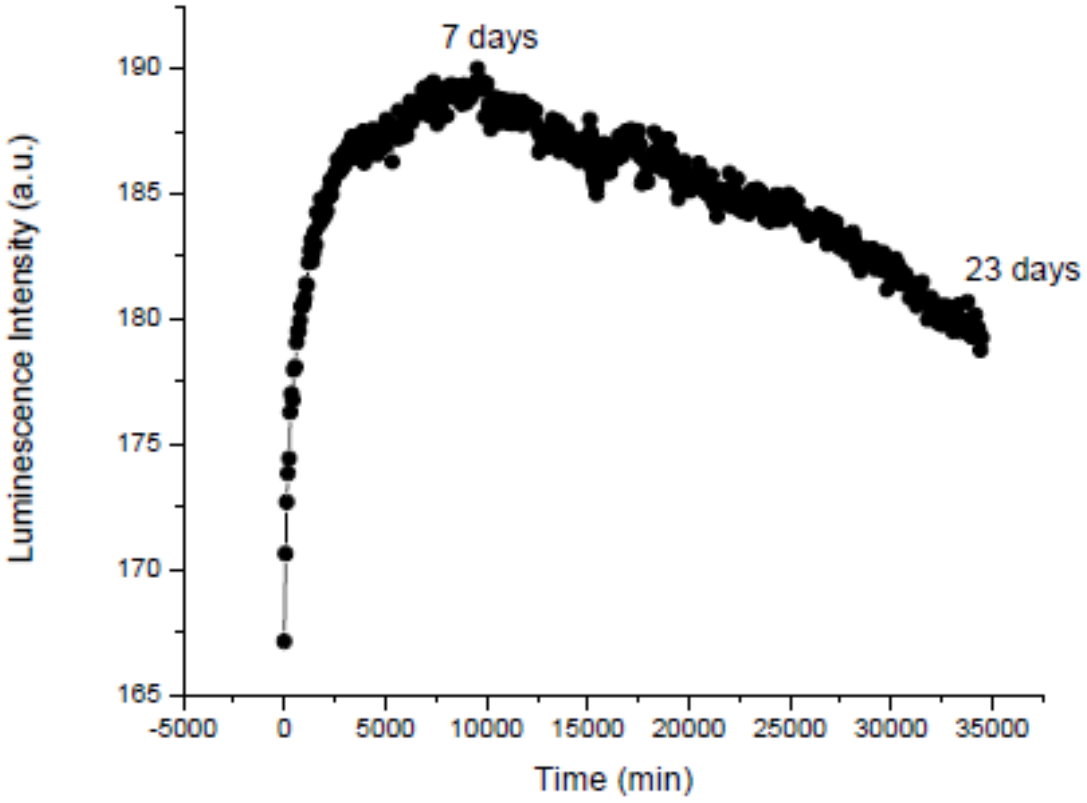

Figure 7-4. Plot of the variation of the luminescence intensity of Eu3+ upon 2,3-naphthlimide excitation versus time. This experiment allowed to quantify the time required for the formation of the most luminescent G3-$(N23)_{32}$:8Eu^{3+} complex by mixing 1 equivalent of 8 Eu^{3+} with 1 equivalents of dendrimer ligand. [G3-$(N23)_{32}$] = 1.67x10^{-6} M in DMSO, λ_{ex} = 332 nm, λ_{em} = 614 nm, 298 K.

To complete this first measurement, a preliminary transmetalation kinetic experiment was performed whereby part of the Tb^{3+} ions coordinated within the G3-$(N23)_{32}$:8Tb^{3+} complex (2.16 x 10^{-6} M) were exchanged by Eu^{3+} ions added to this solution (the concentration of Eu^{3+} solution (5.18 x 10^{-5} M) was equivalent to the total amount of Tb^{3+}, initially present in the G3-$(N23)_{32}$ ligand). The change of the Tb^{3+} signal was monitored using an emission wavelength at 545 nm and the change of the Eu^{3+} signal was probed during the same experiment on two different

transitions located at 590 nm (magnetic-dipolar transition) and 615 nm (electric dipolar) respectively.

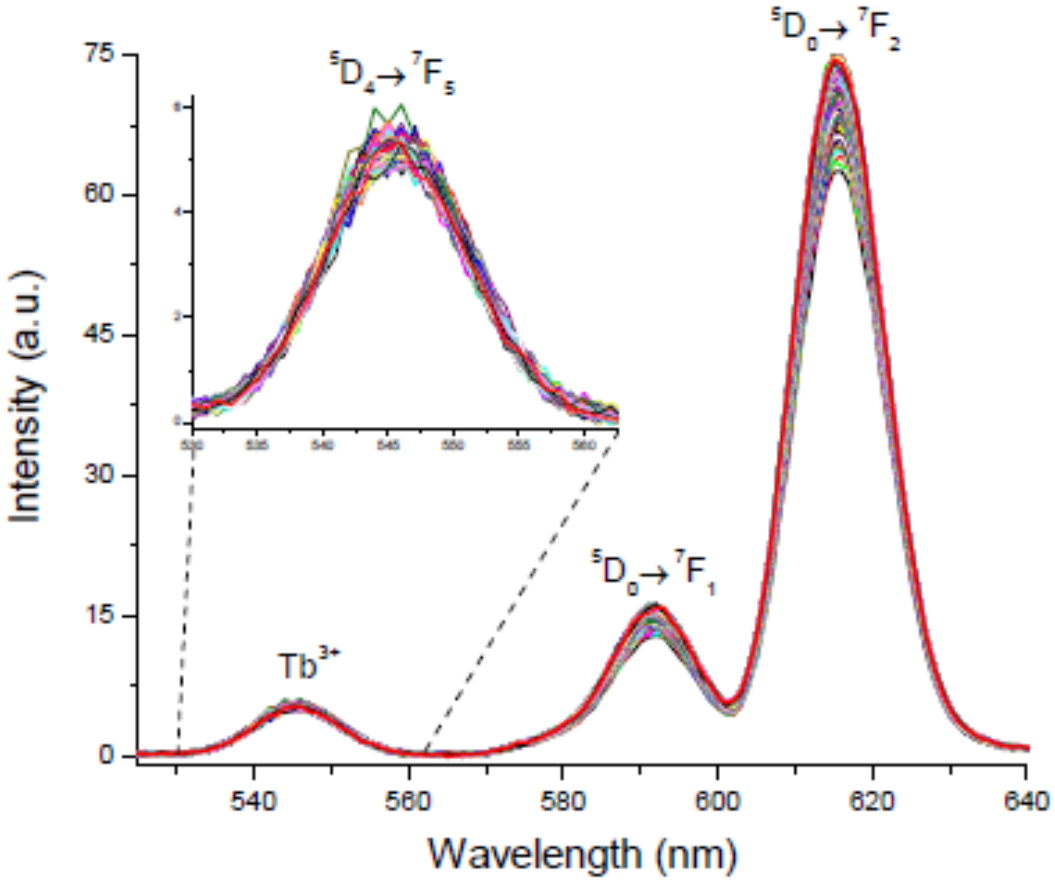

Figure 7-5. Time-resolved transmetalation experiment, demonstrating a simultaneous decrease in one lanthanide signal as another increases. The bands at 590 nm and 615 nm belong to Eu^{3+} transitions, the inset is a Tb^{3+} signal at roughly 545 nm. The concentration of the G3-$(N23)_{32}$:8Tb^{3+} solution is 2.16 x 10^{-6} M in DMSO, to which a 5.18 x 10^{-5} M $Eu(NO_3)_3$ DMSO solution was added. A 20.0 ms total decay time,.0.2 ms delay time, and 5.0 ms gate time are used.

In Figure 7-5, the emission spectra recorded at different times reveal that the luminescence signals arising from Eu^{3+} is increasing as some of the Tb^{3+} lanthanide cations are being replaced by Eu^{3+}. The Tb^{3+} signal decreases as confirmation of its replacement by Eu^{3+}. This preliminary experiment was conducted for approximately four days. It can be observed from this data that both Eu^{3+} and Tb^{3+} signals are still changing after this period of time (Figure 7-6).

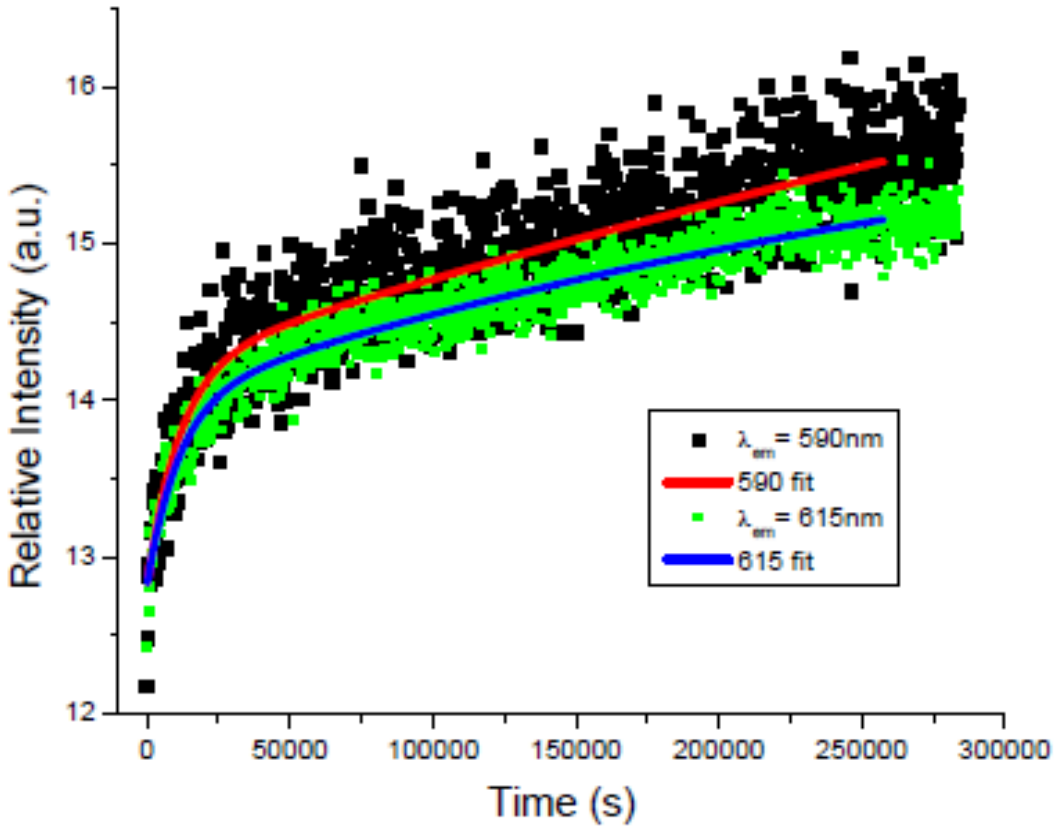

Figure 7-6. Plot of the intensities of the two Eu^{3+} bands, normalized at the initial point of the experiment and fit with bi-exponential decay functions.

The signals recorded on the band maxima of Eu^{3+} and Tb^{3+} were plotted versus time and these data were fit with mono- and multi-exponential functions until the lowest Chi-squared values were obtained. In all three cases, bi-exponentials provided the best fit. Two components were obtained. A relatively short component with a decay (growth) of approximately 3.5 hours was calculated for all three signals, corresponding to each of the three bands (Table 7-2).

Table 7-2. Statistical results of the transmetalation experiment.

Ln^{3+}	Emission Wavelength (nm)	Decay/Growth (s)	Error
Tb^{3+}	545	12787	7622
		1.00E+05	2.00E+05
Eu^{3+}	590	11470	1382
		1.00E+06	9.00E+05
	615	11319	777
		3.70E+05	74806

The second component represents a much longer-lived component that is on the order of the entire experimental time scale itself, confirming that the overall process is not terminated after four days. As a result, the error associated with the fitted value of the long component is extremely large (up to 200%).

The two decay curves obtained from Eu^{3+} were normalized from the origin time of the experiment and compared (Figure 7-6). It appears that the Eu^{3+} may grow faster through the electric-dipole transition than the magnetic-dipole transition. Since the dipolar electric transition is more sensitive to the environment around the luminescent lanthanide cation, this observation may be the direct consequence of a change of environment from lower symmetry to higher symmetry during the kinetic experiment. More experiments must be conducted in an attempt to collect a level baseline and corroborate any physical interpretation of the results.

Photophysical Properties of the G3-$(N23)_{32}$:8Ln^{3+} Complexes. The UV/Vis absorption spectra of several G3-$(N23)_{32}$:8Ln^{3+} complexes formed with different lanthanides in DMSO solution, the concentrations of which are diluted 100x with respect those listed in Table 7-2, have been recorded. These results are reported in Figure 7-7. The UV/Vis absorption spectra of these different solutions of complexes have no significant differences in their maxima positions and in their extinction coefficients. Compared to the uncoordinated ligand (Figure 7-8), the G3-$(N23)_{32}$:8Ln^{3+} complexes all possess a) a shoulder located at 295 nm and b) two bands with lower extinction coefficient maxima at 340 nm and 360 nm.

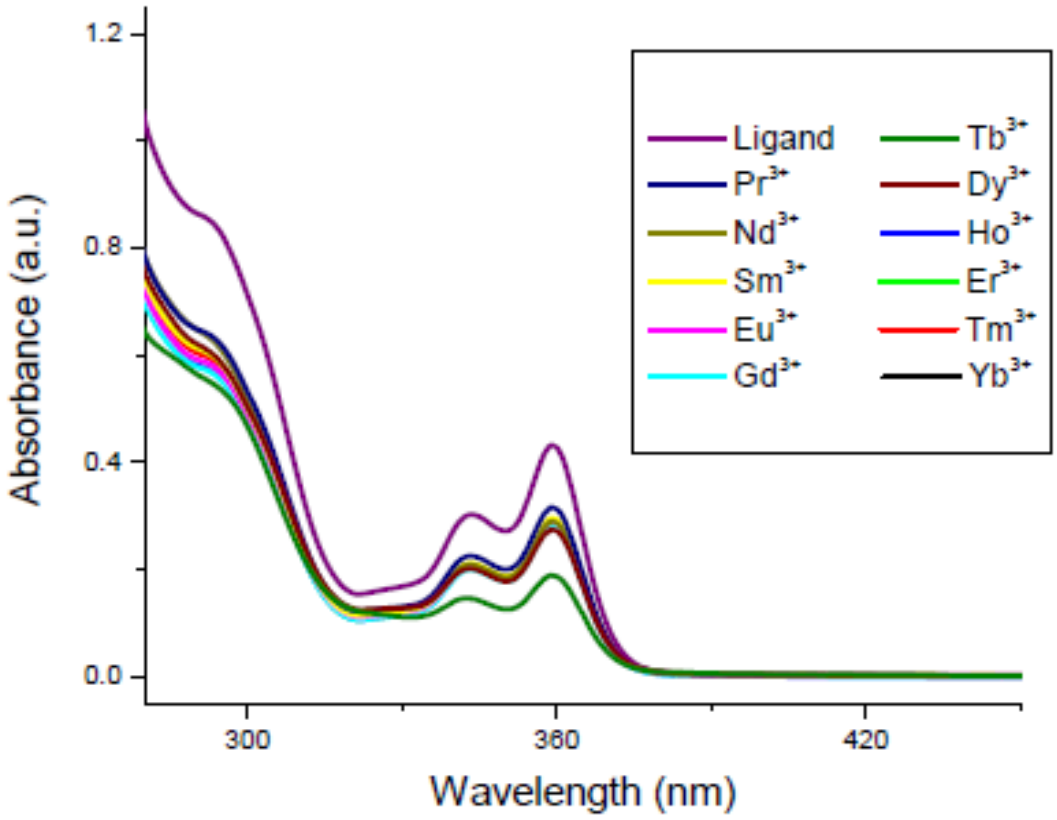

Figure 7-7. Absorption spectra of G3-$(N23)_{32}$:8Ln^{3+} complexes, diluted 100x with respect to the approximately $3x10^{-4}$ M in DMSO solutions listed in Table 7-1.

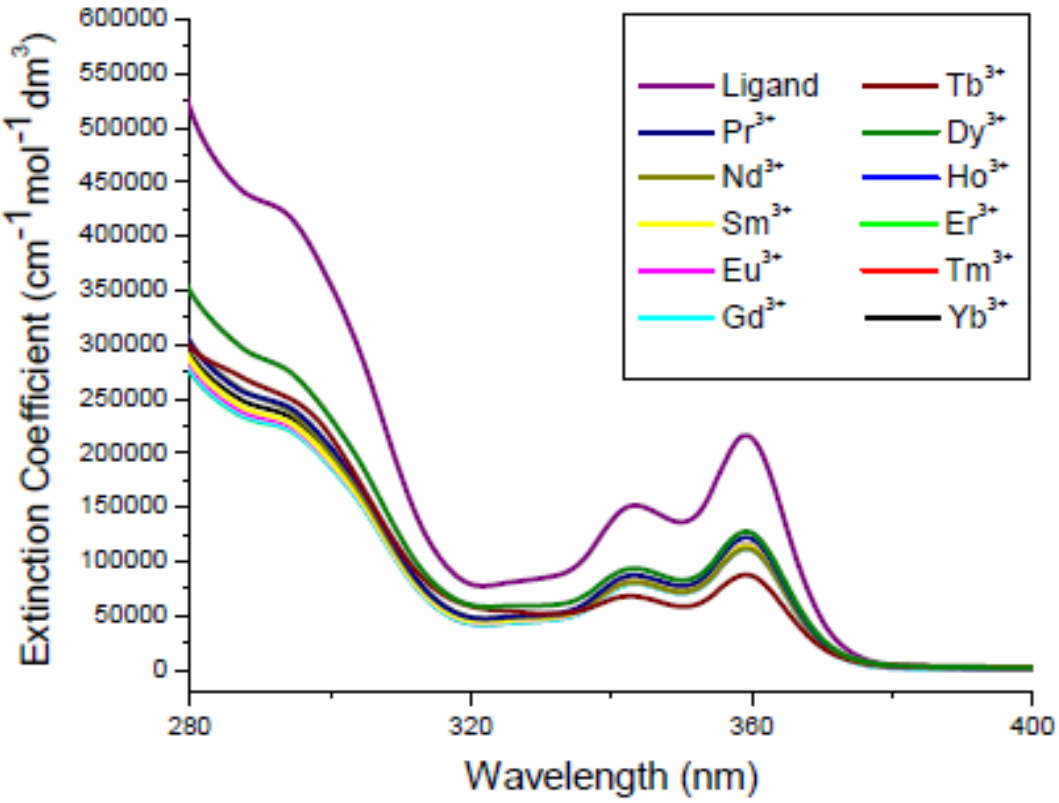

Figure 7-8. Extinction coefficients of the G3-$(N23)_{32}$:8Ln^{3+} complexes, calculated from the absorbance values in Figure 7-7.

The extinction coefficients differ between the free dendrimer ligand and its lanthanide complexes. This observation reveals the effect that coordination has on the electronic structure of the naphthalimide; the presence of the 3+ charge on the lanthanides, in proximity of the 2,3-naphtahlimide groups, results in a decrease of the extinction coefficients. The similar absorption spectra recorded for the different lanthanide cations indicate that this effect is equivalent for the different cations, an indication that complexes with similar properties are formed with the different lanthanide cations.

These extinction coefficient (ε) values are relatively large in comparison to lanthanide complexes based on small organic chromophores,[240] and result from the presence of thirty-two chromophoric groups attached to each discrete dendrimer unit. Such an increase in absorption for these complexes will result in an increase of the number of photons emitted by the lanthanide cations.

Electronic Structure of the Coordinated G3-$(N23)_{32}$:8Ln^{3+}. Trivalent gadolinium and lanthanum cations are suitable non-luminescent lanthanide probes for the monitoring of the electronic levels (singlet and triplet) of the 2,3-naphthalimide sensitizer. This is possible because the accepting levels of Gd^{3+} are too high in energy to be accessed from the excited ligand, and La^{3+} lacks f-electrons. Regardless, either Gd^{3+} or La^{3+} will induce the same type of perturbation to the 2,3-naphthalimide ligand as each of the luminescent lanthanide cations would. As a result, the energy resulting from the absorption of light by the 2,3-naphtahlimide will be released in part as photons, either from the singlet state(s) as fluorescence signal or from the triplet states of the ligand as phosphorescence, in addition to non-radiative routes of energy transfer. The monitoring of the phosphorescence is facilitated by lowering the temperature to 77 K, which decreases the efficiency of vibrational deactivation and thus increases its population and the intensity of the resulting phosphorescence bands. A G3-$(N23)_{32}$:8Gd^{3+} complex was synthesized and its fluorescence and phosphorescence spectra were recorded in DMSO, see Figure 7-9.

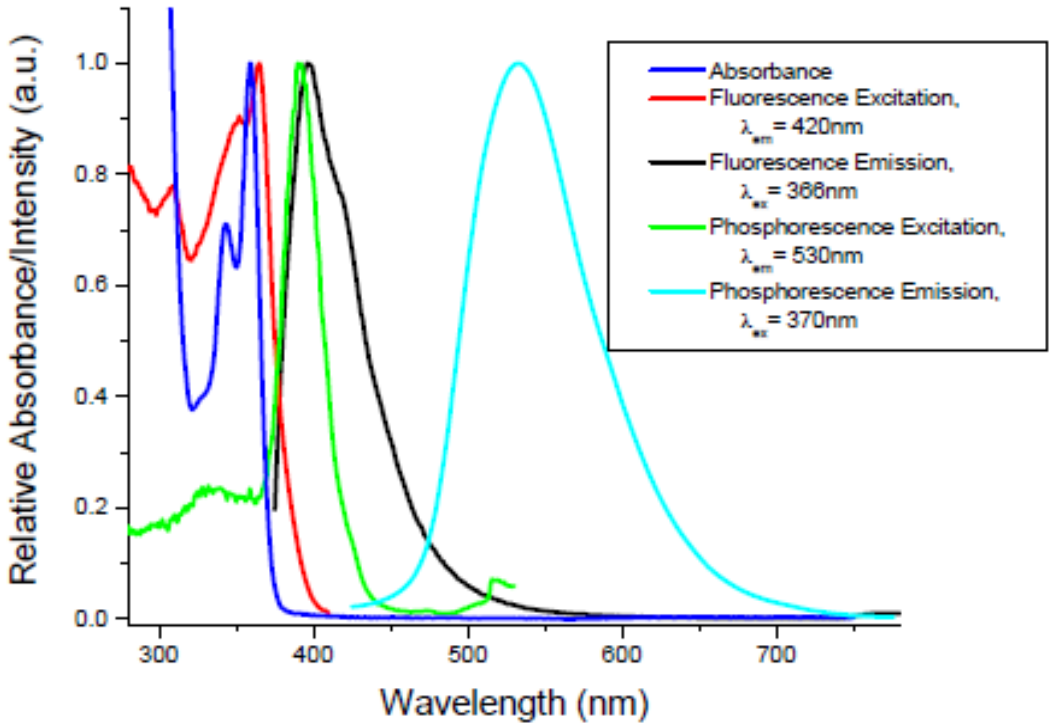

Figure 7-9. Normalized overlay of absorbance, fluorescence and phosphorescence spectra of the G3-$(N23)_{32}$:8Gd^{3+} complex in DMSO. All concentrations of the complex used were 2.52E-04 M except for the absorption measurements, 2.52E-06 M.

The fluorescence excitation and emission spectra of the luminescence arising from the G3-$(N23)_{32}$ ligand in complexes formed with ten different luminescent lanthanide cations (Ln^{3+} = Pr^{3+}, Nd^{3+}, Sm^{3+}, Eu^{3+}, Tb^{3+}, Dy^{3+}, Ho^{3+}, Er^{3+}, Tm^{3+}, Yb^{3+}) have been recorded in DMSO solutions. As it can be observed from Figure 7-10 and Figure 7-11, all complexes have similar ligand-centered steady-state emission and excitation profiles. The similar features indicate that the differences between the lanthanides have little or no effect on the singlet-state electronic structure of these ligands. The presence of the residual ligand fluorescence also indicates that a

part of the energy is not fully transferred to the accepting levels of the lanthanide cations and that the sensitizer-to-lanthanide energy transfer may be further optimized.

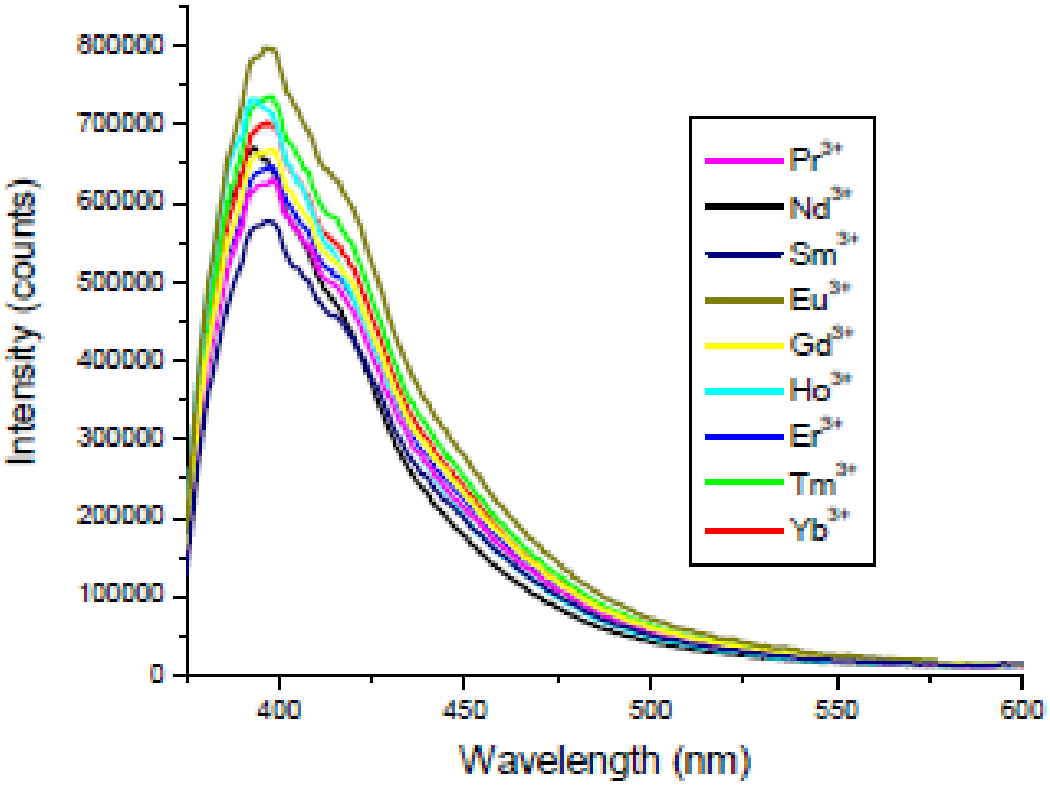

Figure 7-10. Ligand-centered emission spectra of the G3-$(N23)_{32}$:8Ln^{3+} complexes, excitation wavelength λ_{ex} = 366nm, concentrations are approximately $3x10^{-4}$ M in DMSO with more precise values listed in Table 7-1.

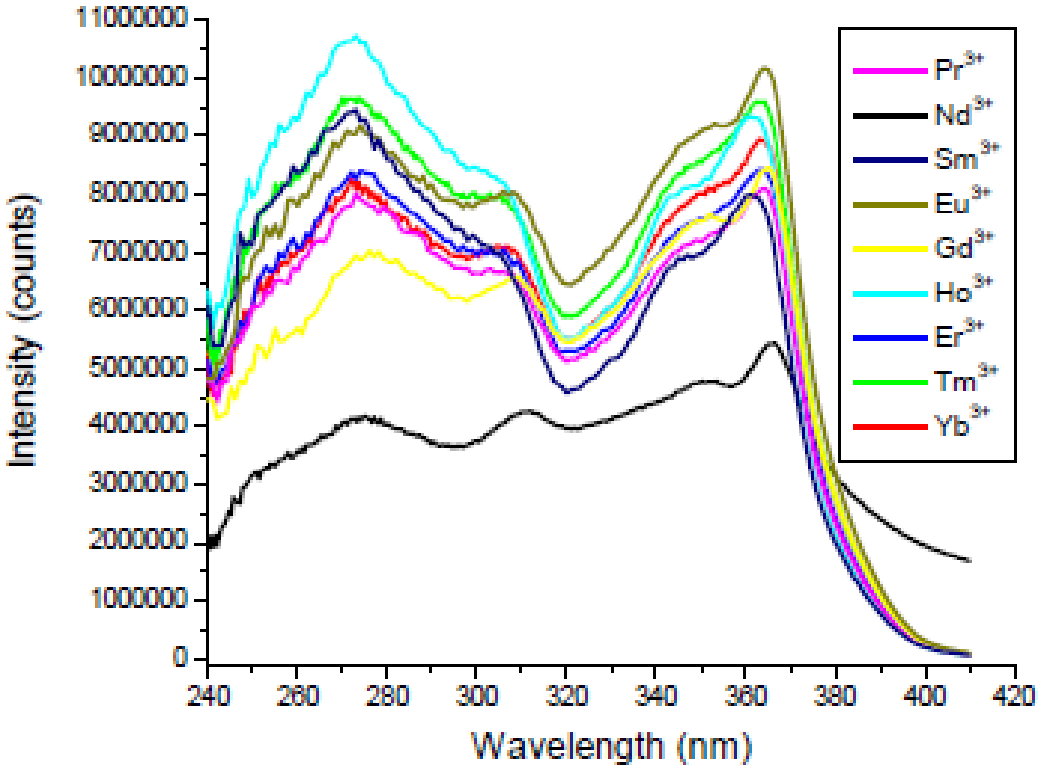

Figure 7-11. Ligand-centered excitation spectra of the G3-$(N23)_{32}$:8Ln^{3+} complexes, emission wavelength λ_{em} = 430nm. The concentration of the complexes were approximately $3x10^{-4}$ M in DMSO with more precise values listed in Table 7-1.

A 3D (excitation, emission versus intensity) phosphorescence spectra of the G3-$(N23)_{32}$:8Gd^{3+} complex has been recorded at 77K. This combination of spectra reveals one broad emission band with an apparent intensity maximum position located at 18,340cm^{-1}. At lower wavelengths of excitation, this apparent excitation maximum shifts until roughly 450nm, the corresponding emission maximum being also located at lower energy, 16,700cm^{-1}. This observation suggests the presence of two independent energy paths going through the 2,3-naphthalimide group.

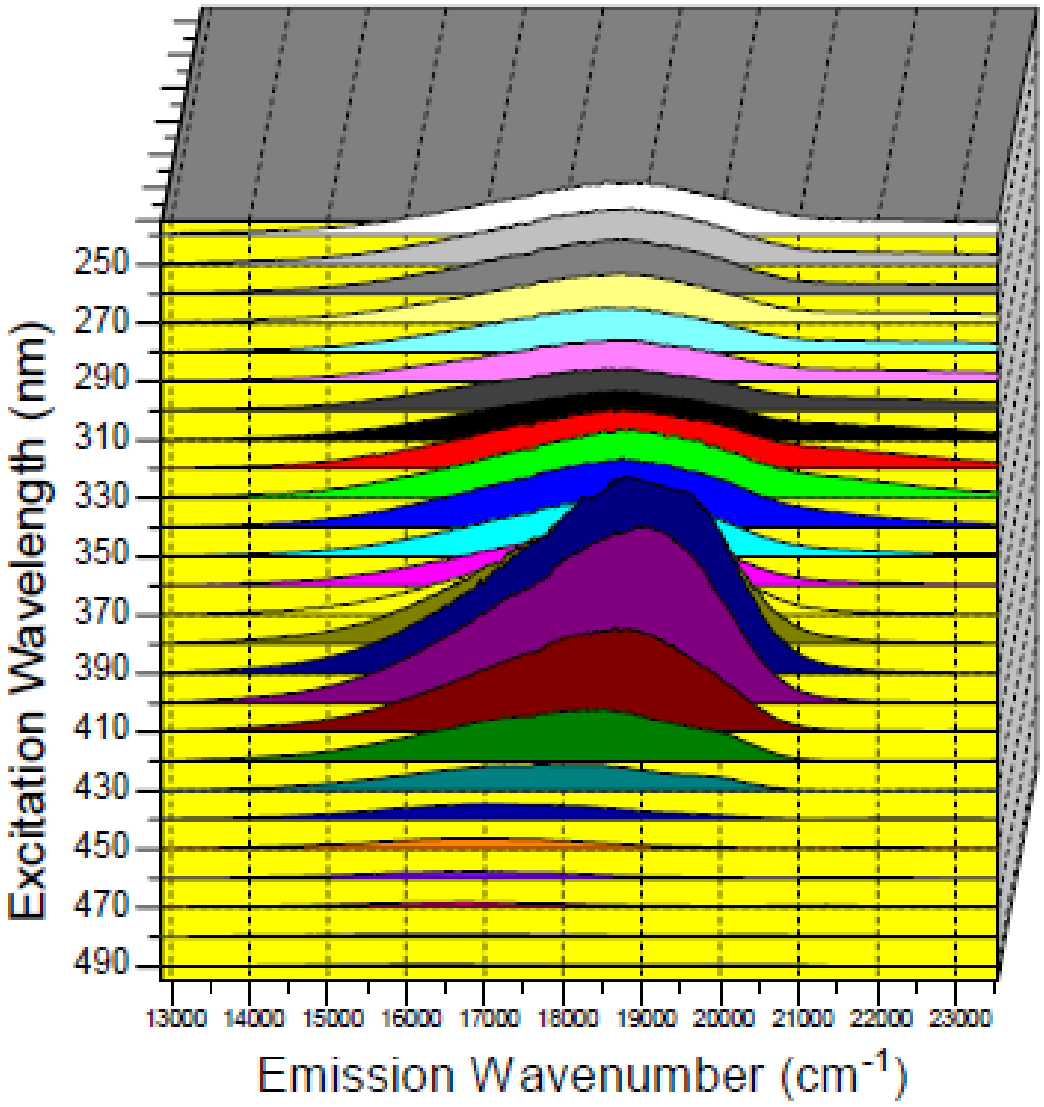

Figure 7-12. A 3D time-resolved spectra of the G3-$(N23)_{32}$:8Gd^{3+} complex, recorded at 77K. A 20.0 ms total decay time, 1.0 ms delay time, and 5.0 ms gate time are used.

To analyze more finely the different excitation and emission wavelengths, the phosphorescence spectra were normalized to the maximum of the individually most intense bands (see Figure 7-13). Upon this treatment, three additional emission bands/shoulders that may

be attributed to additional triplet state become more apparent. One is located at higher energy around 23,500cm^{-1}, whose maximum of intensity corresponds to an excitation wavelength of 290nm (34,483 cm^{-1}) (see Figure 7-13), a second shoulder located at roughly 21,000cm^{-1} with a distinctly different maximum intensity upon excitation at 320nm (see Figure 7-13), and another shoulder located between 19,000cm^{-1} and 21,000cm^{-1} whose intensity is maximized at excitation wavelengths comprised between 420 nm and 430 nm. These different phosphorescence bands correspond to different triplet states that may be suitable for the energy transfer for specific lanthanides. These additional phosphorescence bands, that have different relative emission intensities, are also interesting because they are observed within a region of energy that coincides with accepting levels belonging to several lanthanides.

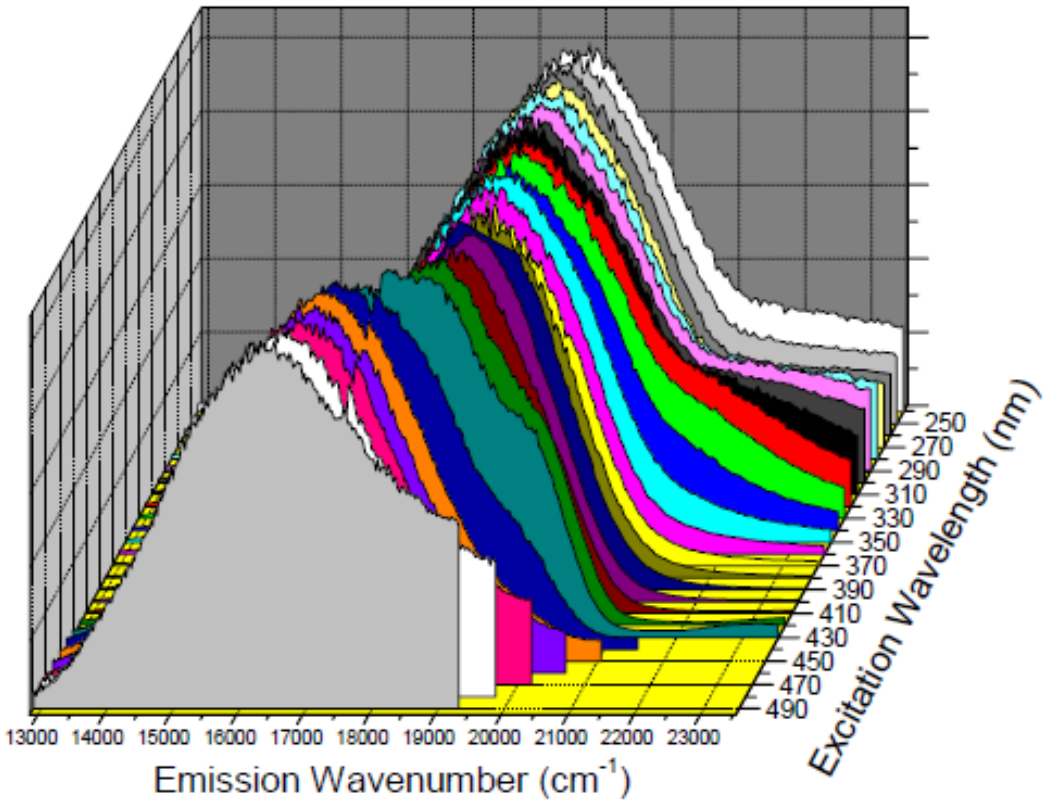

Figure 7-13. 3D time-resolved spectra of the Gd^{3+} complex, 2.52E-04 M in DMSO, the apparent maxima being normalized to 1 and overlaid as a function of excitation wavelength. A 20.0 ms total decay time, 1.0 ms delay time, and 5.0 ms gate time are used.

At this stage, these experiments suggest the presence of several independent populated triplet states within the energy region where energy transfer to the lanthanide cations could occur. Such a situation has never been reported for luminescent lanthanide complexes formed with so many lanthanide cations.

To further test the hypothesis of the presence of several triplets, luminescence lifetimes have been recorded by exciting the naphthalimide, analyzing the phosphorescence of the 2,3-naphtahlimide. The compound was excited at 337nm with a pulsed nitrogen laser and was

monitored at 484nm on a sample at 77K of G3-$(N23)_{32}$:8Gd^{3+} in DSMO. The experimental curve (Figure 7-14) fitted best with a biexponential decay. The two values obtained, 0.16 +/- 0.01 s and 2.9 +/- 0.4 s correspond to long lived excited states and can therefore only arise from triplet states. This preliminary experiment confirms the presence of at least two independent triplet states located in a energy domain close to the emission wavelength.

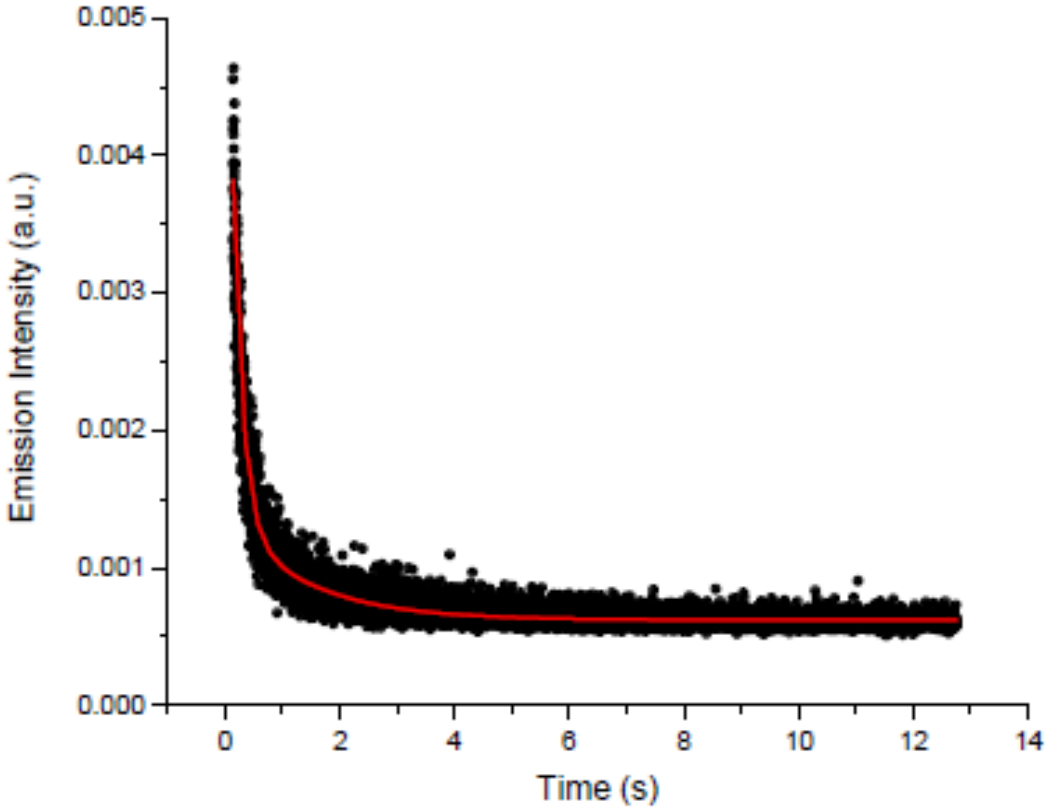

Figure 7-14. Example of fitted luminescence lifetime decay curve for G3-$(N23)_{32}$:8Ln^{3+}, with a concentration of $2.16x10^{-5}$ M. 77 K., and excitation wavelength λ_{ex} = 337 nm.

Emission Properties of the Luminescent Lanthanide Complexes. The ligand G3-$(N23)_{32}$ is suitable for the sensitization of several different lanthanide cations emitting in the visible and NIR regions. A series of G3-$(N23)_{32}$:8Ln^{3+} complex solutions with Ln^{3+} = Pr^{3+}, Nd^{3+}, Sm^{3+}, Eu^{3+}, Tb^{3+}, Dy^{3+}, Ho^{3+}, Er^{3+}, Tm^{3+}, Yb^{3+} were prepared in anhydrous DMSO. Emission spectra are reported in Figure 7-15. They indicate that, in addition to the sensitization of Eu^{3+} that we have previously demonstrated,[237] the other visible-emitting lanthanides, Sm^{3+}, Tb^{3+} and Dy^{3+}, as well as all of the NIR-emitting lanthanides Pr^{3+}, Nd^{3+}, Ho^{3+}, Er^{3+} and Yb^{3+}, can be sensitized with the 2,3-naphthalimide groups when located in the dendrimer. *To the best of our knowledge, this is the first report of a chromophoric group being able to sensitize ten different luminescent lanthanide cations using a common sensitizer* (and a common excitation wavelength). This result is exciting and surprising considering that the luminescent lanthanide ions have different accepting level energies and thus potentially different sensitization requirements.

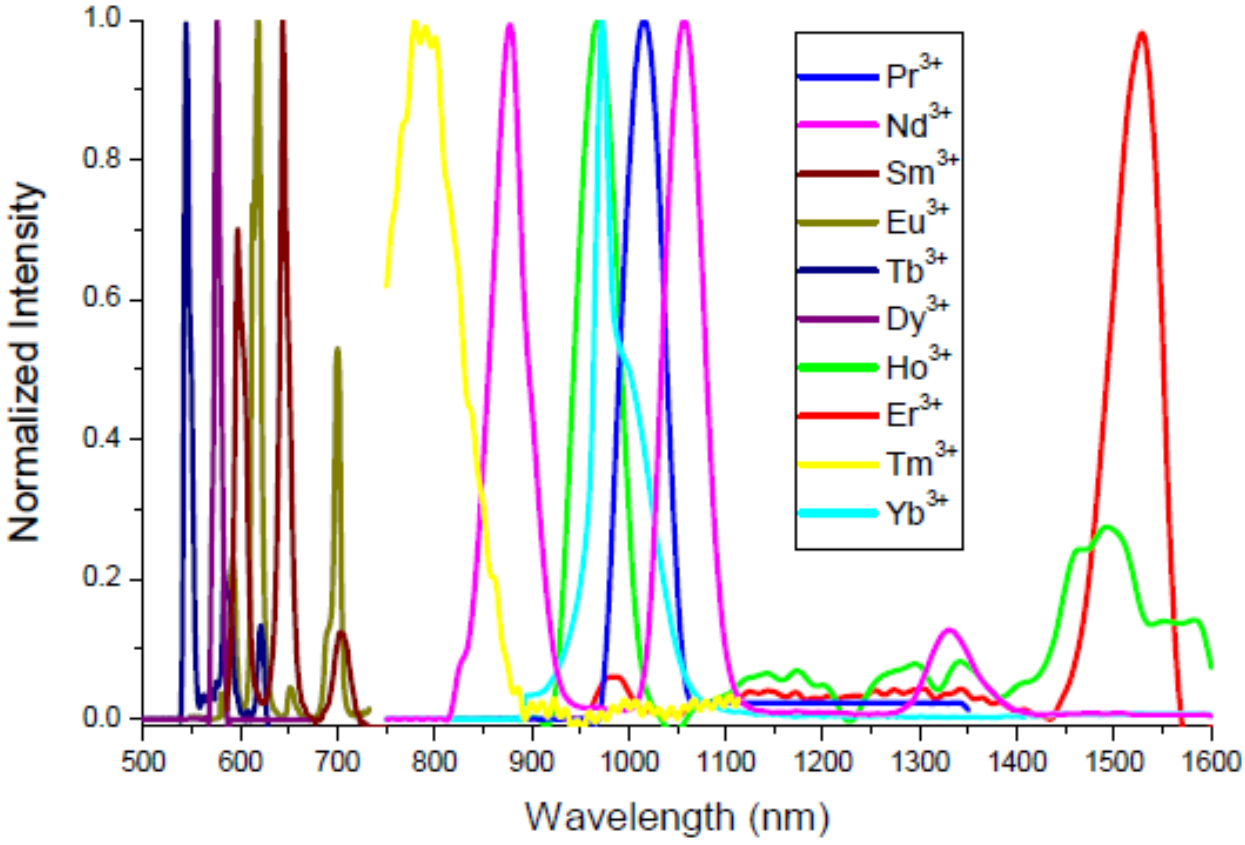

Figure 7-15. Normalized emission spectra of ten luminescent lanthanide complexes formed in anhydrous DMSO with the ligand G3-$(N23)_{32}$. Concentrations of the lanthanide complexes are approximately $3x10^{-4}$ M in DMSO with more precise values listed in Table 7-1. Excitation wavlength λ_{ex} = 325 nm.

In this experiment, it has been hypothesized that excitation of the lanthanide cation can be achieved using a common wavelength of 325 nm, corresponding to a sensitization pathway occurring through an electronic state of the 2,3-naphtahlimide group located in the branch termini of the dendrimer.

To confirm this hypothesis, we have overlaid the lanthanide-centered excitation spectra for all the studied lanthanide complexes (Figure 7-16). The analysis of these spectra reveals a

significant amount of common excitation bands amongst the different lanthanide complexes, indicating that a common part of energy routes transit through the 2,3-naphthalimide groups to populate the excited states of the different luminescent lanthanide cations. In addition, the direct excitation of the electronic states of the luminescent lanthanides (selective excitation of their excited states, bypassing the sensitizer) would result in different excitation spectra for each individual complex formed with the different lanthanide cations. Furthermore, these excitation spectra would contain atom-like emission bands reflecting the shielded orbitals that are characteristic of the electronic structures of each lanthanide. It is worth noticing that some of the narrow bands observed in the excitation spectra of some of the lanthanide complexes correspond to such direct excitation bands, but the more common, broader bands correspond to excitation through the 2,3-naphthalimide levels, indicating that both modes of excitation are possible.

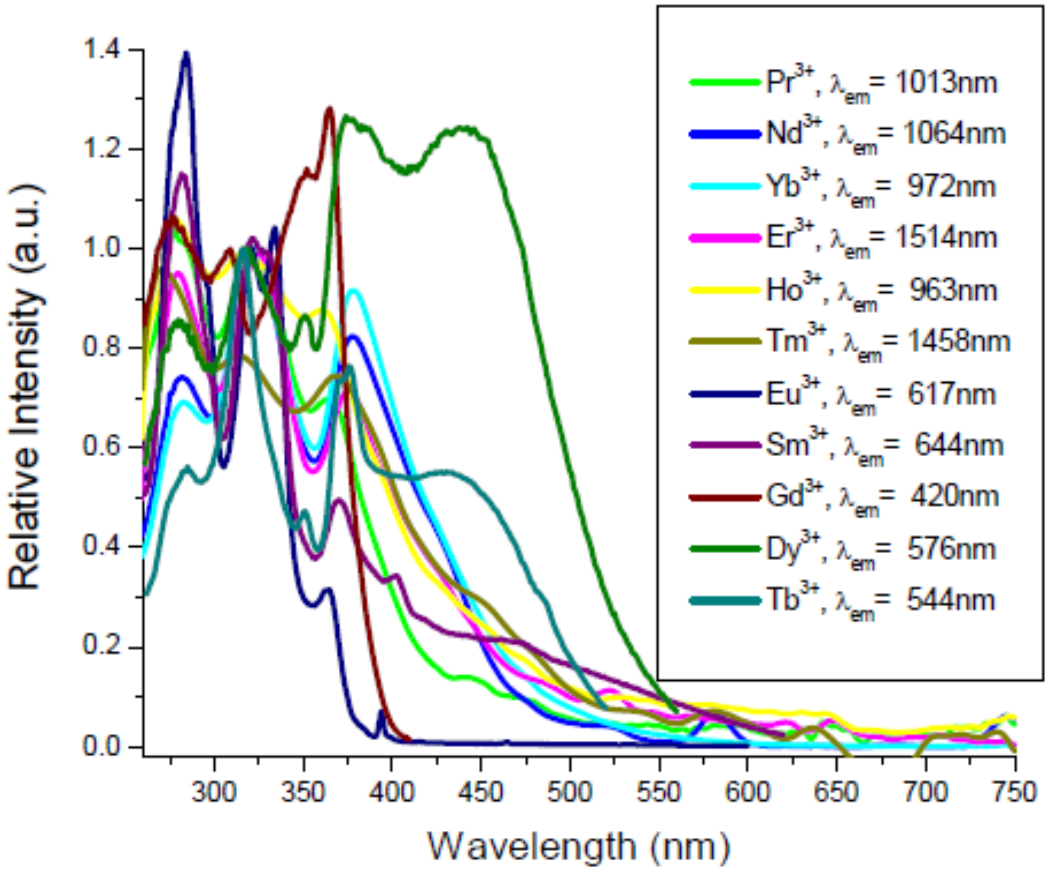

Figure 7-16. Overlay of the lanthanide-centered excitation spectra of ten luminescent lanthanide complexes formed in anhydrous DMSO with the ligand G3-$(N23)_{32}$. Concentrations of the lanthanide complexes are approximately $3x10^{-4}$ M in DMSO with more precise values listed in Table 7-1. The Ln^{3+}-centered excitation wavlengths for each lanthanide complex are Pr^{3+} = 1013 nm, Nd^{3+} = 1064 nm, Yb^{3+} = 972 nm, Er^{3+} = 1514 nm, Ho^{3+} = 963 nm, Tm^{3+} = 1458 nm, Eu^{3+} = 617 nm, Sm^{3+} = 644 nm, Gd^{3+} = 420 nm, Dy^{3+} = 576 nm, Tb^{3+} = 544 nm.

It should also be noticed that most of the lanthanide complexes have multiple excitation maxima, having different relative intensities, indicating that the sensitization of the lanthanides may be occurring through more than one energy pathway through the electronic levels of the sensitizers.

In order to quantify the efficiency of these lanthanide complexes in converting energy from the sensitizer to the lanthanide cations, quantum yields have been measured upon excitation of the 2,3-naphthalimide electronic levels and monitoring the corresponding lanthanide emission. These quantum yield values represent the efficiency of the sensitizer to lanthanide energy transfer and the protection of the lanthanide against non-radiative deactivations.

Table 7-3. Summary of the quantum yield values measured for the G3-$(N23)_{32}$:8Ln^{3+} complexes, see Table 7-1 for concentration of the visible emitting lanthanides (Ln*) and c = 3E-6 M for all the remaining lanthanide complexes, all solutions in DMSO.

Ln^{3+}	**Excitation Wavelength (nm)**	**Absolute Quantum Yield Value**	**Extinction Coefficient ($mol^{-1}dm^3cm^{-1}$)**	**Relative Brightness***
Yb	330	1.35(3)E-04	4.81E+04	51.9
	340	1.12(10)E-04	7.53E+04	67.4
	360	7.9(7)E-05	1.14E+05	72.1
Nd	330	2.1(3)E-05	4.92E+04	8.3
	340	1.36(8)E-05	7.45E+04	8.1
	360	7.6(7)E-06	1.11E+05	6.7
Er	330	3.2(6)E-06	4.55E+04	1.2
	340	2.8(2)E-06	7.32E+04	1.6
	360	1.7(3)E-06	1.12E+05	1.5
Pr	330	2.0(4)E-06	5.06E+04	0.8
	340	8(2)E-07	7.97E+04	0.5
	360	5.0(8)E-07	1.21E+05	0.5
Ho	330	1.5(5)E-07	4.56E+04	0.1
Eu*	340	7.9(2)E-03	7.45E+04	4707.8
	360	3.9(2)E-03	1.13E+05	3536.1

Table 7-3 (continued).				
Sm*	340	2.2(2)E-04	7.45E+04	131.1
	360	8.1(9)E-05	1.13E+05	73.3
Tb*	340	4.9(3)E-05	6.50E+04	25.5

The last column in Table 7-3 is of particular interest for our polymetallic system with high absorbance because the benefits we gain from using the dendrimer structure to confine multiple emitters and sensitizers per discrete molecule are by nature not reflected by the measured quantum yield values. The quantum yield (Φ) is a measurement that reflects how well the absorbed photons are converted into lanthanide signal per unit emitter and how well the lanthanide cations are protected from nonradiative deactivations. To quantify the benefit of our system to provide lanthanide compounds emitting a larger number of photons, by possessing a large absorbance and by coordinating several luminescent lanthanide emitters, we have defined the "relative brightness" of these compounds by multiplying the quantum yield values by the molar absorptivity at each excitation wavelength and by the number of emitters per molecule.

In general, it can be observed that the quantum yield values that have been recorded are extremely small, being all below 1%. This situation can be explained by the fact that for none of these lanthanide complexes was the 2,3-naphthalimide to lanthanide energy transfer was complete, as indicated by the presence of remaining sensitizer–centered fluorescence. Nevertheless, despite these very small values, we have been able to record the emission spectra for ten different lanthanide cations with good signal-to-noise ratios, and this for the first time.

We have been able to quantify extremely small values of quantum yields with a good accuracy for the same reason (sufficient sensitivity due to sufficient number of photons). These exciting results can be rationalized as the demonstration of the validity of our approach where the formation of polymetallic lanthanide complexes, with a dendrimer ligand having large absorbencies, compensate for these small quantum yields.

7.6 CONCLUSIONS

We report here a novel approach to sensitize luminescent lanthanide cations emitting in the visible and in the near-infrared, where low values of quantum yields are not an absolute limitation for the observation of good signal-to-noise ratios. We have used a derivative of a generation-3 PAMAM dendrimer ligand that can coordinate a large number of lanthanide emitters through its amide groups and which can be substituted with a broad variety of sensitizers to maximize the overall absorption of each discrete molecule. The 2,3-naphthalimide group was used as the sensitizer and was located in the branch termini of the dendrimer. With this combination, we have established the first report that it is possible to sensitize 10 different lanthanide cations with the same combination of dendrimer-sensitizer ligand.

We have quantitatively demonstrated the validity of this approach: the quantum yields for all these lanthanides remain small. The 2,3-naphthalimide have the appropriate electronic structure to access the accepting levels of the lanthanide cations (as demonstrated by the excitation spectra). Preliminary experiments have demonstrated the presence of several triplet states with different energies which may allow to fine tune the sensitization of specific

luminescent lanthanide cations. In order to detect the signal of these 10 different lanthanides, we need to have the *synergetic effect* between the electronic structure of the sensitizer and the advantages provided by the dendrimer macro molecule: the large epsilon and the large number of lanthanide emitters. This demonstrates that this approach broadens the field of applications that lanthanide cations may someday enjoy by allowing the complexes to emit a larger number of photons with a broader range of lanthanide cations. The generation of 10 distinguishable colors with the same excitation wavelengths open unprecedented perspectives for the development of multiplex assays.

8.0 A POLYMETALLIC NEODYMIUM DENDRIMER COMPLEX AS A NEAR INFRARED REPORTER FOR LUMINESCENCE MICROSCOPY IN LIVING CELLS

8.1 CHAPTER PREFACE

The aim of this work was to demonstrate biological application with the luminescent dendrimer synthetic strategy we introduced in Chapter 7.0. Specifically, we used a PAMAM dendrimer with eight Nd^{3+} cations as a near-infrared reporter in living cells. We chose 1,8-naphthalimide as the sensitizer to include at the periphery of the dendrimer complex. The fully functionalized luminescent dendrimer had low water solubility and required the aid of microinjection to be incorporated in the cell, however, this prototype system served as an important basis for future work presented in Chapters 9.0 and 10.0. In addition to our experimental work, we engaged in a collaboration with researchers at the Center for Biologic Imaging at the University of Pittsburgh to achieve this goal of biological applications. The material contained in this chapter has been organized for publication.

List of authors: Chad M. Shade, Grzegorz P. Filipczyk Jason P. Cross Patrick G. Calinao Wesley B. Smith Paul D. Badger Simon C. Watkins Claudette M. St. Croix, Stéphane Petoud

Author contribution: The author of this dissertation was responsible for the photophysical characterization of the complex including Ln^{3+}-centered luminescence lifetimes and quantum yields, absorption and NIR fluorescence excitation and emission profiles, providing interpretation of the results and contributing to the preparation of the manuscript.

8.2 ABSTRACT

A novel polymetallic lanthanide complex emitting in the near- infrared has been used for the first time as a reporter for a luminescence microscopy experiment in living cells. This experiment has been made possible by the use of a novel conceptual approach where the number of photons per unit volume is maximized using a polymetallic lanthanide complex having high extinction coefficients.

8.3 INTRODUCTION

Near-infrared (NIR) luminescence is advantageous for bioanalytical applications and biological imaging for several complementary reasons. The native NIR fluorescence signal arising from biological systems is extremely low,[169,241] which results in low background emission (autofluorescence), improving the signal-to-noise ratio and the corresponding detection sensitivity. For imaging purposes, NIR photons scatter less than visible ones, allowing the

acquisition of images with higher resolution.[22,242] A robust luminescent reporter that can emit in the NIR is the crucial requirement for imaging application in biological media. So far, several organic fluorophores[243,244] and luminescent semiconductor nanocrystals (”quantum dots”)[22,242] have been successfully tested as NIR reporters for cellular imaging applications. NIR-emitting lanthanide cations, due to their electronic structure, could provide additional and complementary advantages: a) lanthanide emission appears as narrow emission bands whose wavelengths are not affected by experimental conditions (such as temperature, pressure, pH or biological environment), allowing easy spectral discrimination from background signal for improved detection sensitivity; b) several lanthanide cations emit in the NIR[4,245] with signals that do not overlap between each other for potential multiplex detection; c) luminescent lanthanide complexes tend to be more photostable than organic fluorophores, allowing for longer imaging experiments and the repetition of these experiments.

Since the direct excitation of lanthanides is inefficient, the f-f transitions being forbidden by the Laporte rule, in order to obtain compounds able to emit a large number of photons, the luminescent lanthanide cations must be sensitized by a suitable antenna.[28] Some lanthanide complexes emitting in the visible have been recently demonstrated to be promising reporters for visible luminescence microscopy in cells.[34,175,211,246-250] Several NIR lanthanide complexes formed with small molecule ligands have been described to emit in solution if sensitized through suitable antennae, possessing the appropriate electronic structure.[13,251-257] Bimetallic lanthanide helicates have been demonstrated to be good cellular imaging candidates.[258] Although the possibility of incorporating NIR-emitting lanthanides within the helicates has been explored,[208] the combination of NIR luminescence with microscopy had not been achieved. To date and, to the best of our knowledge, no NIR-emitting lanthanide complex has been reported in a

luminescent microscopy experiment within a living cell. One reason that can explain this situation is the limited number of NIR photons emitted per unit of volume by small molecules, reducing detection sensitivity below the capabilities of luminescence microscopes.

8.4 EXPERIMENTAL

Chemicals. The PAMAM generation-3 dendrimer solution, in anhydrous methanol (26.03% by weight), was purchased from Dendritech (Michigan). 1,8-naphthalic anhydride was purchased from TCI America (New York). Methylsulfoxide extra dry with molecular sieves, and N,N-Dimethylformamide, extra dry with molecular sieves, were purchased from Acros Organics. $Nd(NO_3)_3 \cdot 6H_2O$ (99.999%) was purchased from Strem Chemicals.

Ligand Synthesis. PAMAM dendrimer G(3)-NH_2 (390mg, 0.0565mmol) was treated with an 8 molar excess of 1,8-naphthalic anhydride (total 40 moles per 1 mol of dendrimer) with respect to the total number of primary amine groups on the dendrimer (445 mg, 2.245 mmol) and refluxed in DMF ($10cm^3$) for 48 hours under a nitrogen atmosphere, while monitoring for the disappearance of the naphthalic anhydride by thin layer chromatography (silica gel). The functionalized dendrimer was obtained after removal of the solvent and trituration in hot dioxan to remove any excess unreacted 1,8-naphthalic anhydride. The title compound was isolated as a brown flocculent solid (518 mg, 72%);. Found: C 62.06, H 6.04, N 12.57, $C_{686}H_{736}N_{122}O_{124}*32H_2O$ requires: C 62.18, H 6.09, N 12.90. UV/Vis (DMSO) λ_{max} ($\varepsilon/dm^3\ mol^{-1}cm^{-1}$) 286 nm (135,050), 336 nm (312,630) and 350 nm (272,070); ν_{max} (Nujol/cm^{-1}) 3304

(broad, N-H), 3067, 2952, 2850, 1701, 1659, 1589, 1540, 1438, 1384, 1345, 1236 and 780; 1H-NMR [300MHz; $(CD_3)_2SO$] 2.01-2.29 (120 H, broad s, $COCH_2CH_2N$), 2.60 (56 H, broad s, $CONHCH_2$), 2.99 (64 H, broad s, $N(CO)_2CH_2CH_2NH$), 3.06 (64 H, broad s, $N(CO)_2CH_2CH_2NH$), 3.34 (180H, broad s, $N(CH_2)_3$), 4.04 (60 H, broad s, NH), 7.70 (64H, broad s, 3-H and 6-H), 7.93 (64H, broad s, 4-H and 5-H), 8.30 (64H, broad s, 2-H and 7-H), 13C-NMR [75MHz; $(CD_3)_2SO$], 33.11, 36.38, 36.55, 36.78, 40.65, 49.31, 52.17, 66.32, 122.04 (ArC), 127.00 (ArC), 130.46 (ArC), 131.13 (ArC), 133.95 (ArC), 163.42 (NHCO), 171.45 [$N(CO)_2$].

Nd^{3+} Polymetallic Complex. A batch spectrophotometric titration was performed with PAMAM:Ln solutions in DMSO, where PAMAM = generation-3 poly(amidoamine) dendrimer, Ln = Nd^{3+} ions from nitrate salt. The following PAMAM:Ln ratios were used, keeping the total number of moles of PAMAM (ligand) constant and increasing the amount of Ln: 1:2, 1:3, 1:4, 1:5, 1:6, 1:6.5, 1:7, 1:7.5, 1:8, 1:8.5, 1:9, 1:9.5, 1:10. The initial ligand concentration was 2.003×10^{-4} mol L^{-1}, the concentration of the Nd^{3+} salt solution was 2.030×10^{-3} mol L^{-1}. Each complex solution was diluted to the concentration of 2.00×10^{-5} mol L^{-1}. The luminescence intensity was monitored every two days until unchanged to ensure thermodynamic equilibrium, which was typically reached after seven days at room temperature. The metal-centered NIR emission was collected using a 715nm cut-off filter to prevent ligand second order emission. Each spectrum was corrected for the fluctuation of the intensity of the instrument lamp for each day of measurement by recording the signal of quinine sulfate solution as a reference. Three independent sets of solutions were prepared and used for the analysis of each PAMAM:Ln ratio. The corrected emission bands were integrated using the software provided by Jobin Yvon-Horiba with the Fluorolog instrument. Plots of integrated intensity of emission versus PAMAM:Ln ratio

and of integrated intensity divided by the number of Nd^{3+} ions versus the PAMAM:Ln ratio were drawn.

Luminescence Measurements. Emission and excitation spectra were measured using a JY Horiba Fluorolog-322 spectrofluorometer equipped with a Hamamatsu R928 detector for the visible domain and an Electro-Optical Systems, Inc. DSS-IGA020L detector for the NIR domain. The NIR luminescence relative quantum yields were measured with multiples experiments using two different references: i) a Sm(2-hydroxyisophthalamide macrobicycle). This Sm complex has a known quantum yield of $\Phi = 0.00073$ in 0.01 M TRIS buffer.[3] Samarium emits in both the visible and NIR range, which allowed for a simple method of cross calibrating the visible detector of the Fluorolog-322 with the NIR detector. ii) A NIR-emitting $KYb(Trop)_4$ complex ($\Phi = 0.019$ in DMSO) as reference.[4] Spectra were corrected for the instrumental function for both excitation and emission. Values were calculated using Equation 8-1:

$$\Phi_x/\Phi_r = [A_r(\lambda_r)/A_x(\lambda_x)][I(\lambda_r)/I(\lambda_x)][\eta_x^2/\eta_r^2][D_x/D_r]$$

Equation 8-1

Where subscript r stands for the reference and x for the sample; A is the absorbance at the excitation wavelength, I is the intensity of the excitation light at the same wavelength, η is the refractive index($\eta = 1.333$ in TRIS buffer, $\eta = 1.479$ in DMSO), and D is the measured integrated luminescence intensity.

The luminescence lifetime measurements were performed by excitation of solutions in 1 cm quartz cells using a Nd:YAG Continuum Powerlite 8010 Laser at 354 nm (3rd harmonic) as

excitation source. Emission was collected at a right angle to the excitation beam, the emission wavelength selected with a Spectral Products CM 110 1/8 meter monochromator. The signal was monitored by a cooled photomultiplier (Hamamatsu R316-2) coupled to a 500 MHz bandpass digital oscilloscope (Tektronix TDS 754D). The signals to be treated (at least 15,000 points resolution for each trace) were averaged from at least 500 individual decay curves. Luminescence decay curves were imported into Origin 7.0 scientific data analysis software. The decay curves were analyzed using the Advanced Fitting Tool module. Reported luminescence lifetimes are averages of at least three independent determinations.

Live Cell Imaging. Primary cultures of rat pulmonary microvascular endothelial cells (RPMVEC, VEC Technolgies, Rensselar, NY) were seeded on glass coverslips and placed into a thermocontrolled (37ºC) stage insert and imaged using a Nikon TE2000E inverted microscope. Microinjection of lanthanide-based reporter molecules as DMSO/water solution was accomplished using an InjectMan NI2, Femtojet, and Femtotips II (Eppendorf, Westbury, NY) using approximately 100mg/ml of compound and an injection pressure of 180 hpa between 0.5-1.5s. G3-PAMAM-(1,8-naphthalimide)$_{32}$/Nd$_8$ was excited using a Xenon light source and an excitation filter wheel (Sutter, Novato, CA) equipped with a 380 nm excitation filter and 790LP emission filter (Chroma, Brattleboro, VT). Images were collected with an NIR sensitive CCD camera (Rolera, Q Imaging, Vancouver, Canada) and MetaMorph software (Molecular Devices, Downington, PA).

8.5 RESULTS AND DISCUSSION

We have used a conceptual approach in order to create a NIR lanthanide complex that can emit a high number of photons per unit of volume by synthesizing a polymetallic lanthanide complex that possesses a high absorption coefficient through the incorporation of a large number of chromophores within its structure (Figure 8-1).

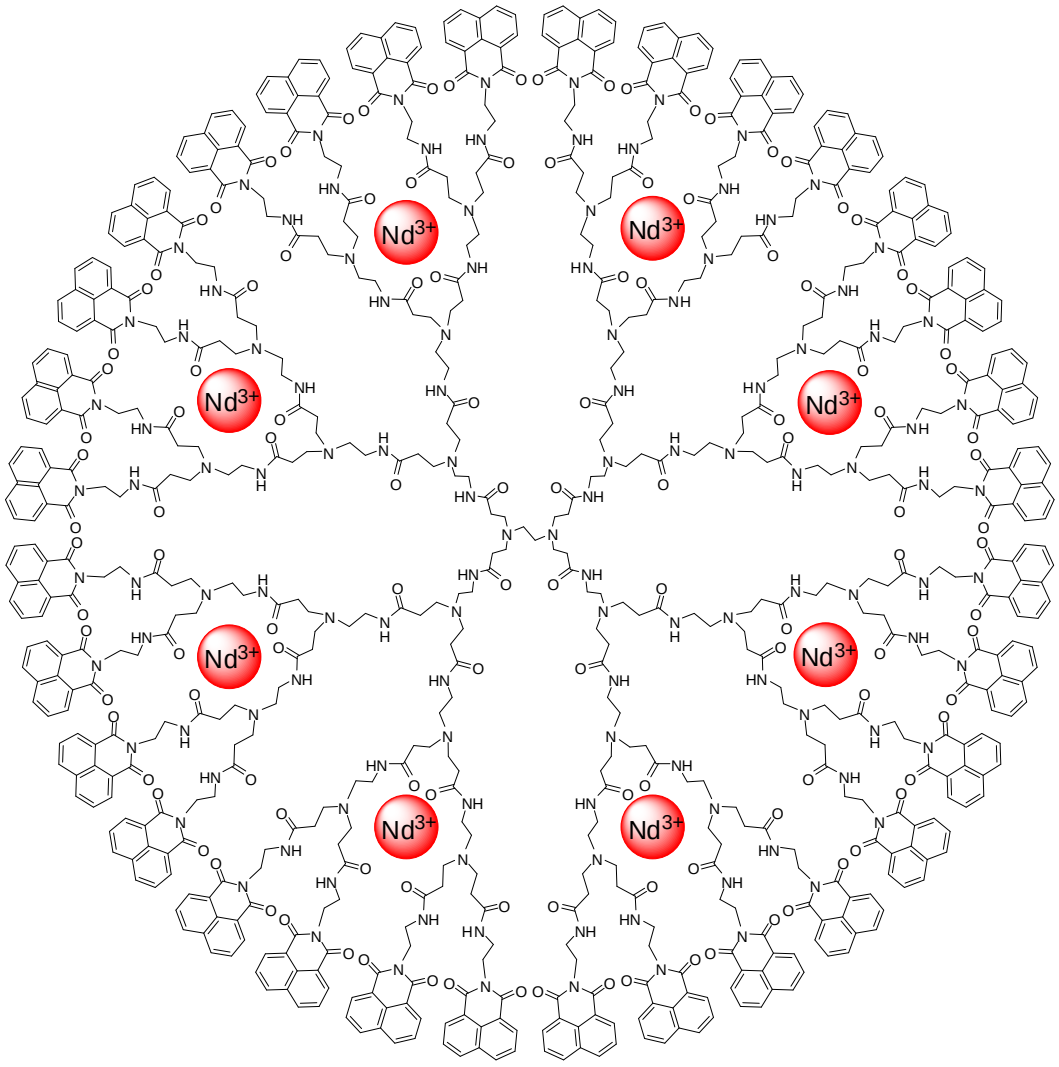

Figure 8-1. Model image of a proposed polymetallic lanthanide Nd^{3+} complex based on a generation-3 PAMAM dendrimer ligand, carrying thirty-two 1,8-naphthalimide sensitizing groups on its surface to provide the "antenna effect" to eight lanthanide cations (G(3)-PAMAM-(1,8-naphthalimide)$_{32}$:8Nd).

Dendrimer structures are appealing for the synthesis of mono- or polymetallic complexes.[234,259] The ligand that we have synthesized to realize our strategy has been built on the basis of a generation-3 poly(amidoamine) (PAMAM) dendrimer,[215,237,260] since this structure has shown promise for the coordination of multiple[237] luminescent lanthanide cations. To generate the antenna effect, thirty-two chromophoric groups have been covalently appended to the branch termini of the dendrimer. The 1,8-naphthalimide chromophoric group has been chosen to sensitize NIR-emitting Nd^{3+} lanthanide cations upon the hypothesis that the energy position of its triplet state (18,519 cm^{-1})[220] is a suitable match for the energy of the accepting levels of Nd^{3+}.[4,245] It is important to notice that, if this group has been used previously to sensitize the visible-emitting Eu^{3+},[231] it has never been reported as a sensitizer for any of the NIR-emitting lanthanide cations. The polymetallic complex was formed by slow reaction of eight Nd^{3+} cations per dendrimer ligand in anhydrous DMSO.

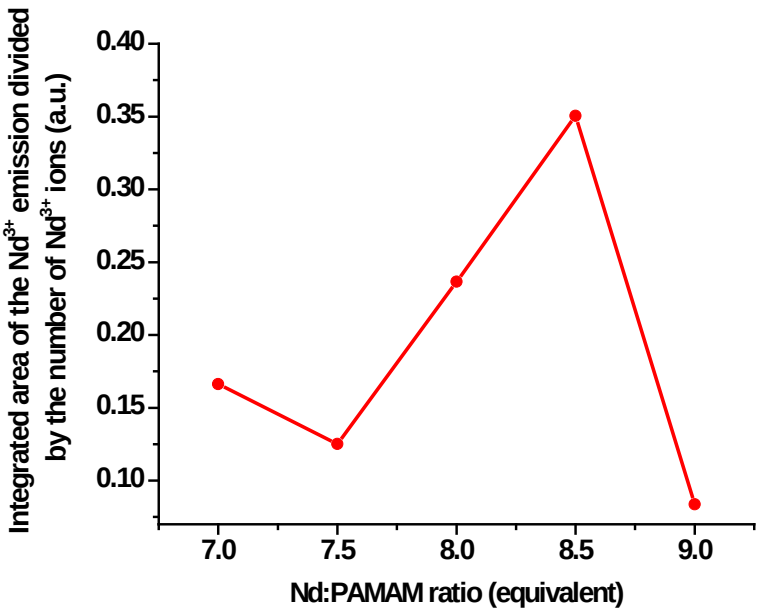

Figure 8-2. Example of a batch titration of G3-PAMAM-(1,8-naphthalimide)$_{32}$ solution with increasing amounts of $Nd(NO_3)_3$ in anhydrous DMSO. Nd^{3+} centered emission intensity for each complex was integrated and divided by the number of Nd^{3+} ions.

The formation of the polymetallic Nd^{3+} dendrimer complex was characterized using luminescence titrations while monitoring the Nd^{3+} emission upon ligand excitation (see Figure 8-2). The titrations show that each discrete dendrimer ligand molecule can coordinate a value comprised between 8 and 9 Nd^{3+} cations (G(3)-PAMAM-(1,8-naphthalimide)$_{32}$:8Nd). Seven days were required to obtain a species that emits a stable NIR emission signal, an indication of a slow kinetic formation of the complex. The metal-to-dendrimer stoichiometry and synthetic time required for the formation of the lanthanide complex are fairly similar to the result obtained for a visible emitting Eu^{3+} complex that we have described previously based on a generation-3 PAMAM dendrimer substituted with different chromophoric groups.[215,260]

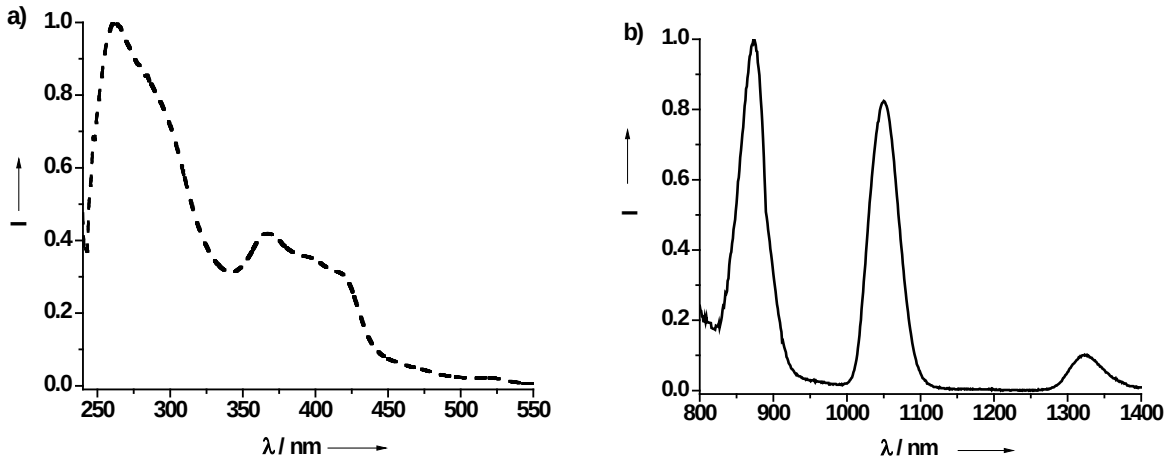

Figure 8-3. Near-IR luminescence characterization. a) Excitation spectrum recorded upon Nd^{3+} emission (λ_{em}=1060 nm, $^4F_{3/2} \rightarrow {}^4I_{11/2}$ transition), and b) Near-infrared emission spectrum upon ligand excitation at 380 nm of the G(3)-PAMAM-(1,8-naphthalimide)$_{32}$:8Nd complex (2.00×10^{-5} M in DMSO containing 130 ppm H_2O).

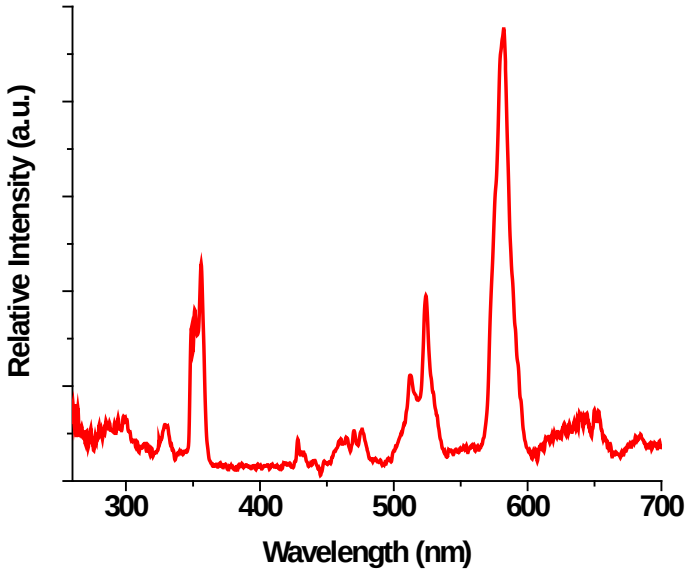

Figure 8-4. Excitation (λ_{em} = 1060 nm) of a $Nd(NO_3)_3$ salt solution 1.0E-1 M in anhydrous DMSO.

The excitation spectrum (Figure 8-3a) of the complex, upon monitoring the Nd^{3+} emission signal at 890 nm ($^4F_{3/2} \rightarrow {}^4I_{11/2}$ transition), appears as a series of broad bands that are attributed to π-π* transitions located on the 1,8-naphthalimide chromophore since the spectrum corresponding to the direct excitation of the electronic levels of the free Nd^{3+} lanthanide would be characterized by sharp emission bands (see Figure 8-4 for comparison). This result demonstrates that the 1,8-naphthalimide group is a suitable sensitizer for Nd^{3+}. The NIR emission spectrum (Figure 8-3b) of the complex recorded upon ligand excitation at 380 nm reveals the three typical, narrow emission bands arising from the transitions of the Nd^{3+} cations. The luminescence lifetime was measured to be 1.53 ± 0.02 μs. The Nd^{3+}-centered quantum yield (representing the total number of photons emitted by all eight Nd^{3+} cations over the total number

of photons absorbed by the thirty-two 1,8-naphthalimide (λ_{ex} = 360 nm) of each discrete lanthanide dendrimer complex) has been measured on a 1.6×10^{-6} M DMSO solution at room temperature. The obtained value of $6(1)\times10^{-5}$ is relatively small in comparison to those reported in the literature for several Nd^{3+} complexes in solution.[34,174,175,211,246,248-250]

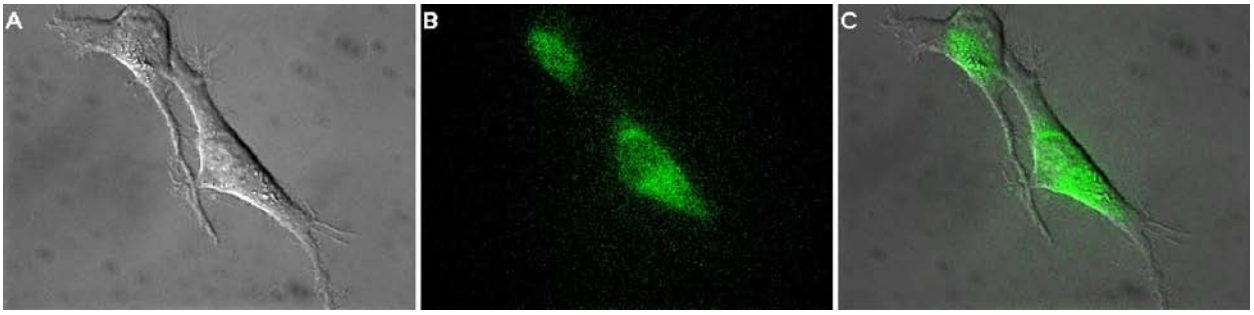

Figure 8-5. Microscopy images of a living rat pulmonary microvascular endothelial cell (RPMVEC, Vec Technologies) microinjected with the NIR-emitting Nd^{3+} complex G(3)-PAMAM-(1,8-naphthalimide)$_{32}$:8Nd;. A: Light microscopy image. B: NIR luminescence microscopy image obtained by illuminating the sample with λ_{ex} = 380 nm. The contribution of visible light was removed by using a 790 nm cut-off filter. C: Overlay of the images obtained with light and NIR luminescence microscopy. Concentration of the DMSO stock solution microinjected in the cell: 100 mg/ml of G(3)-PAMAM-(1,8-naphthalimide)$_{32}$:8Nd.

To establish quantitatively that this NIR emitter can effectively operate in state of the art practical applications, we have tested its ability to function as a NIR luminescent reporter for luminescence microscopy in a living cell. We hypothesized that, with our strategy to synthesize

nanoscale complexes with 1) a large number of emitting lanthanide cations for each discrete complex (per unit of volume), and 2) a large extinction coefficient, resulting from the thirty-two 1,8-naphthalimide groups, a sufficient number of photons would be emitted to allow sensitive detection despite the small quantum yield value. Since it does not have the ability to passively cross cell membranes, the Nd^{3+} dendrimer complex was microinjected into a living rat pulmonary microvascular endothelial cell as a water/DMSO solution. The NIR luminescence arising from the cell was then monitored using an inverted microscope equipped with a NIR-sensitive camera. The images obtained during this experiment are reported in Figure 8-5. The center picture represents the spatially resolved NIR signal as recorded by the NIR-sensitive camera of the microscope. In this picture, it is possible to visually assess that such NIR luminescence microscopy images can be obtained with a good signal-to-noise ratio. In addition, the weak background signal contributes to the good signal-to-noise ratio and to the detection sensitivity. To the best of our knowledge, this experiment is the first report of a NIR luminescence microscopy experiment in a living cell using NIR-emitting lanthanide complexes as reporters. In order to obtain such detection sensitivity in a NIR luminescence microscopy experiment, the complex must fulfill two major requirements: 1) It must be able to emit a sufficient number of photons to allow good signal-to-noise detection (sensitivity) 2) The complex must not dissociate completely in solution when diluted at low concentration in the living cell. This experiment demonstrates quantitively that the herein reported polymetallic dendrimer Nd^{3+} complex fulfills both conditions.

8.6 CONCLUSIONS

In summary, we report two novelties in this article. First, we have synthesized a dendrimer ligand that utilizes a generation-3 PAMAM dendrimer substituted with thirty-two 1,8-naphthalimide groups for the sensitization of NIR-emitting lanthanide cations: Nd^{3+}. This ligand has been demonstrated to be suitable for the coordination and sensitization of eight NIR-emitting Nd^{3+} cations. Secondly, this work also establishes the first proof of principle that, despite their modest quantum yields, highly absorbing polymetallic NIR-emitting lanthanide complexes can emit a sufficient number of photons to allow NIR luminescence microscopy imaging in a living cell. This experiment illustrates quantitatively the validity of our strategy to compensate small quantum yields values by designing ligand systems that can bind a large number of NIR lanthanide emitters and that possess a large absorption coefficient due to the large number of chromophores. This work also demonstrates that the NIR luminescence of lanthanide cations offers exciting possibilities for NIR luminescence microscopy that will complement those of organic fluorophores and luminescent semiconductor nanocrystals. Future work in the lab will include the modification of the dendrimer ligand to allow the luminescent dendrimer complex to cross cell membranes and to allow the complex to be excited at a wavelenghth corresponding to lower energy in order to minimixe photonic damage to biological samples. The toxicity of these luminescent dendrimer complexes in cells will also be quantified and reported in the future.

9.0 LUMINESCENCE TARGETING AND IMAGING USING A NANOSCALE GENERATION 3 DENDRIMER IN AN IN VIVO COLORECTAL METASTATIC RAT MODEL

9.1 CHAPTER PREFACE

The aim of this work was a further demonstration of biologic application with the near-infrared luminescent dendrimer described in Chapter 8.0. Specifically, we used a PAMAM dendrimer with eight Eu^{3+} and functionalized 1,8-naphthalimide sensitizers with amino groups to address the issue of water solubility. In addition to our experimental work, we were fortunate in establishing a collaboration with researchers at the Hillman Cancer Center who were interested in developing new surgical procedures for delivering cancer-targeted. This current chapter focuses on the liver cannulation technique where tumors have been grown in a rat model through splenic injection of cancerous cells. Chapter 10.0 is a more chemical representation of the collaborative effort and may be considered a companion piece. The material contained in this chapter has been published in advance as a full paper in the journal *Nanomedicine: Nanotechnology, Biology and Medicine;* (DOI: 10.1016/j.nano.2010.09.002).

List of authors: Marco A. Alcala, Shu Ying Kwan, Chad M. Shade, Megan Lang, Hyounsoo Uh, Manyan Wang, Stephen G. Weber, David L. Bartlett, Stéphane Petoud, Yong J. Lee

Author contribution: The author of this dissertation was responsible for the photophysical characterization of the complex including the absorption profile, collecting the photo-stability measurements on a fluorescence microscope, assisting with surgical procedures and fluorescence macroscopy experiments with whole animals, providing interpretation of the results and contributing to the preparation of the published manuscript.

9.2 ABSTRACT

Surgery is currently the best approach for treating either primary or metastatic hepatic malignancies. Because only 20% of hepatic cancers are operable in patients, several types of regional therapy (RT) are emerging as alternate treatment modalities. However, RTs can have their own limitations at controlling tumor growth or may lack the ability to detect such metastases. Additional strategies can be implemented to enhance their efficacy. An animal model of hepatic metastases coupled with a gastroduodenal artery (GDA) cannulation technique may provide a site to apply such therapies. In our study, splenic injections were performed with CC531 adenocarcinoma cells, which generated metastatic hepatic tumors in WAG/RijHsd rats. Cannulation of GDA was achieved via a polyethylene catheter. Infusion of generation 3 polyamidoamine 4-amino-1,8-naphthalimide dendrimer containing 8 europium ions (Eu-G3P4A18N) via the GDA resulted in luminescence of the hepatic metastatic nodules. Imaging of the metastatic hepatic nodules was obtained with the help of a digital charge coupled device (CCD) camera.

9.3 INTRODUCTION

The liver is the most common site of distant metastases of colorectal cancer. About 150,000 Americans are diagnosed with colorectal cancer each year and about 50,000 of them will die from metastases of this disease.[2] Approximately 50% of patients with colorectal cancer develop metastatic liver disease, of these patients, only 20% are operable. Once liver metastases have occurred, the patient's prognosis declines to a 5 year survival rate of 5%.[1] For operable patients, surgery is the best treatment for liver metastases in comparison with the available regional therapies, such as radiofrequency ablation,[261] transarterial chemoembolization (TACE) or radiation, resulting in a 5-year survival rate of 30%. Survival to 5 years is 5-9% in patients with unresected hepatic metastases who have received only conventional systemic chemotherapy.[262] Some of the current therapies include local tumor ablation (i.e., applying alcohol or acetic acid directly into the metastatic lesions, cryotherapy or radiofrequency ablation), isolated hepatic perfusion, TACE and external radiation therapy. To treat patients with inoperable liver metastases better, current regional therapies need to be better understood and their efficacy need to be improved by being able to combine detection and treatment functions. The survival studies in our rat model have allowed us to use a cannulation technique in which to deliver our functionalized dendrimer. Several studies have developed rat models of liver metastases[263-265] but the surgical techniques were not adequately detailed. Gupta et al described a liver infusion model by cannulating through the GDA with catheter placement into the hepatic artery.[266] Others have also described directly cannulating the hepatic artery[267] as well as the portal vein.[268] The approach described here allows the main blood supply to the liver to be spared from trauma and the GDA to be ligated, mimicking the clinical application of RTs where isolated hepatic perfusion is initiated via the GDA. We are now reporting an in vivo hepatic colorectal metastases

rat model via splenic injections with CC531 colorectal cancer cells. Previous studies have shown that colorectal metastases can be initiated by injecting cancer cells via the portal vein and superior mesenteric vein.[269] These approaches led to small diffuse lesions in the liver.[270] In this study, we chose the splenic injection method. Metastasis by way of injecting the spleen has allowed us to mimic more closely the clinical patient and study a more relevant model than those models in prior studies.

The field of polymer chemistry has enabled the development of dendrimer nanotechnology for application in cancer therapy.[271-273] Polycationic polymers, such as poly(lysine)s, poly(ethylene-imine)s, diethylaminoethyl dextrans and polyamidoamine (PAMAM) dendrimers, have demonstrated great potential for application in cancer therapy. Through the iterative coupling of dendrons (the monomer of dendrimers), versatile "carrier devices" on the nanometer scale can be synthesized. Dendrimers are built from successive layers or generations of dendron coupling, so the diameters grow linearly and the number of coordinating groups grows geometrically. This characteristic allows for a concentration of various types of metal ions within a discrete dendrimer, offering the advantage of a relatively small but dense functional molecule.[274] PAMAM dendrimers have shown good biocompatibility and in vivo deliverability without significant degradation.[275,276] The branch termini of the PAMAM family of dendrimers contain chemical groups, such as terminal primary amines, alcohol or carboxylic groups, that enable the dendrimers to be functionalized with suitable groups such as 1,8-naphthalimide chromophores to serve as photon emitters, or targeting molecules. In this study we used a novel dendrimer, which we have developed, that incorporates generation 3 (G3) PAMAM with derivatives of 1,8-naphthalimide groups covalently substituted on all 32 terminal groups. Eight Eu^{3+} cations were encapsulated within the available binding sites

present along the interior branches of each dendrimer, resulting in robust luminescent probes that possess maximum signal intensity per unit volume. Our studies reveal that this new dendrimer Eu-G3P4A18N, which contains 8 europium ions, can become luminescent for imaging studies to detect the distribution sites of metastatic hepatic colorectal tumors in our in vivo rat model.

9.4 EXPERIMENTAL

Animal Model. Four- to 6-week-old male WAG/RijHsd rats were purchased from Harlan, Netherlands. Rats were fed ad libitum and maintained in environments with a controlled temperature of 22 °–24 °C and 12-hour light and dark cycles. All procedures involving the rats were in accordance with the Guide for the Care and Use of Laboratory Animals (National Research Council, 1996) and on a protocol approved by the Institutional Animal Care and Use Committee of the University of Pittsburgh.

Cell Culture and Generation of Colorectal Metastasis by Splenic Injection. The CC531 cell line is a moderately differentiated colon adenocarcinoma syngeneic to WAG/RijHsd rats. Tumor cells were tested and found to be virus- and mycoplasma-free. CC531 cells were cultured in Dulbecco's modified eagle medium (DMEM) (Gibco, Grand Island, New York, USA) supplemented with 10% fetal bovine serum. Cells were maintained by serial passage. Tumor cells were harvested with a solution of 0.25% trypsin (Sigma, St. Louis,Missouri, USA), washed three times in a 0.9% NaCl solution buffered with 1.4 mM phosphate (PBS) and adjusted to a suspension containing 2×10^6 viable (trypan blue exclusion test) tumor cells per 200 μL of PBS,

which were then injected into the spleen to generate metastatic tumor nodules in the liver. Metastatic lesions in the liver were revealed 15-20 days later after a midline incision was performed. Figure 9-1, A and B both show the metastatic nodules in a rat liver after 2 and 4 weeks, respectively.

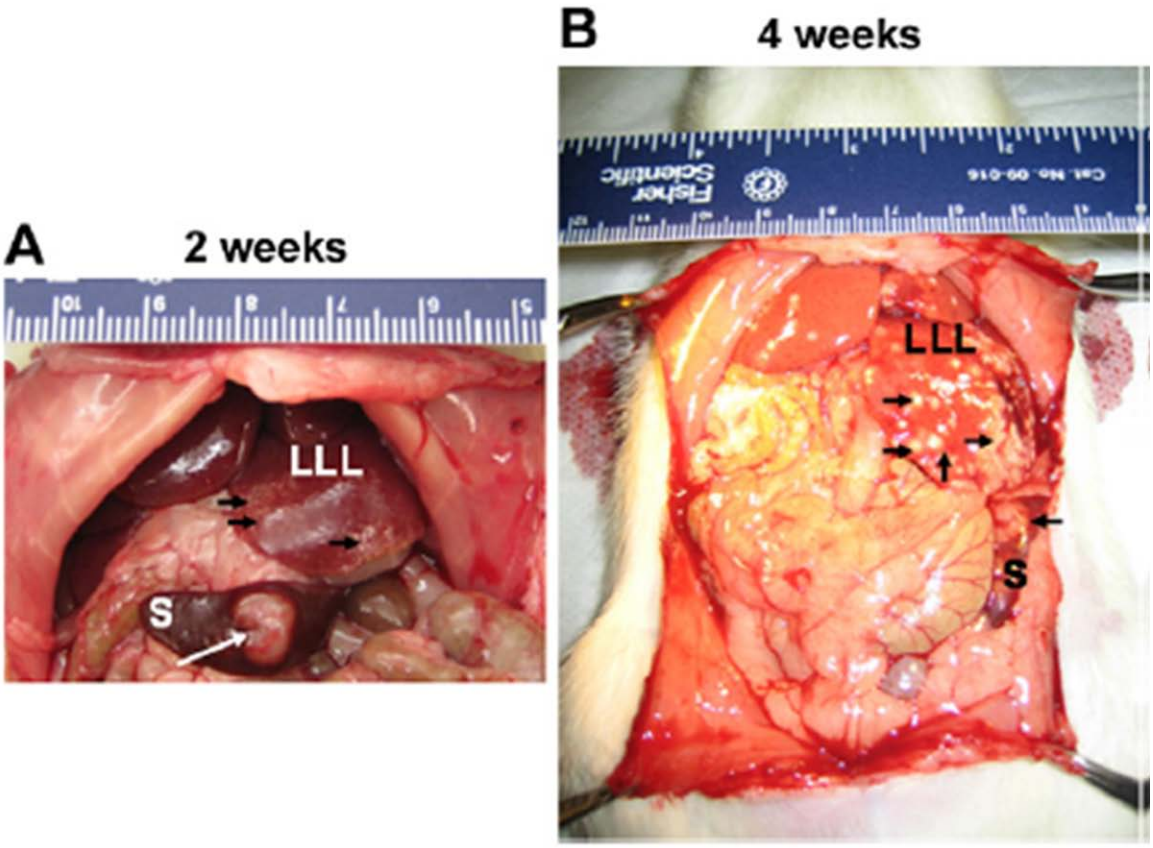

Figure 9-1. Tumorigenicity and metastasis of CC531 cells in WAG/RijHsd rats. Syngeneic rat colon carcinoma CC531 cells (2×10^6 cells in 0.2 ml of PBS) were injected into the spleen of rats and tumor formation was observed after 2 weeks (A) or 4 weeks (B). Tumors were observed in the spleen (S) and the left lateral lobe (LLL). Arrows point out the location of tumors.

Anesthesia. Rats were anesthetized with a single intraperitoneal injection of 70 mg/kg of Ketamine (Bedford Labs, Ohio, USA) and 2.5 mg/kg of Acepromazine (Boehringer Ingleheim Vetmedica, Inc., Missouri, USA). An intramuscular injection of 0.1 mg/kg of buprenorphine (Bedford Labs, Ohio, USA) was also administered for analgesia before incision and 12-24 hours later if the rats displayed any sign of distress.

GDA Cannulation Procedure. The GDA cannulation procedure with Eu-G3P4A18N (generation 3 polyamidoamine 4-amino-1,8-naphthalimide containing 8 europium ions). Once anesthetized, the rat was placed in the supine position on a heating pad (Deltaphase Isothermal Pad, Braintree Scientific, Massachusetts, USA) to maintain body temperature. The abdomen was shaved and sterilely prepared; all subsequent steps were performed aseptically; nonglare bright lighting was obtained with a fiber optic light source (Ehrenreich Photo Optical Industries, New York, USA). A 5 cm midline incision was made using a #10 scalpel and carried down into the peritoneal cavity, and hemostasis was achieved with sterile gauze and pressure. The bowel was then brought to the surface and flipped to the left of the abdomen, revealing the hepaticoduodenal ligament, the portal vein, the hepatic artery, bile duct and inferior aspect of the liver. The portal vein was isolated using a 6-0 silk suture, and fine-tipped tweezers (Miltex, Pennsylvania, USA) were used to reveal the vein, allowing clear visualization of the hepatic artery running posterior and adherent to it. After the hepatic artery was separated from the portal vein, the artery was then isolated with a 6-0 silk suture (Figure 9-2, A). The hepatic artery was traced inferiorly to the branching point where it meets the GDA. The GDA was also isolated using a 6-0 silk suture at the most inferior point and skeletonized using fine-tipped tweezers. Two 6-0 silk sutures were placed about 3 mm apart at the superior portion of the GDA and tied

on loosely for control of the catheter after placement (Figure 9-2, A). Fine-tipped, 4.5 inch curved iris scissors (Miltex, Pennsylvania, USA) were used to make a 0.5 mm arteriotomy into the middle of the GDA without bisecting it. Hemostasis was achieved with the superiorly placed 6-0 silk sutures. A 30-gauge needle bent halfway was used as a “hook” to help guide a polyethylene (PE-10) catheter (Becton, Dickinson and Company, New Jersey, USA) retrograde into the GDA and placed just before the bifurcation of the hepatic artery and the GDA (Figure 9-2, B). The catheter was inserted into the arteriotomy and placed approximately 4 mm into the GDA, stopping before the GDA-hepatic artery junction. The superiorly placed suture along with a second one placed 1 mm next to it was tied down to secure the catheter (Figure 9-2, A).

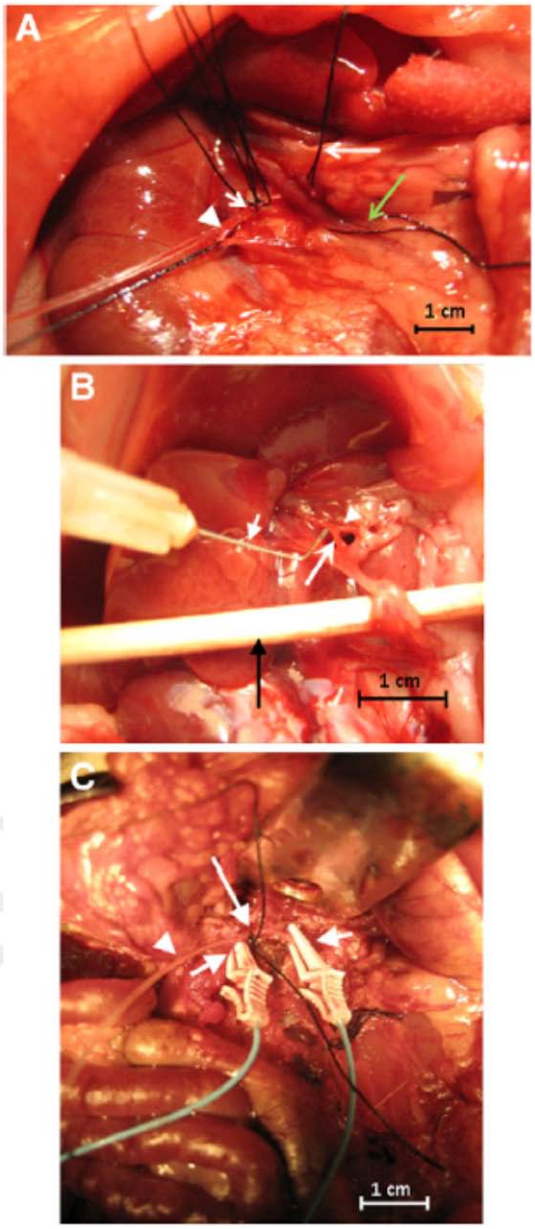

Figure 9-2. GDA cannulation technique. Photograph (A) shows the inferior aspect of the liver showing the silk sutures around the hepatic artery (long arrow), portal vein (green long arrow), proximal and distal ends of the GDA (short arrow) and the catheter placed into the GDA (arrowhead). Photograph (B) shows a 30-gauge needle (short arrow) being used as a hook for control when inserting the catheter into the GDA (long arrow); arrowhead indicates the hepatic artery; a swab is shown at the bottom (black arrow) to display the vascular network and photograph. Photograph (C) shows the placement of the PE-10 catheter (arrowhead) cannulated into the GDA and anchored down with a silk suture (long arrow) and the two vascular clamps (short arrows) on the portal vein and the hepatic artery.

To prevent inflow of blood into the liver, micro vessel clamps were placed on the portal vein and the hepatic artery (Figure 9-2, C). Catheter placement was confirmed by visualizing blood return in the catheter upon drawing back on the syringe and patency was confirmed with an infusion of 1-2 mL of normal saline. Complete isolation of the liver was achieved through occlusion of the suprahepatic inferior vena cava (IVC) with cotton swabs during infusion of Eu-G3P4A18N.

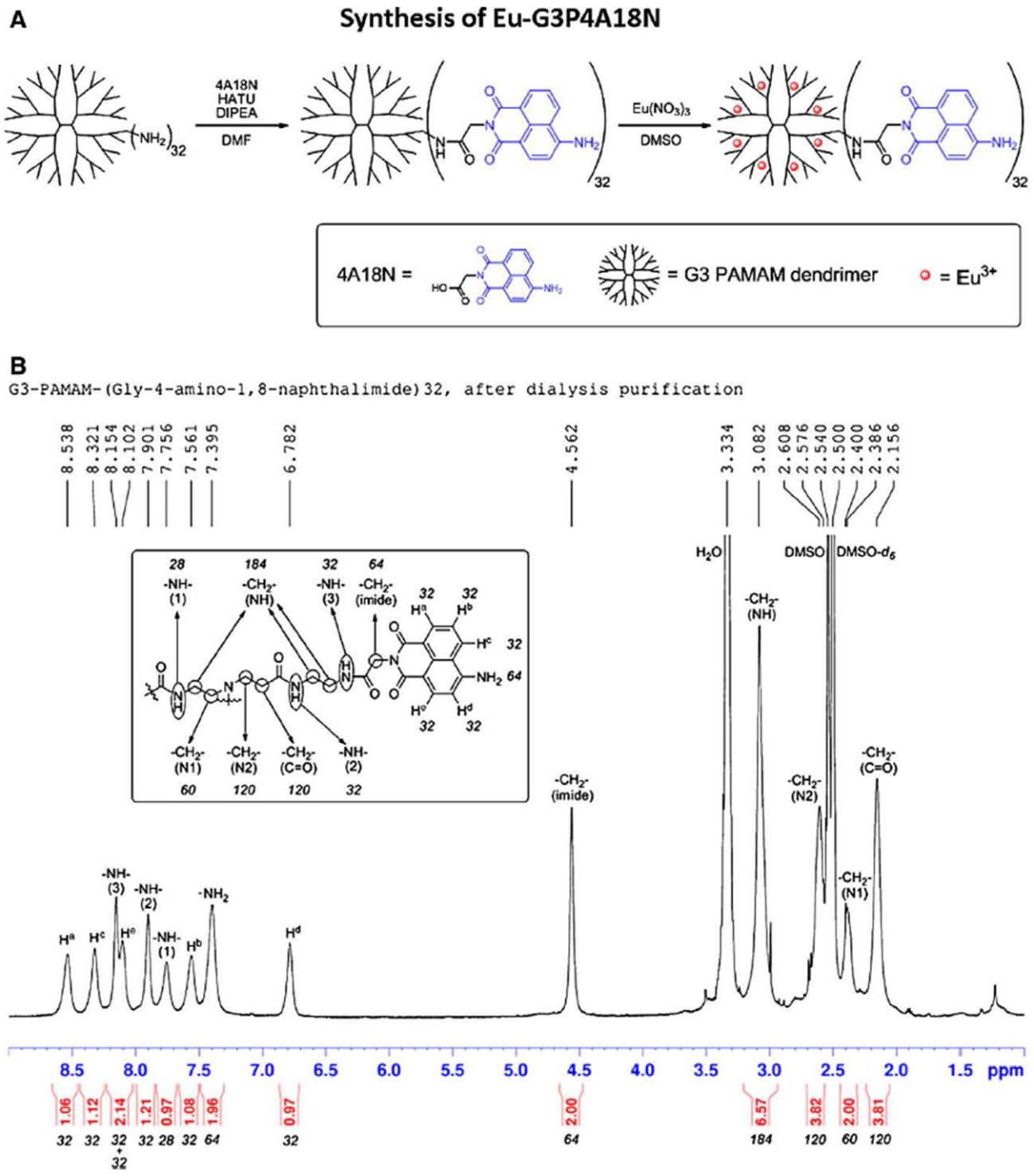

Figure 9-3. Synthesis, characterization and structure of Eu-G3P4A18N. (A) Synthetic scheme of Eu-G3P4A18N. (B) Characterization of G3P4A18N by NMR.

Synthesis of Eu-G3P4A18N. Glycine-conjugated 4-amino-1,8-naphthalimide was synthesized by a reported method.[277] Glycine-conjugated 4-amino-1,8-naphthalimide was attached on the amine-terminated G3 PAMAM dendrimer by a standard amide coupling condition: 54.1 mg (2.00×10^{-4} mol) of glycine-naphthalimide conjugate was added to a solution of 29.4 mg (4.26×10^{-6} mol) of G3 PAMAM dendrimer (Dendritech Inc.; Midland, MI, USA) in 5 mL of DMF (dimethylformamide) (Sigma-Aldrich, St. Louis, Missouri, USA). 92.1 mg (2.42×10^{-4} mol) of HATU (O-(7-Azabenzotriazol-1-yl)-*N*,*N*,*N*′,*N*′-tetramethyluronium hexafluorophosphate) (Aldrich, St. Louis, Missouri, USA) and 70 μL (52 mg; 4.0×10^{-4} mol) of DIPEA (N,N-Diisopropylethylamine) (Sigma-Aldrich, St. Louis, Missouri, USA) were added (Figure 9-3, A). The reaction mixture was stirred at 20-25 ^{o}C for 2 days under nitrogen atmosphere while researchers monitored for the disappearance of G3 PAMAM dendrimer by TLC (thin-layer chromatography). The compound was purified by dialysis using a regenerated cellulose membrane (nominal molecular weight cut-off [MWCO] 12,000-14,000; Fisher Scientific, Pittsburgh, Pennsylvania, USA) in dimethyl sulfoxide (DMSO) for three days. The solution recovered from the dialysis membrane was dried in a vacuum oven (40 °C, 50 mbar) to yield G3P4A18N as brown solid (52.5 mg, 82%). G3P4A18N was characterized by ^{1}H-NMR (nuclear magnetic resonance) (300 MHz, DMSO-d_6) (Figure 9-3, B): δ 8.54 p.p.m. (br s, 32 H), 8.32 (br s, 32 H), 8.15 (br s, 32 H), 8.10 (br s, 32 H), 7.90 (br s, 32 H), 7.76 (m, 28 H), 7.56 (br s, 32 H), 7.40 (br s, 64 H), 6.78 (br s, 32 H), 4.56 (br s, 64 H), 3.08 (m, 184 H), 2.61 (m, 120 H), 2.39 (m, 60 H), 2.16 (m, 120 H); analysis (% calcd, % found for $C_{750}H_{864}N_{186}O_{156}$·32DMSO·64H2O): C (52.47, 51.74), H (6.40,6.29), N (13.98, 13.76). The Eu^{3+} complex of G3P4A18N (Eu-G3P4A18N) was synthesized by the following method adapted from one of our methods:[237] 22.67 mg (1.513×10^{-6} mol) of G3P4A18N (generation 3 polyamidoamine 4-amino-1,8-

naphthalimide) was dissolved in 10 mL of DMSO. Furthermore, 647.5 μL of 18.7 mM $Eu(NO_3)_3$ solution in DMSO (1.21×10^{-5} mol) was added to the dendrimer solution. Formation of Eu^{3+} complexes with the G3 PAMAM dendrimer was confirmed as described previously.[237] The mixture was diluted to 25.00 mL and incubated at room temperature for seven days. The resulting solution (conc. = 60.5 μM) was used as obtained and the final configuration is seen in Figure 9-4, C.

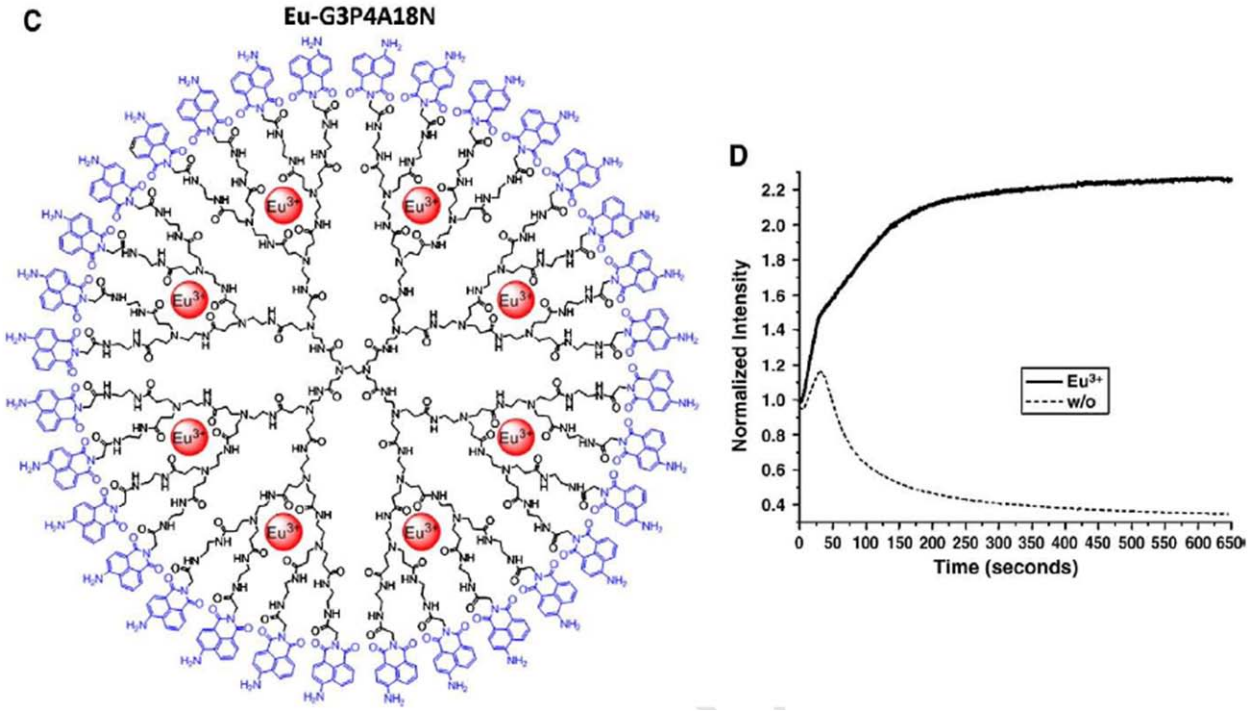

Figure 9-4. Synthesis, characterization and structure of Eu-G3P4A18N. (C) Structure of Eu-G3P4A18N, which contains thirty-two 4-amino-1,8-naphthalimide units and eight europium cations. (D) Photobleaching analysis of Eu-G3P4A18N dendrimer. The fluorescence from the 1,8 naphthalimide derivative was monitored as a function of time upon exposure to excitation light.

Luminescence of Eu-G3P4A18N. As explained above, we have developed the synthesis of Eu-G3P4A18N dendrimer. The absorption and emission spectra of this dendrimer were measured (data not shown). The absorption spectrum displays a maximum at approximately 440 nm. The fluorescence emission spectrum displays a prominent band with an intensity maximum at 555 nm. For the photobleaching experiment (Figure 9-4, D), Eu-G3P4A18N dendrimer and its control G3P4A18N dendrimer at 10 μM were sealed in capillary tubes to minimize effects from solvent evaporation and diffusion. Each sample was focused in an IX81 inverted fluorescence microscope (Olympus, Melville, New York, USA) coupled with a cooled charge coupled device (CCD) (ORCA-ER High Resolution Digital B/W CCD Camera, B&B Microscopes Limited, Pittsburgh, Pennsylvania, USA). A Cermax® 300 W Xenon Arc lamp (PE300BF, PerkinElmer Optoelectronics, Fremont, California, USA) in the microscope was used as the excitation source (dry 40x NA 0.95 UPlanSAPO objective lens from Olympus). Image processing was performed by the image-acquisition software SimplePCI from Compix Inc (Sewickley, Pennsylvania, USA). A fluorescence cube (DAPI EX D350/50X BS400 EM460/50) filter was used for the experiments, exposing a 40x selected area with the xenon lamp. Transmittance spectra of the excitation and emission filters were used in the photobleaching experiment.

Luminescence Imaging of Hepatic Tumors. The luminescence of Eu-G3P4A18N (300 μL of a 60 μM solution in 10% DMSO/H_2O) was captured while selectively associating with the liver tumors. The imaging system used to detect the luminescence of the dendrimer is custom -made, combining either an Andor DU 434-BR-DD CCD camera (Andor Technology; South Windsor, Connecticut, USA) or a Rolera XR fast digital CCD camera (QImaging, Surrey, Canada) fitted with a 50 mm AF Nikkor lens containing a minimum aperture of F16 and maximum aperture of

F1.4. The emission filter used was 610/30 nm (Chroma Technologies, Bellows Falls, Vermont, USA). The rat livers were excited using four 450 nm emitting 5 Watt LEDs (Lumileds Lighting, San Jose, California, USA). Qcapture software (QImaging, Surrey, Canada) was used for the data acquisition.

Histopathology of Liver Tumor Sections. Tissue sections (10 microns) from dendrimer-infused livers were also processed for immunohistochemistry staining. Tissues were fixed with 2% paraformaldehyde for 2 hours at 4 °C, and then left overnight in 30% sucrose at 4 °C. The samples were frozen in a liquid nitrogen-cooled bath of 2-methyl-butane and cryosectioned. Sections were labeled with monoclonal CD31 (ABR MA1-26196) and Alexa Fluor 647 phalloidin (Invitrogen A22287). The application of goat antimouse Cy3 secondary antibody for CD31 and DAPI followed. Images were then taken on an Olympus FV1000 confocal microscope.

9.5 RESULTS

Establishment of Rat Liver Metastasis Model with Syngeneic Rat Colon Carcinoma Cells. We established the CC531 colorectal rat metastasis model in our laboratory to have a relevant animal model in which to study imaging of hepatic metastasis. A rat model (WAG/RijHsd) was established for investigating the production of hepatic metastases by CC531 syngeneic rat colon carcinoma cells. Rats were anesthetized, the abdomens were opened, and then CC531 cells (2×10^6) suspended in 0.2 mL of phosphate-buffered saline (PBS) were directly injected into the

spleen. Over 2-4 weeks after intrasplenic injection of CC531 cells, the rats were inspected by midline incision. The tumors in the liver reached 1-2 mm in diameter 4 weeks after intrasplenic injection (Figure 9-1).

Photostability of Eu-G3P418N. Due to the presence of the lanthanide cations, the luminescent compound is predicted to be resistant to photobleaching. To examine this possibility, the fluorescence from the 1,8-naphthalimide derivative was monitored as a function of time upon exposure to excitation light (Figure 9-4, D). In the absence of Eu^{3+} the signal intensity increased for the first 30 seconds but gradually decreased for the remainder of the experiment. This behavior indicates that the complex is subject to photobleaching. However, the photophysical properties of Eu-G3P4A18N dendrimer are different (Figure 9-4, D). In the presence of Eu^{3+} the signal intensity increased during the first 30 seconds, continuously increased and then maintained at a constant value. These data suggest that Eu^{3+} appears to stabilize the 32 1,8-naphthalimide chromophores against photobleaching.

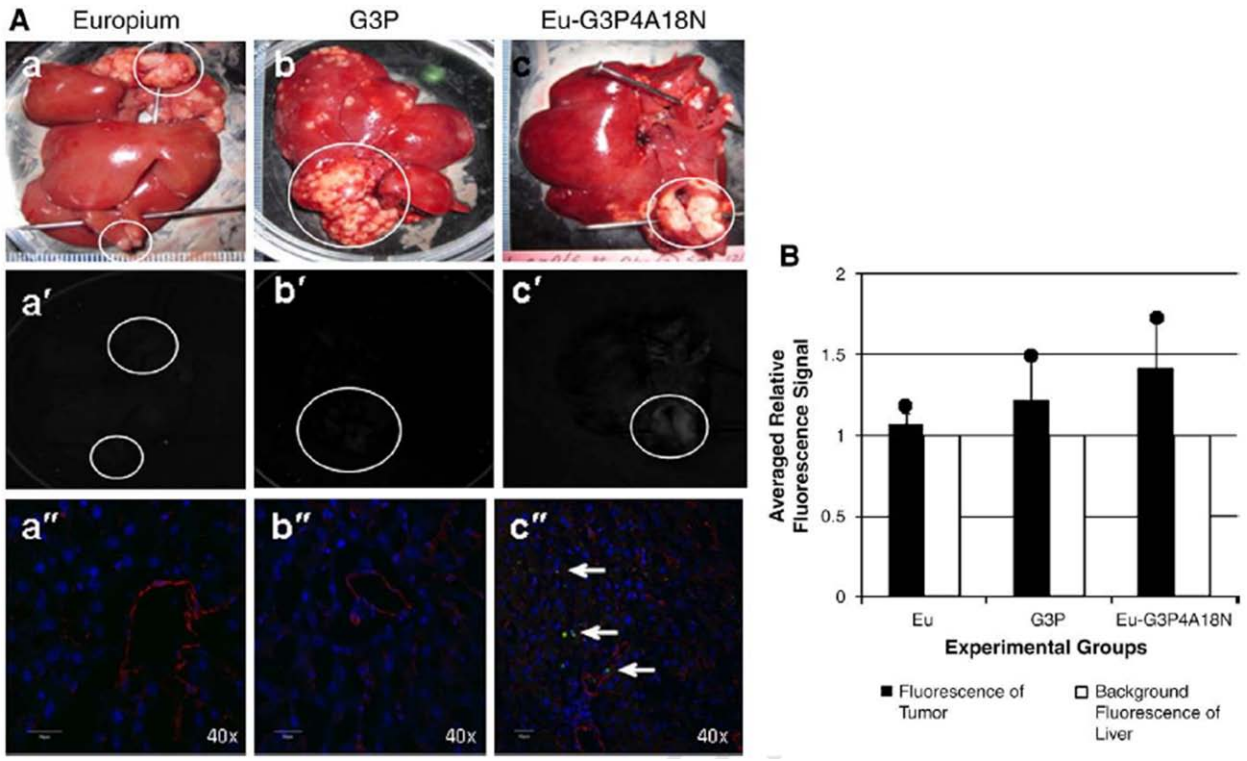

Figure 9-5. In vivo cannulation with Eu^{3+}, G3P and Eu-G3P4A18N with luminescence imaging and analysis. (A) Gross photographs, luminescence and confocal microscopic images at 40x magnification of the livers containing tumors (circles) that were injected in the spleen 15 - 20 days prior to infusion and excised at 0 h time point. Photos (a), (a′) and (a″) were from infusion of Eu^{3+} only at 0 h. Photos (b), (b′) and (b″) were from infusion of G3P (non - functionalized dendrimer without Eu^{3+}) and at 0 h. Photos (c), (c′) and (c″) were from liver infused with Eu - G3P4A18N at 0 h. Arrows show the luminescence of Eu-G3P4A18N in the confocal microscopic images in photo (c″). (B) Average tumor luminescence was corrected for background autofluorescence in the resulting graph. Two rats per each experimental group were used.

Multiple Tumor Imaging with Eu-G3P4A18N. Multiple metastatic tumor nodules were generated in a rat liver via a splenic injection of CC531 colorectal cancer cells. After infusion of Eu-G3P4A18N via the GDA cannulation technique, the rat liver was excised and imaged by luminescence. Figure 9-5, A shows the gross and corresponding luminescence images of ex vivo livers after being infused with a volume of 300 μL of a 60 μM solution of Eu^{3+} only, generation 3 PAMAM (G3P) dendrimer only, or Eu-G3P4A18N in 10% DMSO/H_2O (Figure 9-5, A a-c and a′-c′). To identify the luminescent signal in the liver and tumor tissue, tissue slices were examined with a confocal microscope (Figure 9-5, A a″-c″). Photograph (a) describes a control liver that was infused with Eu^{3+} (europium only) and showed no luminescence in any of the corresponding photographs (a′ or a″). Photograph (b) shows another control liver that was infused with G3P dendrimer and very little to no luminescence was observed in either photograph (b′) or (b″). Photograph (c) shows the experimental liver that was infused with Eu-G3P4A18N and does show luminescence to be present in the corresponding tumors in photograph (c′) and (c″). Figure 9-5, B shows the relative fluorescence signal that was observed in all three experiments. It demonstrates that the luminescence in the Eu-G3P4A18N-infused liver was brighter than that of the controls. Although the fluorescence signal does not penetrate through all the tissue, our data demonstrate that the metastatic nodules display a more intense luminescence signal than either the background or the controls after infusion with Eu-G3P4A18N.

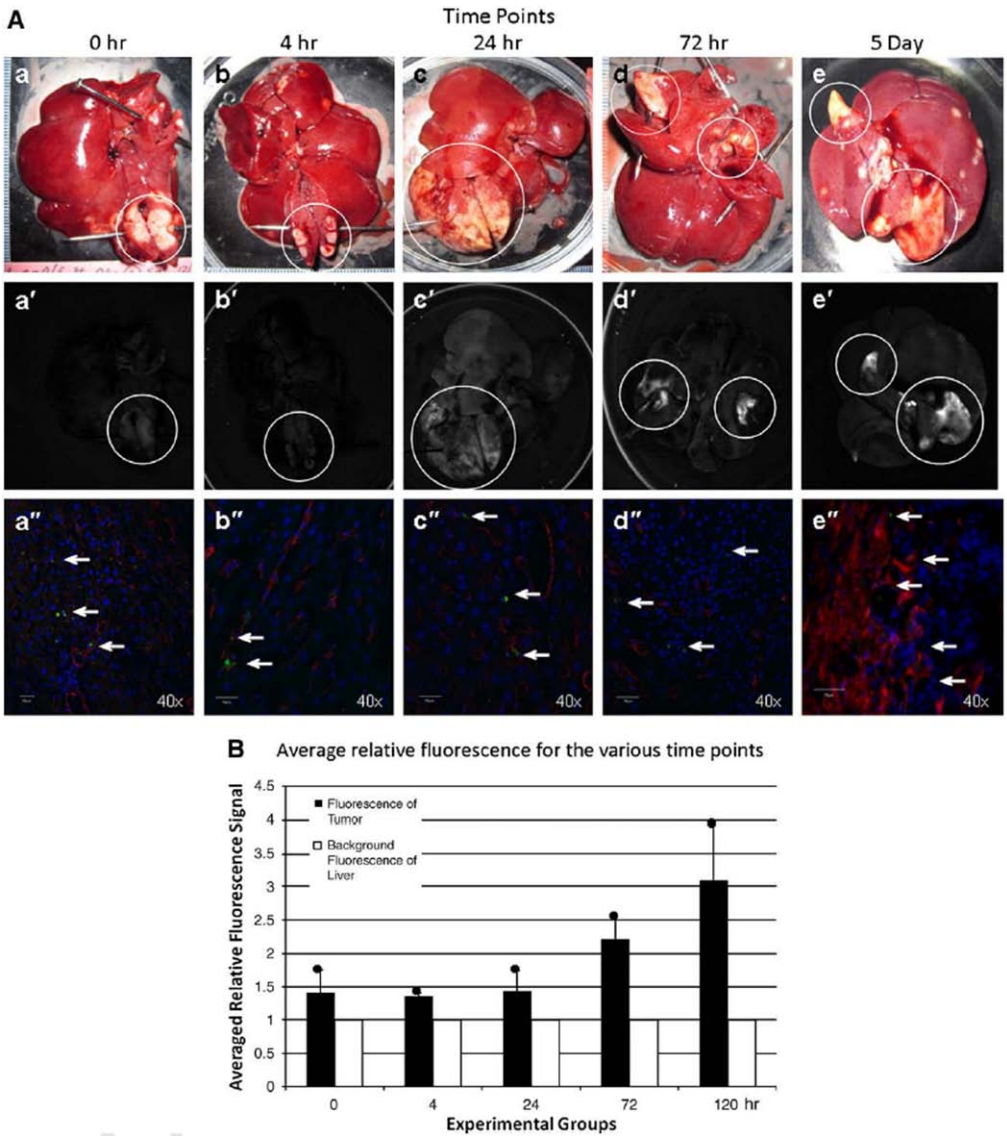

Figure 9-6. In vivo hepatic infusions with Eu-G3P4A18N over several time points with analysis of the tumor luminescence. (A) Gross photographs of the livers containing tumors (circles) that were injected in the spleen 15 – 20 days before infusion of Eu-G3P4A18N and excised at 0 h, 4 h, 24 h, 72 h and 5 day time points (a – e). Images (a′ – e′) were from the same liver and tumor tissue and same hepatic infusions with Eu-G3P4A18N under fluorescence imaging displaying grossly the tumor luminescence. In addition, 40x magnifications of confocal microscopic images (a″ - e″) were also obtained from the same liver and tumor tissue and same corresponding time points displaying luminescence signaling in all time points (arrows). (B) Average signals obtained from the tumors were compared to that of tissue autofluorescence and displayed in the resulting graph. Two rats per each experimental group were used.

Retention Time of the Eu-G3P4A18N in Tumors. To determine the retention time of the dendrimer in the tumor post infusion, rats were injected intrahepatically via the GDA with Eu-G3P4A18N and sacrificed at the following time points: 0 hour, 4 hours, 24 hours, 72 hours and 5 days (Figure 9-6, A). Sustained luminescence signals from the tumors were observed at all time points post infusion as well as an increase in luminescence signal intensity over time (Figure 9-6, A a′ - e′). The corresponding confocal microscopic images, which identified the Eu-G3P4A18N in the liver and tumor tissue, also demonstrate the uptake of the Eu-G3P4A18N in the hepatic nodules (Figure 9-6, A a″ - e″). Background autofluorescence of the liver was accounted for and the resulting bar graph (Figure 9-6, B) demonstrates that luminescence signals from the tumors were present up to 5 days post infusion with Eu-G3P4A18N. It also describes a correlation between signal intensity and time.

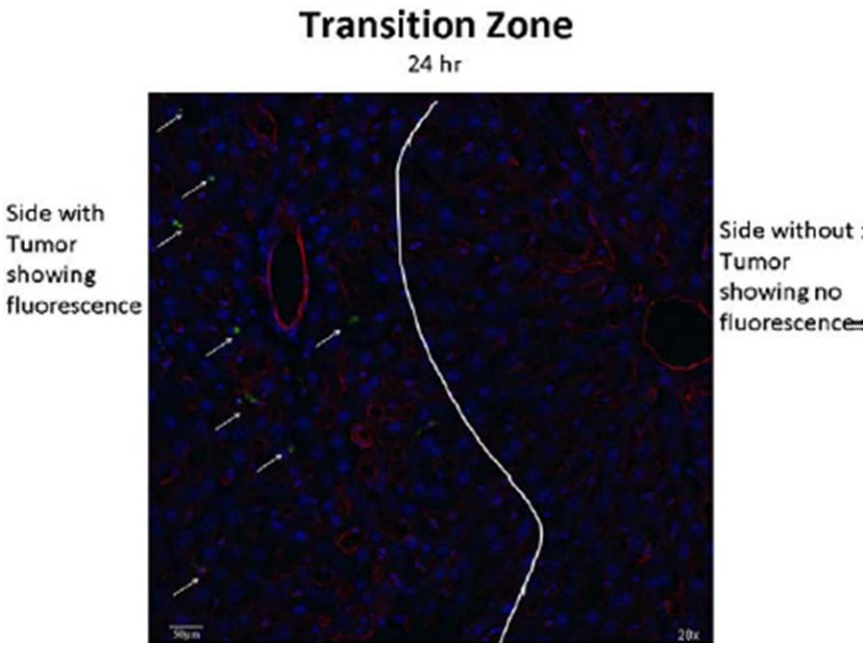

Figure 9-7. Transition zone between normal liver and tumor. A 20× confocal microscopic image of a rat liver containing a metastatic tumor that was infused with Eu-G3P4A18N, and the liver was excised 24 h later. The transition zone between the healthy normal liver (right of the white line) and the tumor (left of the white line) is seen. The arrows point to the green luminescence given off from the Eu-G3P4A18N itself, and it is not seen on the healthy liver side.

Selective Tumor Targeting by Eu-G3P4A18N. Confocal microscopy helps to identify the location that the Eu-G3P4A18N targets. Figure 9-7 demonstrates, in a 20× magnified confocal microscopic image, that the uptake of Eu-G3P4A18N is apparent on the tumor section of a liver (left of the white line) and not found in the normal liver parenchyma (right of the white line) 24 hours after it was infused. The luminescence of the Eu-G3P4A18N is depicted by the arrows and to the left of the white line.

9.6 DISCUSSION

We have demonstrated, by way of cannulating the GDA, that we can deliver a novel PAMAM dendrimer targeting system into the livers of rats. We have been able to use a clinically relevant colorectal metastases model, and through isolated hepatic perfusion, have localized the tumors by way of luminescence imaging. We have taken advantage of a disorganized tumor vasculature and been able to deliver our approximately 3 nm sized dendrimer through the widened interendothelial junctions and fenestra that range from 400 to 800 nm in size,[278] since tumor vasculature is "leaky" and allows larger molecules to extravasate the vascular endothelium into the extravascular space and in the process bypass normal liver parenchyma. The relatively small size of our dendrimer[279] facilitates its exit through the fenestra and allows it to be trapped in the extravascular spaces of the tumor. The confocal microscopy observations are consistent with the hypothesis that Eu-G3P4A18N has increased extravasation from the leaky tumor vasculature and, therefore, is more likely to be trapped in the perivascular spaces of the tumor. This is believed to provide us with the immediate luminescence that is observed at the 0 hour time point. However, it is also observed that an accumulation or an increase of luminescence intensity is seen after 24 hours. This probably could be due to a movement of Eu-G3P4A18N from the immediate perivascular space into more distal areas of the tumor.

Metastasis to the liver from colorectal cancer is what decreases survival rates and is therefore an appropriate focus for therapeutic strategies requiring hepatic infusion. Any animal model designed to study hepatic infusion must mimic the clinical setting through (1) employing

an adenocarcinoma cell type, (2) using vascular access, which is used in the clinical setting of RTs, and (3) being able to undergo multiple surgeries. An additional advantage of this model is that the CC531 rat tumor model has been used for studies that include TACE and laser-induced therapy for treatment of liver metastases but used a subcapsular tumor cell injection in contrast with the splenic injection technique described. Splenic injections and metastases to the liver provide for better imaging applications to be studied and more important, it is a better clinical model. The combination of the hepatic colorectal metastatic model and the GDA cannulation technique provides a model that reflects isolated hepatic perfusion performed on humans[258,280] and can also be implemented to study treatments that include hyperthermia combined with chemotherapeutics. Treatments that are currently in place for hepatic metastatic disease have led to only slight improvement in survival rates over the years, but that result has only come from using different combinations of regional chemotherapies, surgical resection, RFA or isolated hepatic perfusion. These treatments can be enhanced to become more effective clinically when combined with new innovative treatment strategies that are currently under way in the laboratory setting.

Polyamidoamine (PAMAM) dendrimers are biocompatible,[275] nonimmunogenic,[276] and water soluble and have been attached to metals,[260,274] as well as many biological molecules such as antibodies, synthetic drugs and small molecules.[272,273,281] Previous studies reveal that dendrimers can be used as multifunctional carriers capable of combining targeted drug delivery and imaging in pharmaceutical applications.[271,282] In this study we introduced the use of novel dendrimers that incorporate a core constituted of generation 3 PAMAM with terminal branch modifications. Europium ions are incorporated into the dendrimer to stabilize it for its use as an imaging agent. The dendrimer compounds provide improved detection in biological media

because of their near infrared (NIR) emission (lower autofluorescence in this energy domain). Biological tissues do not have significant NIR luminescence. Therefore, use of NIR eliminates background fluorescence, one of the most important issues for biological imaging. However, the disadvantage of this approach is that fluorescent signal does not penetrate through all the tissue and therefore is not quantitative.

9.7 CONCLUSIONS

Our studies demonstrate that our modified dendrimer preferentially accumulated in metastatic tumors and had a long retention time. In future studies we will take advantage of these observations for developing a novel nanotechnology therapy in combination with conventional therapy. As an example, we believe that this dendrimer can serve as a target for a noninvasive low-power radiofrequency (RF) field that in turn releases heat to generate localized hyperthermia. This idea is based on previous observations that europium ion-cored dendrimers are excellent conductors of electrical and thermal energy and can be used as thermal conductors of noninvasive low-power radiofrequency ablation to generate hyperthermia. Previous studies reveal that hyperthermia acts synergistically with ionizing radiation,[283-285] with several chemotherapeutic agents,[286-288] and with various cytokines.[289-291] We believe that the multimodality approach with hyperthermia + radiation + chemotherapeutic agent + cytokine will improve the treatment for metastasized hepatic colorectal cancer.

To drive clinical improvements further, investigation of mechanisms of TACE therapy can be better understood using our animal model. Radiofrequency ablation using a probe inserted

into the liver has a role in the therapy for liver metastasis. However, it can potentially play a larger role based on the animal model described here. This treatment would avoid surgery altogether as described by Gannon et al.[292,293] Tumor targeting is a problem for most researchers, but it, too, can be investigated closely in the animal model. The importance of a reliable tumor model system, coupled with an unambiguous method for isolated perfusion that mimics the clinical setting, is the enabling of preclinical development and the evaluation of new approaches and technologies for regional therapies. This preclinical development will result in facile translation for positive clinical impact for patients with hepatic metastases of colorectal cancer.

Acknowledgments

The authors thank Per Basse,M.D., Ph.D., DMSci for making available the CC531 colorectal cancer cells.

10.0 IN VIVO TUMOR TARGETING AND IMAGING BY FUNCTIONALIZED LUMINESCENT DENDRIMER LANTHANIDE COMPLEXES

10.1 CHAPTER PREFACE

The aim of this work was to describe more fully the biologic application presented in the previous chapter. Specifically, we used the same Eu^{3+} dendrimer with amine modified 1,8-naphthalimide sensitizers as a luminescent marker in a rat liver model. In collaboration with researchers at the Hillman Cancer Center, we expanded our project to include a more rigorous spectroscopic characterization of the luminescent dendrimer system. The tumors in this work were grown by both implantation and splenic injection methods which allowed us to compare the ability of our luminescent lanthanide dendrimer to report on the location of tumors across a broader range of environments. The material contained in this chapter has been organized for publication as a full paper that has been submitted for publication and is currently under revision.

List of authors: Marco A. Alcala, Chad M. Shade, Hyounsoo Uh, Shu Ying Kwan, Matthias Bischof, Zachary P. Thompson, Kristy A. Gogick, David L. Bartlett, Ruth A. Modzelewski, Yong J. Lee, Stéphane Petoud, Charles Komen Brown

Author contribution: The author of this dissertation was responsible for the photophysical characterization of the complex including absorption and fluorescence excitation and emission profiles, overall luminescence quantum yield, Eu^{3+}-centered luminescence lifetimes, collecting the photo-stability measurements on a UV/Vis spectrometer, assisting with surgical procedures and fluorescence macroscopy experiments with whole animals, providing interpretation of the results and contributing to the preparation of the manuscript.

10.2 ABSTRACT

We have created a novel dendrimer complex suitable for liver tumor targeting and luminescence imaging by substituting thirty-two naphthalimide fluorophores on the surface of the dendrimer and incorporating eight europium cations within the branches. We demonstrate the utility and performance of this luminescent dendrimer complex to detect hepatic tumors generated via direct subcapsular implantation or via splenic injections of colorectal cancer cells (CC531) into WAG/RijHsd rats. Luminescence imaging of the tumors after injection of the dendrimer complex via hepatic arterial infusion revealed that the dendrimer complex can target liver tumors specifically. Further investigation indicated that dendrimer luminescence in hepatic tumors persisted *in vivo*. Due to the incorporation of lanthanide cations, this luminescence agent presents a strong resistance against photobleaching. These studies show the dendrimer complex has great potential to serve as an innovative targeting and imaging agent for the detection of metastatic tumors in our rat hepatic model.

10.3 INTRODUCTION

Approximately one-third to one-half of the 150,000 Americans diagnosed with colorectal cancer (CRC) each year[2] will develop hepatic metastasis, and only about 20% of these patients are operable. The five-year survival rate for patients with liver metastasis without treatment is only 5%.[1] Current therapies for treating metastatic lesions include local tumor ablation (i.e., radiofrequency ablation, cryotherapy or direct injection of alcohol or acetic acid directly into the metastatic lesions)[261], transarterial chemoembolization (TACE)[188], embolization with radioactive microspheres, surgical resection and/or systemic therapy consisting of chemotherapeutic and biological agents[258]. While all of these strategies can be used to treat hepatic malignancies, some are surgically invasive and others are associated with significant systemic toxicity due to lack of tumor-specific targeting. However, the attainment of a tumor-specific agent that maximizes treatment efficacy while minimizing systemic toxicity remains a difficult feat in cancer therapeutics.

One of our aims is to target with high specificity and image liver tumors in colorectal liver metastases with *in vivo* and *ex vivo* WAG/RijHsd rat models. A main requirement to achieve the goal of targeting and evidencing liver metastasis is the creation of a luminescent reporter that will allow for the specific targeting of this type of tumor and which will emit a stable luminescence signal that can be easily discriminated from autofluorescence present in biological systems. In this study we have developed a nanoscale dendrimer that specifically targets tumors in a rat hepatic metastasis model and demonstrated its capacity to optically image liver tumors *in vivo*.

Dendrimers are discretely organized polymers whose versatility in the fields of drug-delivery, site-specific targeting and labeling have been the subject of many articles and reviews.

[18,208,294-298] Apart from the core of the dendrimer, the interior branches and surface functional groups offer two regions which can be manipulated in a versatile way to meet the needs of the designers, such as being functionalized to incorporate luminescent molecules. [299] As often observed with small organic fluorophores, photobleaching can be a strong limitation by leading to fluorescent signal decay thereby preventing their use for long-term or repetitive measurements in biological applications. Trivalent lanthanide cations such as europium (Eu^{3+}) offer a unique solution to curtail the effects of photobleaching. [300] In this work, we have attached luminescent moieties to the surface of the dendrimer through the end branches, leaving the internal sites available for the coordination of Eu^{3+}. We have observed that the luminescence located in the tumor was visible within seconds following hepatic arterial infusion of the dendrimer. This rapid visualization compares favorably with other fluorescent agents, such as pH sensitive fluorescent markers, [301] of which the incorporation may take hours in order to achieve observable fluorescence, or green fluorescent proteins (GFPs) and luciferase-based strategies, where there is also limited control over timing of genetic expression. In addition, luciferase-based strategies require tumor cells to express this gene prior to inducing tumors, a method that is not compatible with clinical studies. Moreover, small molecule fluorophores such as fluorescein and cyanine dyes tend to photobleach rapidly, thus limiting their usefulness in the diagnostic setting. In this paper, we demonstrate the unique luminescence stability of our newly reported dendrimer-lanthanide complex and its application in our WAG/RijHsd rat models.

10.4 EXPERIMENTAL

Synthesis and Spectroscopic Characterization of Eu-G3P4A18N. Eu-G3P4A18N was synthesized by adapting one of our current methods.[237] Amine-terminated G3 PAMAM dendrimer was functionalized with glycine-conjugated 4-amino-1,8-naphthalimide[277] by a standard amide coupling condition, followed by Eu^{3+} complexation. Characterization of the uncomplexed dendrimer was performed with ^{1}H-NMR and elemental analysis. Photobleaching properties and characterization of the Eu-G3P4A18N complex was performed with absorbance, luminescence excitation and emission, overall steady-state quantum yield.

Synthesis of Eu-G3P4A18N. Glycine-conjugated 4-amino-1,8-naphthalimide was synthesized by a reported method. [277] Glycine-conjugated 4-amino-1,8-naphthalimide was attached on the amine-terminated G3 PAMAM dendrimer by a standard amide coupling condition: 54.1 mg (2.00×10^{-4} mol) of glycine-naphthalimide conjugate was added to a solution of 29.4 mg (4.26×10^{-6} mol) of G3 PAMAM dendrimer (Dendritech Inc.; Midland, MI, USA) in 5 mL of DMF (Sigma-Aldrich; St. Louis, MO, USA). 92.1 mg (2.42×10^{-4} mol) of HATU (Aldrich; St. Louis, MO, USA) and 70 µL (52 mg; 4.0×10^{-4} mol) of DIPEA (Sigma-Aldrich; St. Louis, MO, USA) were added. The reaction mixture was stirred at room temperature for two days under nitrogen atmosphere while monitoring for the disappearance of G3 PAMAM dendrimer by TLC. The compound was purified by dialysis using a regenerated cellulose membrane (nominal MWCO 12,000-14,000; Fisher Scientific; Pittsburgh, PA, USA) in DMSO for three days. The solution recovered from the dialysis membrane was dried in a vacuum oven (40 °C, 50 mbar) to yield G3P4A18N as brown solid (52.5 mg, 82%). ^{1}H-NMR (300 MHz, DMSO-d_6): δ 8.54 p.p.m. (br s, 32 H), 8.32 (br s, 32 H), 8.15 (br s, 32 H), 8.10 (br s, 32 H), 7.90 (br s, 32 H), 7.76 (m, 28 H), 7.56 (br s, 32 H), 7.40 (br s, 64 H), 6.78 (br s, 32 H), 4.56 (br s, 64

H), 3.08 (m, 184 H), 2.61 (m, 120 H), 2.39 (m, 60 H), 2.16 (m, 120 H); analysis (% calcd, % found for $C_{750}H_{864}N_{186}O_{156}$·32DMSO·64$H_2O$): C (52.47, 51.74), H (6.40,6.29), N (13.98, 13.76). The Eu^{3+} complex of G3P4A18N (Eu-G3P4A18N) was synthesized by the following method adapted from one of our methods[237]: 22.67 mg (1.513×10^{-6} mol) of G3P4A18N was dissolved in 10 mL of DMSO. 647.5 µL of 18.7 mM $Eu(NO_3)_3$ solution in DMSO (1.21×10^{-5} mol) was added to the dendrimer solution. The mixture was diluted to 25.00 mL, incubated at room temperature for seven days. The resulting solution (conc. = 60.5 µM) was used as obtained.

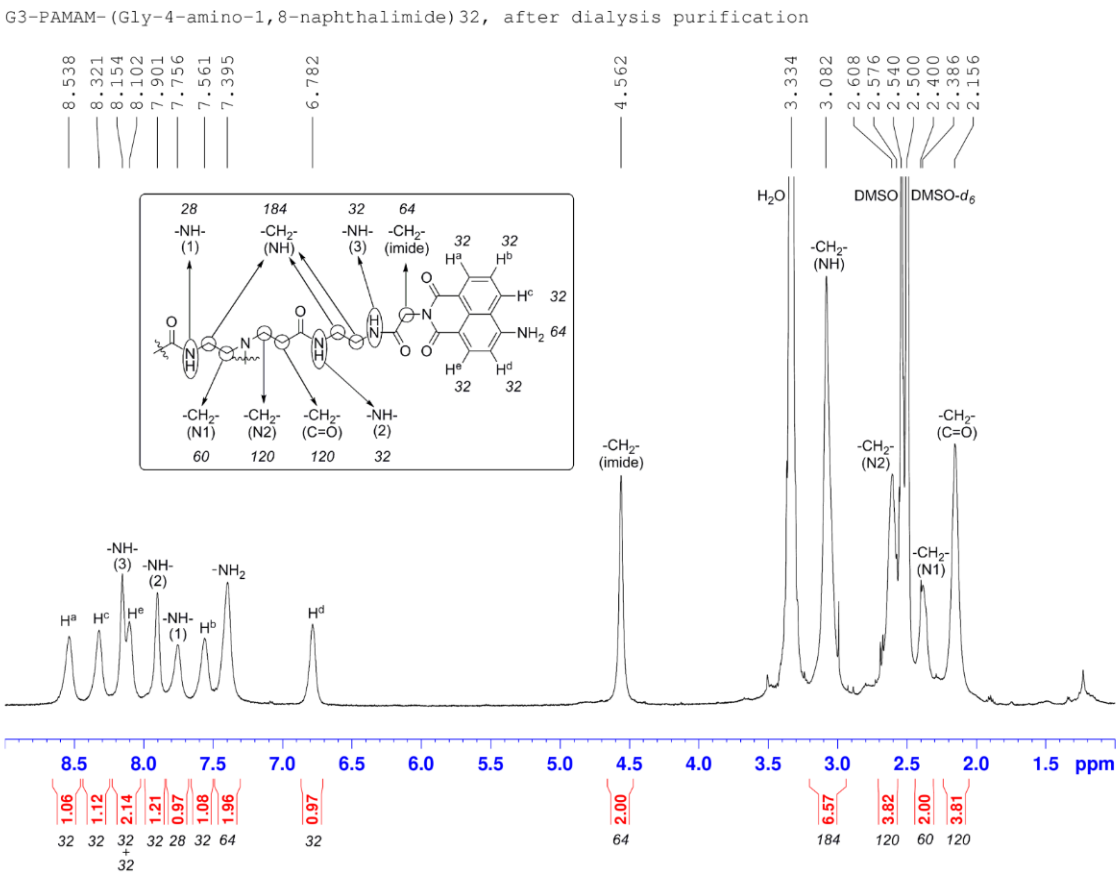

Figure 10-1. ^{1}H-NMR spectrum and peak assignment of G3P4A18N.

Spectroscopic Characterization of Eu-G3P4A18N. Absorption spectra were recorded on samples in a Perkin-Elmer Lambda 9 BX Spectrometer, coupled with a personal computer using software supplied by Perkin-Elmer (Waltham, MA, USA).

Steady-state emission and excitation spectra were analyzed using a modified Horiba Jobin Yvon Spex Fluorolog-322 Spectrofluorometer, coupled to a personal computer with software supplied by Horiba Jobin Yvon Inc. (Edison, NJ, USA). Emission and excitation spectra were corrected for the instrumental function. Samples were placed in 1 mm quartz fluorescence cells purchased from NSG Precision Cells, Inc. (Farmingdale, NY, USA).

For the photobleaching experiments, approximately 0.9 mL of each solution (0.2 μM in 30% DMSO/H_2O) was transferred into a 0.9 mL semimicro absorbance cuvette supplied by Varian (catalog number 66-100127-00). The cuvette was stoppered and parafilmed at the beginning of each trial to prevent solvent evaporation. Photobleaching was quantified with a Perkin-Elmer UV/Vis, collecting at 240 λ/nm scan rates. Samples were exposed to white light from the Xenon lamp of the Horiba Jobin Yvon Spex Fluorolog-322 Spectrofluorometer in-between scans. A water circulator was used to maintain constant room temperature (23 °C) within the fluorimeter during long periods of exposure.

For the quantum yield experiments, spectra were collected and analyzed using the Horiba Jobin Yvon Spex Fluorolog-322 fitted with an integrating sphere[203] using quartz tubes as sample holders. A 20 μM solution of Eu-G3P4A18N in 30% DMSO/H_2O was used for this analysis, and all spectra were corrected for the response of the lamp before integrating. Integrated values were used to determine the quantum yield by calculating the ratio of the photons into the sample to the photons emitted by the sample.

Animals. Four- to six-week-old male WAG/RijHsd rats were purchased from Harlan, Netherlands. Rats were fed ad libitum and maintained in environments with controlled temperature of 22 – 24 °C and 12 h light and dark cycles. All procedures involving the rats were in accordance with the Guide for the Care and Use of Laboratory Animals (National Research Council, 1996) and on a protocol approved by the Institutional Animal Care and Use Committee of the University of Pittsburgh.

Generation of Colorectal Metastasis by Single Tumor Implantation. While others have initiated colorectal metastasis by injecting cancer cells via the portal vein, superior mesenteric vein[269] or spleen[302], these approaches lead to small diffuse lesions, which are difficult to study[270]. We generated the isolated hepatic colorectal metastasis model by way of implanting CC531 tumor pieces into rat livers. Fourteen twenty-to-thirty-week-old WAG/RijHsd rats were anesthetized with a single intraperitoneal injection of 70 mg/kg of Ketamine (Bedford Labs; OH, USA) and 2.5 mg/kg of Acepromazine (Boehringer Ingleheim Vetmedica, Inc.; MO, USA). An intramuscular injection of 0.1 mg/kg of Buprenorphine (Bedford Labs; OH, USA) was also administered for analgesia prior to incision. Following midline incision, CC531 tumor nodules (1 × 2 mm weighing 25 mg) were implanted in the subcapsular area of the left lateral lobe (LLL) of the rat. These implanted tumor nodules were isolated from CC531 tumors grown hepatic implants in WAG/RijHsd rats. The tumors were placed about 5 mm deep to the subcapsular area of the LLL of the liver where it was easily found 20 – 30 days later when the rat underwent a second laparotomy for GDA cannulation and hepatic infusion of the Eu-G3P4A18N solution.

Cell Culture and Generation of Colorectal Metastasis by Splenic Injection. CC531 cell line is a moderately differentiated colon adenocarcinoma syngeneic to WAG/RijHsd rats. [303] Tumor cells were tested and found to be virus- and mycoplasma-free. CC531 cells were cultured in Dulbecco's modified eagle medium (DMEM) (Gibco; Grand Island, NY, USA) supplemented with 10% fetal bovine serum. Cells were maintained by serial passage. Tumor cells were harvested with a solution of 0.25% trypsin (Sigma; St. Louis, MO, USA), washed three times in 0.9% NaCl solution buffered with 1.4 mM phosphate (PBS) and adjusted to a suspension containing 2×10^6 viable (trypan blue exclusion test) tumor cells per 200 µL of PBS, which were

then injected into the spleen to generate metastatic tumor nodules in the liver. Metastatic lesions to the liver were revealed 20 – 25 days later after a midline incision was performed.

Luminescence Imaging of Hepatic Tumors. *In vivo* administration of the Eu-G3P4A18N (300μL of a 60 μM solution in 10%DMSO/H_2O) was captured as it was being infused and selectively associating with the liver tumor. The imaging system used to detect the luminescence of the dendrimer is custom-made, combining either a Andor DU 434-BR-DD cooled charge coupled device (CCD) camera (Andor Technology, South Windsor, Connecticut) or Rolera XR fast digital CCD camera (QImaging; Surrey, Canada) fitted with a 50 mm AF Nikkor lens containing a minimum aperture of F16 and maximum aperture of F1.4. The emission filters used were 610 / 30 nm and a 740 / 140 nm cutoff in wavelength (Chroma Technologies; VT, USA). The rat livers on living animals were excited using four, 5 Watt LEDs, emitting at 450 nm (Lumileds Lighting; CA, USA). Qcapture software (QImaging, Surrey, Canada) was used for the data acquisition.

Luminescence imaging of 10 μm tumor sections following hepatic arterial infusion of functionalized dendrimers was accomplished with an Olympus FV1000MPE multi photon laser-scanning unit fitted to an IX81 microscope (Olympus Corp.; Tokyo, Japan). Illumination for two-photon excitation at 820 nm was provided by a mode-locked Chameleon Ultra Ti:Sapphire laser (Coherent Inc.; Santa Clara, CA, USA). An Olympus 25x objective with N.A. of 1.05 was used to acquire images. Luminescence emission was collected with an external photomultiplier tube using a 570 – 625 nm bandpass filter. Scan resolution was set to 1024 × 1024 pixels at 4096 grey scales.

Histopathology of Liver Tumors Sections. Tissue sections (10 microns) from dendrimer-infused livers were also processed for routine hematoxylin and eosin (H&E) and immunohistochemistry staining. Tissues were fixed with 2% paraformaldehyde for 2 h at 4 °C, and then left overnight in 30% sucrose at 4 °C. The samples were frozen in a liquid nitrogen-cooled bath of 2-methyl-butane and cryosectioned. Sections were labeled with monoclonal CD31 (ABR MA1-26196) and Alexa Fluor 647 phalloidin (Invitrogen A22287). Goat anti mouse Cy3 secondary antibody for CD31 and DAPI followed. Images were then taken on the Olympus FV1000 confocal microscope.

10.5 RESULTS

Functionalized Dendrimer with Eu^{3+}. We have designed and synthesized a nanoscale dendrimer complex that achieves site-specificity requirements and tested its use in live animal imaging. The dendrimer provides a versatile organic framework to which multiple fluorophores have been covalently attached. Covalently attaching organic fluorophores to the surface of the dendrimer can drastically improve the stability of the association when compared to occupying the interior cavities and being secured by secondary interactions. As a luminescent moiety, we have chosen 4-amino-1,8-naphthalimide because the fully functionalized dendrimer is hypothesized to emit a significant amount of photons in the red/near-infrared region of the electromagnetic spectrum. Such emission wavelengths allow for sensitive detection due to the absence of native fluorescence of biological systems in this spectral region (improvement of the signal-to-noise ratio). Higher generation dendrimers have a greater number of terminal branches,

which correlates to the number of fluorophores which can be substituted on the surface of each dendrimer, thereby increasing the overall absorptivity and number of emitted photons per unit volume and further improving signal intensity.

By providing alternate routes of energy transfer with respect to photoreaction, luminescent lanthanide cations such as Eu^{3+} can partially depopulate the excited state(s) of fluorophores when the donor-acceptor energy levels are sufficiently matched, thereby preventing photobleaching mechanisms from occurring. Poly(amidoamine) dendrimers (PAMAM) contain numerous binding sites along the alternating amide bond architecture of their arms, a requirement for coordinating metal cations.[304] A lanthanide complex was based on a generation-3 PAMAM dendrimer (G3 PAMAM or G3P), capable of coordinating multiple Eu^{3+} cations within the interior. The thirty-two amino end branches of the generation-3 dendrimer were functionalized with 4-amino-1,8-naphthalimide fluorophores (4A18N) using glycine linkers to yield the functionalized dendrimer: generation-3-PAMAM-(glycine-4-amino-1,8-naphthalimide)$_{32}$ (G3P4A18N). The complete functionalization of each dendrimer branch was confirmed by ^{1}H-NMR and elemental analysis (see Experimental). Eight Eu^{3+}cations were coordinated within the branches to yield the Eu^{3+} complex Eu-G3P4A18N by following a procedure that we have previously developed for a dendrimer carrying different fluorophores.[237] We hypothesized that the increased photophysical stabilization provided by the polymetallic Eu^{3+} complex would permit longer exposure times and repeated measurements within the same experiment. The chemical structure of Eu-G3P4A18N is depicted in Figure 10-1*A*. Substitution of end branches is designated by “R”, defined in the lower right corner with glycine-conjugated 4A18N. The gray spheres indicate the hypothesized coordination of the lanthanide, Eu^{3+}, within the dendrimer nanocomplex.

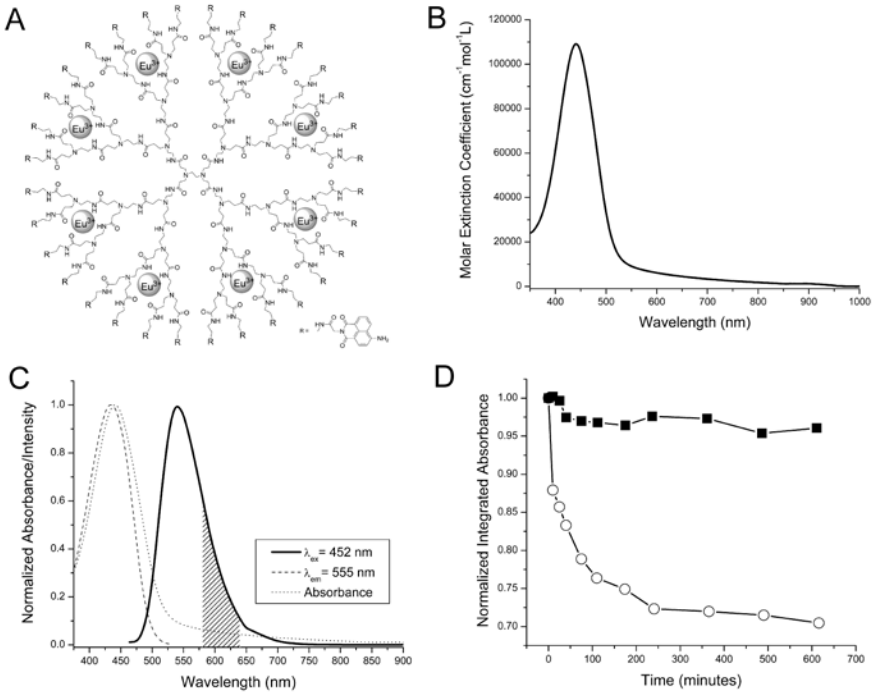

Figure 10-2. Structure, absorption and emission spectra and photobleaching analysis of dendrimer used in luminescence imaging. Generation-3 PAMAM dendrimer with Eu^{3+} (Eu-G3P4A18N) (*A*) The chemical structure of the Eu-G3P4A18N dendrimer. Substitution of the end branches is designated by R, glycine-conjugated 4-amino-1,8-naphthalimide (shown at the bottom right corner). The gray spheres indicate the hypothesized coordination of eight lanthanide cations (Eu^{3+}) within the dendrimer nanocomplex (modified dendrimer size approximately 3 nm). (*B*) The absorption spectrum displays a maximum at approximately 440 nm with a tail extending to significantly longer wavelengths, with extinction coefficients almost two times greater than Photofrin at 630 nm. (*C*) The luminescence emission spectrum displays a prominent band with an intensity maximum at 550 nm and a tail extending into the red/NIR part of the spectrum (solid line). The shaded area of the emission spectrum indicates the luminescence signal detected during the confocal microscopy experiments. A steady-state excitation spectrum (dashed line), collected upon monitoring the maximum intensity of the luminescence band (555 nm), overlaps significantly with the absorption spectrum (dotted line). (*D*) The absorbance of G3P4A18N was monitored as a function of time upon exposure to white light. In the absence of Eu^{3+} (open circle), the absorption decreased exponentially for the duration of the experiment, leading to an overall decrease approaching 30%. The trend observed in the presence of Eu^{3+} (filled square) was a modest decrease in absorbance during the first minutes, followed by an impressive level of stability for the same duration.

The absorption spectrum indicates an apparent maximum at approximately 440 nm; however, it is worth noting that the compound does absorb significantly at longer wavelengths with molar extinction coefficients almost two times greater than Photofrin at 630 nm[305] (Figure 10-2*B*). Absorption at longer wavelengths is attractive for biological imaging since photons at these wavelengths generate very little autofluorescence and since such photons are not harmful for biological systems, preventing any perturbation of the system to be monitored. The luminescence emission spectrum indicates the presence of a prominent broad band with a significant component in the red/NIR part of the electromagnetic spectrum (Figure 10-2*C*, solid line). The quantum yield of the compound upon excitation at 450 nm is 2.9 (±0.1)%. This value is relatively low, but the overall sensitivity provided by the imaging agent will be related to the number of emitted photons per unit of volume and, in this case, the small quantum yield will be compensated by the high density of luminescent 4-amino-1,8-naphthalimide groups.

When specific conditions are met, the electronic structures of lanthanide cations can stabilize the excited states of organic fluorophores against photobleaching (Figure 10-2*D*). To demonstrate this hypothesis, the absorbance from the 1,8-naphthalimide derivative was monitored as a function of time upon exposure to white excitation light. In the absence of Eu^{3+}, the absorbance of G3P4A18N decreased exponentially. This behavior indicates that the fluorophores are vulnerable to photobleaching. In the presence of Eu^{3+}, the absorbance of Eu-G3P4A18N indicates a modest decrease within the first hour of exposure to white light; however, the absorbance maintained constant values for the remainder of the experiment. The results are consistent with our hypothesis that the eight Eu^{3+} stabilize the electronic structure of the thirty-two 4-amino-1,8-naphthalimide fluorophores, preventing their photobleaching.

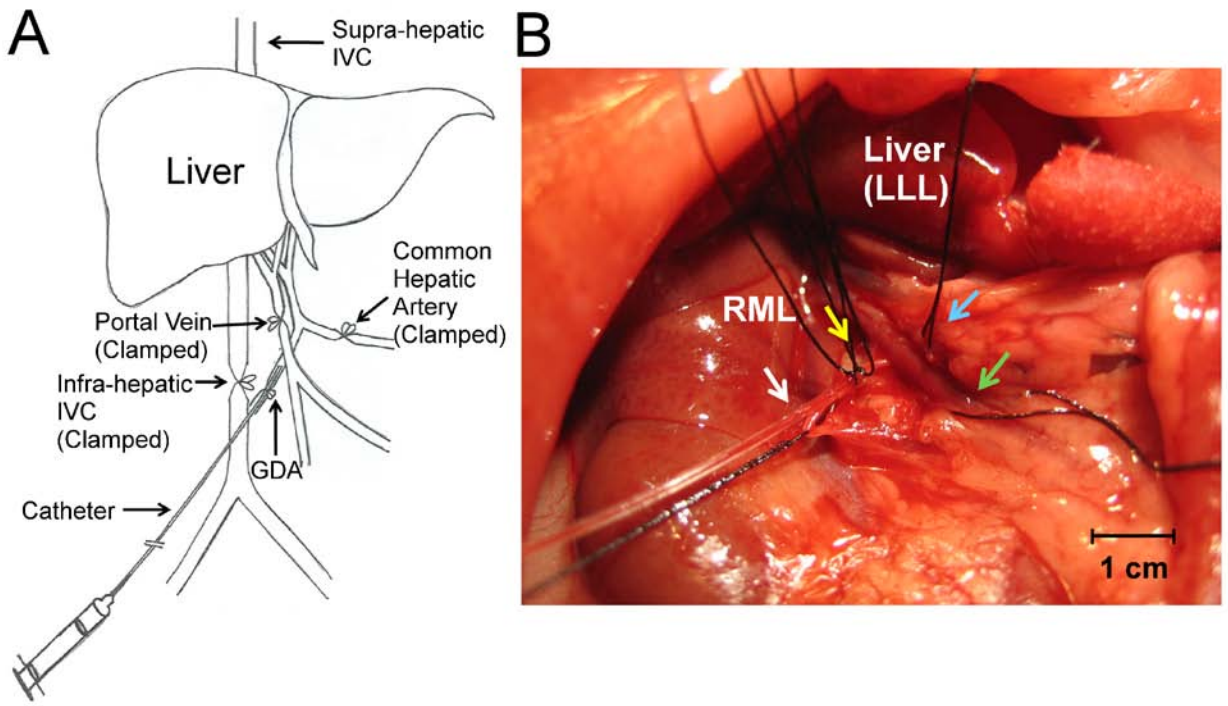

Figure 10-3. Cannulation of the gastroduodenal artery (GDA). (*A*) Diagram of the GDA cannulation illustrating isolation of the liver with clamping of the major vessels: portal vein, infra-hepatic inferior vena cava, and the common hepatic artery. The cannulation is indicated by a syringe and catheter leading into the site of the GDA. (*B*) A 1 mm polyethylene catheter was inserted into the GDA (white arrow) and then secured with two 6-0 silk ties (yellow arrow). The hepatic artery was isolated with a silk tie (blue arrow). The portal vein was also isolated using a silk tie (green arrow). The liver is shown above with the dome of the left lateral lobe (LLL) reflected at the top of the photo and the right medial lobe (RML) immediately to the left of the LLL. Liver is being shown in the anterior to posterior view.

Hepatic Arterial Infusion of Eu-G3P4A18N. Regional hepatic delivery of Eu-G3P4A18N was made possible by infusion via the gastroduodenal artery (GDA) of 160 – 330 gm WAG/RijHsd rats. This technique involves isolation of the vasculature of the liver by clamping closed the common hepatic artery, portal vein and infra-hepatic inferior vena cava (Figure 10-3*A*). A polyethylene 10 (PE-10) catheter was inserted retrograde into the GDA for a length of approximately 4 mm and secured with two 6-0 silk sutures (Figure 10-3*B*). Infusion of 7 mL of 100 units/mL of heparinized normal saline was made into the GDA of a live WAG/RijHsd rat to temporarily evacuate the hepatic blood volume prior to delivery of the functionalized dendrimer complex. To demonstrate its tumor targeting specificity, Eu-G3P4A18N (0.8 μg/g total body weight) was infused through the GDA followed by 5 mL of normal saline to ensure full distribution of the dendrimer into the liver. The liver was excised following infusion to evaluate the luminescence signal emitted by the Eu-G3P4A18N in the tumor and the background liver parenchyma.

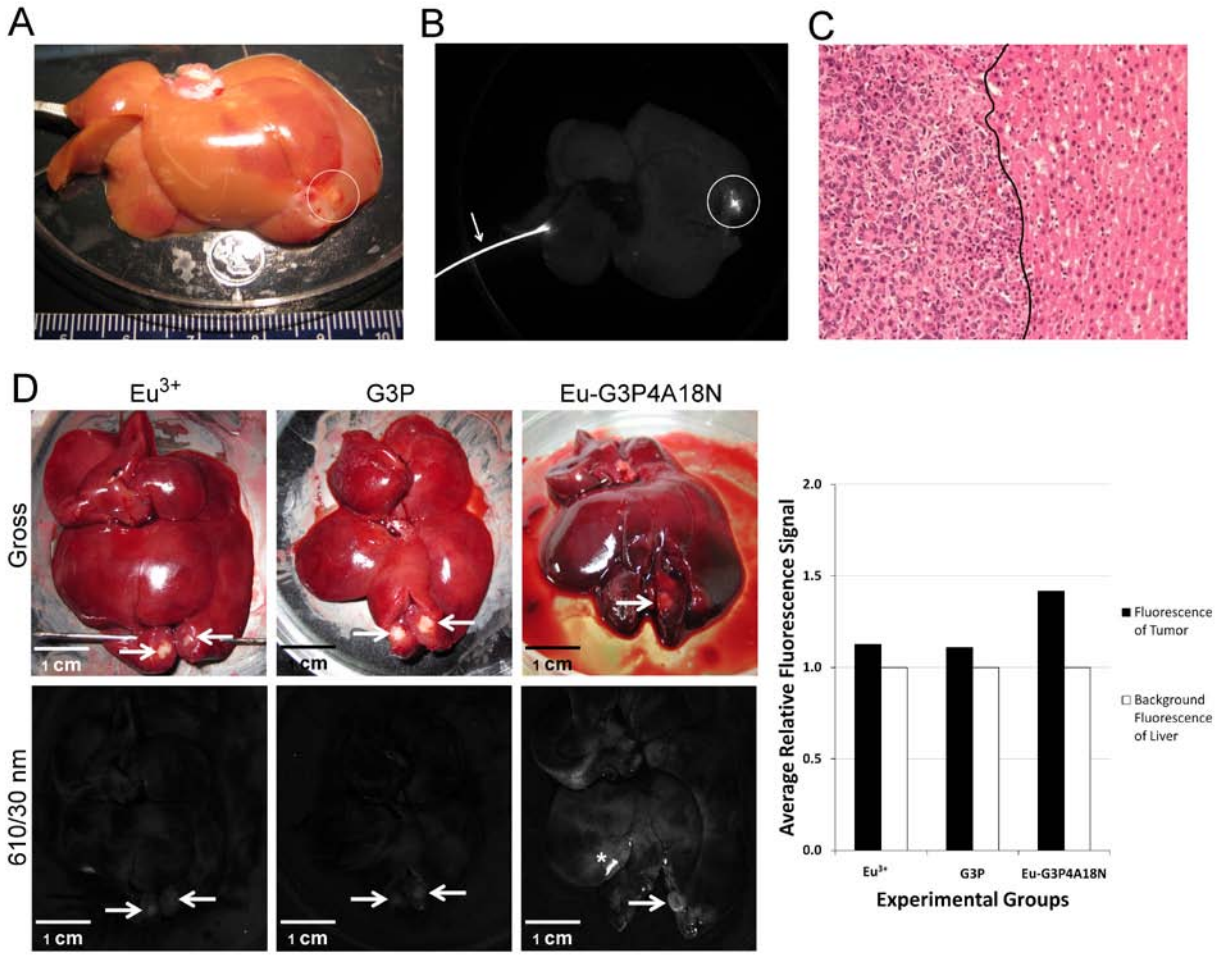

Figure 10-4. A cannulated *ex vivo* liver infused with Eu^{3+}, G3P or Eu-G3P4A18N with luminescence imaging and analysis. (*A*) White light image of an *ex vivo* liver with an established tumor implant. The white circle indicates the location of the tumor within the liver. (*B*) Luminescence image of liver after Eu-G3P4A18N infusion with an excitation wavelength of 450 nm and emission filter of 610 nm with a 30 nm bandpass. The circle shows the luminescence emitted by the tumor area only seconds after infusion of Eu-G3P4A18N. (*C*) 20x, H&E stained section of the tumor from the same liver showing the transition zone between adenocarcinoma on the left and normal liver parenchyma on the right of the solid black line. (*D*) Gross photographs (top row) and luminescence images (bottom row) of the livers containing tumors (arrows) that were implanted 20 – 30 days prior to infusion and excised at 0 h time point. Images are from liver infused with Eu^{3+} only (first column), G3P (non-functionalized dendrimer without Eu^{3+}; second column) or Eu-G3P4A18N (third column). Average tumor luminescence was corrected for background autofluorescence in the resulting graph. Asterisks represent specular reflection of the liver. Scale bars represent 1 cm.

***Ex vivo* Imaging of Eu-G3P4A18N Infusion**. Imaging of *ex vivo* rat livers demonstrated that high-intensity luminescence was evident in the tumors only seconds following an *ex vivo* Eu-G3P4A18N infusion (Figure 10-4*A, B*) when observing emission signal at 610 nm and 740 nm. Although there were some minor uptakes by the non-tumorous portion of the liver, these background signals were negligible in the red/NIR range of imaging. In animals with extra-hepatic intra-abdominal tumor deposits, no luminescence was observed in these tissues (data not shown). To confirm that Eu-G3P4A18N enhancement is occurring specifically in the tumor tissues, histological evaluation of the luminescent foci demonstrated that they were adenocarcinomas (Figure 10-4*C*).

To verify that only Eu-G3P4A18N has the capacity labeling tumors in the liver, rat livers were infused *in vivo* with Eu^{3+} cations only, dendrimers without Eu^{3+} and naphthalimide (G3P), or Eu-G3P4A18N. Figure 10-4*D* demonstrates the gross and luminescence images of the livers infused with the three different molecules or cations. The Eu^{3+}-only infusion and the dendrimer-only infusion both show minimal or no luminescence arising from the tumor when compared to the tissue autofluorescence. However, intrahepatic Eu-G3P4A18N infusion demonstrated specific higher-intensity luminescence in the tumor. These data are represented quantitatively in Figure 10-4*D.*

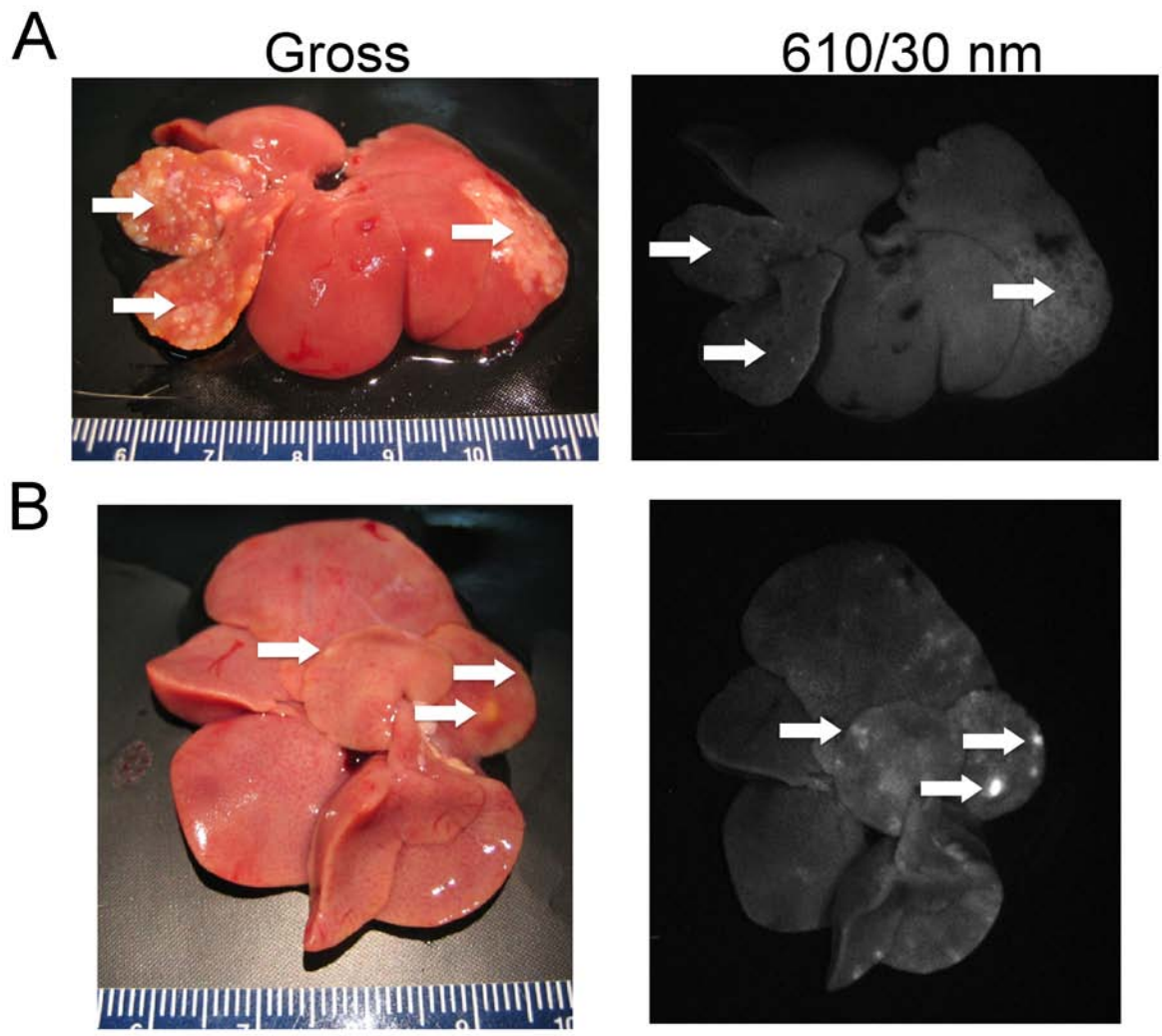

Figure 10-5. Colorectal metastasis to the liver (*A*) without and (*B*) with infusion of Eu-G3P4A18N. (*A*) Arrows show tumor nodules in the liver of a rat generated after a splenic injection of CC531 tumor cells. No dendrimer was infused into this liver. The second image shows the absence of luminescence in the nodules. (*B*) Arrows show metastatic lesions in another liver of a rat from a splenic injection of CC531 tumor cells. The liver was infused with Eu-G3P4A18N (300 µL of a 60 µM solution in 10%DMSO/H_2O). Luminescence image were taken with a CCD camera (excitation light of 450 nm and emission filter of 610 nm with a 30 nm bandpass filter).

Multiple Tumor Imaging with Eu-G3P4A18N. Multiple metastatic tumor nodules were generated in a rat liver via a splenic injection of CC531 colorectal cancer cells. After infusion of Eu-G3P4A18N, the rat liver was excised and imaged by luminescence. Figure 10-5*A* shows the gross and corresponding luminescence photographs of an *ex vivo* liver. This liver was used as a control and was not infused with the dendrimer complex to demonstrate that the metastatic tumor nodules themselves have minimal native fluorescence within the spectral region of detection (595 to 625 nm). Figure 10-5*B* presents the gross and corresponding luminescence photographs of another *ex vivo* rat liver with metastatic lesions. The metastatic nodules display a more intense luminescence signal than the background after infusion of Eu-G3P4A18N.

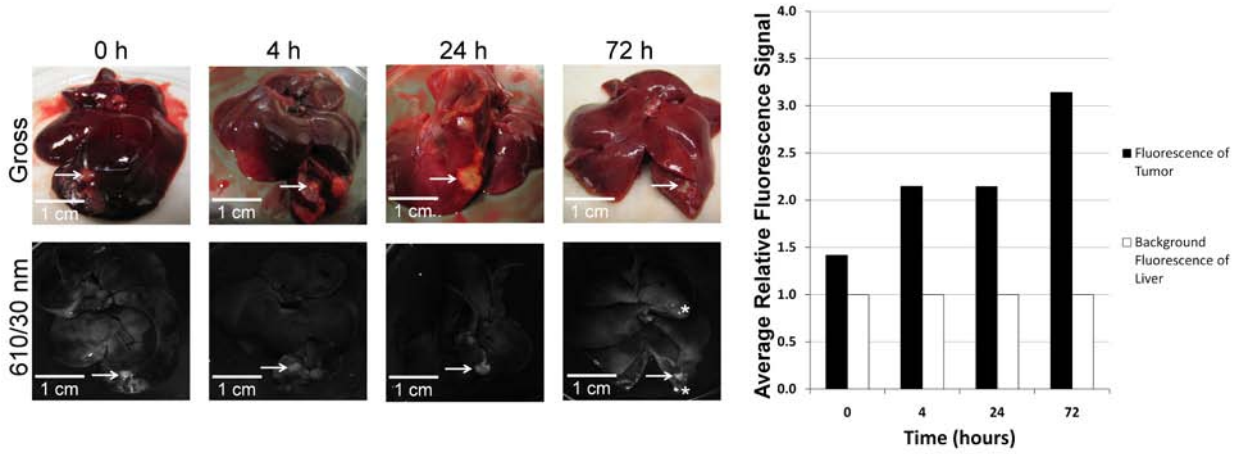

Figure 10-6. Gross and luminescent photographs of tumors in the livers of rats with analysis of the tumor luminescence. Gross (top row) and luminescent (bottom row) images of the livers containing tumors (arrows) that were implanted 20 – 30 days prior to infusion and excised at 0 h, 4 h, 24 h and 72 h time points after hepatic infusion with Eu-G3P4A18N. Average signals obtained from the tumors were compared to that of tissue autofluorescence and displayed in the resulting graph. Asterisks represent specular reflection. Scale bars represent 1 cm.

Retention Time of the Eu-G3P4A18N in Tumors. To determine the retention time of the dendrimer in the tumor post infusion, rats were injected intrahepatically with Eu-G3P4A18N and sacrificed at the following time points: 0 h, 4 h, 24 h, and 72 h (Figure 10-6). Sustained luminescence signals from the tumors were observed at all time points post infusion. Background autofluorescence of the liver was accounted for and the resulting bar graph (Figure 10-6) demonstrates quantitatively that signals from the tumors were present up to 72 h post injection.

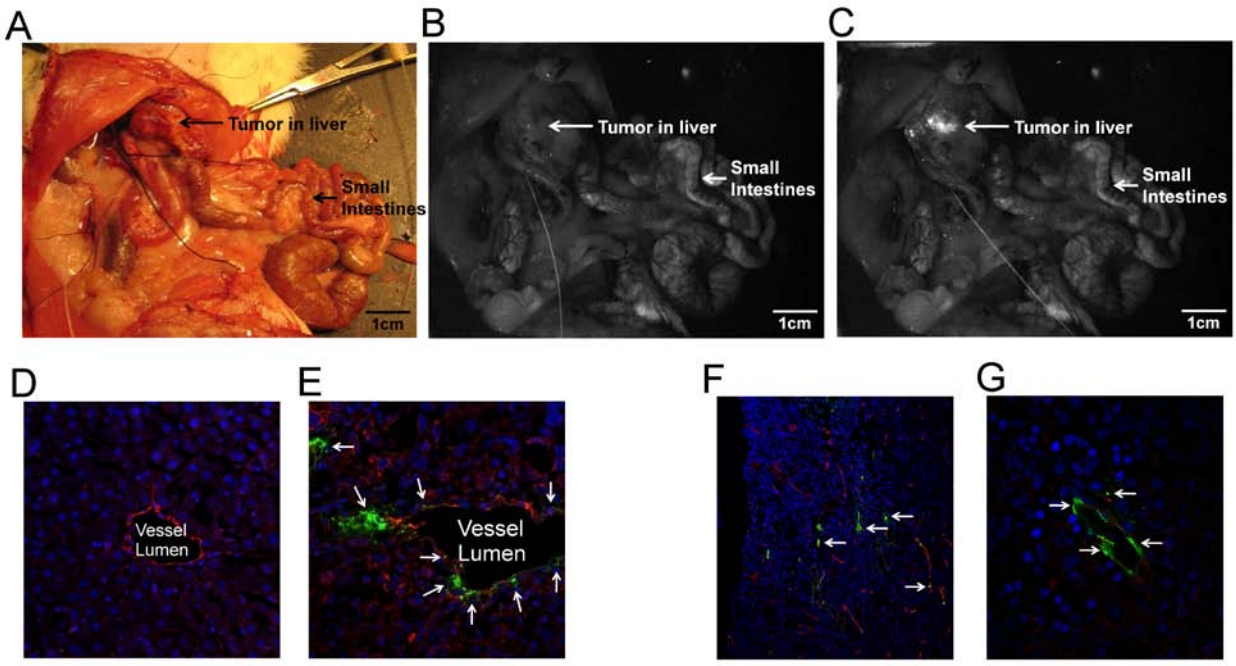

Figure 10-7. *In vivo* colorectal hepatic tumor localization after the infusion of Eu-G3P4A18N and histological imaging using confocal and multi-photon scanning microscopy. (*A*) White light photograph of an *in vivo* rat liver containing a tumor; Luminescent images of the abdominal cavity of the rat before (*B*) and after (*C*) Eu-G3P4A18N infusion (excitation 450 nm and emission filter of 610 nm with a 30 nm bandpass). (*D*) 20x confocal microscopic image of a section of liver without the tumor after Eu-G3P4A18N infusion, no luminescence of the dendrimer is seen. The excitation wavelength was 488 nm and emission wavelength was 567 nm. Vessels are labeled with CD-31 (red), nuclei of hepatocytes with dapi (blue) and dendrimer (green). (*E*) Eu-G3P4A18N can be seen in green (arrows) with the 40x magnification of a confocal microscopic image of tumor in the liver after infusion. The same colored labels are used. (*F*) 25x magnification of a tumor section in a rat liver after infusion of Eu-G3P4A18N. The two-photon excitation was 820 nm and the luminescence emission was 570 – 625 nm. The nuclei of cancer cells are seen in blue, the aberrant vessels are depicted in red and the dendrimer is designated in green (arrows) to show the association of Eu-G3P4A18N with the tumor vasculature seen in red. (*G*) 60x magnification of another section of tumor within the same liver also demonstrating the same concept.

***In vivo* Imaging of Eu-G3P4A18N Infusion.** To evaluate the tumor-targeting specificity of our functionalized dendrimer *in vivo*, *in vivo* intrahepatic infusion of Eu-G3P4A18N in anesthetized rats (Figure 10-7*A*-*C*) was performed. Localized luminescence was observed in the tumor tissues within seconds following infusion. This result is consistent with our previous observations in the *ex vivo* setting. The infused liver was excised and sectioned for red/NIR microscopy. We found that the signal-to-noise ratio was improved when luminescence was detected at 740 nm/140 nm (image not shown) as compared to 610/30 nm.

Use of a two-photon excitation scanning confocal microscope allowed us to confirm that the luminescence signal of the dendrimer was present within the vasculature of the liver (Figure 10-7*D*). Higher magnifications of the tissue sections revealed that the luminescence is located outside of the vessels in the perivascular space (Figure 10-7*E*). Figure 10-7*F*-*G* also show a section of tumor from a rat liver that was infused with Eu-G3P4A18N displaying the same association of the dendrimer with the vasculature under confocal microscopy. Tumor vasculature is disorganized and displays widened inter-endothelial junctions and fenestrae that range from 400 – 800 nm in size. [278] Thus, tumor vasculature is often described as “leaky”, allowing for larger molecules to extravasate the vascular endothelium into the extravascular space and in the process bypass normal liver parenchyma. The relatively small size of our dendrimer[279] facilitates its exit through the fenestrae and allows it to be trapped in the extravascular spaces of the tumor. The confocal microscopy observations are consistent with the hypothesis that Eu-G3P4A18N has increased extravasation from the leaky tumor vasculature and, therefore, is more likely to be trapped in the perivascular spaces of the tumor.

10.6 DISCUSSION

We have designed and synthesized a new luminescent marker based on a generation-3 dendrimer covalently substituted with thirty-two luminescent 4-amino-1,8-naphthalimide groups via glycine linkers, and complexed with eight equivalents of trivalent europium cations (Eu-G3P4A18N). The large number of luminescent groups results in more sensitive detection due to the large number of fluorophores per unit volume. Lanthanide cations coordinated within the dendrimer branches allow for stabilization of the fluorophores against photobleaching and result in a robust luminescent marker. These unique properties make real-time luminescence imaging of hepatic tumors in the WAG/Rij Hsd rat model possible. Our modified dendrimers, estimated to be approximately 3 nm in diameter,[279] are significantly smaller than the 100 nm and 300 nm sized nanoparticles used in other tumor detection studies,[306] minimizing disturbance of the biological system to be observed. Size-specificity is advantageous for improved distribution, thereby maximizing potential tumor tissue penetration and targeting.[307] In our proposed metastatic tumor model, we have demonstrated our ability to unambiguously detect the presence of a tumor within seconds post-infusion and up to 72 h *in vivo* within the liver tumor tissue. The enhanced viability of the luminescent dendrimer complex localized within tumor tissue avails the strategy to multiple potential clinical applications in both imaging and therapeutic settings. As demonstrated in this study, by utilizing the nanoscale size and photophysical stability of the Eu^{3+} dendrimer complex, we were able to target and image tumor tissue in our rat hepatic metastasis model with near-infrared imaging.

Peptide molecules, such as the RGD peptide,[308,309] and tumor-specific antibodies have been demonstrated to have tumor targeting specificity.[310-312] The attachment of such peptide and antibody entities to the dendrimer complex described in this report is anticipated to further

improve the tumor-targeting specificity. The versatility of our functionalized dendrimer platform allows us to adapt this targeting system to address a wide array of biological questions. The many opportunities which exist for modifying the dendrimer platform will lead to a broad field of applications in detecting and monitoring biological events.

Acknowledgements

We thank Per Basse, M.D., Ph.D., DMSci for making available the CC531 colorectal cancer cells. We would like to thank Guang Jin, M.D., Ph.D., Congrong Ma, Katie Lyn Leschak, VT, BA and Diane Mazzei, LAT for their contribution and assistance with in vitro and animal experiments. We would also like to thank Byron Ballou, Ph.D. and Simon C. Watkins, Ph.D. for their contributions in the biological imaging sciences.

11.0 DECORATED CARBON NANOTUBES WITH UNIQUE OXYGEN SENSITIVITY

11.1 CHAPTER PREFACE

The work described in this chapter is the result of a collaborative effort formed with the intention of constructing a single-walled carbon nanotube (SWNT) device with an overlying organic layer that is sensitive to the presence of oxygen gas. The electrical and spectroscopic response of the device at room temperature and under ambient pressure far exceded expectations, however, the behavior ran completely counterintuitive to our experiences. The luminescence arising from our Eu^{3+}-containing dendrimer allowed us to address the energy transfer mechanisms involved in the oxygen sensing process. In addition to our experimental work, we engaged in a collaboration with other material chemists working in the SWNT field to work towards these practical sensing applications. The material contained in this chapter was published as a research paper in the journal *Nature Chemistry*, and the 2009 copyright is retained by the authors listed below. The chapter contents have been reproduced with permission from the Nature Publishing Group, and the full citation is listed as Reference 204 in the bibliography section.[204]

List of authors: Douglas R. Kauffman Chad M. Shade, Hyounsoo Uh, Stéphane Petoud, Alexander Star

Author contributions: The author of this dissertation was responsible for the photoluminescence spectroscopy and luminescence lifetime measurements of the device, contributed to the design of the experiments, interpretation of the results and preparation of the published manuscript.

11.2 ABSTRACT

The relatively simple and robust architecture of microelectronic devices based on carbon nanotubes, in conjunction with their environmental sensitivity, places them among the leading candidates for incorporation into ultraportable or wearable chemical analysis platforms. We used single-walled carbon nanotube (SWNT) networks to establish a mechanistic understanding of the solid-state oxygen sensitivity of a Eu^{3+}-containing dendrimer complex. After illumination with 365 nm light, the SWNT networks decorated with the Eu^{3+} dendrimer show bimodal (optical spectroscopic and electrical conductance) sensitivity towards oxygen gas at room temperature under ambient pressure. We investigated the mechanism of this unique oxygen sensitivity with time-resolved and steady-state optical spectroscopy, analysis of excited state luminescence lifetimes and solid-state electrical transport measurements. We demonstrate a potential application of this system by showing a reversible and linear electrical response to oxygen gas in the tested range (5–27%).

11.3 INTRODUCTION

Molecular oxygen is a ubiquitous requirement for human life so the need for ultraportable or wearable personal safety devices to monitor the ambient oxygen level is paramount for a wide array of civilian and military applications. Such sensor platforms could operate as personal safety devices for workers in confined spaces or as sensors for ambient oxygen levels in enclosed working environments. As a result, researchers have worked to develop microelectronic sensor platforms based on chemically sensitive resistors (chemiresistors) to detect oxygen gas at room temperature. The advantage of a room-temperature oxygen-sensor design over state-of-the-art oxygen-sensor technology, such as optical spectroscopy[313,314], solid-state or solution-phase electrochemistry[315,316] and resistive metal–oxide semiconductors[316,317], is the potential to miniaturize robust low-power devices without the need to maintain high operating temperatures. Although progress has been made[318,319], the complicated fabrication techniques required to produce the sensing elements inhibit the wide-scale adoption of this technology. Towards this end, ultra-small and low-power microelectronic devices based on carbon nanotubes[320,321], especially those fabricated from networks of SWNTs[322], have shown great promise as candidates for the development of robust and low-cost chemical detection platforms[323,324]. However, SWNTs have shown reversible oxygen sensitivity only with the aid of vacuum instrumentation[325,326], which illustrates a fundamental limitation in the development of this technology.

Here we describe the spectroscopic and electrical behavior of simple chemiresistor devices composed of SWNT networks decorated with an oxygen-sensitive Eu^{3+}-containing dendrimer complex, abbreviated here as Eu_8 and illustrated in Figure 11-1a,b. Complexes that contain lanthanides show solution-phase sensitivity towards oxygen[231,327], which we exploit by

immobilizing Eu_8 on highly conductive and optically transparent SWNT based devices[328], as shown in Figure 11-1c–e. We use a combined approach[329,330] of optical spectroscopy[331,332] and electrical transport measurements[333,334] on SWNT-based devices to show that the oxygen sensitivity of the solid-state Eu_8 does not rely on the typical excited-state quenching phenomenon observed in the solution phase. Specifically, we show that it requires a preliminary illumination with ultraviolet light (365 nm) to populate electron traps in the substrate surface. This approach is unique compared with other solid-state techniques because we have used simple chemiresistor devices to transduce chemical events in the overlying molecular layer. Also, the Eu_8-decorated SWNT (Eu_8-SWNT) devices demonstrate a linear sensitivity towards oxygen gas in the environmentally relevant concentration range of 5–27% when they operate at room temperature and ambient pressure, which represents an important step in the development of small-scale and low-power detection platforms for oxygen.

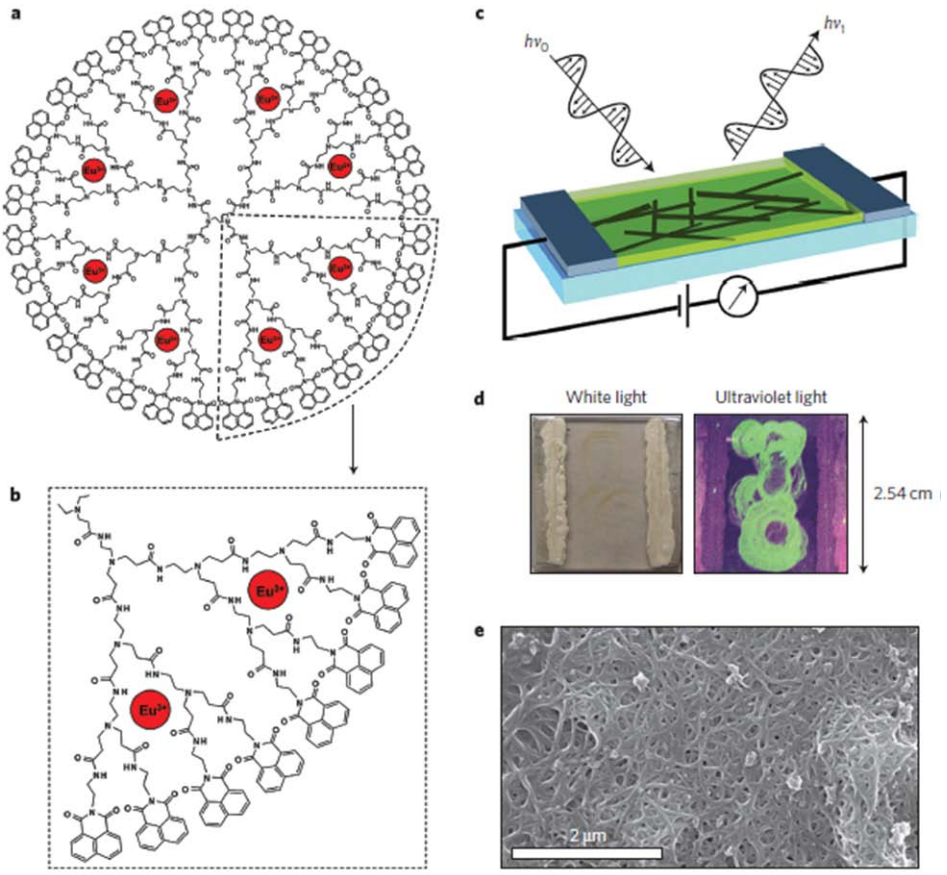

Figure 11-1. Chemical structure of the Eu^{3+}-containing dendrimer complex (Eu_8) and presentation of decorated SWNT devices. a, Chemical structure of the Eu_8 complex, which contains eight Eu^{3+} cations (red circles) coordinated within a 1,8-naphthalimide-terminated, G3-PAMAM dendrimer core. b, Expanded view of the Eu_8 structure that illustrates the coordination of the Eu^{3+} ions. c, Cartoon representation of an optically transparent and electrically conductive Eu_8-SWNT device composed of a SWNT network decorated with Eu_8 (green layer) for simultaneous spectroscopic and electrical conductance measurements. d, Digital photographs of 6.45 cm^2 Eu_8-SWNTdevices decorated with a drop-cast layer of Eu_8 under white light (left) and 365 nm light (right); the green color of the Eu_8 layer is the complex photoluminescence. e, Scanning electron microscope (SEM) image of a typical device surface that shows the Eu_8-decorated SWNT network; here, the Eu_8 molecules coat the underlying SWNT network. Energy dispersive X-ray (EDX) spectroscopy confirmed the presence of europium on the Eu8-SWNT device surface, and for comparison an SEM image and EDX spectrum of a typical bare SWNT network is given in Figure 11-2.

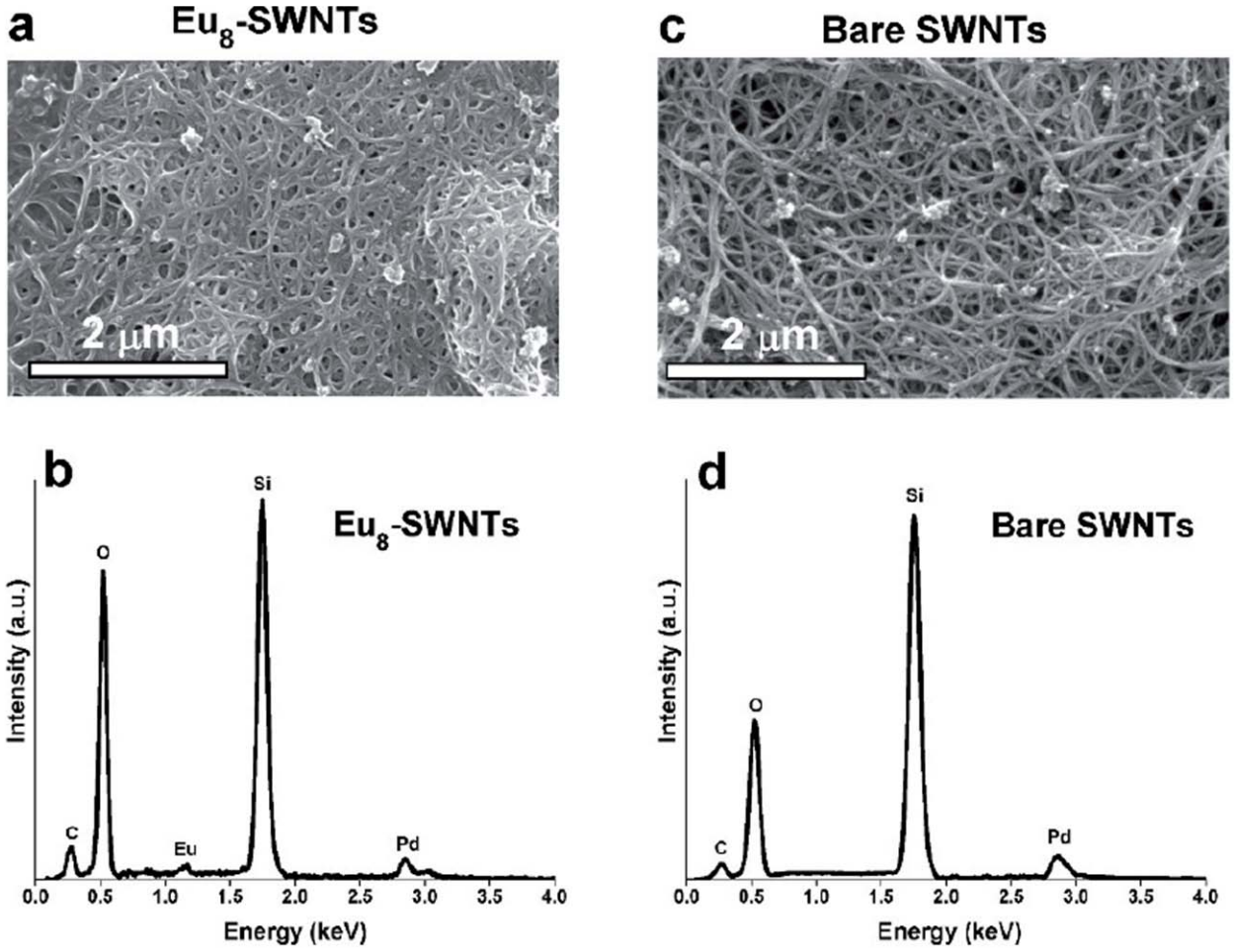

Figure 11-2. Scanning electron microscopy (SEM) and energy dispersive X-ray (EDX) spectroscopy of bare- and Eu_8-SWNTs. (a) the SEM image of the Eu_8-SWNT network shows a coating of Eu_8 on top of the SWNT network, and (b) the EDX spectrum confirms the presence of Eu at approximately 1.2 keV. (c) the bare SWNT network is composed of bundles of individual SWNTs, and (d) as expected, the Eu signature is absent from the EDX spectrum. The scale bar represents 2 μm in both SEM images. In the EDX spectra of both samples, the strong O and Si signatures are due to the underlying quartz (SiO_2) substrate; the Pd signature results from sputter coating the sample with Pd prior to imaging, which was done to prevent charging of the insulation quartz substrate during SEM operation.

11.4 EXPERIMENTAL

Synthesis of G3-PAMAM-(1,8-naphthalimide)$_{32}$. Poly(amidoamine) (PAMAM) dendrimer G3-NH_2 (390.5 mg, 0.0565 mmol) and 1,8-naphthalic anhydride (447.9 mg, 2.26 mmol) were suspended in DMF (25.0 ml) and stirred at 95 ^{o}C for 48 hours under a nitrogen atmosphere. The compound was purified by dialysis using a regenerated cellulose membrane (Fisher; nominal MWCO 12,000–14,000) in dimethyl sulfoxide (DMSO) for three days. The solution in the dialysis membrane was dried in a vacuum oven to yield the G3-PAMAM-(1,8-naphthalimide)$_{32}$ as a brown solid (517.6 mg, 72.4%); ^{1}H NMR spectra (300 MHz; $CDCl_3$, δ): 8.23 (broad (br) s, 64H, Ar H), 7.97 (br s, 64H, Ar H), 7.69 (m, 60H, –NH), 7.49 (br s, 64H, Ar H), 4.12 (br s, 64H, –$N(CO)_2CH_2$–), 3.51 (br s, 64H, –$NHCH_2$–), 3.19 (m, 56H, –$NHCH_2$–), 2.90–2.40 (m, 60H, –NCH_2CH_2NH–), 2.27 (m, 120H, –NCH_2CH_2CO–), 1.93 (m, 120H, –$COCH_2$–). Figure 11-3 shows the ^{1}H NMR spectrum of G3-PAMAM-(1,8-naphthalimide)$_{32}$.

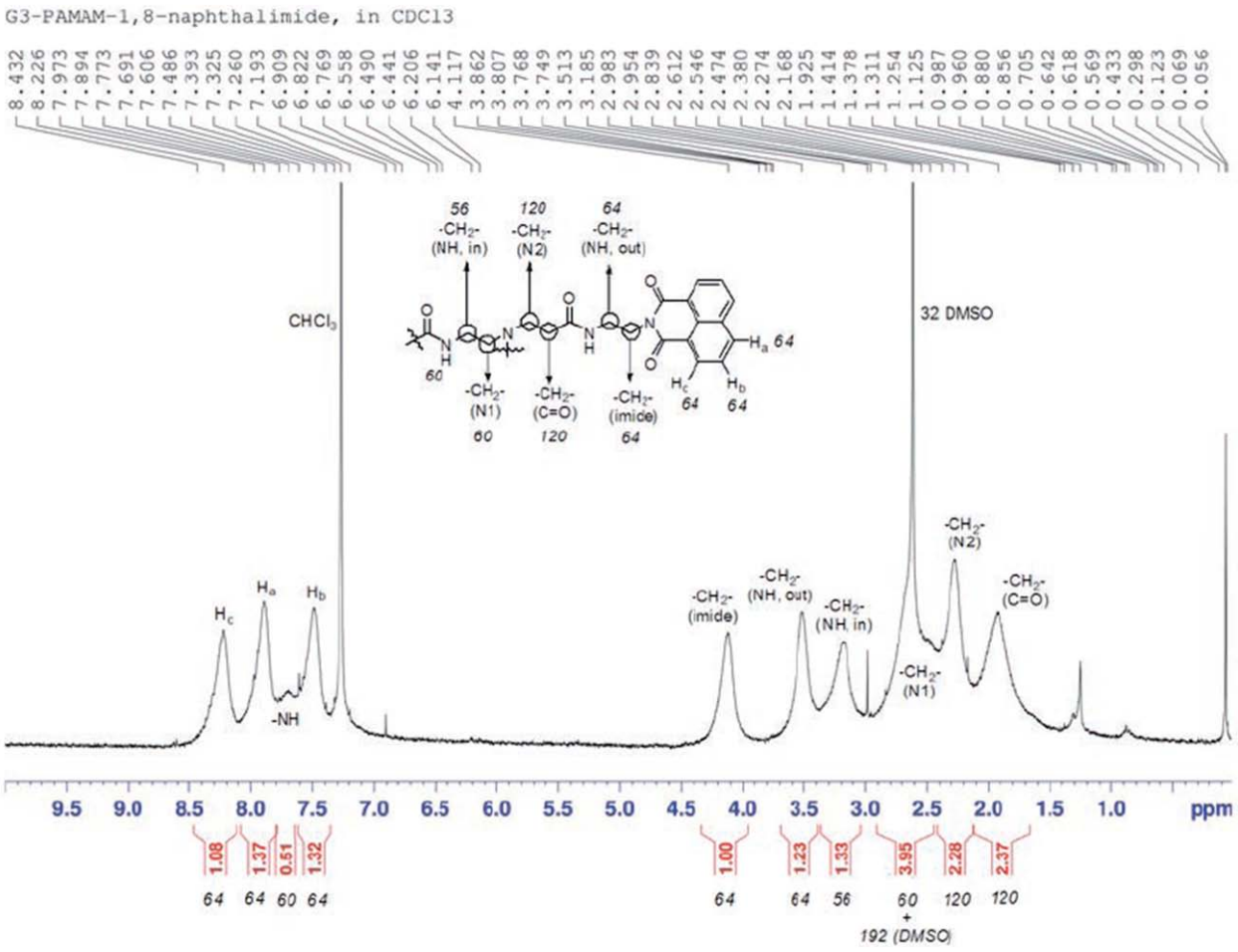

Figure 11-3. ^{1}H NMR spectra of the synthesized G3-PAMAM-(1,8-naphthalimide)$_{32}$.

Synthesis of Eu$_8$-G3-PAMAM-(1,8-naphthalimide)$_{32}$, Eu$_8$:G3-PAMAM-(1,8-naphthalimide)$_{32}$ (16.81 mg, 1.326 x 10^{26} mol) was dissolved in DMSO (5.0 mL) and a solution that contained 1.397 mM of $Eu(NO_3)_3$ solution in DMSO (7.593 ml, 1.061 x 10^{25} mol) was added. The mixture was incubated for seven days. DMSO was then evaporated in a vacuum oven, and the residual solid was dissolved in 10.0 mL of DMF to obtain 1.40 x 10^{24} M solution.

SWNT Device Fabrication. Optically transparent and electrically conductive SWNT network devices were fabricated and measured as described previously. Briefly, commercially available SWNTs (Carbon Solutions, P2 SWNTs; reported purity 70–90%) were suspended in DMF using sonication without further purification. Fused quartz (SiO_2) plates (1 in^2 (6.45 cm^2) x 0.0625 in (0.159 cm) thick; Quartz Scientific; reported specific resistance of 10 x 10^{18} Ω cm^{-3} at 20 ^oC) served as the device substrates, and were cleaned prior to SWNT deposition with acetone, rinsed with water and dried under compressed air. After spray casting the SWNT networks with a commercial air brush (Iwata) onto the heated quartz plates, aluminum tape and silver paint were used to form the device electrodes. To create devices with two SWNT networks a cotton-tipped applicator soaked in acetone was used to wipe clean a section of the spray-cast SWNT network. Two devices were created from the bisected SWNT network by individually connecting electrodes to each section with aluminum tape and silver paint. Quartz plates with additional hydroxyl surface groups were created by soaking overnight in Piranha solution (1 : 3 H_2SO_4:H_2O_2 v/v; Warning: Piranha is a vigorous oxidant and this solution should be handled appropriately). Nanotube field-effect transistor (NTFET) devices consisted of interdigitated gold electrodes (10 μm pitch size) on a Si–SiO_2 substrate, and dilute suspensions of Carbon Solutions P2 SWNTs in DMF were drop cast onto heated devices to form the conduction channel.

Device Decoration and Measurement. SWNT devices were heated to just above the solvent boiling temperature and 200 μL (4 μL for NTFETs) of a particular molecule was drop cast evenly onto the surface of the device. For NTFET devices, all measurements were conducted in ambient conditions with a drain-source bias voltage of 100 mV with two Keithley model 2400 SourceMeters interfaced with LabVIEW 7.1 software.

UVVNIR absorption spectra were recorded with a Perkin Elmer Lambda 900 UVVNIR spectrophotometer, and steady-state excitation and emission spectra, as well as the luminescence lifetime measurements, were recorded using a custom-designed JY Horiba Fluorolog-322 spectrofluorimeter and a Tektronix TDS model 754D oscilloscope. At least 1,000 luminescence decay curves, each containing 50,000 points, were averaged and treated to calculate the lifetimes using Origin Pro 7.0 software. The reported lifetime for a particular excited state is the average of at least two independent measurements. For multiexponential fittings, we used the amplitude of the major component as a criterion to isolate the values reported in Table 11-1; components with amplitudes less than 1% were discarded. Time-resolved excitation and emission spectra of the Eu_8 solutions were measured using a Varian Cary Eclipse spectrofluorimeter.

For the optically transparent SWNT devices, the ultraviolet-exposure and gas sensitivity measurements were performed in a custom-built gas-delivery chamber housed within the spectrometers for simultaneous electrical and optical measurements; the device conductance was measured at a bias voltage of 500 mV using a Keithley model 2400 SourceMeter interfaced to LabVIEW 7.1 software. The network conductance of two devices on a single quartz substrate was simultaneously measured at 500 mV with a Keithley 2602 SourceMeter and a Keithley 708A switching matrix using Zephyr data-acquisition software (Zephyr is an open source, Java-based data acquisition and measurement program freely available for download at http://zephyr.sourceforge.net/). The atmosphere inside the chamber was controlled with flowing research-grade gases at a constant flow rate of 1,000 standard cubic centimeters per minute; all gases were dry unless otherwise noted. Atmospheres of 43% relative humidity were created by passing the gases over the headspace of a sealed container of saturated K_2CO_3 solution (literature relative humidity, 43.2±0.3% at 20^{o}C).[335] The ultraviolet lamp used for device illumination was a

UVP Model UVGL-55 hand-held unit (365 nm; 250 μW cm^{-2}; **Warning**: Ultraviolet light can be dangerous and appropriate eye protection should be worn). All measurements were conducted at room temperature and ambient pressure. SEM and EDX spectroscopy were conducted on a Phillips XL30 FEG microscope operated at an accelerating voltage of 10 kV; samples were sputter coated with palladium prior to imaging to prevent charging of the insulating quartz substrate.

11.5 RESULTS

Solution-Phase Behaviour of Eu_8. Figure 11-4a presents the emission spectra of a Eu_8 solution in dimethylformamide (DMF) saturated with either argon or oxygen; oxygen saturation results in a decrease of the apparent emission intensity. The Eu_8-emission profile contains a broad band that arises from the excited states of 1,8-naphthalimide groups centered around 469 nm, and three narrow emission bands located at lower energies characteristic of the Eu^{3+}-centered transitions. In the Eu_8 structure, the 1,8-naphthalimide groups act as sensitizing agents (Figure 11-5). Specifically, photoexcited electrons in the excited naphthalimide singlet state undergo intersystem crossing (ISC) into a triplet state (T_3) and subsequent energy transfer into the accepting levels of the Eu^{3+} ions produces the sharp Eu^{3+}-centered emission bands[237]. The reversible and reproducible quenching effect of oxygen on the solution-phase Eu_8-emission intensity is in accordance with its predicted behaviour. However, we find that the Eu^{3+}-centred emission bands show a larger sensitivity to oxygen compared with the 1,8-naphthalimide band. For example, Figure 11-4b shows the relative emission intensity of the naphthalimide centered

(469 nm, open squares) and Eu^{3+} $^5D_0 \rightarrow {}^7F_2$ (615 nm, filled circles) bands in a solution cycled several times between oxygen and argon saturation. The larger relative change in the Eu^{3+} emission spectrum suggests that oxygen deactivates the Eu^{3+} excited state more effectively compared with 1,8-naphthalimide, through the introduction of non-radiative pathways.

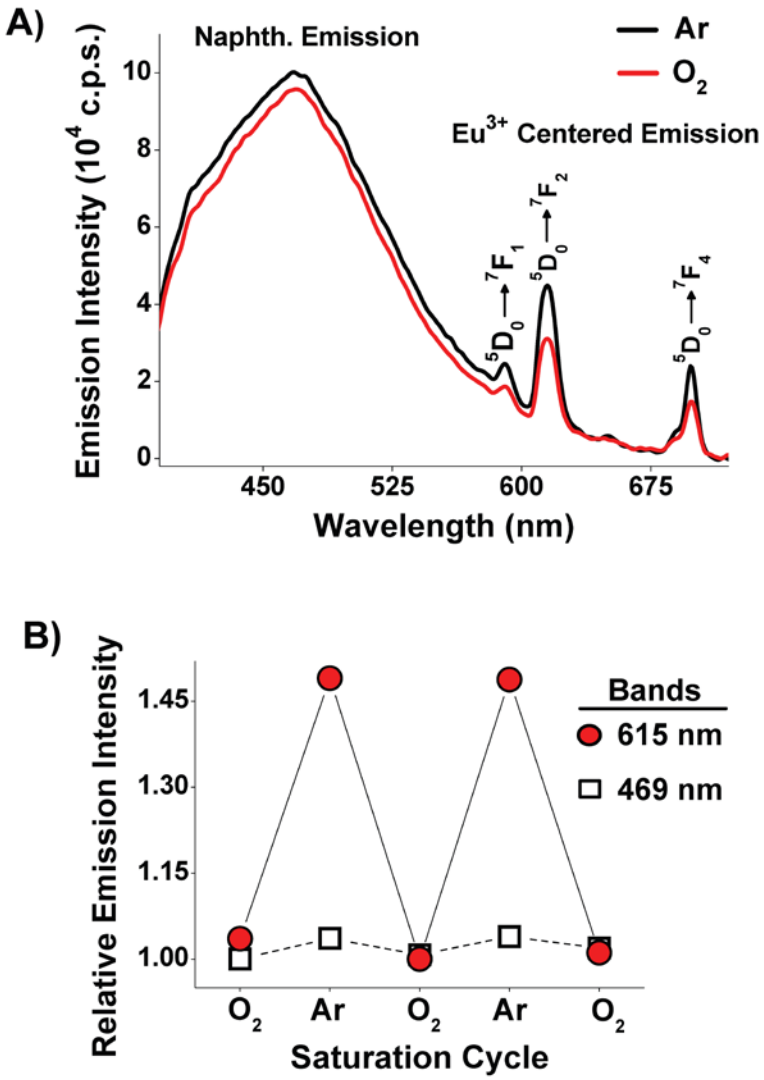

Figure 11-4. Solution-phase oxygen sensitivity of the Eu_8 complex. a, Steady-state emission spectrum of a Eu_8 solution (in DMF, 1.45×10^{-5} M; $\lambda_{excitation}$ = 354 nm) saturated with oxygen (black curve) and argon (red curve). b, Relative emission intensity of the 1,8-naphthalimide-centred ($\lambda_{emission}$ = 469 nm, open squares) and Eu^{3+} $^5D_0 \rightarrow {}^7F_2$-centred ($\lambda_{emission}$ = 615 nm, filled circles) emission bands cycled between argon and oxygen saturation. c.p.s.=counts per second.

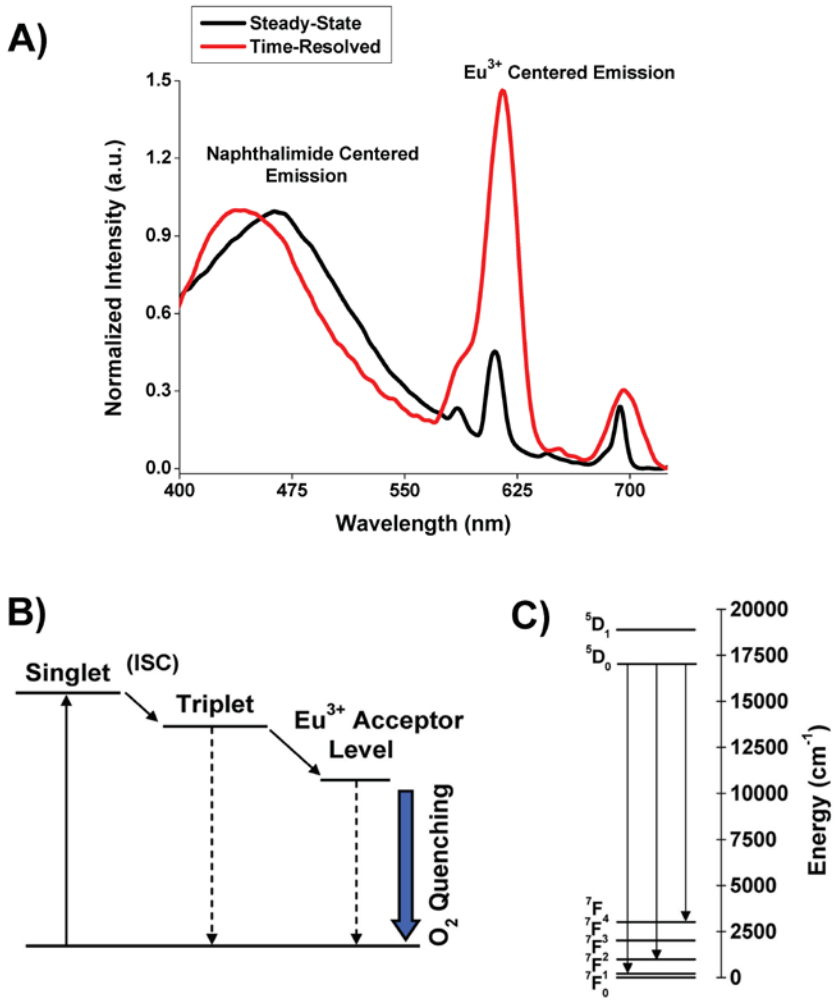

Figure 11-5. Luminescence spectra and energy level diagram for Eu_8. a, Normalized steady-state (black curve) and time-resolved (red curve; delay of 4 ms) emission spectra of a solution of Eu_8 (in DMF; 1.45×10^{-5} M) recorded under ambient conditions; $\lambda_{excitation}$ = 354 nm. The spectra were normalized at the height of the apparent maximum of the naphthalimide emission band. b, Diagram of Eu_8 describing the energy transfer from the naphthalimide triplet state into accepting levels of Eu^{3+}, as well as the proposed location of the O_2-induced non-radiative relaxation pathway for solution phase Eu_8. c, Energy level diagram showing the Eu^{3+} centered transitions.

Solid-State Behaviour of Eu_8. The relative emission intensity of solid-state Eu_8 (drop cast onto a quartz substrate) was constant when cycled between atmospheres of pure oxygen and argon (Figure 11-6), which highlights a fundamental difference between the behavior of solid-state and solution-phase samples. However, after illuminating the sample with 365 nm light for 30 minutes (in flowing argon), the emission profile of the solid-state Eu_8 developed a sensitivity towards oxygen such that the intensity decreased after illumination and partially restored under flowing oxygen. The observed behavior is quite interesting compared to the solution-phase behavior of Eu_8 and to the solid-state behavior of other oxygen-sensitive photoluminescent complexes[336].

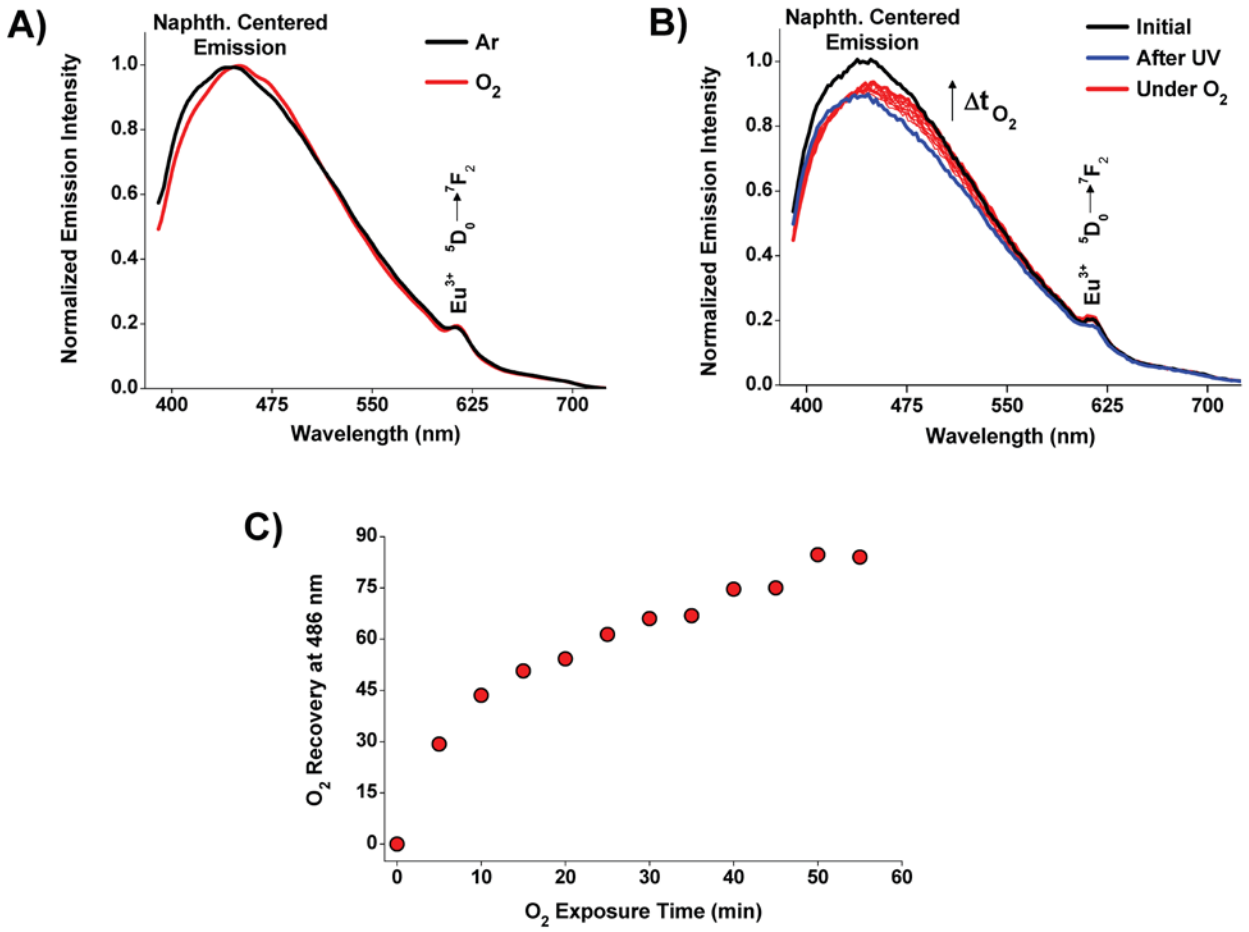

Figure 11-6. Solid-state oxygen sensitivity of the Eu_8 complex. a, Normalized emission spectra of Eu_8 (on quartz) in flowing Ar (black line) and pure O_2 (red line). b, Emission spectra of Eu_8 before (black line) and after (blue line) UV illumination in flowing Ar, and in flowing O_2 (red lines); spectra in flowing O_2 were recorded every minute. c, Naphthalimide centered emission intensity as a function of O_2 exposure time as measured at 486 nm. $\lambda_{excitation}$ = 354 nm for all plots.

To further explore the solid-state behavior of Eu_8, we drop-cast solutions onto optically transparent and electrically conductive SWNT devices. We observed minimal changes in the spectroscopic signatures of both the SWNT network and the overlying Eu_8 layer after the devices had been decorated, and separate field-effect transistor measurements of Eu_8-SWNT networks suggest that the dominant effect of the overlying Eu_8 layer was the introduction of charge scattering sites[337] along the SWNT network (Figure 11-7).

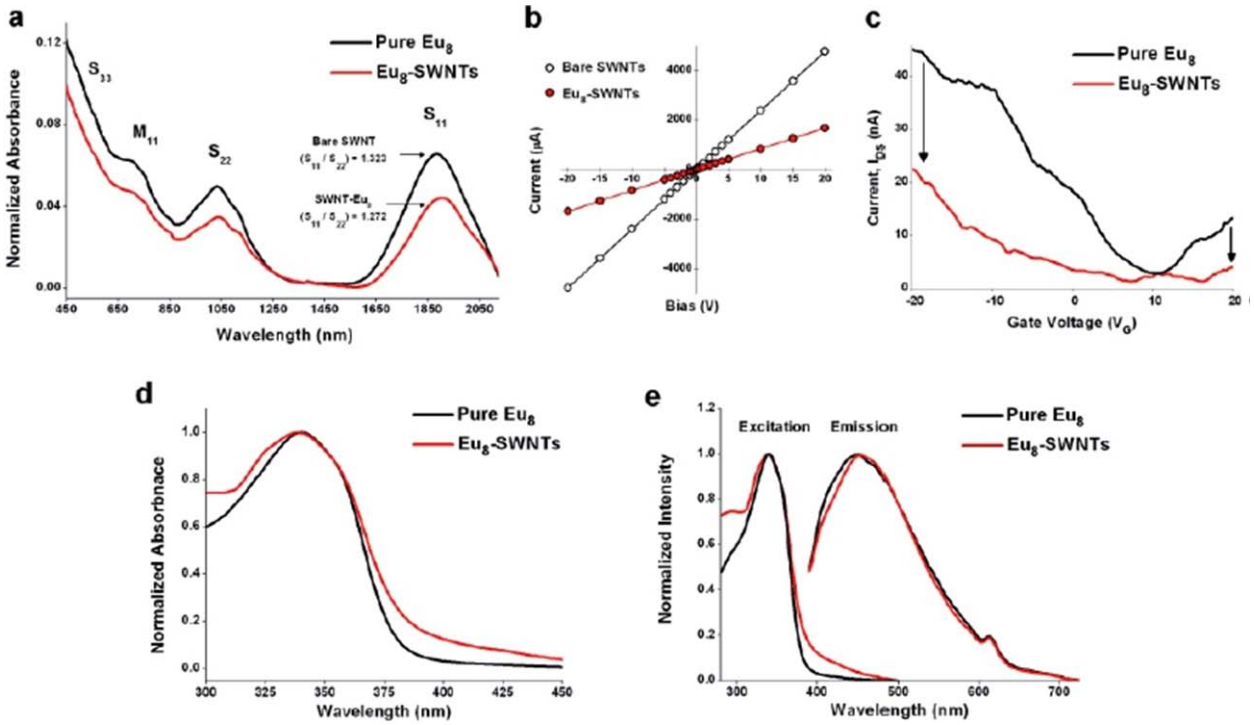

Figure 11-7. Characterization of Eu_8-decorated SWNT devices. a, UV-vis-NIR absorbance spectra of an optically transparent SWNT device (on quartz) before (black curve) and after (red curve) decoration with Eu_8; spectra were normalized at 1375 nm. b, Current versus bias voltage curves of the device shown in panel a before (white labels) and after (red labels) decoration with Eu_8. c, Field-effect transistor transfer characteristics showing the drain-source current (IDS) versus gate voltage (VG) of a SWNT network dropcast onto interdigitated electrodes before (black curve) and after (red curve) decoration with Eu_8; the applied drain-source bias voltage was 100 mV. Normalized (d) absorbance as well as (e) excitation (λ_{em} = 615 nm) and emission (λ_{ex} = 354 nm) spectra of Eu_8 on quartz (black curve) and on top of a quartz-immobilized SWNT network (red curve).

Figure 11-9a shows the emission spectra of a Eu_8-SWNT device before (black curve) and after (blue curve) exposure to 365 nm light, and during exposure to pure oxygen (red curves). After 30 minutes of illumination with 365 nm light (in flowing argon), the Eu_8-SWNT device experienced a 25% decrease in the emission intensity of the naphthalimide band and a 20% decrease in the emission intensity of the Eu^{3+}-centered band. The spectroscopic behavior of Eu_8 after illumination and oxygen exposure was comparable on bare quartz as well as on the SWNT networks (as shown in Figure 11-6), which strongly suggests that the observed behavior is an intrinsic property of solid-state Eu_8 on quartz.

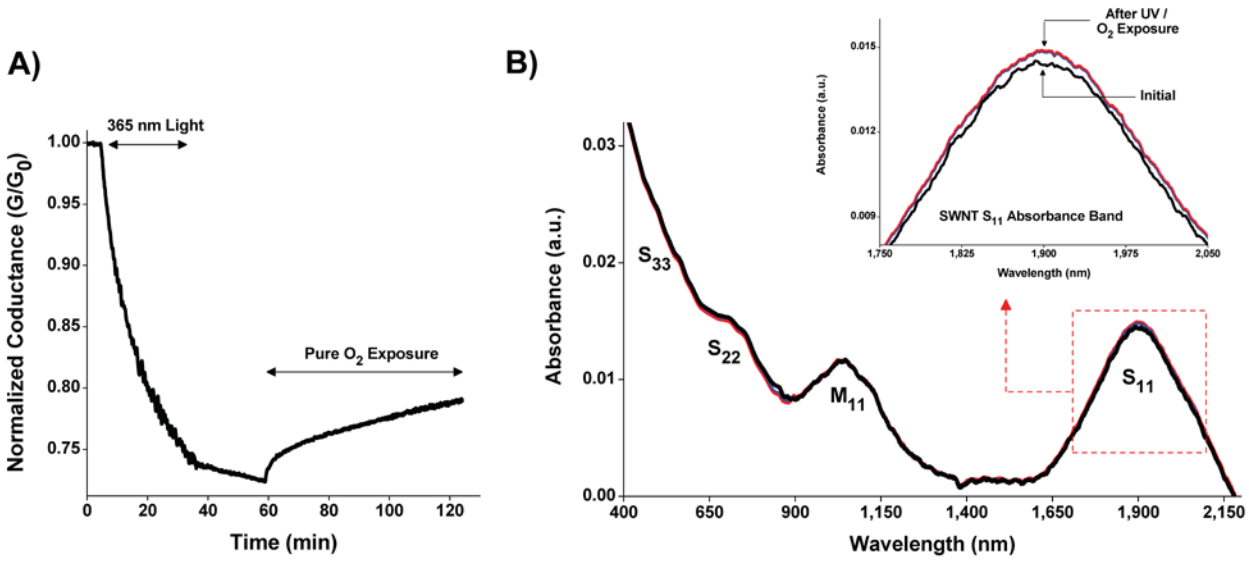

Figure 11-8. Response of bare SWNT to UV light and oxygen gas. Simultaneously recorded (a) normalized network conductance (G/G_0) and (b) spectroscopic response (not normalized) of a bare SWNT network upon a 30 minute period of illumination with 365 nm light(in flowing Ar) and subsequent 60 minute exposure to pure O_2.

Behaviour of Eu_8-SWNT Networks. Using simultaneous ultraviolet–visible–near infrared (UV–vis–NIR) absorbance spectroscopy and network conductance measurements on Eu_8-SWNT devices, we found that the underlying SWNT network was able to transducer changes in the electronic properties of the Eu_8 layer during illumination with 365 nm light and exposure to pure oxygen gas. After an illumination period of 30 minutes the device experienced a decrease in the first semiconducting SWNT absorption band, labeled S_{11} in Figure 11-9b.[338,339] Additionally, illumination triggered an increase in the network conductance (Figure 11-9c), which we call the photogenerated ON-state. We found that the ON-state conductance abruptly increased after termination of the ultraviolet light and then slowly decayed as a function of time. To test the reproducibility of the Eu_8-SWNT response to ultraviolet light we exposed nine individual devices to 365 nm light for 30 minutes. Each device's behavior was qualitatively similar, but we found that the magnitude of the response scaled inversely with the initial device conductance (Figure 11-8). This behavior differs drastically from the response of undecorated SWNTs to ultraviolet light, which show a decrease in the SWNT network conductance and an increase in the S_{11} absorption band (Figure 11-11)[340,341].

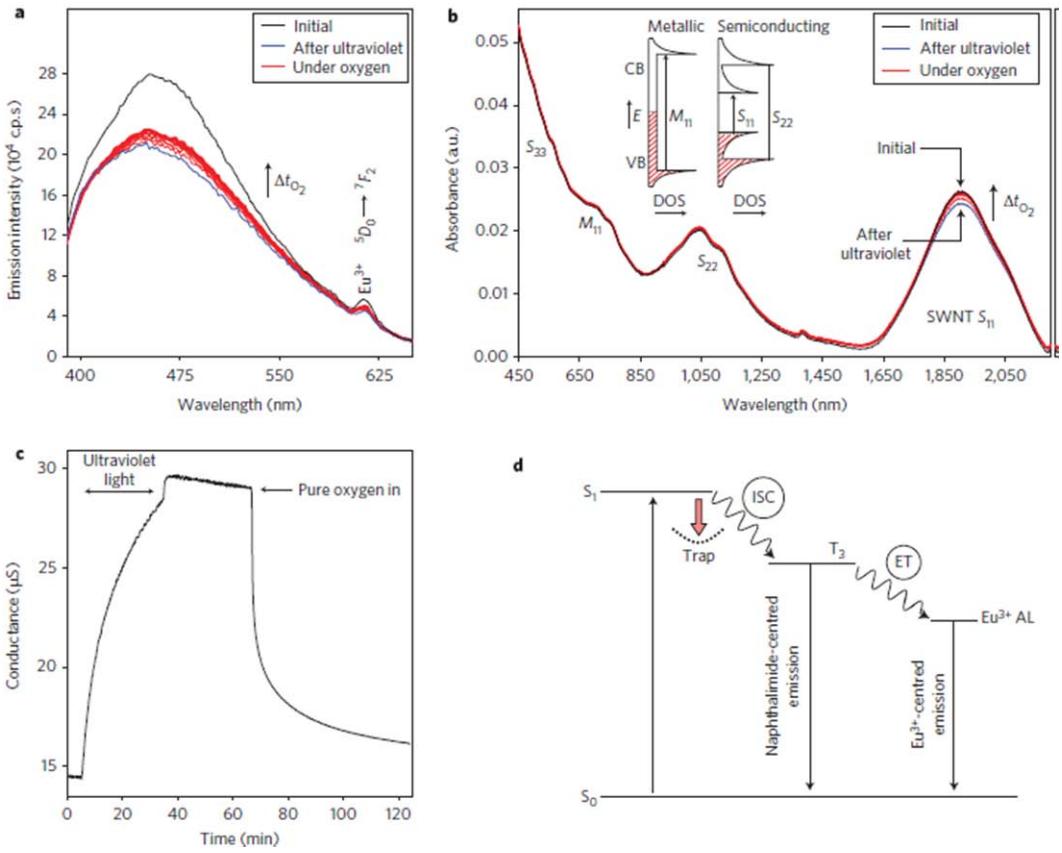

Figure 11-9. Bimodal oxygen sensitivity of the Eu_8-decorated SWNT devices. a, Emission ($\lambda_{excitation}$ = 354 nm) spectra of a Eu_8-SWNT device before (black curve) and after (blue curve) 30 minutes of illumination with 365 nm light (in flowing argon) and during one hour of oxygen exposure (red curves); the ultraviolet- and gas-exposure times are identical in a–c. b, UV–vis–NIR absorbance spectra of the Eu_8-SWNTdevice before and after illumination with 365 nm light (in argon) and during oxygen exposure. The first three semiconducting SWNT (labeled S_{11}, S_{22} and S_{33}) and the first metallic SWNT (labeled M_{11}) absorbance bands correspond to the electronic transitions between van Hove singularities in the SWNT valence band (VB) and conduction band (CB), as shown in the partial density of states (DOS) diagram (inset). c, Network conductance of the Eu_8-SWNTdevice during 365 nm illumination and sustained photogenerated ON-state (in flowing argon), followed by the introduction of pure oxygen; the network conductance was measured simultaneously with the UV–vis–NIR absorption spectra (b). d, Proposed mechanism to describe the Eu_8-SWNT oxygen sensitivity in terms of the Eu_8 electronic structure. Here, the 1,8-naphthalimide ground and excited singlets (S_0 and S_1), and excited triplet (T_3) states are shown in relation to the Eu^{3+} AL; the red arrow indicates energy donation into the trap states. c.p.s. = counts per second; E = energy; ET = energy transfer.

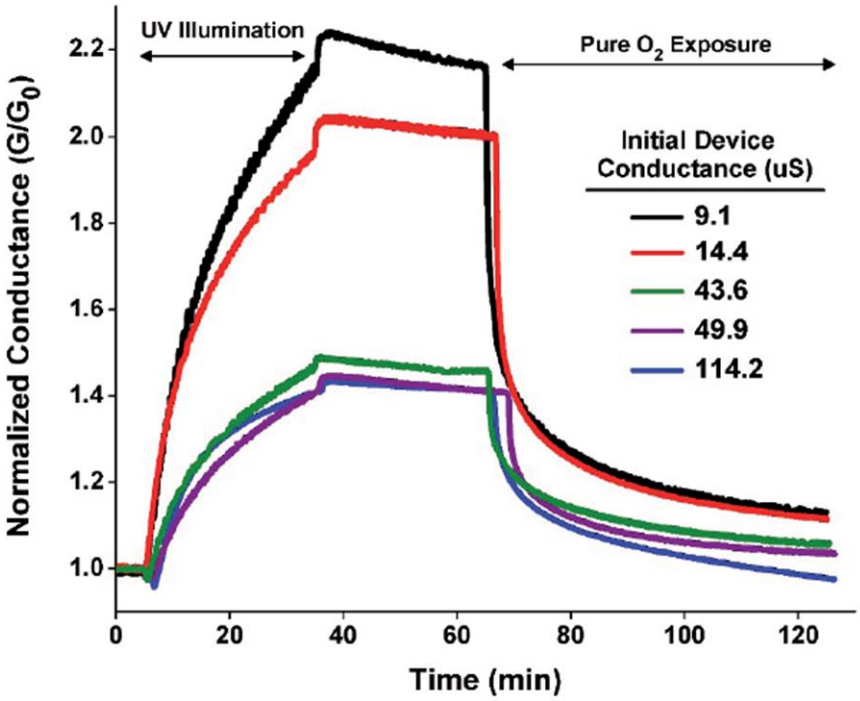

Figure 11-10. The normalized conductance of five different Eu_8-SWNT devices during 365 nm illumination and subsequent O_2 exposure. The initial device conductance (in flowing Ar before 365 nm illumination) is listed for each curve.

After exposure to 365 nm light for 30 minutes, we found that the device conductance decreased rapidly in the presence of oxygen, such that nine individually tested devices experienced a 60±10% decrease after exposure for 200 seconds to pure, flowing oxygen, regardless of the initial network conductance. After exposure to pure oxygen for an hour, we observed nearly 100% restoration of the S_{11} absorbance band and approximately 90% recovery of the initial device conductance. This electrical behavior was also reproducible, but after one hour of exposure to oxygen some devices demonstrated a response larger than 100%, which

stemmed from an increased defect site density in the quartz substrate (Figure 11-10 and Figure 11-14). We found that the absorbance change of the SWNT S_{11} band displayed a time dependency like that of the network conductance during oxygen exposure (Figure 11-12), which indicates that the device response stems from perturbations in the electronic density of the SWNT valence band rather than from a modification of the potential barriers at the interface between the SWNT network and device electrodes[342]. Throughout these experiments, the intensity of the first metallic SWNT (labelled M_{11}) transition remained constant. Although the metallic component of the SWNT network[343] may contribute to the electrical response of the SWNT devices, the finite Fermi-level electron density of metallic SWNTs (Figure 11-9b inset) renders the M_{11} transition intensity somewhat unaffected by changes in the local charge environment[344].

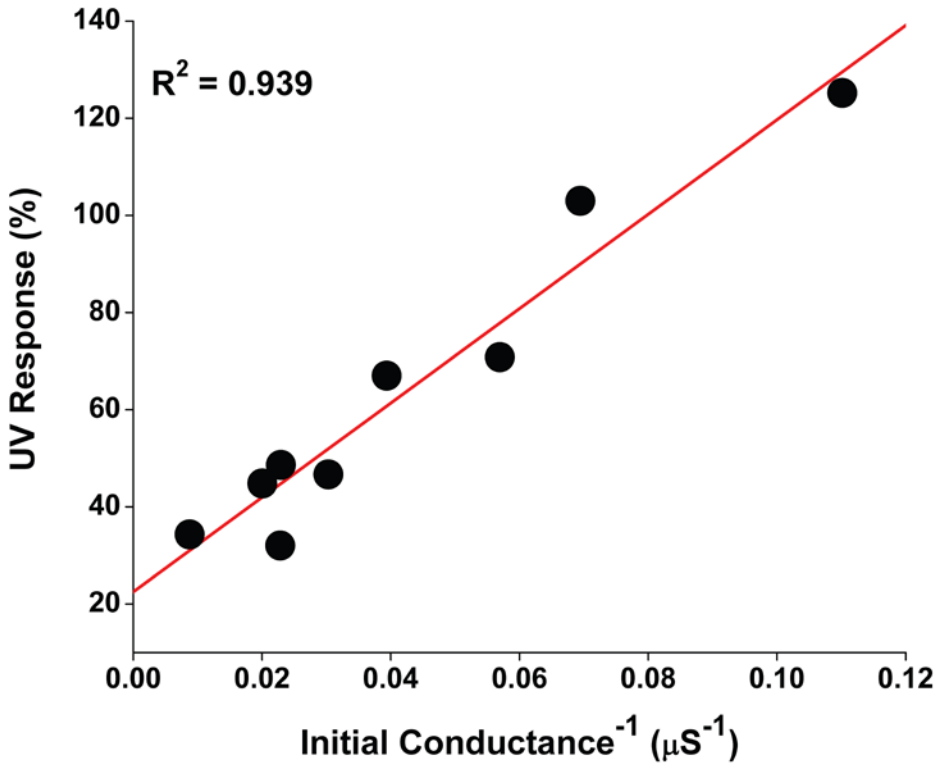

Figure 11-11. Response versus initial conductance of multiple Eu_8-SWNT devices. The response of nine individually tested Eu_8-SWNT devices after a 30-minute exposure to 365 nm light (in flowing N_2 or Ar). We found that all of the SWNT-Eu_8 devices showed qualitatively similar response towards UV light, however devices with lower initial conductance demonstrated a larger relative increase in conductance. The device conductance can be viewed as a measure of the SWNT network density, where higher conductance devices have a higher SWNT network density. We believe that lower density networks allowed more contact between Eu_8 and the electron traps at the quartz substrate—producing a larger response during illumination with 365 nm light. Furthermore, the lower SWNT network density of low conductance devices may indicate a higher semiconducting SWNT contribution to the electrical properties. This observation follows the accepted hypothesis that semiconducting SWNTs show larger response to their local charge environment, as compared to metallic SWNTs.[324]

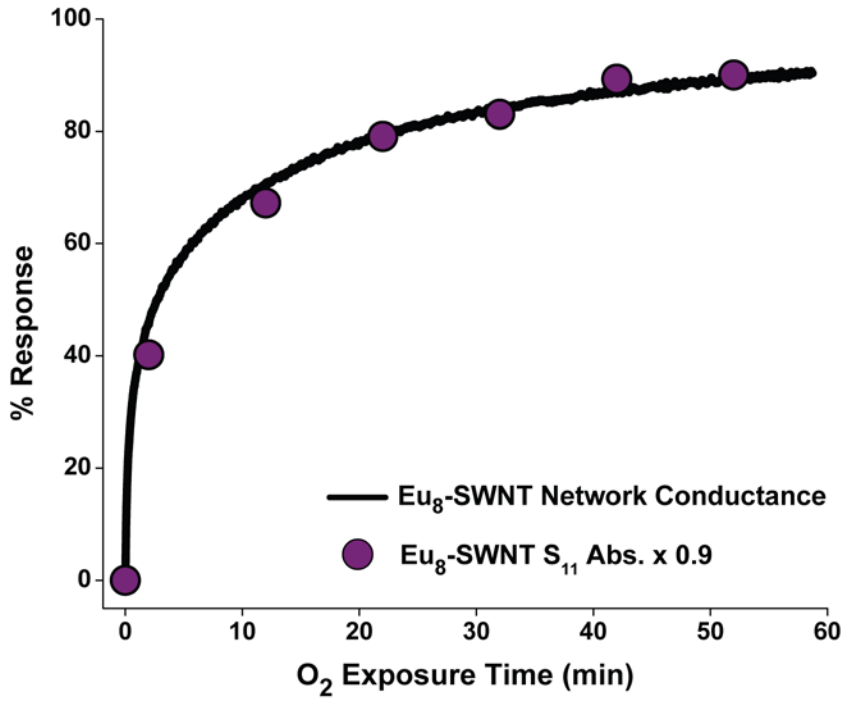

Figure 11-12. Overlay of spectroscopic and electrochemical response during oxygen exposure. Simultaneously recorded O_2 response of the Eu_8-SWNT device network conductance (black line) and S_{11} band absorption (purple labels) of the Eu_8-SWNT device shown in Figure 11-9. The dotted red line is the fitted response, and a scaling factor of 0.9 was applied to the S_{11} response.

Further control experiments were conducted on SWNT networks individually decorated with each component of the Eu_8 complex, including the generation-three poly(amidoamine) (G3 PAMAM) dendrimer with and without the 32 naphthalimide groups and the 1,8-naphthalic anhydride molecule alone. Additionally, SWNT networks were decorated with an iron-containing tetraphenylporphyrin as an analogue to a haem-containing moiety (Figure 11-13). We found that only the SWNT networks decorated with the 1,8-naphthalimide-terminated G3 PAMAM dendrimer demonstrated both a photoresponse and oxygen sensitivity comparable to those of the Eu_8-SWNT networks, which indicates that the 1,8-naphthalimide-terminated G3 dendrimer component of Eu_8 was responsible for the observed behavior.

Luminescence Lifetimes. The presence of Eu^{3+} ions in the Eu_8-SWNT networks allowed a quantitative comparison between the luminescence lifetimes of the Eu_8 T_3 and the Eu^{3+} acceptor level (Eu^{3+} AL). In essence, the Eu^{3+} AL emission serves as a spectroscopic beacon that can help identify the electronic processes that occur in the Eu_8-SWNT system. We measured the luminescence lifetimes of Eu_8 T_3 and Eu^{3+} AL before and after illumination with 365 nm light (in flowing argon), and after the reintroduction of pure oxygen gas. The data presented in Table 11-1 show that the luminescence lifetime of the T_3 state was not strongly affected by 365 nm illumination or the presence of oxygen. However, we observed an increase in the lifetime of Eu^{3+} AL after 365 nm illumination, which began to decrease towards its initial value after one hour of oxygen exposure.

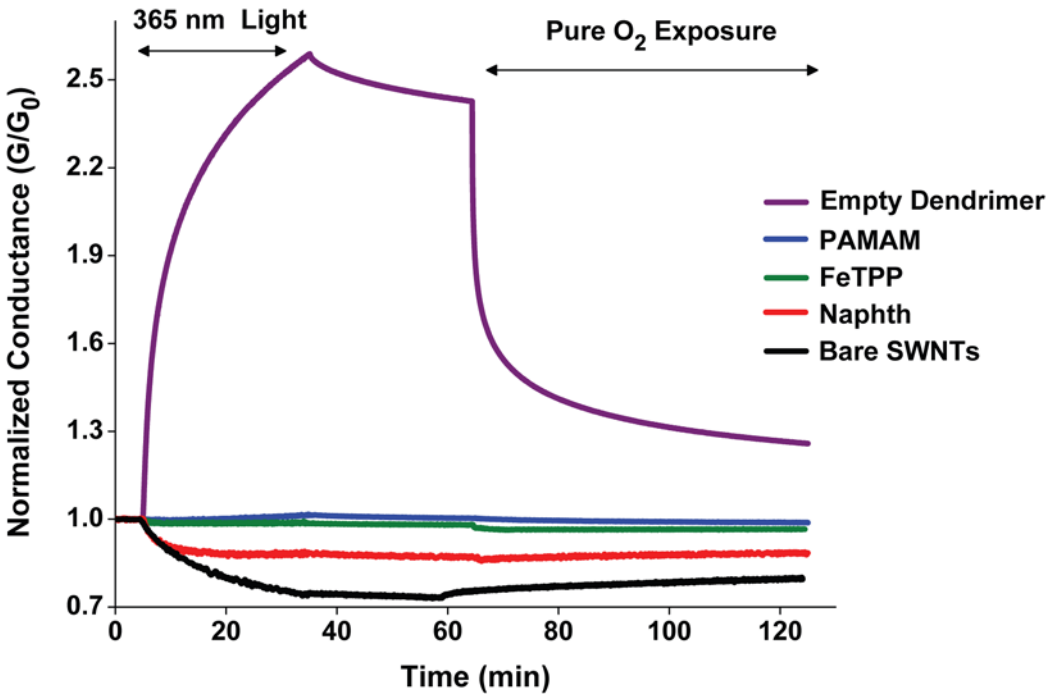

Figure 11-13. Effect of molecular decoration on device conductance. Normalized conductance of SWNT networks decorated with various components of the Eu_8 complex including: the 1,8-naphthalimide terminated G-3 PAMAM dendrimer (labeled Empty Dendrimer; purple curve), the G3 PAMAM dendrimer without the terminating 1,8-naphthalimide groups (labeled PAMAM; blue curve), and 1,8-naphthalic anhydride (labeled Naphth; red curve). Also presented is a SWNT device decorated with and an iron containing porphyrin meso-Tetraphenylporphyrin Fe (III) chloride (labeled as FeTPP; green curve); a bare SWNT film is also presented for comparison (labeled Bare SWNTs; black curve). We found that only the SWNT devices functionalized with the Empty Dendrimer demonstrated behavior similar to the Eu_8-SWNT devices during 365 nm illumination and oxygen exposure. This observation strongly suggests that the 1,8-naphthalimide terminated PAMAM structure is responsible for the increased conductance after UV illumination and the sensitivity towards O_2 exposure.

Table 11-1. Measured luminescence lifetimes (τ, milliseconds) of Eu_8 triplet state (T_3) and Eu^{3+} acceptor level (Eu^{3+} AL).

	T_3	**Eu^{3+} AL**
Initial	0.3900 (± 0.0001)	0.657 (± 0.001)
After ultraviolet	0.370 (± 0.001)	2.73 (± 0.07)
After oxygen	0.4000 (± 0.0002)	1.76 (± 0.07)

11.6 DISCUSSION

Photoresponse. It has been reported that SWNTs donate electronic density into the photodepleted ground state of an overlying chromophore during illumination with light[345]. The combined electrical and steady-state spectroscopic behavior of the Eu_8- SWNT device fits this hypothesis. The increased device conductance and decreased SWNT S_{11} band absorbance during 365 nm illumination suggests that the photodepleted ground state of the Eu_8 complex exerted an attraction towards SWNT valence band electrons during this illumination.

The sustained Eu_8-SWNT photogenerated ON-state conductance after illumination with 365 nm light closely resembles the behavior of optoelectronic memory devices composed of polymer-decorated SWNTs[346,347]. In such systems, a so-called metastable ON-state persists after photoexcitation through the excitonic (separated electron-hole pairs) filling of electron traps at

the SiO_2 surface[348]. SiO_2 electron traps include SiOH groups[349], water molecules hydrogen bonded to the device surface[350] and a variety of other defects[351,352]. The abrupt increase in the network conductance immediately after the termination of ultraviolet light was described recently as a characteristic of photoinduced exciton separation and charge-trap filling in polymer-decorated SWNT devices[353]. Moreover, the observation of a slight decay in the photogenerated ON-state conductance of the Eu_8-SWNT networks is a consequence of the gradual recombination of spatially separated excitons[354].

In contrast to polymer-decorated SWNT optoelectronic devices, which typically require an externally applied gate voltage to restore the initial conductance under ambient conditions, the photogenerated ON-state of the Eu_8-SWNT system was sensitive towards oxygen. To explain this behaviour, we propose a model based on the relative energy levels of the Eu_8 electronic states[355] and on electron traps in the quartz substrate, as described in Figure 11-9d. For example, 365 nm illumination serves to desorb oxygen from the device surface. Additionally, 365 nm illumination photoexcites electronic density from the ground singlet state (S_0) of the Eu_8 complex into an excited singlet state (S_1), which results in energy transfer to the electron traps at the quartz surface.

After illumination, we observed a comparable decrease in both the naphthalimide- and Eu^{3+}-centered emission bands, but the lifetime of the T_3 state was not affected strongly. This suggests that the electron traps are close in energy to the S_1 state of the Eu_8 complex. In this configuration, the traps can accept energy from the S_1 state (red arrow in Figure 11-9d) and inhibit ISC into the T_3 state, and thereby act as an electronic bottleneck. The trap-induced inhibition of ISC serves to decrease the electronic population in both T_3 and Eu^{3+} AL states, which produces the observed decrease in emission intensities. Subsequently, a Coulombic

attraction[356] develops between the photodepleted S_0 state and electrons in the SWNT valence band, which effectively p-dopes the SWNT valence band. This phenomenon produces the increased Eu_8-SWNT network conductance during ultraviolet illumination, sustained metastable ONstate conductance after the termination of ultraviolet illumination and decreased absorbance in the SWNT S_{11} band.

Oxygen response. Oxygen has been shown to passivate quartz charge traps, such as SiOH, through the introduction of nonradiative relaxation pathways[357]. Consequently, we suggest that the introduction of oxygen results in adsorption on the device surface and passivation of the electron traps through the addition of nonradiative pathways. The adsorption of oxygen removes the electronic bottleneck, increases ISC and leads to the restoration of both the naphthalimide and Eu^{3+}-centered emission band intensities. The increased lifetime of the Eu^{3+}-centered transition after 365 nm illumination is a consequence of oxygen desorption, which removes any oxygen-induced non-radiative pathways in the Eu^{3+} electronic structure. Finally, exciton recombination in the naphthalimide S_0 state eliminates the Coulombic attraction between the Eu_8 ground-state holes and SWNT valence-band electrons, which decreases the Eu_8-SWNT network conductance and increases the absorption of the SWNT S_{11} band.

To summarize the proposed response mechanism (Figure 11-9d), we suggest that photoexcitation of the Eu_8-SWNT system promotes Eu_8 ground-state electrons into an excited state, which subsequently fill electron traps at the quartz substrate surface. This leads to a Coulombic attraction between SWNT valence-band electrons and the depleted Eu_8 ground-state orbital, effectively p-doping the SWNT valence band. Upon the introduction of oxygen gas, nonradiative relaxation pathways allow electrons to return from the quartz electron traps back

into the Eu_8 ground state. This alleviates the Coulombic attraction between the SWNT valence band and Eu_8 ground state and reverses the SWNT p-doping.

As a control, we modified the quartz surface to understand how an intentional increase in the number of surface electron traps (SiOH groups and water molecules) would affect the Eu_8-SWNT sensitivity to ultraviolet light and oxygen exposure in atmospheres of 0% and 43% relative humidity (Figure 11-14). We found that devices with increased trap sites behaved in a qualitatively similar manner, but the response to an hour-long exposure to oxygen was consistently greater than 100%. We observed that this phenomenon was more pronounced in atmospheres with 43% relative humidity, which indicates that the density of charge traps has an important influence on device behaviour in the presence of oxygen.

Oxygen Detection. Using the Eu_8-SWNT devices in a chemiresistor configuration, we found a linear electrical response to oxygen in the concentration range tested (5–27%). By exploiting the stability of the Eu_8-SWNT photogenerated ON-state conductance we were able to create a baseline for measuring oxygen response. For example, an initial 365 nm illumination in dry argon (left-most blue asterisk in Figure 11-16a) established a baseline at an arbitrary network conductance (G_{ON}). Sequential pulses of dry oxygen gas (diluted in argon) produced a concentration-dependent decrease in the network conductance (Figure 11-16a). Oxygen exposure (indicated with dashed lines, Figure 11-16a) was followed by short periods of 365 nm illumination (marked with blue asterisks) to return the device to its arbitrarily defined ON-state conductance.

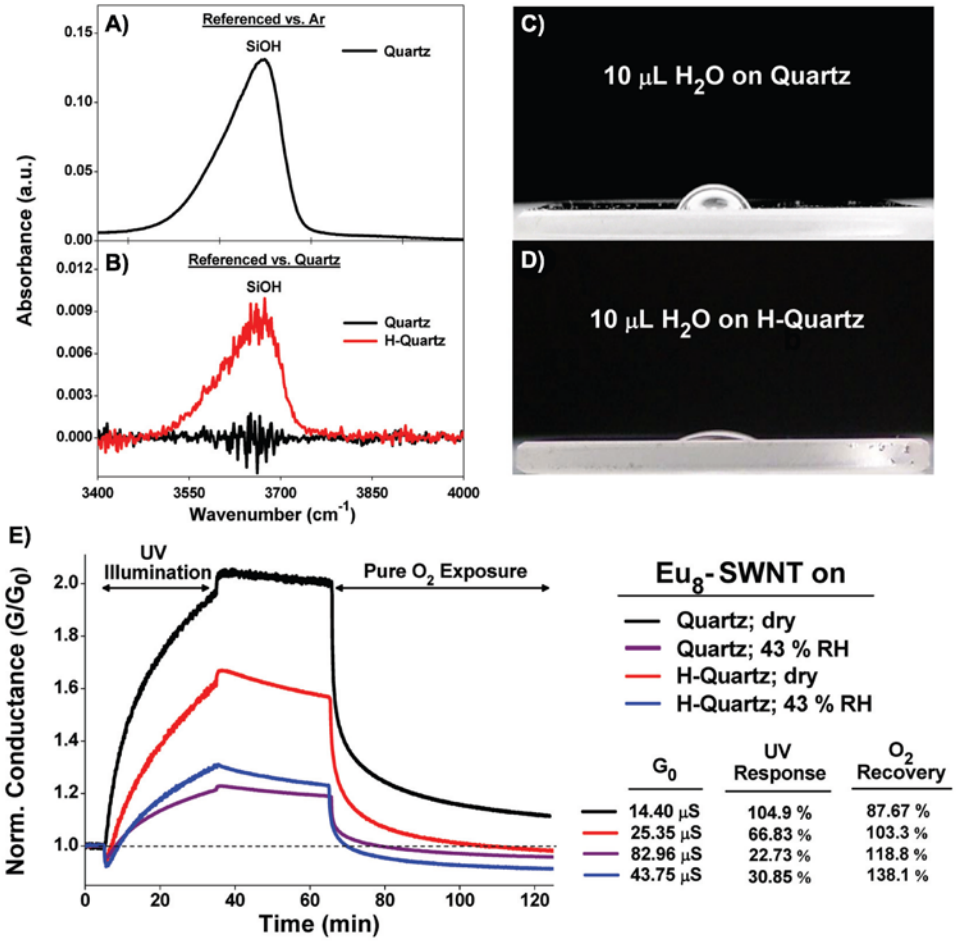

Figure 11-14. Eu_8-SWNT response to UV light (365 nm) and O_2 on hydroxylated quartz surface. a, NIR optical absorption spectrum of quartz in Ar (referenced against Ar). b, NIR optical absorption spectra of quartz and hydroxylated quartz (H-quartz; soaked in a 3:1 solution of conc. H_2SO_4 and 30% H_2O_2 overnight) in Ar (referenced against quartz). Digital photographs of a 10 μL H_2O droplet on (c) quartz and (d) H-quartz. e, Normalized response of Eu_8-SWNT networks on quartz in dry (black curve) and 43% relative humidity (RH; purple curve) atmospheres, as well as on H-quartz in dry (red curve) and 43% RH (blue curve) atmospheres.

During the oxygen-exposure periods of 200 seconds the device response did not saturate, but we found that the rate of change in the network conductance scaled with the concentration of oxygen. Figure 11-16b shows the rate of conductance change (ΔG relative to G_{ON}) during oxygen-exposure cycles. Based on the standard deviation in the ON-state conductance before the first oxygen exposure, we calculated a signal-to-noise ratio of 4.44 for the device response to 5% oxygen. The linear response to oxygen and repeated return to the ON-state conductance indicate that the Eu_8-SWNT network did not experience any photodegradation or chemical damage during operation. Using a value three times the standard deviation of the ON-state conductance as the minimum detection limit (MDL), we determined that the MDL of our unoptimized devices is approximately 0.8% oxygen for an exposure time of 200 seconds, which is comparable with state-of-the-art, high-temperature metal–oxide semiconductor sensor platforms[358].

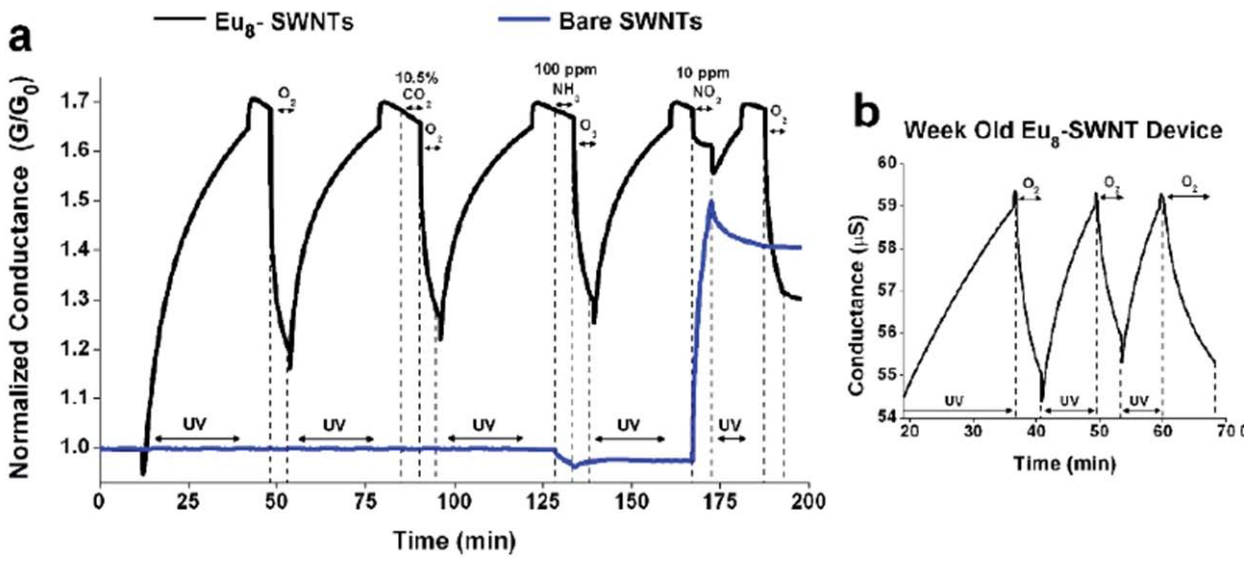

Figure 11-15. Single device containing two individually addressable SWNT networks. a, Simultaneously recorded conductance of a Eu_8-SWNT network (black curve) and bare SWNT network (blue curve) on a single quartz substrate during illumination with 365 nm UV light (in flowing N_2) and exposure to pure O_2, 10.5 % CO_2, 100 ppm NH_3 and 10 ppm NO_2. The bare SWNT device was masked as to eliminate illumination with UV light. After each UV light exposure the device remained in flowing N_2 for a period of five minutes, and each gas exposure was for a period of five minutes. After CO_2, NH_3 and NO_2 exposures the device was exposed again to pure O_2, and the device conductance was returned to its ON-state conductance with UV light. We found that the Eu_8-SWNT device showed insignificant response to CO_2 and NH_3. Specifically, the average drift of the device in flowing N_2 after each UV light exposure was -2.7 ± 0.3%, and the response during CO_2 and NH_3 exposure was -3.0% and -2.4%, respectively. We found that the Eu_8-SWNT network did respond to NO_2, but comparing the response of the Eu_8-SWNT network to the bare SWNT network during NO_2 exposure is a convenient means to eliminate the false positive. Since bare SWNT networks will readily respond to most oxidizing and reducing species, this method creates an internal reference against false response. b, Response of the Eu_8-SWNT device to multiple 200 second O_2 exposures after restoration of the ON-state conductance with 365 nm light one week after the initial measurement shown in panel a; the full UV exposure is not shown. We found that the Eu_8-SWNT couple retained electrical sensitivity to 365 nm light and O_2 even after storing the device under ambient conditions for one week after the initial measurement, suggesting again that UV illumination under inert conditions did not induce chemical damage or oxidation of the device surface.

Finally, the Eu_8-SWNT devices showed a comparable photoresponse with nitrogen as the carrier gas, demonstrated insignificant response to CO_2 and NH_3, were not affected adversely by relative humidity (0–43%, Figure 11-14) and retained good oxygen sensitivity, even with storage of the device in ambient conditions up to one week after the initial measurement. Typical of most solid-state oxygen sensors, we observed sensitivity towards NO_2. To identify false positives caused by oxidizing species we created a device that contained both a Eu_8-SWNT network and a bare SWNT network (Figure 11-16). Bare SWNTs respond to oxidizing gases, such as NO_2, [324] but do not respond to oxygen, so this device design provides an internal reference against the measurement of false positives. By monitoring the simultaneous conductance of both networks during ultraviolet, oxygen and NO_2 exposure we determined the difference between a true oxygen response and a false response caused by NO_2 (for further discussion, see Figure 11-15).

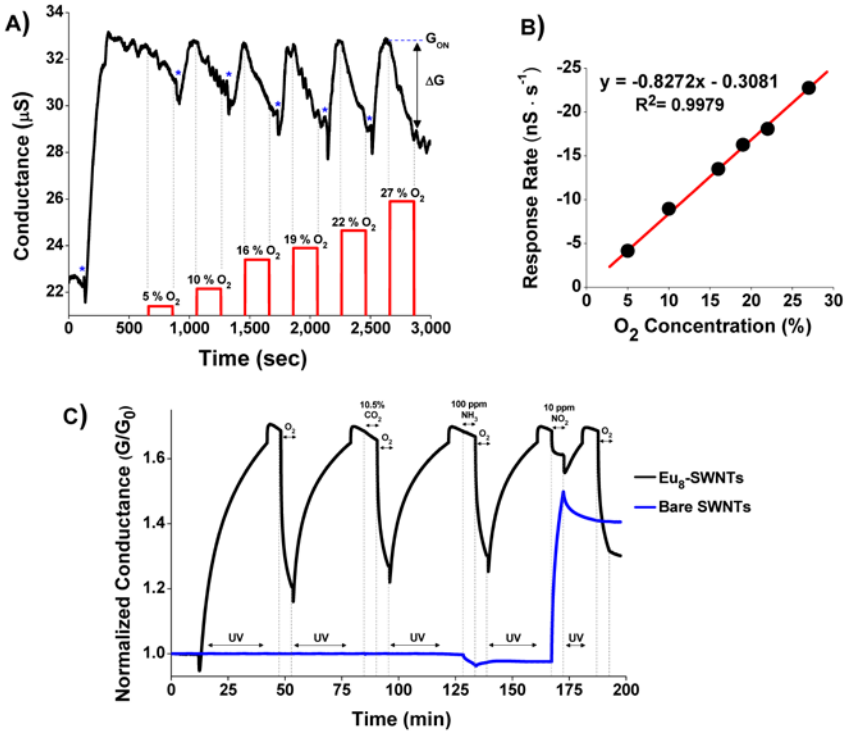

Figure 11-16. Electrical response of a Eu_8-SWNT device with varying oxygen concentrations. a, Network conductance of the Eu_8-SWNT device during gas exposure cycles (200 seconds) of pure argon and increasing oxygen concentrations (in argon) at 0% relative humidity. The dotted lines represent the period of oxygen delivery, the red bars represent the delivered oxygen concentration and the blue asterisks represent the initiation of brief ultraviolet illumination periods (365 nm light, flowing argon) that returned the device to a designated ON-state conductance (G_{ON}). During the first several seconds of ultraviolet illumination the device experienced abrupt, but temporary, decreases in network conductance, before increasing towards the photogenerated ON-state conductance. b, Electrical response rate of the Eu_8-SWNTdevice to increasing oxygen concentrations during an exposure cycle of 200 seconds; the response rate is defined as the change in network conductance (ΔG as measured from G_{ON}) during an oxygen-exposure period. c, Simultaneously recorded conductance of a Eu_8-SWNT network (black curve) and bare SWNT network (green curve) on a single quartz substrate during illumination with 365 nm ultraviolet light (in flowing nitrogen) and exposure to pure oxygen, 10.5% CO_2, 100 ppm NH_3 and 10 ppm NO_2. The bare SWNT device was masked to eliminate illumination with ultraviolet light. After each ultraviolet light exposure the device remained in flowing nitrogen for a period of five minutes, and each gas exposure was for a period of five minutes. After CO_2, NH_3 and NO_2 exposures the device was exposed again to pure oxygen, and its conductance returned to that of its ON-state with ultraviolet light.

The insignificant sensitivity towards CO_2 and NH_3, identifiable response to an oxidizing species (NO_2) and comparable device operation in nitrogen and humid atmospheres indicate that this system holds promise as a low-temperature platform for monitoring oxygen levels under ambient conditions. However, in the design of a field-usable platform we need to take into consideration the requirement for a small reservoir of inert gas, such as nitrogen or argon, to purge the sample chamber during illumination with a compact ultraviolet light source.

11.7 CONCLUSIONS

We have used SWNT networks as a tool to establish a mechanistic understanding of the solid-state oxygen sensitivity observed in the Eu_8 system. When incorporated into electrically conductive and optically transparent devices, the Eu_8-SWNT system shows bimodal (optical spectroscopic and electrical conductance) sensitivity to oxygen gas at room temperature and ambient pressure. Using Eu_8-SWNT devices as chemiresistors, we have demonstrated a linear and reversible response to environmentally relevant oxygen concentrations between 5 and 27%, with a calculated MDL of 0.8% oxygen. The response of Eu_8-SWNTs towards ultraviolet light and oxygen gas is completely unlike that of bare SWNTs, and allows us to explore the mechanisms of device behavior without the controversy concerning the direct interaction between SWNTs and oxygen[359]. Ultimately, incorporation of the Eu_8-SWNT system into low-power, microelectronic devices may find a broad range of applications in civilian and military arenas as personal safety devices for workers in confined spaces or for ambient-level oxygen

sensors for enclosed working environments in which space, weight and energy consumption are at a premium, such as in mines, aircraft, submarines or spacecraft.

Acknowledgements

The authors thank D. H. Waldeck for his comments, and acknowledge the facilities, scientific and technical assistance of the Materials Micro-Characterization Laboratory of the Department of Mechanical Engineering and Materials Science, Swanson School of Engineering, University of Pittsburgh. This work was performed in support of ongoing research in sensor systems and diagnostics at the National Energy Technology Laboratory under RDS contract DE-AC26-04NT41817.

12.0 HYDROPHOBIC CHROMOPHORE CARGO IN MICELLAR STRUCTURES: A DIFFERENT STRATEGY TO SENSITIZE LANTHANIDE CATIONS

12.1 CHAPTER PREFACE

The aim of this work was to develop a new strategy whereby the antenna effect can be studied between luminescent lanthanide cations and organic chromophores eventhough the organic ligands may not possess chelating moieties. This work is also another example of the concept of maximizing the density of lanthanide cations and lanthanide sensitizers per unit volume. Our work presented in Chapter 7.0 informed our choice of 2,3-naphthalimide as a suitable antenna to demonstrate the usefulness of such a technique. Here we intended to highlight a new and rapid tool to serve researchers interested in luminescent lanthanide chemistry. In addition to our experimental work, we engaged in a collaboration with other lanthanide chemists working in the field of MRI contrast agents. The material contained in this chapter was published as a communication in the journal *Chemical Communications*; the figures in this chapter have been reproduced with permission from *Chem. Commun.* **2010**, *46(1)*, 124. Copyright 2010 Royal Society of Chemistry (RSC); the full citation is listed as Reference 360 in the bibliography section.[360]

List of authors: Célia S. Bonnet, Laurent Pellegatti, Frédéric Buron, Chad M. Shade, Sandrine Villette, Vojtěch Kubíček, Gérald Guillaumet, Franck Suzenet, Stéphane Petoud, Éva Tóth

Author contributions: The author of this dissertation was responsible for the Eu^{3+}-centered luminescence lifetime measurements of the micelles above and below the critical micelle concentration (cmc) in H_2O and D_2O and performing the q-value analysis, contributed to the design of the experiments, interpretation of the results and preparation of the published manuscript.

12.2 ABSTRACT

We propose a new approach for the versatile sensitization of luminescent lanthanide cations. A hydrophobic chromophore is incorporated into a micellar assembly formed by the amphiphilic lanthanide chelate. The sensitizer to lanthanide energy transfer occurs between the two moieties without covalent linkage.

12.3 INTRODUCTION

Lipid-based colloidal aggregates such as liposomes, micelles or microemulsions are gaining importance in molecular imaging since they allow for a marked sensitivity enhancement due to

the great payload of magnetic or optical reporters within a single particle.[361,362] Their further functionalization can provide biocompatibility or targeting ability.[361,362] Amphiphilic systems are also extensively exploited in vivo as carriers of hydrophobic drugs.[363] Micellar aggregations allow exploiting dynamic interactions promoted between molecules being part of the same micelle, even if they are not linked by a covalent bond. The micelle and its molecular content behave as a self-assembled, multicomponent nanosized device. For instance, intramicellar energy and electron transfer can be realized between a fluorophore and a lipophilic metal complex to create molecular logic gates,[364] fluorescent micellar sensors for ions[365] or pH.[366]

Lanthanide complexes are used as luminescent reporters in several biological applications.[28,33,367] They require a chromophore to sensitize their luminescence in order for the compound to emit a sufficient number of photons.[30] To ensure efficient energy transfer, this chromophore needs to be placed in close proximity of the luminescent cation. Classically, this goal is achieved by covalently linking the appropriate chromophore to the metal chelating moiety which often requires difficult and time-consuming synthetic procedures. The efficiency of the chromophore can only be determined by the test of the final compound.

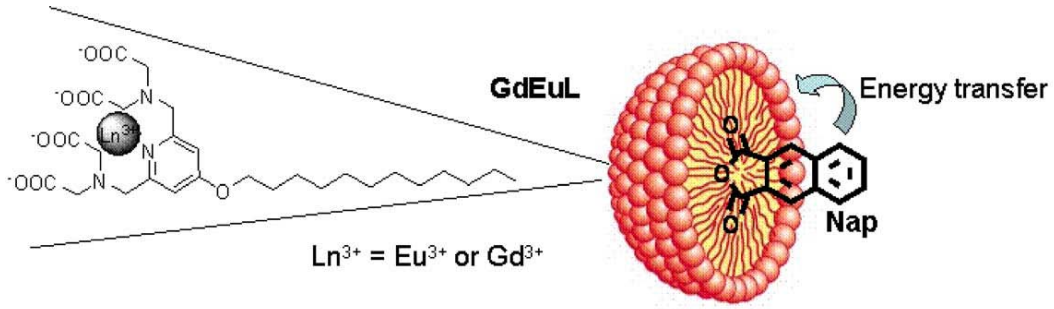

Figure 12-1. Schematic representation of the micelle with the inclusion of the naphthalimide.

We propose here an alternative strategy for the rapid development and screening of luminescent lanthanide compounds and sensitizers. Our approach is to incorporate the hydrophobic chromophore in a micelle that consists of amphiphilic chelates of the luminescent lanthanide and to use the energy transfer between the two non-covalently linked moieties (Figure 12-1). This concept combines several advantages: (i) the use of hydrophobic chromophores including large aromatic moieties with a high level of conjugation that are poorly soluble in aqueous solution, (ii) the use of chromophores that do not possess binding groups for the formation of coordination bonds with the lanthanide cations, (iii) the formation of polymetallic lanthanide compounds. These micelles contain both the lanthanide and the chromophore in a large amount which allows maximizing the overall absorbance and the number of emitted photons per unit of volume for more sensitive detection even with low quantum yields.

Hydrophobic fluorescence dyes, like pyrene derivatives, exhibit different fluorescence characteristics depending upon the properties of the solubilizing medium and have been used for a long time to study micellization.[368] More recently, aggregation induced emission of

fluorophores has been exploited to monitor micelle formation.[369] On the other hand, in DELFIA dissociative luminescent assays, amphiphilic surfactants are commonly used to protect the lanthanide compound from dissociation and from non-radiative deactivation in a micelle-like structure.[370] We emphasize that our strategy is fundamentally different from any of these approaches since it takes advantage of the micellar structure as a platform to integrate both the lanthanide complex and the chromophore in close proximity, without covalent linkage.

12.4 EXPERIMENTAL

Synthesis of Diethyl 4-hydroxy-2,6-pyridinedicarboxylate (1). Concentrated sulphuric acid (566µL, 0.011mol, 20 mol %) was added dropwise to a suspension of commercially available chelidamic acid (10.63g, 0.053mol) in ethanol (350mL). The solution was refluxed and stirred during 24 hours. The solvent was evaporated under reduced pressure after return at room temperature. Water and ethyl acetate are added to the oily residue and the organic layer was dried over $MgSO_4$ and concentrated under reduced pressure. The compound **(12)** (10.905g) was obtain by purification on column chromatography (CH_2Cl_2/MeOH; 98:2 to 95:5) as a white solid. Yield: 86%. **NMR^{1}H (DMSO)** δ **(ppm):** 7.57 (s, 2H, H3/5); 4.35 (q, 4H, H8, J_3=7.0Hz); 1.33 (t, 6H, H9, J_3=7.0Hz). **NMR^{13}C (DMSO)** δ **(ppm):** 166.0 (C7); 164.3 (C4); 149.9 (C2/6); 115.2 (C3/5); 61.4 (C8); 14.1 (C9). **IR:** ν (cm^{-1}) 2985, 1738, 1722, 1603, 1458, 1332, 1228, 999, 791. **MS (Ionspray®)** m/z: 240 $(M+H)^+$, 262.5 $(M+Na)^+$. **T_f :** 121-122°C.

Synthesis of Diethyl 4-dodecyloxy-2,6-pyridinedicarboxylate (2). Potassium carbonate (1.49g, 10.78mmol, 5.0 equiv.) was added to a solution of 4-hydroxy-2,6-pyridinedicarboxylatediethyle **(1)** (516mg, 2.16mmol) in acetonitrile (25mL). 1-Bromododecane (1.34mL, 5.54mmol, 1.0 equiv) was added dropwise. The mixture was refluxed with vigorous stirring during 18 hours. Water was added to the cooled reaction until total dissolution of the potassium carbonate. Acetonitrile was evaporated under reduced pressure and the aqueous layer was extract with CH_2Cl_2. Organics layers were dried over $MgSO_4$ and concentrated. The compound **(2)** (2.135g) was obtain after purification on column chromatography (CH_2Cl_2/MeOH; 98:2) as a white solid. Yield: 95%. **NMR^{1}H ($CDCl_3$)** δ **(ppm) (see Figure 12-2):** 7.77 (s, 2H, H3/5); 4.47 (q, 4H, H8, J_3=7.3Hz); 4.13 (t, 2H, OCH_2, J_3=6.5Hz); 1.84 (qt, 2H, CH_2alkyl, J_3=6.5Hz); 1.46 (m, 8H, CH_2alkyl, H9); 1.26 (m, 16H, CH_2alkyl); 0.88 (t, 3H, CH_3alkyl, J_3=6.5Hz). **NMR^{13}C ($CDCl_3$)** δ **(ppm) (see Figure 12-3):** 167.2 (C7); 164.9 (C4); 150.2 (C2/6); 114.5 (C3/5); 69.2 (CH_2alkyl); 62.5 (C8); 32.0 (CH_2alkyl); 29.8 ($2CH_2$alkyl); 29.7 (CH_2alkyl); 29.6 (CH_2alkyl); 29.4 (CH_2alkyl); 28.9 (CH_2alkyl); 26.0 (CH_2alkyl); 22.8 (CH_2alkyl); 14.3 (C9); 14.2 (CH_3alkyl). **IR :** ν (cm^{-1}) 2917, 2848, 1714, 1598, 1340, 1249, 1108, 1031, 785. **MS (Ionspray®)** m/z : 408.5 $(M+H)^+$. **T_f :** 47-48°C.

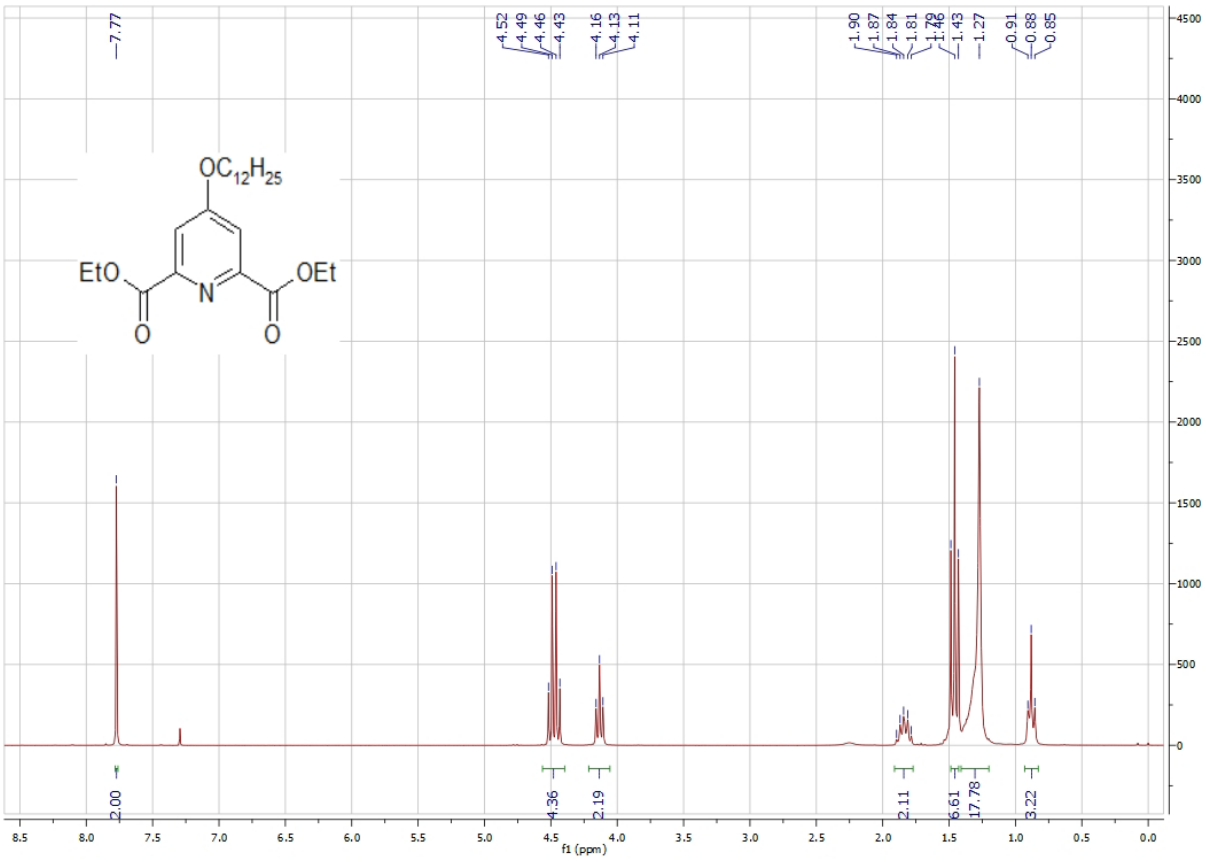

Figure 12-2. ^{1}H NMR spectra of the synthesized diethyl 4-dodecyloxy-2,6-pyridinedicarboxylate (2).

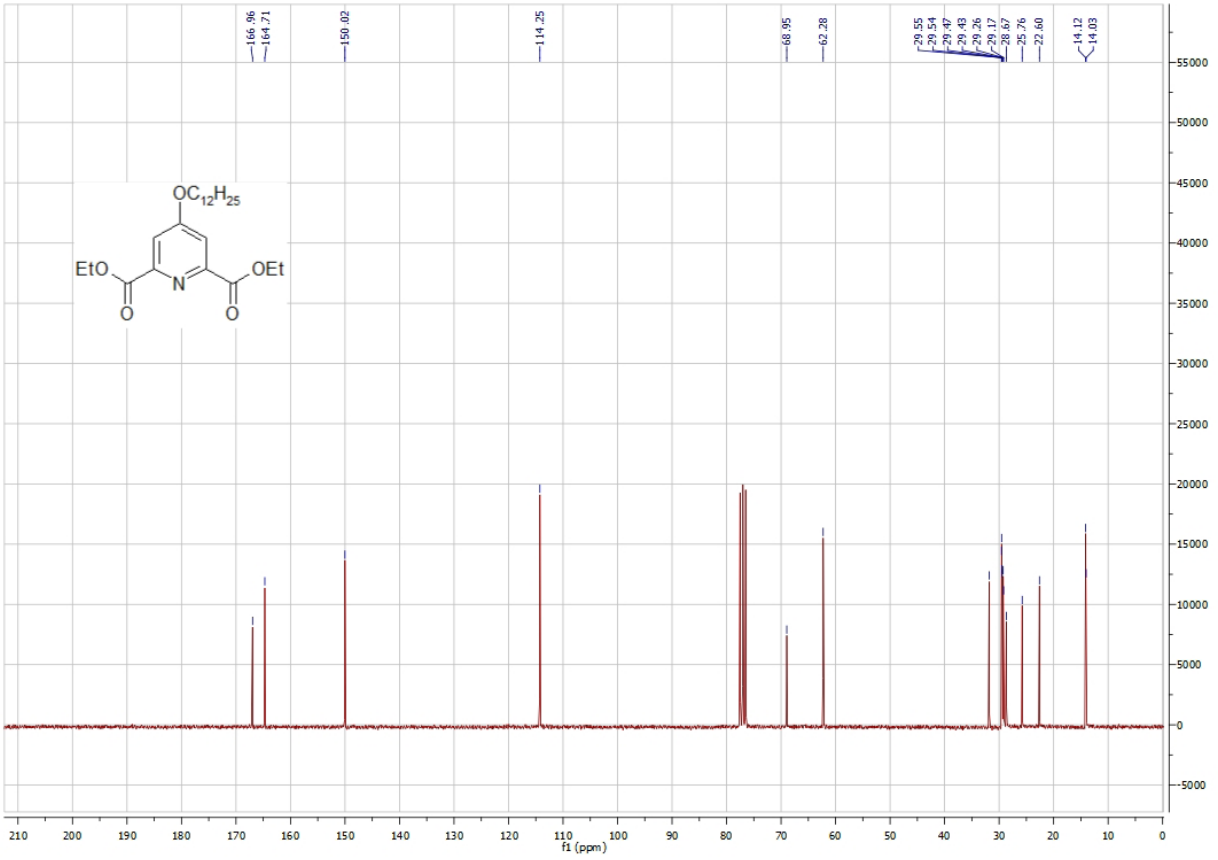

Figure 12-3. ^{13}C NMR spectra of the synthesized diethyl 4-dodecyloxy-2,6-pyridinedicarboxylate (2).

Synthesis of 4-Dodecyloxy-2,6-dihydroxymethylpyridine (3). MeOH (15mL) was added over a period of 1h to a boiling mixture of 4-dodecyloxy-2,6-pyridinedicarboxylatediethyle **(2)** (300mg, 0.74mmol) and $NaBH_4$ (140mg, 1.1mmol, 1.5 eq.)) in THF (40mL). The reaction mixture was refluxed for an additional 2 hours, then cooled and slowly diluted with H_2O (30mL). The precipitate was filtered. The compound **(3)** (238mg) is obtained without purification as a white solid. Yield: 92%. **NMR^{1}H (MeOD) δ (ppm) (see Figure 12-4):** 6.97 (s, 2H, H3/5); 4.62 (s, 4H, H7); 4.11 (t, 2H, O-CH_2, J_3=6.5Hz); 1.82 (qt, 2H, CH_2alkyl, J_3=6.75Hz); 1.48 (m, 2H,

CH_2alkyl); 1.30 (s, 18H, CH_2alkyl); 0.90 (s, 3H, CH_3alkyl, J_3=6.75Hz). **NMR^{13}C (MeOD)** δ **(ppm) (see Figure 12-5):** 168.9 (C); 163.7 (C); 106.5 (C); 69.4 (CH_2); 65.4 (CH_2); 33.2 (CH_2); 30.90 (CH_2); 30.88 (CH_2); 30.84 (CH_2); 30.82 (CH_2); 30.60 (CH_2); 30.57 (CH_2); 30.2 (CH_2); 27.2 (CH_2); 23.9 (CH_2); 14.6 (CH_3). **IR :** ν (cm^{-1}) 3323, 2921, 2847, 1599, 1463, 1354, 1325, 1156, 1035, 866. **T_f :** 84°C.

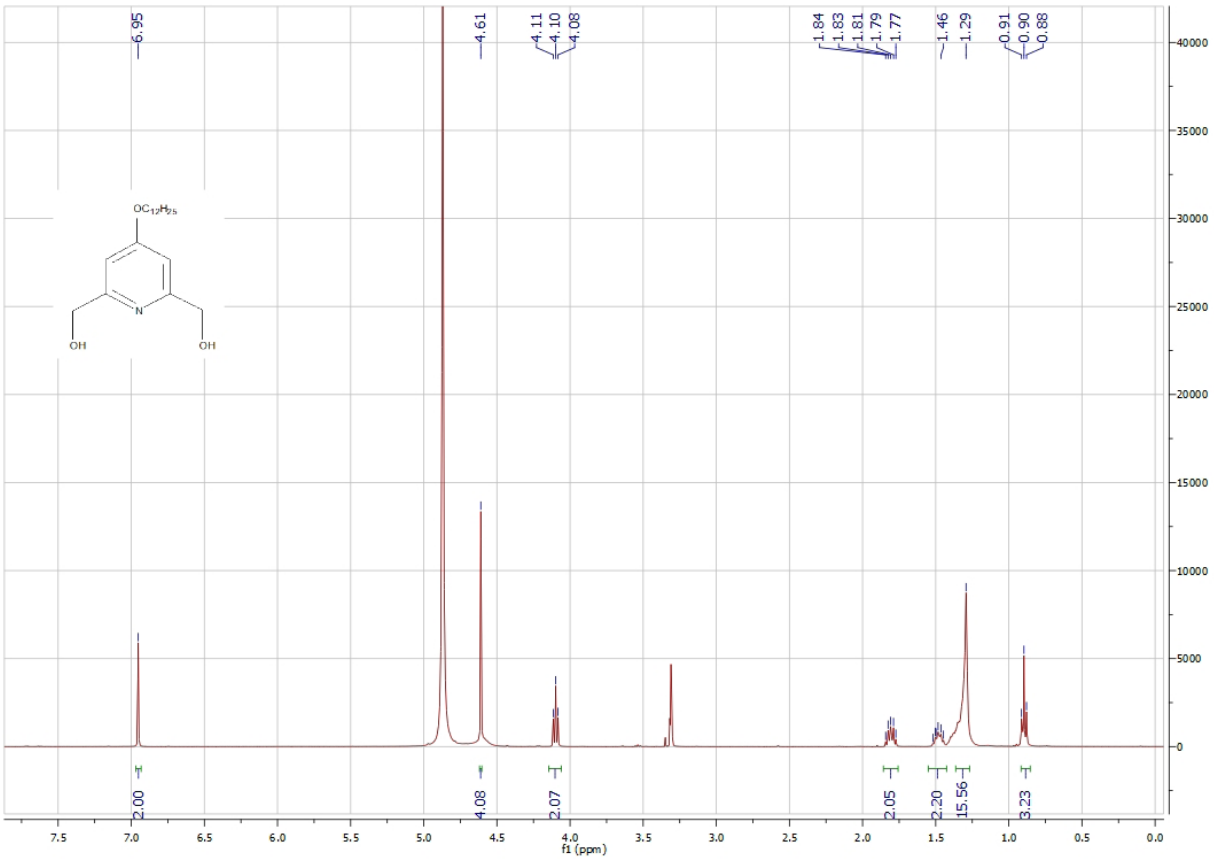

Figure 12-4. ^{1}H NMR spectra of the synthesized 4-dodecyloxy-2,6-dihydroxymethylpyridine (3).

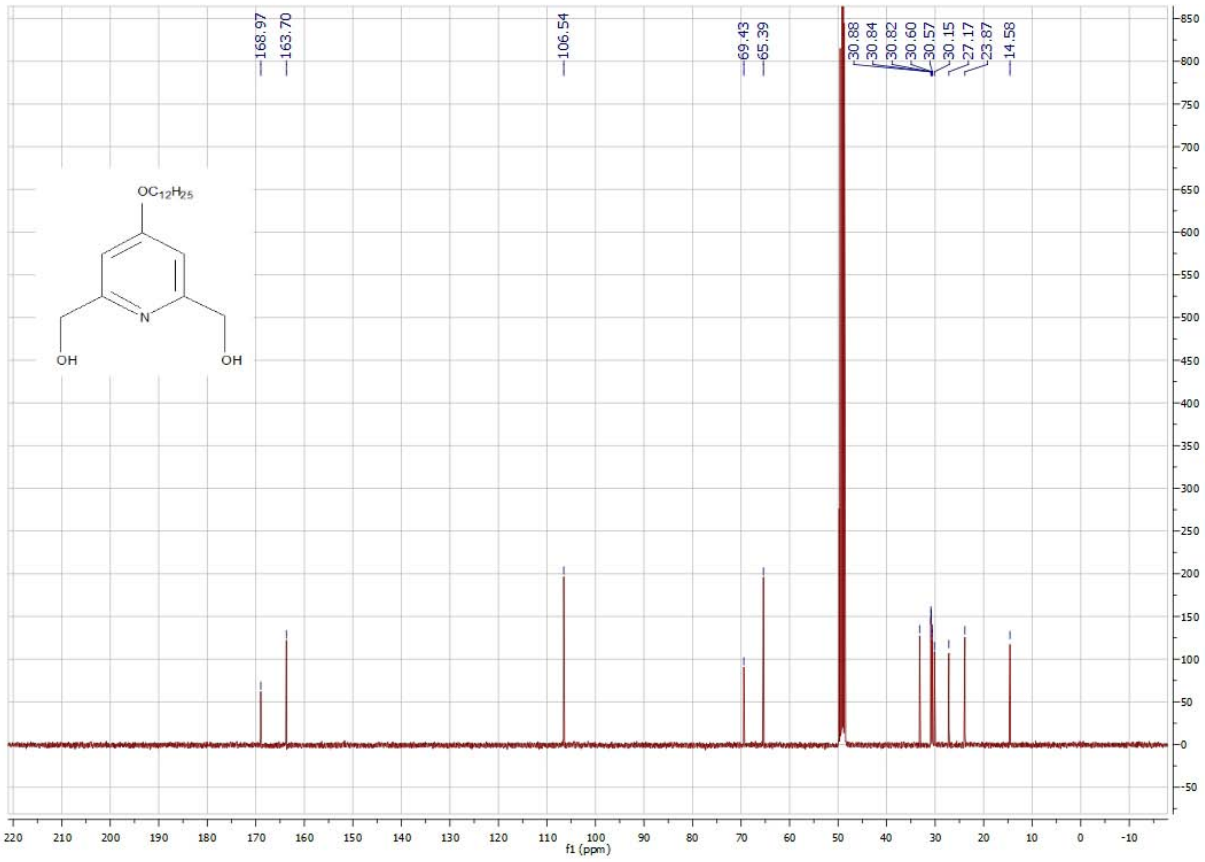

Figure 12-5. ^{13}C NMR spectra of the synthesized 4-dodecyloxy-2,6-dihydroxymethylpyridine (3).

Synthesis of 4-Dodecyloxy-2,6-dibromomethylpyridine (4). PBr_3 (511µL) in $CHCl_3$ (20mL) was added dropwise to a suspension of 4-dodecyloxy-2,6-dihydroxymethylpyridine **(3)** (220mg) in $CHCl_3$ (20mL) at room temperature. The mixture was refluxed during 16 hours. After cooling at room temperature we added $NaHCO_3$ 1M (100mL) and the solution is stirred during 1 hour until it became clear. The organic layer was dried and concentrated under reduced pressure. The compound **(4)** was obtained without purification by filtration as a white solid. Yield: 100%. **NMR^{1}H ($CDCl_3$) δ (ppm) (see Figure 12-6):** 6.87 (s, 2H, H3/5); 4.47 (s, 4H, H7); 4.02 (t, 2H,

O-CH_2, J_3=6.5Hz); 1.80 (qt, 2H, CH_2alkyl, J_3=6.75Hz); 1.43 (m, 2H, CH_2alkyl); 1.27 (s, 18H, CH_2alkyl); 0.88 (s, 3H, CH_3alkyl, J==6.75Hz). **NMR^{13}C ($CDCl_3$) δ (ppm) (see Figure 12-7):** 166.7 (C4); 158.1 (C2/6); 109.3 (C3/5); 68.4 (CH_2alkyl); 33.7 (C7); 31.9 (CH_2alkyl); 29.6 (CH_2alkyl); 29.6 (CH_2alkyl); 29.5 (CH_2alkyl); 29.5 (CH_2alkyl); 29.3 (CH_2alkyl); 29.3 (CH_2alkyl); 28.8 (CH_2alkyl); 25.9 (CH_2alkyl); 22.7 (CH_2alkyl); 14.1 (CH_3alkyl). **IR :** ν (cm^{-1}) 2921, 2850, 1596, 1467, 1341, 1163, 1038, 891, 653. **T_f :** 52°C.

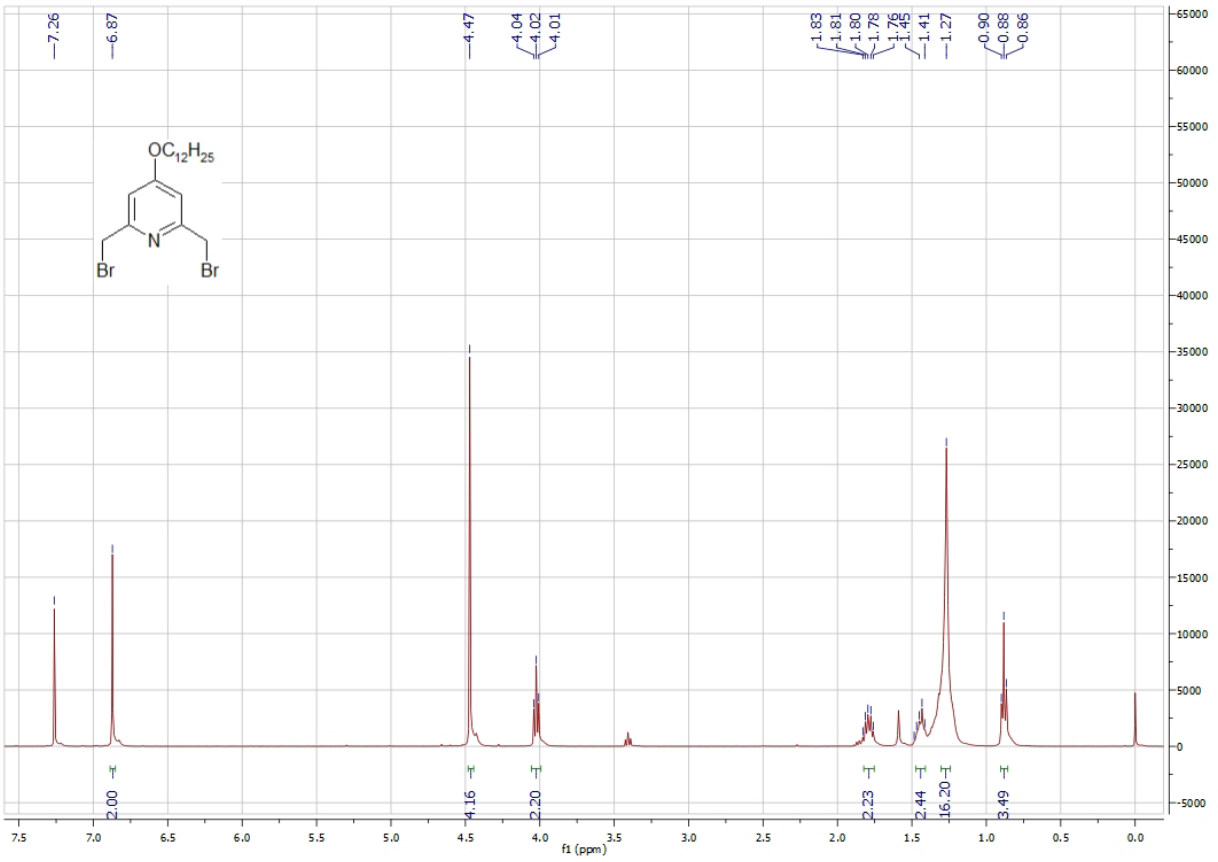

Figure 12-6. ^{1}H NMR spectra of the synthesized 4-dodecyloxy-2,6-dibromomethylpyridine (4).

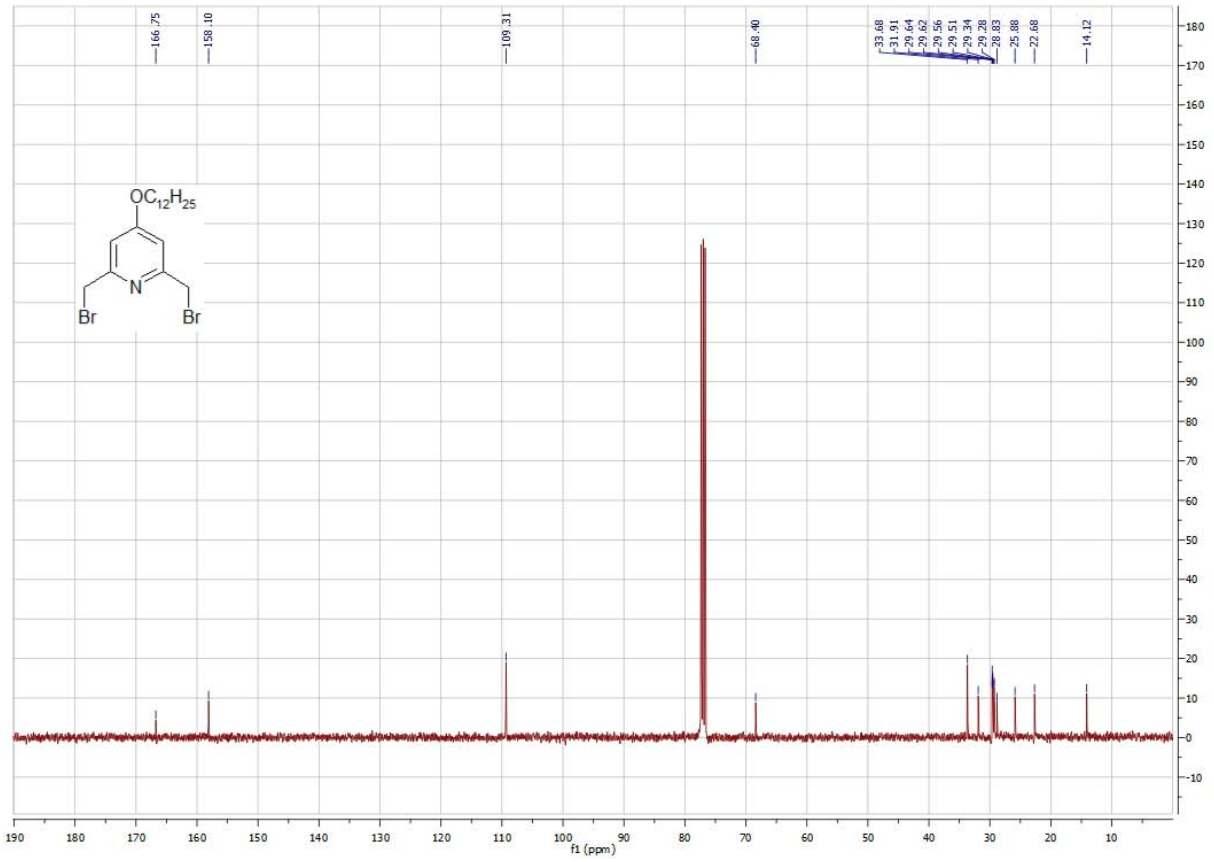

Figure 12-7. ^{13}C NMR spectra of the synthesized 4-dodecyloxy-2,6-dibromomethylpyridine (4).

Synthesis of 4-Dodecyl-2,6-((bis(ethylcarboxymethyl)amino)methyl)pyridine (5). A mixture of 4-dodecyloxy-2,6-dibromomethylpyridine (**4**) (305mg, 0.8mmol) , potassium carbonate (375mg, 3.2mmol, 4 eq.) and potassium iodide (225mg, 1.6mmol, 2eq.) was dissolved into acetonitrile (50mL). Iminodiethyl acetate (237µL, 1.6mmol, 2 eq.) is then added. The mixture was refluxed during 12 hours. After cooling to room temperature, the excess of potassium carbonate was dissolved by adding water and acetonitrile is evaporated. The aqueous layer was extracted with methylene chloride and the crude was concentrated under reduced pressure. The

compound **(5)** was obtained without purification as a pale yellow solid paste (330mg). Yield: 75%. **NMR^{1}H ($CDCl_3$)** δ **(ppm) (see Figure 12-8):** 7.05 (s, 2H, H3/5); 4.17 (q, 8H, H10, J_3=7.2Hz); 4.00(t, 2H, OCH_2, J_3=6.4Hz); 3.98 (s, 4H, H7); 3.60 (s, 8H, H8); 1.77 (qt, 2H, CH_2alkyl, J_3=6.4Hz); 1.44 (m, 2H, CH_2alkyl); 1.27 (m, 28H, CH_2alkyl, H11); 0.88 (s, 3H, CH_3alkyl, J_3=6.8Hz). **NMR^{13}C ($CDCl_3$)** δ **(ppm) (see Figure 12-9):** 175.9 (C9); 171.4 (C4); 160.0 (C2/6); 107.6 (C3/5); 67.9 (OCH_2alkyl); 60.5 (C10); 59.9 (C7); 54.9 (C8); 31.9 (CH_2alkyl); 29.7 (CH_2alkyl); 29.6 (CH_2alkyl); 29.6 (CH_2alkyl); 29.5 (CH_2alkyl); 29.4 (CH_2alkyl); 29.3 (CH_2alkyl); 29.2 (CH_2alkyl); 25.9 (CH_2alkyl); 22.7 (CH_2alkyl); 14.2 (C11); 14.1 (CH_3alkyl). **IR:** ν (cm^{-1}) : 3019, 2927, 1739, 1215, 745. **MS (Ionspray®)** m/z: 666.5 $(M+H)^+$, 688.5 $(M+Na)^+$.

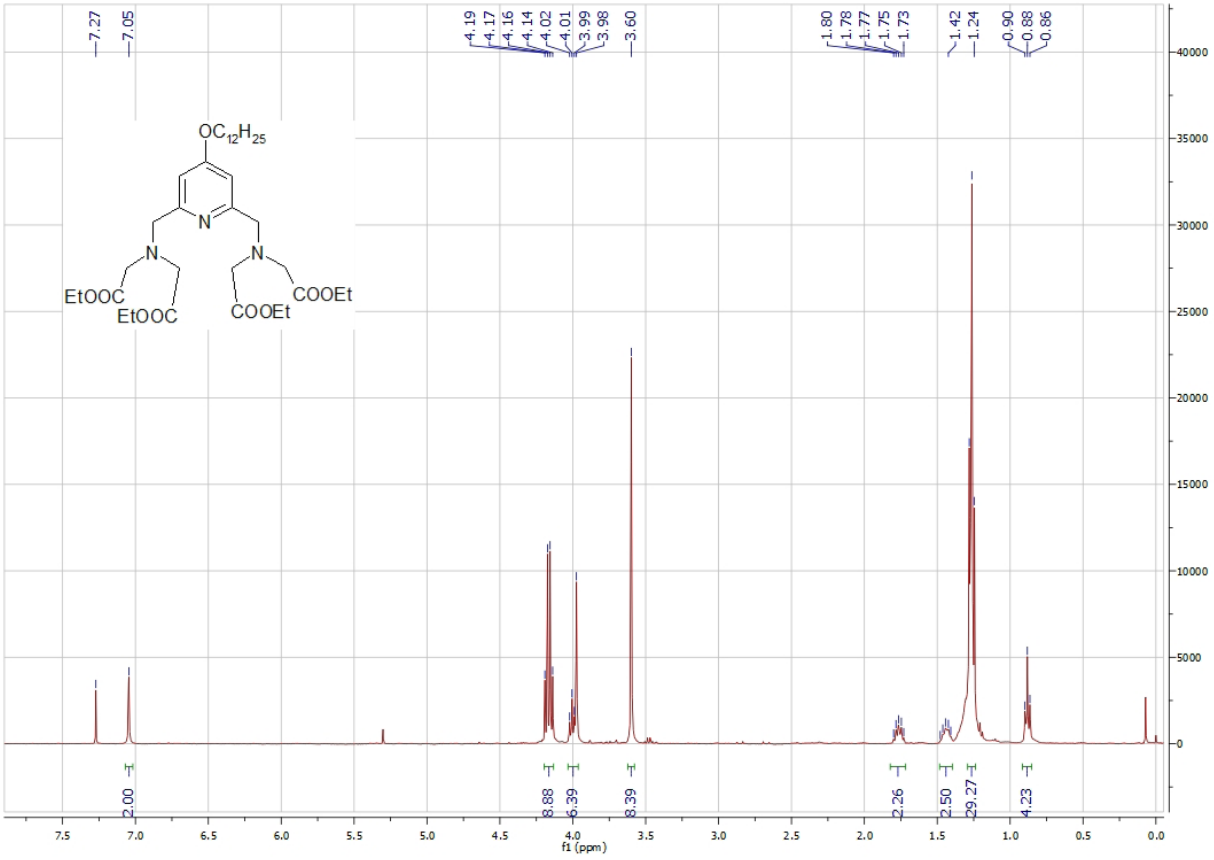

Figure 12-8. ^{1}H NMR spectra of synthesized 4-dodecyl-2,6-((bis(ethylcarboxymethyl)amino)methyl)pyridine (5).

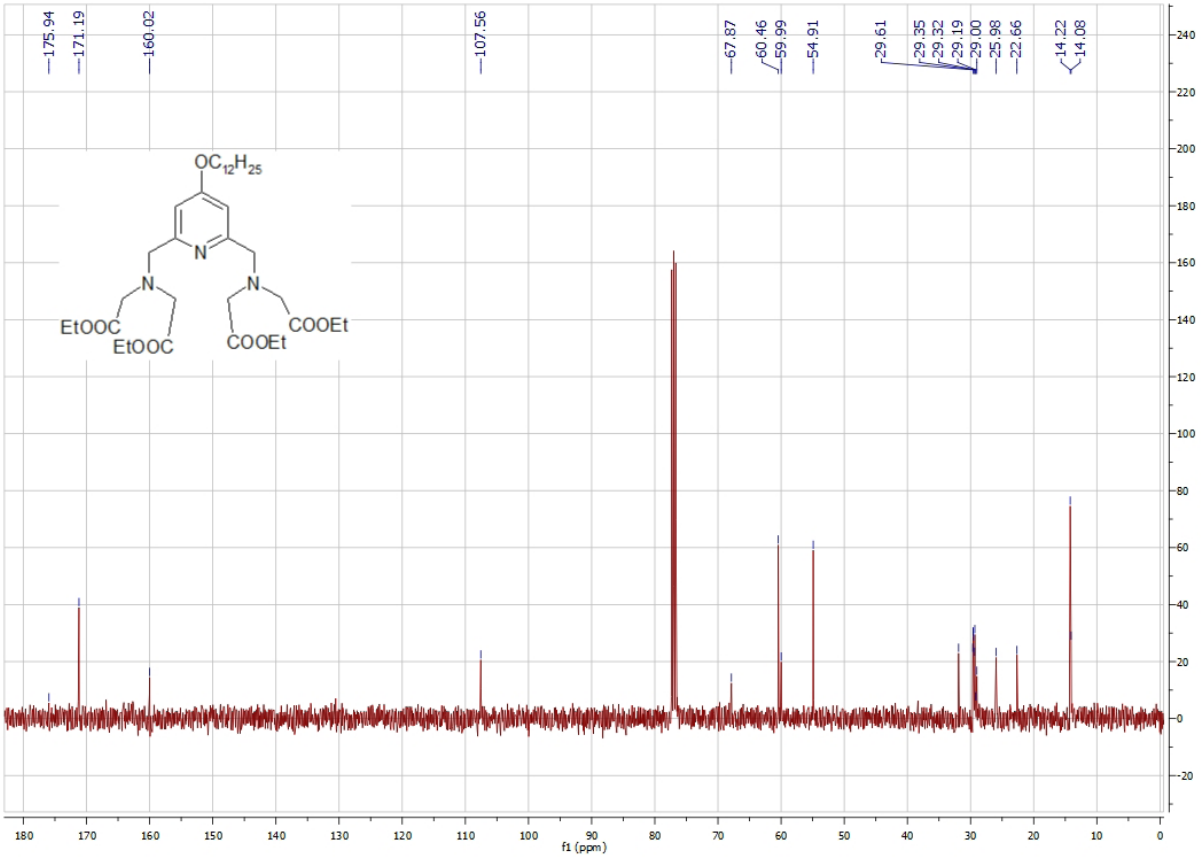

Figure 12-9. ^{13}C NMR spectra of synthesized 4-dodecyl-2,6-((bis(ethylcarboxymethyl)amino)methyl)pyridine (5).

Synthesis of 4-Dodecyl-2,6-((bis(carboxymethyl)amino)methyl)pyridine (6). Esters **(5)** (1.42g, 2.12mmol) was dissolved in THF (25mL) and water (25mL) was added. The mixture was cooled to 0°C. LiOH (12eq., 0.61g, 25.52mmol) was then added and the medium was stirred at room temperature during 5 hours. The organic solvent was evaporated and the aqueous mixture was purified on an anionic exchange resin (DOWEX 1X2-100Cl) (washed with H_20/MeOH; 99/1 and eluted with formic acid 1M) to furnish the ligand **(6)** (573.4mg, 77% yield) as a white solid. **NMR^{1}H (DMSO) δ (ppm) (see Figure 12-10):** 7.08 (s, 2H, H3/5); 4.06(t, 2H, O-CH_2,

J_3=6.4Hz); 3.95 (s, 4H, H7); 3.47 (s, 8H, H8); 1.72 (qt, 2H, CH_2alkyl, J_3=6.4Hz); 1.38 (m, 2H, CH_2alkyl); 1.24 (m, 16H, CH_2alkyl); 0.85 (t, 3H, CH_3alkyl, J_3=6.8Hz). **NMR^{13}C (DMSO)** δ **(ppm) (see Figure 12-11):** 172.6 (C); 166.3 (C); 160.1 (2C); 107.1 (2C); 67.7 (CH_2); 58.8 (CH_2); 54.9 (CH_2); 31.3 (CH_2); 29.0 (CH_2); 28.9 (3xCH_2); 28.3 (CH_2); 25.4 (CH_2); 22.1 (CH_2); 13.9 (CH_3). **IR:** ν (cm^{-1}): 3448, 2996, 2922, 1725, 1610. **T_f :** 129-130°C

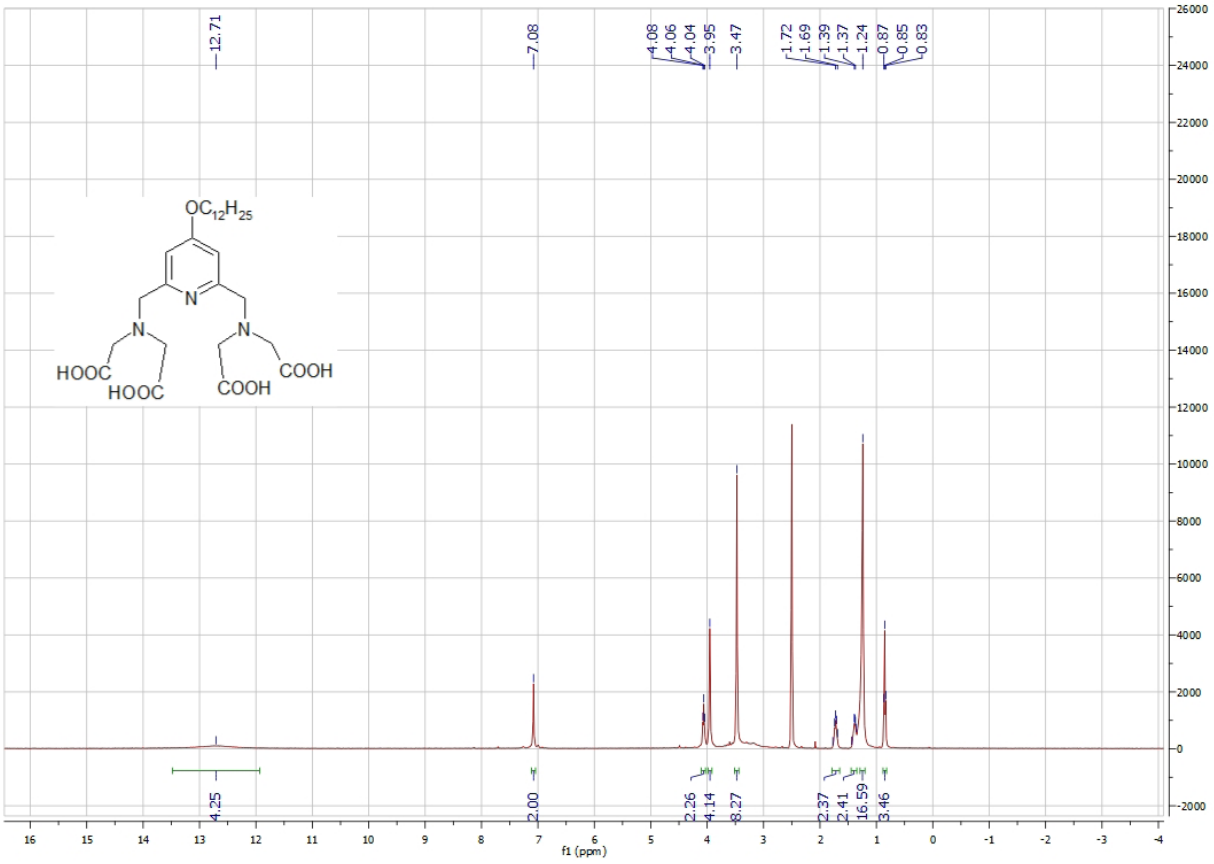

Figure 12-10. ^{1}H NMR spectra of synthesized 4-Dodecyl-2,6-((bis(carboxymethyl)amino)methyl)pyridine (6).

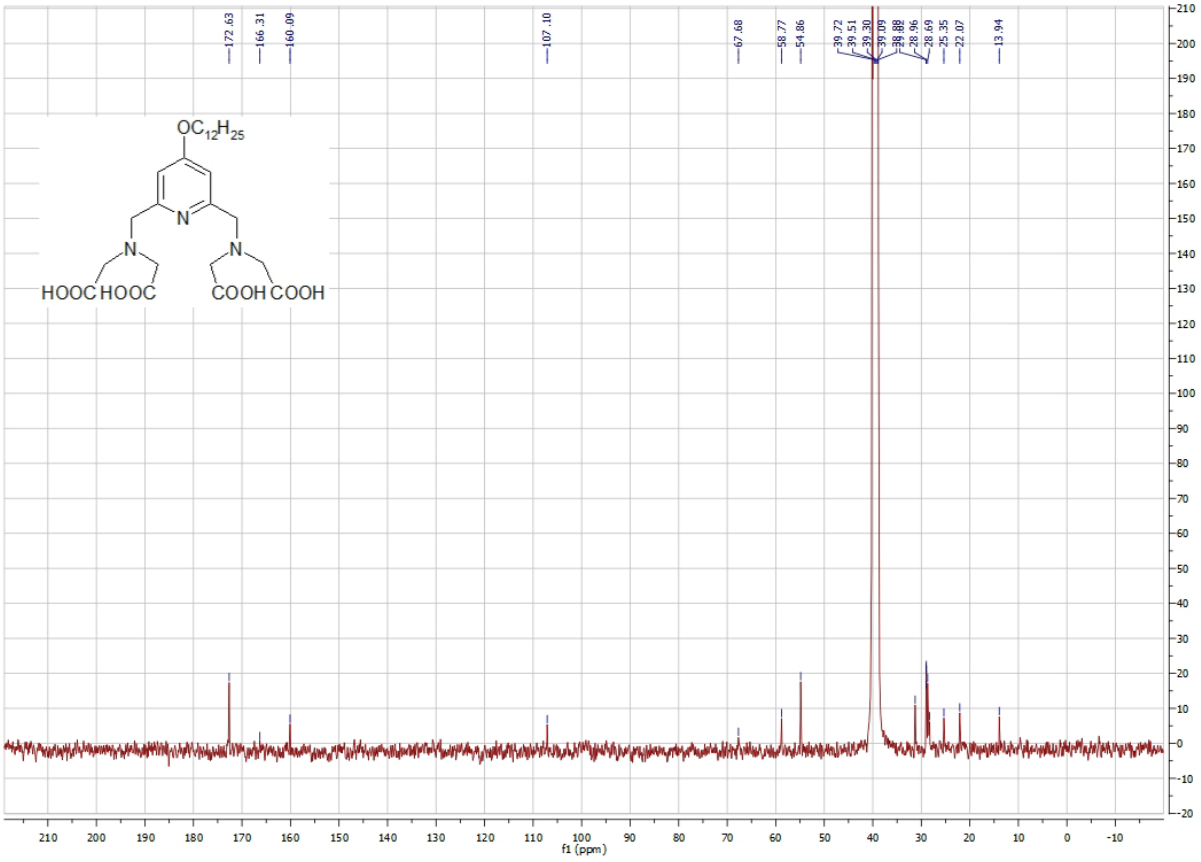

Figure 12-11. ^{1}H NMR spectra of synthesized 4-Dodecyl-2,6-((bis(carboxymethyl)amino)methyl)pyridine (6).

Photophysical Measurements. Absorbance UV spectra were performed on an Uvikon spectrophotometer. Emission and excitation spectra were measured using modified Jobin-Yvon Horiba Fluorolog-322 spectrofluorimeter equipped with a Hamamatsu R928 detector. Spectra were recorded in a quartz triangular luminescence cell. Settings for time-delayed fluorescence were: time delay after flash of 0.1 ms, sample window of 2 ms, time per flash of 61 ms and 10 flash counts. The emission spectra were recorded using a 385 nm cut-off filter, after an excitation

at 345 nm. The excitation spectra were recorded with a 495 nm cut-off filter, monitoring the emission at 614 nm.

The Eu^{3+} luminescence lifetime measurements were performed by excitation of solutions in 1 mm quartz cells (NSG Precision Cells, Inc.) using a Nd:YAG Continuum Powerlite 8010 laser (266nm, fourth harmonic) as the excitation source. Emission was collected at a right angle to the excitation beam, and wavelengths were selected by means of a Spectral Products CM 110 1/8 meter monochromator (with two independent gratings). The signal was monitored by a Hamamatsu R928 photomultiplier to a 500 MHz bandpass digital oscilloscope (Tektronix TDS 620B). Signals from > 2000 flashes were collected and averaged. Quality of luminescence lifetime data was confirmed by at least two independent measurements. Experimental luminescence decay curves were imported into Origin 7.0 scientific data analysis software, and analyzed using the Advanced Fitting Tool module. The decay curves were best fit with a double exponential fitting mode, based on a reduced chi-square criteria. The lifetimes corresponding unambiguously to Eu^{3+} are reported in Table 12-1.

Table 12-1. Concentration dependence of luminescence lifetimes of the EuL complex. q- values were calculated using the empirical formula described in the reference.[10]

[EuL] (mM)	τ_{D2O} (ms)	τ_{H2O} (ms)	q
30	1.336(1)	0.401(3)	1.7
15	1.404(2)	0.4043(7)	1.8
7.5	1.487(2)	0.3979(2)	1.8
3.75	1.639(2)	0.3738(6)	2.1
1.875	1.743(3)	0.3900(4)	2.0
0.937	1.984(5)	0.3922(5)	2.0
0.467	2.10(1)	0.387(1)	2.1

Steady-state luminescence quantum yields were collected with a modified JY Horiba Fluorolog-322 Spectrofluorimeter, fitted with an integration sphere developed by Frédéric Gumy and Prof. Jean-Claude G. Bünzli (Laboratory of Lanthanide Supramolecular Chemistry, École Polytechnique Féderale de Lausanne (EPFL), BCH 1402, CH- 1015 Lausanne, Switzerland) as an accessory to the Fluorolog-322 spectrometer (Patent pending), using a quartz tube sample holder.[10] Spectra were corrected for variations in lamp output, the non-linear response of the detector, and the use of neutral density filters, where applicable. The calculated values were determined by integrating the emission profiles, averaged from four separate trials, and substitution into the ratio of emitted photons over absorbed photons.

Relaxometric Measurements. Longitudinal relaxation rates have been recorded on a Stelar SMARtracer Fast Field Cycling NMR relaxometer (0.0110 MHz) and a Bruker WP80 NMR electromagnet adapted to variable field measurements and controlled by the SMARtracer PC-NMR console. The temperature was controlled by a VTC91 temperature control unit and maintained by a gas flow. The temperature was determined according to previous calibration with a Pt resistance temperature probe.

12.5 RESULTS AND DISCUSSION

We have recently described bimodal luminescent and MRI contrast agents formed with pyridine-derivative ligands.[371] This chelator simultaneously provides high MRI efficiency for the Gd^{3+} complex (two inner sphere water molecules) and remarkable optical properties for near-infrared emitting lanthanides. The amphiphilic chelate obtained by conjugation of a C12 hydrophobic chain to the pyridine core forms micelles in aqueous solution. A bimetallic micellar system with 10% Eu^{3+} and 90% Gd^{3+}, **GdEuL**, has been prepared. A hydrophobic chromophore (10% with respect to the ligand) was incorporated within the micelle by sonication of the aqueous micellar solution (9.43 mM overall Ln^{3+} concentration). 2,3-Naphthalimide (**Nap**) was chosen as the chromophore as it cannot coordinate to the lanthanide, and can only interact through hydrophobic interactions with the micelle. It is also known as a sensitizer for Eu^{3+} (Figure 12-13).[237] The micellar solution readily dissolves the **Nap** which is otherwise poorly water soluble.

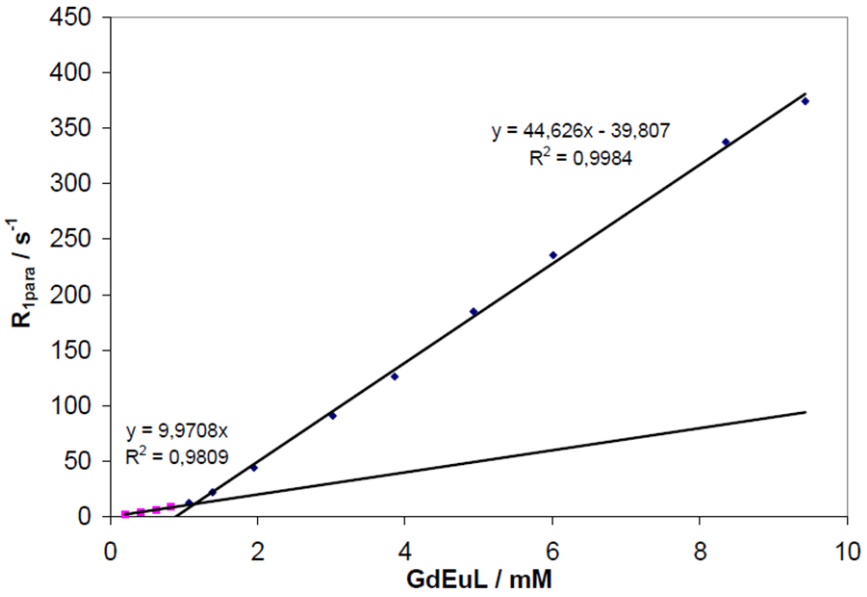

Figure 12-12. Relaxivity measurements and cmc determination. Variation of the water ^{1}H longitudinal relaxation rate of GdEuL-Nap versus the total GdEuL concentration at 40 MHz and 25°C ([Nap] = 0.093 [GdEuL]).

Micelle formation is characterized by the critical micellar concentration (cmc), above which micelles exist in solution. The presence of Gd^{3+} allowed for determining the cmc of **GdEuL–Nap** by ^{1}H relaxivity measurements (40 MHz and 25 ^{o}C; Figure 12-12). It is 1.15 ± 0.05 mM which, in comparison to previously reported analogous amphiphilic Gd^{3+} complexes, falls in the lower range expected for a C12 tail, due to the presence of the rigid pyridine ring.[372] It is also lower than that for GdL without **Nap** (1.48 ± 0.05 mM) since the presence of the hydrophobic **Nap** promotes micellar aggregation. The number of inner sphere water molecules has been obtained by luminescence lifetime measurements on **EuL**. As the parent complex,[371] **EuL** is bishydrated, independently of the concentration above or under the cmc.

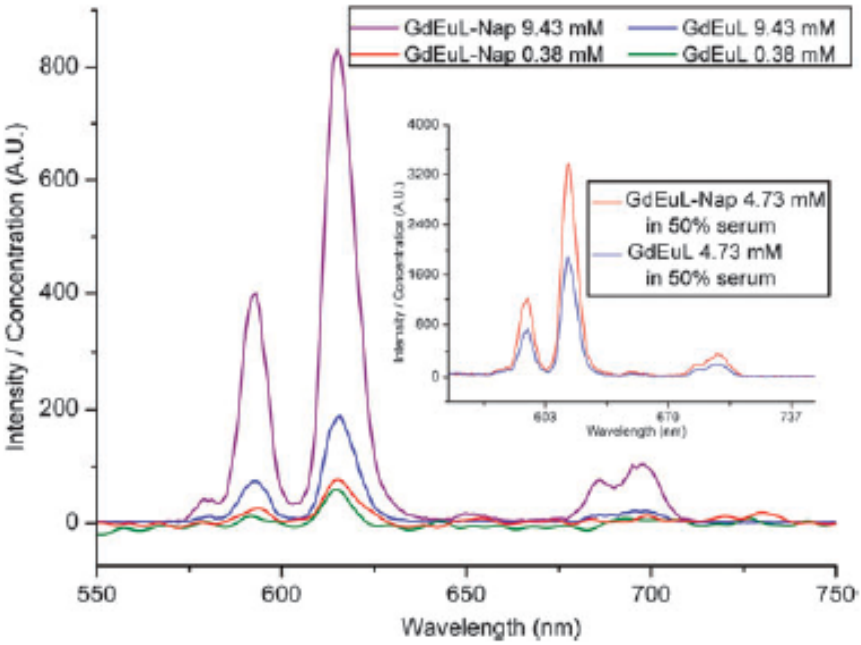

Figure 12-13. Time-delayed emission spectra of GdEuL recorded upon excitation at 345 nm, pH 7; time delay 0.1 ms. The inserted figure shows the emission spectra in fetal bovine serum. The concentrations mentioned are overall concentrations of the lanthanide.

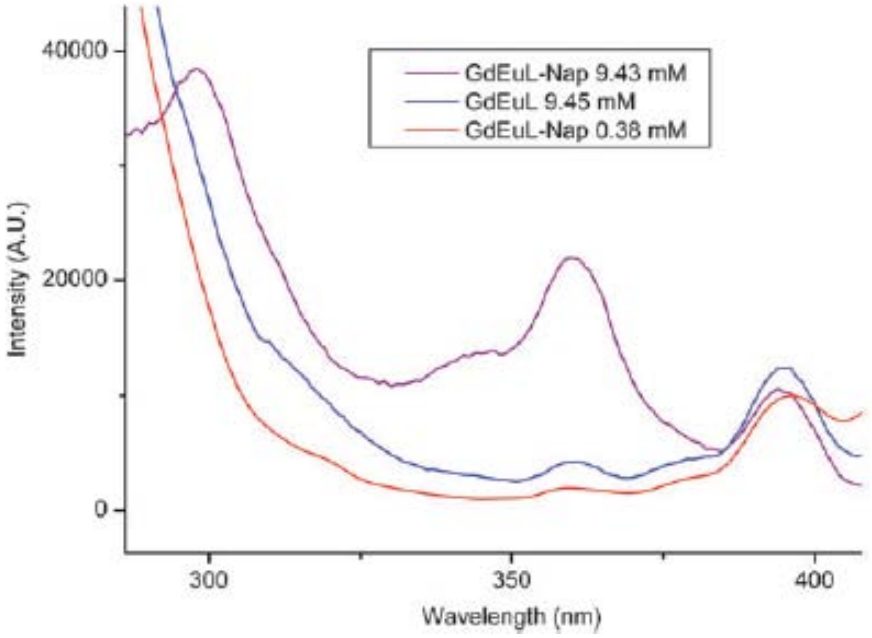

Figure 12-14. Normalized time-delayed excitation spectra of GdEuL recorded at pH 7 centered on the 614 nm Eu^{3+} emission. Intensities are normalized with respect to the 396 nm band ($^7F_0 \rightarrow {}^5L_6$). The concentrations mentioned are overall concentrations of the lanthanide.

The ability of **Nap** to sensitize Eu^{3+} has been investigated in the aqueous micellar solution at pH 7.0. Time-delayed emission spectra were recorded in the presence and in the absence of **Nap** under and above the cmc, with excitation at 345 nm (Figure 12-13). The characteristic Eu^{3+} emission bands are present even in the absence of **Nap** since the pyridine moiety of the chelate also has a sensitizing effect. Nevertheless, it is clearly demonstrated that, above the cmc, the Eu^{3+} emission is enhanced by ca. 400% in the presence of **Nap**, while no enhancement is observed under the cmc. This unambiguously proves that energy transfer between the **Nap** and Eu^{3+} does occur if they are sufficiently close to each other, with the **Nap** trapped in the micellar structure. It is further confirmed by recording the time-delayed excitation

spectra by monitoring the Eu^{3+} emission at 614 nm (Figure 12-14). The excitation bands indicative of **Nap** electronic structure are observed exclusively above the cmc (see Figure 12-15 for UV spectra).

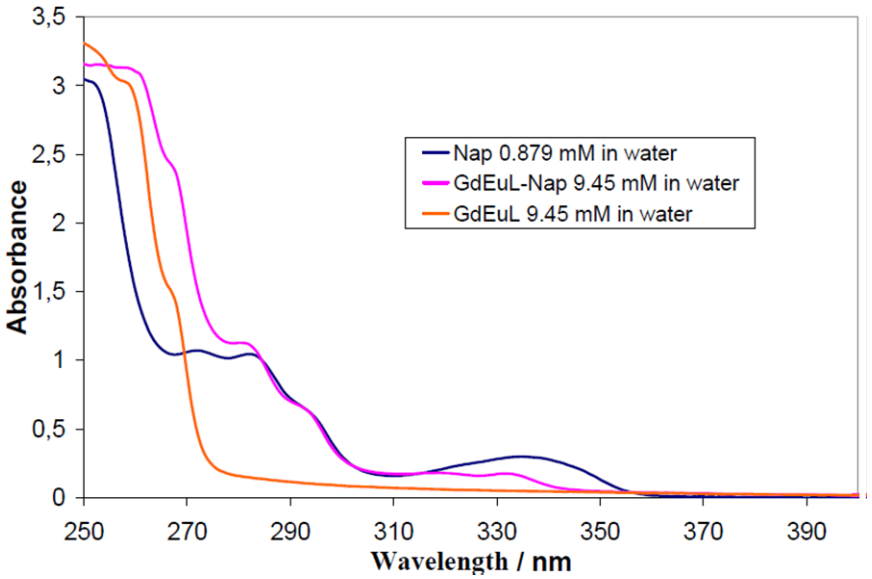

Figure 12-15. UV spectra of GdEuL, GdEuL in the presence of 2,3-naphthalimide and of pure 2,3-naphthalimide in water.

The efficiency of the sensitization provided by **Nap** to Eu^{3+} in the micelles was quantified by measuring the quantum yield for the system which was found to be 0.14 ± 0.02% in H_2O. This quantum yield is in the same range to that reported for dendrimer-**Nap** systems,[237] although it is important to remember that quantum yields do not reflect the absorption efficiency of the antenna.

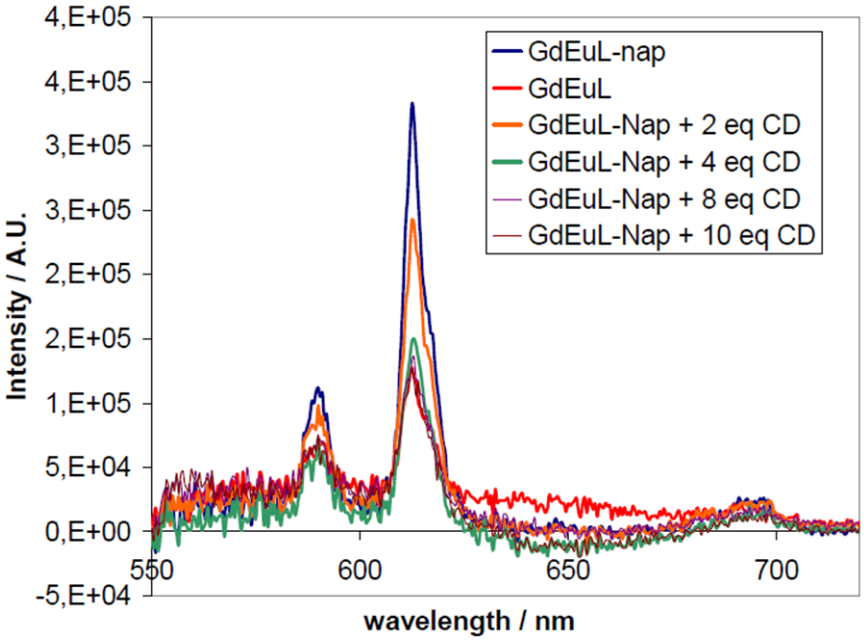

Figure 12-16. Emission spectra of GdEuL complex 4.73 mM at pH 7 in 50% fetal calf serum solution and in the presence of β-cyclodextrin (CD). A 450 nm cut-off filter was used to record those spectra with an excitation at 330 nm, an integration time of 0.5 ms and slit widths for the excitation and the emission of 2 nm.

The presence of an energy transfer from **Nap** to Eu^{3+} is a convenient means to assess if the system is in the micellar form. The time-delayed excitation and emission spectra of **GdEuL–Nap** have been recorded after 1 : 1 dilution of the 9.43 mM solution with fetal bovine serum (FBS) and compared to the **Nap**-free solution (Figure 12-13 inset). In FBS, like in water, there is a remarkable enhancement of the Eu^{3+} intensity in the presence of **Nap**, proving that the system stays mainly in micellar form in this biological medium. The system is stable for several hours, no significant changes are observed in the emission spectrum of the micelle in serum after one day. β-Cyclodextrin (β -CD) is known to destroy micellar aggregates.[373] Luminescence spectra of **GdEuL–Nap** have been recorded upon addition of up to 4 equivalents of β –CD and showed a decrease in the Eu^{3+} emission due to destruction of the micelles (further addition of β -CD results in precipitation).

12.6 CONCLUSIONS

In summary, we have demonstrated that hydrophobic chromophores incorporated into micelles formed by amphiphilic lanthanide complexes can efficiently sensitize lanthanide luminescence. This simple and rapid approach allows for creating luminescent polymetallic particles with a high number of integrated chromophores and lanthanide cations to maximize the luminescence intensity. It also offers a convenient way of screening a variety of hydrophobic chromophores including those with large, non-soluble aromatic moieties, without important synthetic effort. Finally, this strategy can be applied to assess the fate of micellar systems in various types of biological media.

13.0 CONCLUDING REMARKS

The increasing interest in lanthanide nanomaterials for biological reporting and sensing applications necessitates a fundamental understanding of the energy transfer mechanisms that occur in each system. The major avenue for studying such interactions is optical spectroscopy combined with systematic optimization of the spatial and energetic parameters controlled during synthesis. The chapters contained in this document outline the work that I have completed while pursuing a Ph. D. in Stéphane Petoud's research group. In general, the flexibility of each nanomaterial platform has increased with each new set of chapters. The initial work involved doping semiconductor nanocrystals with trivalent lanthanide cations in order to sensitize lanthanide luminescence through the band gap whilst protecting the lanthanide excited states from non-radiative deactivation. Furthermore, the protection provided by the nanocrystal approach was combined with more classical techniques of sensitization through organic chromophores exchanged on the surface. After the nanoparticle chapters, a very recent account of the polymetallic strategy was described for metal-organic frameworks (MOFs), where the lanthanide cations are introduced as a final step to coordination sites within the pores of the architectural units which double as sensitizing groups. The next set of chapters describe the dendrimer strategy which combines elements from all the chapters that precede it, including separation of the sensitizing groups from the coordination groups, as well as exchanging the trivalent lanthanide cations within the internal cavaties of the dendrimer as the final synthetic

step. The final chapter described micelles which are assembled from lanthanide-coordinating groups and separated from organic sensitizers which are soluble within the hydrophobic interior of the micelle, a synthetic strategy which is inversely related to the dendrimer approach. In summary, all chapters describe nanomaterials that incorporate the polymetallic strategy for increasing the number of photons emitted per unit volume to take advantage of the beneficial properties of lanthanide luminescence.

My hope is that this work may serve as a stepping-stone for future researchers striving to further develop an understanding of energy transfer mechanisms for lanthanide-containing nanomaterials. In my opinion, fundamental studies that aim towards elucidating the mechanistic aspects of lanthanide-containing nanomaterials, especially those that luminesce in the near-infrared region of the electromagnetic spectrum, will undoubtedly help develop useful biologic applications.

BIBLIOGRAPHY

(1) Bünzli, J.-C. G. *Chem. Rev.* **2010**, *110*, 2729.
(2) Eliseeva, S. V.; Bünzli, J.-C. G. *Chem. Soc. Rev.* **2010**, *39*, 189.
(3) Petoud, S.; Cohen, S. M.; Bünzli, J.-C.; Raymond, K. N. *J. Am. Chem. Soc.* **2003**, *125*, 13324.
(4) Zhang, J.; Badger, P. D.; Geib, S. J.; Petoud, S. *Angewandte Chemie-International Edition* **2005**, *44*, 2508.
(5) Mathis, G. *J. Biomol. Screen* **1999**, *4*, 309.
(6) Bünzli, J.-C. G.; Choppin, G. R. *Lanthanide probes in life, chemical, and earth sciences : theory and practice*; Elsevier,: Amsterdam ; New York :, 1989.
(7) Bünzli, J.-C. *Accounts of Chemical Research* **2006**, *39*, 53.
(8) Bruchez, M.; Moronne, M.; Gin, P.; Weiss, S.; Alivisatos, A. P. *Science* **1998**, *281*, 2013.
(9) Murray, C. B.; Norris, D. J.; Bawendi, M. G. *J. Am. Chem. Soc.* **1993**, *115*, 8706.
(10) Beeby, A.; Clarkson, I. M.; Dickins, R. S.; Faulkner, S.; Parker, D.; Royle, L.; deSousa, A. S.; Williams, J. A. G.; Woods, M. *J. Chem. Soc., Perkin Trans. 2* **1999**, 493.
(11) Horrocks, W. D.; Sudnick, D. R. *J. Am. Chem. Soc.* **1979**, *101*, 334.
(12) Horrocks, W. D., Jr.; Sudnick, D. R. *Acc. Chem. Res.* **1981**, *14*, 384.
(13) Leif, R. C.; Vallarino, L. M.; Becker, M. C.; Yang, S. *Cytom. Part A* **2006**, *69A*, 767.
(14) Shannon, R., D. *Acta Cryst.* **1976**, *32*, 751.
(15) Badger, P. D. *Ph.D. Thesis, University of Pittsburgh.* **2004**.
(16) Bornhop, D. J.; Hubbard, D. S.; Houlne, M. P.; Adair, C.; Kiefer, G. E.; Pence, B. C.; Morgan, D. L. *Anal. Chem.* **1999**, *71*, 2607.
(17) Hemmila, I.; Mukkala, V. M. *Crit Rev Cl Lab Sci* **2001**, *38*, 441.
(18) Badger, P. D., Novel Ligands for Sensitization and Protection of Near–infrared Luminescent Lanthanide Cations and Synthesis and Protonation of [W(η4-anthracene)(CO)3]2–. Ph.D. Thesis, University of Pittsburgh, Pittsburgh, PA, August 2004.
(19) Lin, Y. H.; Weissleder, R.; Tung, C. H. *Bioconjugate Chemistry* **2002**, *13*, 605.
(20) Stolik, S.; Delgado, J. A.; Perez, A.; Anasagasti, L. *Journal of Photochemistry and Photobiology, B: Biology* **2000**, *57*, 90.
(21) Weissleder, R.; Ntziachristos, V. *Nature Medicine (New York, NY, United States)* **2003**, *9*, 123.
(22) Kim, S.; Lim, Y. T.; Soltesz, E. G.; De Grand, A. M.; Lee, J.; Nakayama, A.; Parker, J. A.; Mihaljevic, T.; Laurence, R. G.; Dor, D. M.; Cohn, L. H.; Bawendi, M. G.; Frangioni, J. V. *Nat. Biotechnol.* **2004**, *22*, 93.

(23) Kim, S.; Lim, Y. T.; Soltesz, E. G.; DeGrand, A. M.; Lee, J.; Nakayama, A.; Parker, J. A.; Mihaljevic, T.; Laurence, R. G.; Dor, D. M.; Cohn, L. H.; Bawendi, M. G.; Frangioni, J. V. *Nat. Biotechnol.* **2003**, *22*, 93.
(24) Kim, S. W.; Zimmer, J. P.; Ohnishi, S.; Tracy, J. B.; Frangioni, J. V.; Bawendi, M. G. *Journal of the Americal Chemical Society* **2005**, *127*, 10526.
(25) Jeng, E. S.; Moll, A. E.; Roy, A. C.; Gastala, J. B.; Strano, M. S. *Nano Lett* **2006**, *6*, 371.
(26) Piszczek, G.; Maliwal, B. P.; Gryczynski, I.; Dattelbaum, J.; Lakowicz, J. R. *Journal of Fluorescence* **2001**, *11*, 101.
(27) Wong, K.-L.; Kwok, W.-M.; Wong, W.-T.; Phillips, D. L.; Cheah, K.-W. *Angewandte Chemie International Edition* **2004**, *43*, 4659
(28) Bünzli, J.-C. G.; Piguet, C. *Chem. Soc. Rev.* **2005**, *34*, 1048.
(29) Sabbatini, N.; Guardigli, M.; Lehn, J. M. *Coord. Chem. Rev.* **1993**, *123*, 201.
(30) Weissman, S. I. *Journal of Chemical Physics* **1942**, *10*, 214.
(31) Petoud, S.; Bünzli, J.-C. G.; Glanzman, T.; Piguet, C.; Xiang, Q.; Thummel, R. P. *Journal of Luminescence* **1999**, *82*, 69.
(32) Bünzli, J.-C. G.; Piguet, C. *Chem. Rev.* **2002**, *102*, 1897.
(33) Parker, D.; Dickins, R. S.; Puschmann, H.; Crossland, C.; Howard, J. A. K. *Chem. Rev.* **2002**, *102*, 1977.
(34) Beeby, A.; Dickins, R. S.; Faulkner, S.; Parker, D.; Williams, J. A. G. *Chem. Commun.* **1997**, 1401.
(35) Beeby, A.; Faulkner, S. *Chem. Phys. Lett.* **1997**, *266*, 116.
(36) Supkowski, R. M.; Horrocks, W. D. *Inorg. Chim. Acta* **2002**, *340*, 44.
(37) Wolbers, M. P. O.; van Veggel, F. C. J. M.; Snellink-Ruel, B. H. M.; Hofstraat, J. W.; Geurts, F. A. J.; Reinhoudt, D. N. *J. Chem. Soc.-Perkin Trans. 2* **1998**, 2141.
(38) Caravan, P.; Ellison, J. J.; McMurry, T. J.; Lauffer, R. B. *Chem. Rev.* **1999**, *99*, 2293.
(39) Chengelis, D. A.; Yingling, A. M.; Badger, P. D.; Shade, C. M.; Petoud, S. *J. Am. Chem. Soc.* **2005**, *127*, 16752.
(40) Petoud, S.; Cohen, S. M.; Bünzli, J.-C. G.; Raymond, K. N. *J. Am. Chem. Soc.* **2003**, *125*, 13324.
(41) Hemmila, I.; Webb, S. *Drug Discov. Today* **1997**, *2*, 373.
(42) Beeby, A.; Clarkson, I. M.; Dickins, R. S.; Faulkner, S.; Parker, D.; Royle, L.; de Sousa, A. S.; Williams, J. A. G.; Woods, M. *J. Chem. Soc.-Perkin Trans. 2* **1999**, 493.
(43) Cao, Y. W. C.; Jin, R. C.; Mirkin, C. A. *Science* **2002**, *297*, 1536.
(44) Rosenthal, S. J. *Nat. Biotechnol.* **2001**, *19*, 621.
(45) Penn, S. G.; He, L.; Natan, M. J. *Curr. Opin. Chem. Biol.* **2003**, *7*, 609.
(46) Chen, W.; Zhang, J. Z.; Joly, A. G. *J. Nanosci. Nanotechnol.* **2004**, *4*, 919.
(47) Wu, X. Y.; Liu, H. J.; Liu, J. Q.; Haley, K. N.; Treadway, J. A.; Larson, J. P.; Ge, N. F.; Peale, F.; Bruchez, M. P. *Nat. Biotechnol.* **2003**, *21*, 41.
(48) Bukowski, T. J.; Simmons, J. H. *Crit. Rev. Solid State Mat. Sci.* **2002**, *27*, 119.
(49) Meech, S. R.; Phillips, D. C. *J. Photochem.* **1983**, *23*, 229.
(50) Qu, L. H.; Peng, X. G. *J. Am. Chem. Soc.* **2002**, *124*, 2049.
(51) Peng, Z. A.; Peng, X. G. *J. Am. Chem. Soc.* **2001**, *123*, 183.
(52) Raola, O. E.; Strouse, G. F. *Nano Lett.* **2002**, *2*, 1443.
(53) Forster, T. *Ann. Physik* **1948**, *2*, 55.
(54) Dexter, D. L. *J. Chem. Phys.* **1953**, *21*, 836.

(55) Mukherjee, P.; Shade, C. M.; Yingling, A. M.; Lamont, D. N.; Waldeck, D. H.; Petoud, S. *J. Phys. Chem. A (submitted)* **2010**.
(56) Dorenbos, P. *J. Phys.: Condens. Matter* **2003**, *15*, 8417.
(57) Dorenbos, P. *J. Lumin.* **2004**, *108*, 301.
(58) Dorenbos, P. *J. Lumin.* **2005**, *111*, 89.
(59) Dorenbos, P. *J. Alloys and Compounds* **2009**, *488*, 568.
(60) Dorenbos, P.; vanderKolk, E. *Appl. Phys. Lett.* **2006**, ***89***, 061122.
(61) Dorenbos, P.; vanderKolk, E. *Opt. Materials* **2008**, *30*, 1052.
(62) Binnemans, K. *Chem. Rev.* **2009**, *109*, 4283.
(63) Bünzli, J.-C. G. *Chem. Rev.* **2010**, *110*, 2729.
(64) Dorenbos, P.; Krumpel, A. H.; Kolk, E. v. d.; Boutinaud, P.; Bettinelli, M.; Cavalli, E.
(65) Hibon, A.; Pierre, V. C. *Anal. Bioanal. Chem.* **2009**, *394*, 107.
(66) Hildebrandt, N.; Löhmannsröben, H.-G. *Curr. Chem. Biol.* **2007**, *1*, 167.
(67) Montgomery, C. P.; Murray, B. S.; New, E. J.; Pal, R.; Parker, D. *Acc. Chem. Res.* **2009**, *42*, 925.
(68) Moore, E. G.; Samuel, A. P. S.; Raymond, K. N. *Acc. Chem. Res.* **2009**, *42*, 542.
(69) Richardson, F. S. *Chem. Rev.* **1982**, *82*, 541.
(70) White, K. A.; Chengelis, D. A.; Gogick, K. A.; Stehman, J.; Rosi, N. L.; Petoud, S. *J. Am. Chem. Soc.* **2009**, *131*, 18069.
(71) Eliseevaa, S. V.; Bünzli, J.-C. G. *Chem. Soc. Rev.* **2010**, *39*, 189.
(72) Carnall, W. T.; Fields, P. R. *Lanthanide/Actinide Chemistry*; American Chemical Society: Washington D. C., 1967; Vol. 71.
(73) Anderson, W. W. *Phys. Rev.* **1964**, *136*, A556.
(74) Bhargava, R. N. *J. Lumin.* **1996**, *70*, 85.
(75) Brennan, J. D.; Capretta, A.; Yong, K.; Gerritsma, D.; Flora, K. K.; Jones, A. *Photochem. Photobiol.* **2002**, *75*, 117.
(76) Chen, Y.; Lu, Z. *Anal. Chim. Acta* **2007**, *587*, 180.
(77) Kim, Y. H.; Baek, N. S.; Kim, H. K. *Chem. Phys. Chem.* **2006**, *7*, 213.
(78) Klik, M. A. J.; Gregorkiewicz, T.; Bradley, I. V.; Wells, J.-P. R. *Phys. Rev. Lett.* **2002**, *89*, 227401.
(79) Palm, J.; Gan, F.; Zheng, B.; Michel, J.; Kimerling, L. C. *Phys. Rev. B* **1996**, *54*, 17603.
(80) Sato, S.; Wada, M. *Bull. Chem. Soc. Jap.* **1970**, *43*, 1955.
(81) Sivakumar, S.; vanVeggel, F. C. J. M.; Raudsepp, M. *Chem. Phys. Chem.* **2007**, *8*, 1677.
(82) Xueyuan, C.; Wenqin, L.; Yongheng, L.; Guokui, L. *J. Rare Earths* **2007**, *25*, 515.
(83) Yang, C.; Fu, L.-M.; Wang, Y.; Zhang, J.-P.; Wong, W.-T.; Ai, X.-C.; Qiao, Y.-F.; Zou, B.-S.; Gui, L.-L. *Angew. Chem. Int. Ed.* **2004**, *43*, 5010.
(84) Streetman, B. G.; Banerjee, S. *Solid State electronic Devices*; 5th ed. New Jersey: Prentice Hall, 2000.
(85) Abiko, Y.; Nakayama, N.; Akimoto, K.; Yao, T. *Phys. Stat. Sol. (b)* **2002**, *229*, 339.
(86) Fuhs, W.; Ulber, I.; Weiser, G.; Bresler, M. S.; Gusev, O. B.; Kuznetsov, A. N.; Kudoyarova, V. K.; Terukov, E. I.; Yassievich, I. N. *Phys. Rev. B* **1997**, *56*, 9545.
(87) Yassievich, I.; Bresler, M.; Gusev, O. *J. Non-Cryst. Solids* **1998**, *226*, 192.
(88) Kühne, H.; Weiser, G.; Terukov, E. I.; Kusnetsov, A. N.; Kudoyarova, V. K. *J. Appl. Phys.* **1999**, *86*, 896.
(89) Tsimperidis, I.; Gregorkiewicz, T.; Bekman, H. H. P. T.; Langerak, C. J. G. M. *Phys. Rev. Lett.* **1998**, *81*, 4748.

(90) Gregorkiewicz, T.; Thao, D. T. X.; Langer, J. M.; Bekman, H. H. P. T.; Bresler, M. S.; Michel, J.; Kimerling, L. C. *Phys. Rev. B* **2000**, *61*, 5369.
(91) Chen, Y. S.; Burgiel, J. C.; Kahng, D. *J. Electrochem. Soc.: Solid State Science* **1970**, *117*, 794.
(92) Godlewski, M.; Światek, K.; Monemar, B. *J. Lumin.* **1994**, *58*, 303.
(93) Godlewski, M.; Zakrzewski, A. J.; Ivanov, V. Y. *J. Alloys and Compounds* **2000**, *300-301*, 23.
(94) Kahng, D. *Appl. Phys. Lett.* **1968**, *13*, 210.
(95) Krupka, D. C. *J. Appl. Phys.* **1972**, *43*, 476.
(96) Przybylinska, H.; Godlewski, M. *Phys. Rev. B* **1987**, *36*, 1677.
(97) Przybylińska, H.; Świa□tek, K.; Sta□por, A.; Suchocki, A.; Godlewski, M. *Phys. Rev. B* **1989**, *40*, 1748.
(98) Światek, K.; Godlewski, M. *Appl. Phys. Lett.* **1990**, *56*, 2192.
(99) Świa□tek, K.; Godlewski, M.; Hommel, D. *Phys. Rev. B* **1990**, *42*, 3628.
(100) Światek, K.; Suchocki, A.; Godlewski, M. *Appl. Phys. Lett.* **1990**, *56*, 195.
(101) Światek, K.; Suchocki, A.; Przybylinska, H.; Godlewski, M. *J. Cryst. Growth* **1990**, *101*, 435.
(102) Bol, A. A.; Beek, R. v.; Meijerink, A. *Chem. Mater.* **2002**, *14*, 1121.
(103) Chen, L.; Zhang, J.; Lu, S.; Ren, X.; Wang, X. *Chem. Phys. Lett.* **2005**, *409*, 144.
(104) Chen, W.; Joly, A. G.; Malm, J.-O.; Bovin, J.-O. *J. Appl. Phys.* **2004**, *95*, 667.
(105) Dong, L.; Liu, Y.; Zhuo, Y.; Chu, Y. *Eur. J. Inorg. Chem.* **2010**, 2504.
(106) Ehrhart, G.; Capoen, B.; Robbe, O.; Beclin, F.; Boy, P.; Turrell, S.; Bouazaoui, M. *Optical Materials* **2008**, *30*, 1595.
(107) Hou, S.; Yuen, Y.; Mao, H.; JiqingWang; Zhu, Z. *J. Phys. D: Appl. Phys.* **2009**, *42*, 215105 (5pp).
(108) Jing-hua, N.; Rui-nian, H.; Wen-lian, L.; Ming-tao, L.; Tian-zhi, Y. *J. Phys. D: Appl. Phys.* **2006**, *39*, 2357.
(109) Planelles-Aragó, J.; Julián-López, B.; Cordoncillo, E.; Escribano, P.; Pellé, F.; Viana, B.; Sanchez, C. *J. Mater. Chem.* **2008**, *18*, 5193.
(110) Qu, S. C.; Zhou, W. H.; Liu, F. Q.; Chen, N. F.; Wang, Z. G.; Pan, H. Y.; Yu, D. P. *Appl. Phys. Lett.* **2002**, *80*, 3605.
(111) Sun, L.; Yan, C.; Liu, C.; Liao, C.; Li, D.; Yu, J. *Journal of Alloys and Compounds* **1998**, *275-277*, 234.
(112) Sun, X. L.; Zhang, G. L.; Tang, G. Q.; Chen, W. J. *Chin. Chem. Lett.* **1999**, *10*, 807.
(113) Wang, L.; Xu, X.; XinYuan *J. Lumin.* **2010**, *130*, 137.
(114) Yang, H.; Yu, L.; Shen, L.; Wang, L. *Mater. Lett.* **2004**, *58*, 1172.
(115) Kallmann, H.; Luchner, K. *Phys. Rev.* **1961**, *123*, 2013.
(116) Luchner, K. M.; Kallmann, H. P.; Kramer, B.; Wachter, P. *Phys. Rev.* **1963**, *129*, 593.
(117) Lakowicz, J. R. *Principles of Fluorescence Spectroscopy*; Third ed.
(118) Speiser, S. *Chem. Rev.* **1996**, *96*, 1953.
(119) *Handbook of Chemistry & Physics*; 53 ed.; CRC Press, 1972-1973.
(120) Singh, J. *Physics of Semiconductors and Their Heterostructures*; McGraw-Hill, 1993.
(121) Brus, L. E. *J. Chem. Phys.* **1984**, *80*, 4403.
(122) Sooklal, K.; Cullum, B. S.; Angel, S. M.; Murphy, C. J. *J. Phys. Chem.* **1996**, *100*, 4551.
(123) Li, L. S.; Pradhan, N.; Wang, Y.; Peng, X. *Nano Lett.* **2004**, *4*, 2261.
(124) Chen, W.; Wang, Z.; Lin, Z.; Lin, L. *J. Appl. Phys.* **1997**, ***82***, 3111.

(125) Blasse, G.; Sabbatini, N. *Mater. Chem. Phys.* **1987**, *16*, 237.
(126) Chen, W.; Malm, J.-O.; Zwiller, V.; Huang, Y.; Liu, S.; Wallenberg, R.; Bovin, J.-O.; Samuelson, L. *Phys. Rev. B* **2000**, *61*, 11021.
(127) Liu, S.-M.; Guo, H.-Q.; Zhang, Z.-H.; Liu, F.-Q.; Wang, Z.-G. *Chin. Phys. Lett.* **2000**, *17*, 609.
(128) Fonoberov, V. A.; Balandin, A. A. *Appl. Phys. Lett.* **2004**, *85*, 5971.
(129) Chestnoy, N.; Harris, T. D.; Hull, R.; Brus, L. E. *J. Phys. Chem.* **1986**, *90*, 3393.
(130) Petoud, S.; Muller, G.; Moore, E. G.; Xu, J.; Sokolnicki, J.; Riehl, J. P.; Le, U. N.; Cohen, S. M.; Raymond, K. N. *J. Am. Chem. Soc.* **2007**, *129*, 77.
(131) Takahei, K.; Taguchi, A.; Nakagome, H.; Uwai, K.; Whitney, P. S. *J. Appl. Phys.* **1989**, *66*, 4941.
(132) Whitney, P. S.; Uwai, K.; Nakagome, H.; Takahei, K. *Appl. Phys. Lett.* **1988**, *53*, 2074.
(133) Thonke, K.; Pressel, K.; Bohnert, G.; Stapor, A.; Weber, J.; Moser, M.; Molassioti, A.; Hangleiter, A.; Scholz, F. *Sernicond. Sci. Technol.* **1990**, *5*, 1124.
(134) Needels, M.; Schlüter, M.; Lannoo, M. *Phys. Rev. B* **1993**, *47*, 15533.
(135) Lazarides, T.; Tart, N. M.; Sykes, D.; Faulkner, S.; Barbieri, A.; Ward, M. D. *Dalton Trans.* **2009**, 3971.
(136) Pedrini, C.; Bouttet, D.; Dujardin, C.; Belsky, A.; Vasil'ev, A. *ed P. Dorenbos and C. W. E. van Eijk (The Netherlands: Delft University Press)* **1996**, p 103.
(137) Sato, S. *J. Phys. Soc. Jpn.* **1976**, *41*, 913.
(138) Thiel, C. W.; Gruguel, H.; Sun, Y.; Lapeyre, G. J.; Macfarlane, R. M.; Equall, R. W.; Cone, R. L. *J. Lumin.*

2001, *94/95*, 1.
(139) Thiel, C. W.; Gruguel, H.; Wu, H.; Sun, Y.; Lapeyre, G. J.; Cone, R. L.; Equall, R. W.; Macfarlane, R. M. *Phys. Rev. B* **2001**, *64*, 085107.
(140) Thiel, C. W.; Sun, Y.; Cone, R. L. *J. Mod. Opt.* **2002**, *49*, 2399.
(141) Jörgensen, C. K. *Modern Aspects of Ligand Field Theory* North-Holland, Amsterdam, 1971.
(142) Carnall, W. T.; Fields, P. R.; Rajnak, K. *J. Chem. Phys.* **1968**, *49*, 4447.
(143) Carnall, W. T.; Fields, P. R.; Rajnak, K. *J. Chem. Phys.* **1968**, *49*, 4450.
(144) Allen, B. L.; Shade, C. M.; Yingling, A. M.; Petoud, S.; Star, A. *Adv. Mater.* **2009**, *21*, 4692.
(145) Baughman, R. H.; Zakhidov, A. A.; de Heer, W. A. *Science* **2002**, *297*, 787.
(146) Kroto, H. W.; Heath, J. R.; O'Brien, S. C.; Curl, R. F.; Smalley, R. E. *Nature* **1985**, *318*, 162.
(147) Iijima, S. *Nature* **1991**, *354*, 56.
(148) Smith, B. W.; Monthioux, M.; Luzzi, D. E. *Nature* **1998**, *396*, 323.
(149) Gaponik, N.; Radtchenko, I. L.; Gerstenberger, M. R.; Fedutik, Y. A.; Sukhorukov, G. B.; Rogach, A. L. *Nano Lett.* **2003**, *3*, 369.
(150) Shchukin, D. G.; Radtchenko, I. L.; Sukhorukov, G. B. *Mater. Lett.* **2003**, *57*, 1743.
(151) Dujardin, E.; Ebbesen, T. W.; Hiura, H.; Tanigaki, K. *Science* **1994**, *265*, 1850.
(152) Ugarte, D.; Chatelain, A.; deHeer, W. A. *Science* **1996**, *274*, 1897.
(153) Seraphin, S.; Zhou, D.; Jiao, J.; Withers, J. C.; Loutfy, R. *Nature* **1993**, *362*, 503.
(154) Mittal, J.; Monthioux, M.; Allouche, H.; Stephan, O. *Chem. Phys. Lett.* **2001**, *339*, 311.
(155) Broz, P.; Driamov, S.; Ziegler, J.; Ben-Haim, N.; Marsch, S.; Meier, W.; Hunziker, P. *Nano Lett.* **2006**, *6*, 2349.

(156) Lamprecht, A.; Saumet, J. L.; Roux, J.; Benoit, J. P. *Int. J. Pharm.* **2004**, *278*, 407.
(157) Hampel, S.; Kunze, D.; Haase, D.; Kramer, K.; Rauschenbach, M.; Ritscbel, M.; Leonbardt, A.; Thomas, J.; Oswald, S.; Hoffmann, V.; Buechner, B. *Nanomedicine* **2008**, *3*, 175.
(158) Rigler, P.; Meier, W. *J. Am. Chem. Soc.* **2006**, *128*, 367.
(159) Shiraishi, M.; Takenobu, T.; Yamada, A.; Ata, M.; Kataura, H. *Chem. Phys. Lett.* **2002**, *358*, 213.
(160) Zhong, D. Y.; Zhang, G. Y.; Liu, S.; Wang, E. G.; Wang, Q.; Li, H.; Huang, X. J. *Appl. Phys. Lett.* **2001**, *79*, 3500.
(161) Allen, B. L.; Kichambare, P. D.; Star, A. *ACS Nano* **2008**, *2*, 1914.
(162) Wei, H.; Li, B. L.; Li, J.; Dong, S. J.; Wang, E. K. *Nanotechnology* **2008**, *19*, 5.
(163) Norman, T. J.; Grant, C. D.; Magana, D.; Zhang, J. Z.; Liu, J.; Cao, D. L.; Bridges, F.; Van Buuren, A. *J. Phys. Chem. B* **2002**, *106*, 7005.
(164) Ajayan, P. M.; Iijima, S. *Nature* **1993**, *361*, 333.
(165) Pugh, T. L.; Heller, W. *Journal of Polymer Science* **1960**, *47*, 219.
(166) Storhoff, J. J.; Lazarides, A. A.; Mucic, R. C.; Mirkin, C. A.; Letsinger, R. L.; Schatz, G. C. *J. Am. Chem. Soc.* **2000**, *122*, 4640.
(167) Zhao, G. L.; Bagayoko, D.; Wang, E. C. *Mod. Phys. Lett. B* **2003**, *17*, 375.
(168) Zhang, J.; Shade, C. M.; Chengelis, D. A.; Petoud, S. *J. Am. Chem. Soc.* **2007**, *129*, 14834.
(169) Muller, M. G.; Georgakoudi, I.; Zhang, Q. G.; Wu, J.; Feld, M. S. *Appl. Optics* **2001**, *40*, 4633.
(170) Comby, S.; Imbert, D.; Chauvin, A. S.; Bünzli, J.-C. G. *Inorg. Chem.* **2006**, *45*, 732.
(171) Gunnlaugsson, T.; Stomeo, F. *Org. Biomol. Chem.* **2007**, *5*, 1999.
(172) Hebbink, G. A.; Grave, L.; Woldering, L. A.; Reinhoudt, D. N.; van Veggel, F. *J. Phys. Chem. A* **2003**, *107*, 2483.
(173) Ronson, T. K.; Lazarides, T.; Adams, H.; Pope, S. J. A.; Sykes, D.; Faulkner, S.; Coles, S. J.; Hursthouse, M. B.; Clegg, W.; Harrington, R. W.; Ward, M. D. *Chem.-Eur. J.* **2006**, *12*, 9299.
(174) Van Deun, R.; Fias, P.; Nockemann, P.; Van Hecke, K.; Van Meervelt, L.; Binnemans, K. *Inorg. Chem.* **2006**, *45*, 10416.
(175) Vicinelli, V.; Ceroni, P.; Maestri, M.; Balzani, V.; Gorka, M.; Vogtle, F. *J. Am. Chem. Soc.* **2002**, *124*, 6461.
(176) Stouwdam, J. W.; van Veggel, F. *Nano Lett.* **2002**, *2*, 733.
(177) Bazzi, R.; Flores, M. A.; Louis, C.; Lebbou, K.; Zhang, W.; Dujardin, C.; Roux, S.; Mercier, B.; Ledoux, G.; Bernstein, E.; Perriat, P.; Tillement, O. *J. Colloid Interface Sci.* **2004**, *273*, 191.
(178) Riwotzki, K.; Meyssamy, H.; Schnablegger, H.; Kornowski, A.; Haase, M. *Angewandte Chemie-International Edition* **2001**, *40*, 573.
(179) Riwotzki, K.; Haase, M. *J. Phys. Chem. B* **2001**, *105*, 12709.
(180) Frindell, K. L.; Bartl, M. H.; Popitsch, A.; Stucky, G. D. *Angewandte Chemie-International Edition* **2002**, *41*, 959.
(181) Wada, Y.; Okubo, T.; Ryo, M.; Nakazawa, T.; Hasegawa, Y.; Yanagida, S. *J. Am. Chem. Soc.* **2000**, *122*, 8583.
(182) Zhang, J.; Badger, P. D.; Geib, S. J.; Petoud, S. *Inorg. Chem.* **2007**, *46*, 6473.

(183) Boyer, J. C.; Vetrone, F.; Cuccia, L. A.; Capobianco, J. A. *J. Am. Chem. Soc.* **2006**, *128*, 7444.
(184) Mai, H. X.; Zhang, Y. W.; Si, R.; Yan, Z. G.; Sun, L. D.; You, L. P.; Yan, C. H. *J. Am. Chem. Soc.* **2006**, *128*, 6426.
(185) Roy, D. M.; Roy, R. *Journal of The Electrochemical Society* **1964**, *111*, 421.
(186) Horrocks, W. D.; Bolender, J. P.; Smith, W. D.; Supkowski, R. M. *J. Am. Chem. Soc.* **1997**, *119*, 5972.
(187) Reinhard, C.; Gudel, H. U. *Inorg. Chem.* **2002**, *41*, 1048.
(188) An, J.; Shade, C. M.; Chengelis-Czegan, D. A.; Petoud, S. p.; Rosi, N. L. *J. Am. Chem. Soc.* **2011**, *133*, 1220.
(189) Uh, H.; Petoud, S. *Rendus Chimie* **2010**, *13*, 668.
(190) Allendorf, M. D.; Bauer, C. A.; Bhakta, R. K.; Houk, R. J. T. *Chem. Soc. Rev.* **2009**, *38*, 1330.
(191) Long, J. R.; Yaghi, O. M. *Chem. Soc. Rev.* **2009**, *38*, 1213.
(192) Chen, B. L.; Wang, L. B.; Zapata, F.; Qian, G. D.; Lobkovsky, E. B. *J. Am. Chem. Soc.* **2008**, *130*, 6718.
(193) Reineke, T. M.; Eddaoudi, M.; O'Keeffe, M.; Yaghi, O. M. *Angewandte Chemie-International Edition* **1999**, *38*, 2590.
(194) White, K. A.; Chengelis, D. A.; Zeller, M.; Geib, S. J.; Szakos, J.; Petoud, S.; Rosi, N. L. *Chem. Commun.* **2009**, 4506.
(195) Chen, B. L.; Xiang, S. C.; Qian, G. D. *Accounts of Chemical Research* **2010**, *43*, 1115.
(196) White, K. A.; Chengelis, D. A.; Gogick, K. A.; Stehman, J.; Rosi, N. L.; Petoud, S. *J. Am. Chem. Soc.* **2009**, *131*, 18069.
(197) An, J.; Fiorella, R.; Geib, S. J.; Rosi, N. L. *J. Am. Chem. Soc.* **2009**, *131*, 8401.
(198) An, J.; Geib, S. J.; Rosi, N. L. *J. Am. Chem. Soc.* **2009**, *131*, 8376.
(199) An, J.; Geib, S. J.; Rosi, N. L. *J. Am. Chem. Soc.* **2010**, *132*, 38.
(200) An, J.; Rosi, N. L. *J. Am. Chem. Soc.* **2010**, *132*, 5578.
(201) Wang, Z. Q.; Cohen, S. M. *Chem. Soc. Rev.* **2009**, *38*, 1315.
(202) Dong, Y. B.; Wang, P.; Ma, J. P.; Zhao, X. X.; Wang, H. Y.; Tang, B.; Huang, R. Q. *J. Am. Chem. Soc.* **2007**, *129*, 4872.
(203) Aebischer, A.; Gumy, F.; Bünzli, J.-C. G. *Physical Chemistry Chemical Physics* **2009**, *11*, 1346.
(204) Kauffman, D. R.; Shade, C. M.; Uh, H.; Petoud, S.; Star, A. *Nat. Chem.* **2009**, *1*, 500.
(205) Luo, F.; Batten, S. R. *Dalton Transactions* **2010**, *39*, 4485.
(206) Shavaleev, N. M.; Moorcraft, L. P.; Pope, S. J. A.; Bell, Z. R.; Faulkner, S.; Ward, M. D. *Chemistry – A European Journal* **2003**, *9*, 5283.
(207) Parker, D.; Williams, J. A. G. *Journal of the Chemical Society-Dalton Transactions* **1996**, 3613.
(208) Deiters, E.; Song, B.; Chauvin, A. S.; Vandevyver, C. D. B.; Gumy, F.; Bünzli, J.-C. G. *Chem.-Eur. J.* **2009**, *15*, 885.
(209) Xie, Z. G.; Ma, L. Q.; deKrafft, K. E.; Jin, A.; Lin, W. B. *J. Am. Chem. Soc.* **2010**, *132*, 922.
(210) Blair, S.; Kataky, R.; Parker, D. *New Journal of Chemistry* **2002**, *26*, 530.
(211) Werts, M. H. V.; Woudenberg, R. H.; Emmerink, P. G.; van Gassel, R.; Hofstraat, J. W.; Verhoeven, J. W. *Angewandte Chemie-International Edition* **2000**, *39*, 4542.
(212) Amao, Y.; Okura, I.; Miyashita, T. *Bull. Chem. Soc. Jpn.* **2000**, *73*, 2663.

(213) Esfand, R.; Tomalia, D. A. *Drug Discov Today* **2001**, *6*, 427.
(214) Tomalia, D. A.; Frechet, J. M. J. *J. Polym. Sci. Pol. Chem.* **2002**, *40*, 2719.
(215) Tomalia, D. A.; Naylor, A. M.; Goddard, W. A. *Angewandte Chemie International Edition* **1990**, *29*, 138.
(216) Nigavekar, S. S.; Sung, L. Y.; Llanes, M.; El-Jawahri, A.; Lawrence, T. S.; Becker, C. W.; Balogh, L.; Khan, M. K. *Pharm Res* **2004**, *21*, 476.
(217) Pan, G. F.; Lemmouchi, Y.; Akala, E. O.; Bakare, O. *J. Bioact. Compat. Polym.* **2005**, *20*, 113.
(218) Wang, S. J.; Brechbiel, M.; Wiener, E. C. *Investigative Radiology* **2003**, *38*, 662.
(219) Dear, J. W.; Kobayashi, H.; Jo, S.-K.; Holly, M. K.; Hu, X.; Yuen, P. S. T.; Brechbiel, M. W.; Star, R. A. *Kidney International* **2005**, *67*, 2159.
(220) Wintgens, V.; Valat, P.; Kossanyi, J.; Biczok, L.; Demeter, A.; Berces, T. *J. Chem. Soc.-Faraday Trans.* **1994**, *90*, 411.
(221) Klink, S. I.; Grave, L.; Reinhoudt, D. N.; van Veggel, F. C. J. M.; Werts, M. H. V.; Geurts, F. A. J.; Hofstraat, J. W. *J. Phys. Chem. A* **2000**, *104*, 5457.
(222) Silva, F.; Malta, O. L.; Reinhard, C.; Gudel, H. U.; Piguet, C.; Moser, J. E.; Bünzli, J.-C. G. *J. Phys. Chem. A* **2002**, *106*, 1670.
(223) Grabchev, I.; Chovelon, J.-M.; Bojinov, V.; Ivanova, G. *Tetrahedron* **2003**, *59*, 9591.
(224) Grabchev, I.; Chovelon, J.-M.; Nedelcheva, A. *Journal of Photochemistry and Photobiology, A: Chemistry* **2006**, *183*, 9.
(225) Grabchev, I.; Chovelon, J.-M.; Qian, X. *New Journal of Chemistry* **2003**, *27*, 337.
(226) Grabchev, I.; Guittonneau, S. *Journal of Photochemistry and Photobiology, A: Chemistry* **2006**, *179*, 28.
(227) Grabchev, I.; Qian, X.; Bojinov, V.; Xiao, Y.; Zhang, W. *Polymer* **2002**, *43*, 5731.
(228) Grabchev, I.; Sali, S.; Chovelon, J.-M. *Chem. Phys. Lett.* **2006**, *422*, 547.
(229) Grabchev, I.; Soumillion, J.-P.; Muls, B.; Ivanova, G. *Photochem. Photobiol. Sci.* **2004**, *3*, 1032.
(230) Grabchev, I.; Staneva, D.; Betcheva, R. *Polymer Degradation and Stability* **2006**, *91*, 2257.
(231) de Sousa, M.; Kluciar, M.; Abad, S.; Miranda, M. A.; de Castro, B.; Pischel, U. *Photochem. Photobiol. Sci.* **2004**, *3*, 639.
(232) Piguet, C.; Bünzli, J.-C. G. **1999**, *28*, 347.
(233) Senegas, J. M.; Koeller, S.; Bernardinelli, G.; Piguet, C. **2005**, 2235.
(234) Kawa, M.; Frechet, J. M. J. *Chem. Mat.* **1998**, *10*, 286.
(235) Ceroni, P.; Vicinelli, V.; Maestri, M.; Balzani, V.; Lee, S. K.; van Heyst, J.; Gorka, M.; Vogtle, F. **2004**, *689*, 4375.
(236) Laus, S.; Sour, A.; Ruloff, R.; Tóth, E.; Merbach, A. E. *Chemistry A European Journal* **2005**, *11*, 3064.
(237) Cross, J. P.; Lauz, M.; Badger, P. D.; Petoud, S. *J. Am. Chem. Soc.* **2004**, *126*, 16278.
(238) Meech, S., R.; Phillips, D. *Journal of Photochemistry* **1983**, *23*, 193.
(239) Haas, Y.; Stein, G., J. *J. Phys. Chem.* **1971**, *75*, 3668.
(240) Williams, D., H.; Fleming, Ian *Spectroscopic methods in organic chemistry*; 5th. ed.; The McGraw-Hill Companies: London, 1995.
(241) Barone, P. W.; Baik, S.; Heller, D. A.; Strano, M. S. *Nat. Mater.* **2005**, *4*, 86.
(242) Ballou, B.; Ernst, L. A.; Andreko, S.; Harper, T.; Fitzpatrick, J. A. J.; Waggoner, A. S.; Bruchez, M. P. *Bioconjugate Chemistry* **2007**, *18*, 389.

(243) Moon, W. K.; Lin, Y. H.; O'Loughlin, T.; Tang, Y.; Kim, D. E.; Weissleder, R.; Tung, C. H. *Bioconjugate Chemistry* **2003**, *14*, 539.
(244) Fletcher, K. A.; Fakayode, S. O.; Lowry, M.; Tucker, S. A.; Neal, S. L.; Kimaru, I. W.; McCarroll, M. E.; Patonay, G.; Oldham, P. B.; Rusin, O.; Strongin, R. M.; Warner, I. M. *Anal. Chem.* **2006**, *78*, 4047.
(245) Zhang, J.; Petoud, S. *Chem.-Eur. J.* **2008**, *14*, 1264.
(246) Klink, S. I.; Alink, P. O.; Grave, L.; Peters, F. G. A.; Hofstraat, J. W.; Geurts, F.; van Veggel, F. C. J. M. *J. Chem. Soc.-Perkin Trans. 2* **2001**, 363.
(247) Van Deun, R.; Fias, P.; Nockemann, P.; Van Hecke, K.; Van Meervelt, L.; Binnemans, K. *Inorg. Chem.* **2006**, *45*, 10416.
(248) Comby, S.; Imbert, D.; Vandevyver, C.; Bünzli, J.-C. G. *Chem.-Eur. J.* **2007**, *13*, 936.
(249) Hasegawa, Y.; Ohkubo, T.; Sogabe, K.; Kawamura, Y.; Wada, Y.; Nakashima, N.; Yanagida, S. *Angewandte Chemie-International Edition* **2000**, *39*, 357.
(250) Foley, T. J.; Harrison, B. S.; Knefely, A. S.; Abboud, K. A.; Reynolds, J. R.; Schanze, K. S.; Boncella, J. M. *Inorg. Chem.* **2003**, *42*, 5023.
(251) Faulkner, S.; Pope, S. J. A.; Burton-Pye, B. P. *Applied Spectroscopy Reviews* **2005**, *40*, 1.
(252) Beeby, A.; Botchwayb, S. W.; Clarksona, I. M.; Faulknerc, S.; Parker, A. W.; Parker, D.; Williams, J. A. G. *Journal of Photochemistry and Photobiology B: Biology* **2000**, *57*, 83.
(253) Charbonniere, L. J.; Hildebrandt, N.; Ziessel, R. F.; Loehmannsroeben, H. G. *J. Am. Chem. Soc.* **2006**, *128*, 12800.
(254) Vereb, G.; Jares-Erijman, E.; Selvin, P. R.; Jovin, T. M. *Biophysical Journal* **1998**, *74*, 2210.
(255) Yu, J. H.; Parker, D.; Pal, R.; Poole, R. A.; Cann, M. J. *J. Am. Chem. Soc.* **2006**, *128*, 2294.
(256) Hanaoka, K.; Kikuchi, K.; Kobayashi, S.; Nagano, T. *J. Am. Chem. Soc.* **2007**, *129*, 13502.
(257) Chauvin, A. S.; Comby, S.; Song, B.; Vandevyver, C. D. B.; Thomas, F.; Bünzli, J.-C. G. *Chem.-Eur. J.* **2007**, *13*, 9515.
(258) Vandevyver, C. D. B.; Chauvin, A. S.; Comby, S.; Bünzli, J.-C. G. *Chem. Commun.* **2007**, 1716.
(259) Balzani, V.; Bergamini, G.; Ceroni, P.; Vogtle, F. *Coord. Chem. Rev.* **2007**, *251*, 525.
(260) Newkome, G. R.; Shreiner, C. D. *Polymer* **2008**, *49*, 1.
(261) Bünzli, J.-C. G.; Eliseeva, S. V. *Journal of Rare Earths* **2010**, *28*, 824.
(262) Kemeny, N.; Huang, Y.; Cohen, A. M.; Shi, W.; Conti, J. A.; Brennan, M. F.; Bertino, J. R.; Turnbull, A. D. M.; Sullivan, D.; Stockman, J.; Blumgart, L. H.; Fong, Y. *New England Journal of Medicine* **1999**, *341*, 2039.
(263) Duijnhoven, F. H.; Tollenaar, R. A. E. M.; Terpstra, O. T.; Kuppen, P. J. K. *Clinical and Experimental Metastasis* **2005**, *22*, 247.
(264) Maataoui, A.; Qian, J.; Mack, M. G.; Khan, M. F.; Oppermann, E.; Roozru, M.; Schmidt, S.; Bechstein, W. O.; Vogl, T. J. *Radiology* **2005**, *237*, 479.
(265) Thomas, C.; Nijenhuis, A. M.; Timens, W.; Kuppen, P. J.; Daemen, T.; Scherphof, G. L. *Invasion and Metastasis* **1993**, *13*, 102.
(266) Gupta, S.; Kobayashi, S.; Phongkitkarun, S.; Broemeling, L. D.; Kan, Z. *Investigative Radiology* **2006**, *41*, 516.
(267) Masyuk, T. V.; Ritman, E. L.; LaRusso, N. F. *American Journal of Pathology* **2003**, *162*, 1175.

(268) Li, X.; Wang, Y.-X. J.; Zhou, X.; Guan, Y.; Tang, C. *Cardiovascular and Interventional Radiology* **2006**, *29*, 1073.
(269) Wittmer, A.; Khazaie, K.; Berger, M. R. *Clinical and Experimental Metastasis* **1999**, *17*, 369.
(270) Kollmar, O.; Schilling, M. K.; Menger, M. D. *Clinical and Experimental Metastasis* **2004**, *21*, 453.
(271) Cheng, Y.; Wang, J.; Rao, T.; He, X.; Xu, T. *Frontiers in Bioscience* **2008**, *13*, 1447.
(272) Patri, A. K.; Kukowska-Latallo, J. F.; Baker, J. R., Jr. *Advanced Drug Delivery Reviews* **2005**, *57*, 2203.
(273) Patri, A. K.; Majoros, I. J.; Baker, J. R., Jr. *Curr. Opin. Chem. Biol.* **2002**, *6*, 466.
(274) Kaczorowska, M. A.; Cooper, H. J. *Journal of the American Society for Mass Spectrometry* **2009**, *20*, 674.
(275) Duncan, R.; Izzo, L. *Advanced Drug Delivery Reviews* **2005**, *57*, 2215.
(276) Roberts, J. C.; Bhalgat, M. K.; Zera, R. T. *Journal of Biomedical Materials Research* **1996**, *30*, 53.
(277) Yuan, D.; Brown, R. G.; Hepworth, J. D.; Alexiou, M. S.; Tyman, J. H. P. *Journal of Heterocyclic Chemistry* **2008**, *45*, 397.
(278) Svenson, S.; Tomalia, D. A. *Advanced Drug Delivery Reviews* **2005**, *57*, 2106.
(279) Maiti, P. K.; Çagin, T.; Wang, G.; Goddard, W. A., III *Macromolecules* **2004**, *37*, 6236.
(280) Alexander, H. R.; Libutti, S.; Pingpank, J.; Bartlett, D.; Helsabeck, C.; Beresneva, T. *Annals of Surgical Oncology* **2005**, *12*, 138.
(281) Shukla, R.; Thomas, T. P.; Peters, J. L.; Desai, A. M.; Kukowska-Latallo, J.; Patri, A. K.; Kotlyar, A.; Baker, J. R., Jr. *Bioconjugate Chemistry* **2006**, *17*, 1109.
(282) Matsuura, N.; Rowlands, J. A. *Medical Physics* **2008**, *35*, 4474.
(283) Dewey, W. C.; Sapareto, S. A.; Betten, D. A. *Radiation Research* **1978**, *76*, 48.
(284) Holahan, E. V.; Highfield, D. P.; Holahan, P. K.; Dewey, W. C. *Radiation Research* **1984**, *97*, 108.
(285) Kampinga, H. H.; Dikomey, E. *International Journal of Radiation Biology* **2001**, *77*, 399
(286) Haas, G. P.; Klugo, R. C.; Hetzel, F. W.; Barton, E. E.; Cerny, J. C. *Journal of Urology* **1984**, *132*, 828.
(287) Herman, T. S.; Sweets, C. C.; White, D. M.; Gerner, E. W. *Journal of the National Cancer Institute* **1982**, *68*, 487.
(288) Ko, S. H.; Ueno, T.; Yoshimoto, Y.; Yoo, J. S.; Abdel-Wahab, O. I.; Abdel-Wahab, Z.; Chu, E.; Pruitt, S. K.; Friedman, H. S.; Dewhirst, M. W.; Tyler, D. S. *Clinical Cancer Research* **2006**, *12*, 289.
(289) Klostergaard, J.; Leroux, E.; Siddik, Z. H.; Khodadadian, M.; Tomasovic, S. P. *Cancer Research* **1992**, *52*, 5271.
(290) Lee, Y. J.; Hou, Z.; Curetty, L.; Cho, J. M.; Corry, P. M. *Journal of Cellular Physiology* **1993**, *155*, 27.
(291) Srinivasan, J. M.; Fajardo, L. F.; Hahn, G. M. *Journal of the National Cancer Institute* **1990**, *82*, 1904.
(292) Gannon, C. J.; Chaerukuri, P.; Yakobson, B. I.; Cognet, L.; Kanzius, J. S.; Kittrell, C.; Weisman, R. B.; Pasquali, M.; Schmidt, H. K.; Smalley, R. E.; Curley, S. A. *Cancer* **2007**, *110*, 2654.
(293) Gannon, C. J.; Patra, C. R.; Bhattacharya, R.; Mukherjee, P.; Curley, S. A. *Journal of Nanobiotechnology* **2008**, *6*, 2.

(294) Tekade, R. K.; Kumar, P. V.; Jain, N. K. *Chem. Rev.* **2008**, *109*, 49.
(295) Majoros, I. J.; Myc, A.; Thomas, T.; Mehta, C. B.; Baker, J. R., Jr. *Biomacromolecules* **2006**, *7*, 572.
(296) Wolinsky, J. B.; Grinstaff, M. W. *Advanced Drug Delivery Reviews* **2008**, *60*, 1037.
(297) Kaminskas, L. M.; Kelly, B. D.; McLeod, V. M.; Boyd, B. J.; Krippner, G. Y.; Williams, E. D.; Porter, C. J. H. *Molecular Pharmaceutics* **2009**, *6*, 1190.
(298) Stiriba, S.-E.; Frey, H.; Haag, R. *Angewandte Chemie International Edition* **2002**, *41*, 1329.
(299) Dykes, G. M. *Journal of Chemical Technology and Biotechnology* **2001**, *76*, 903.
(300) Ye, Z.; Tan, M.; Wang, G.; Yuan, J. *Anal. Chem.* **2004**, *76*, 513.
(301) Urano, Y.; Asanuma, D.; Hama, Y.; Koyama, Y.; Barrett, T.; Kamiya, M.; Nagano, T.; Watanabe, T.; Hasegawa, A.; Choyke, P. L.; Kobayashi, H. *Nature Medicine* **2008**, *15*, 104.
(302) Bouvet, M.; Tsuji, K.; Yang, M.; Jiang, P.; Moossa, A. R.; Hoffman, R. M. *Cancer Research* **2006**, *66*, 11293.
(303) Hagenaars, M.; Ensink, N. G.; Basse, P. H.; Hokland, M.; Nannmark, U.; Eggermont, A. M. M.; van de Velde, C. J. H.; Fleuren, G. J.; Kuppen, P. J. K. *Clinical and Experimental Metastasis* **2000**, *18*, 189.
(304) Imaoka, T.; Horiguchi, H.; Yamamoto, K. *J. Am. Chem. Soc.* **2003**, *125*, 340.
(305) Dougherty, T. J. *Photochemistry and Photobiology* **1987**, *45*, 879.
(306) Liu, P.; Zhang, A.; Zhou, M.; Xu, Y.; Xu, L. X. In *Engineering in Medicine and Biology Society, 2004. IEMBS '04. 26th Annual International Conference of the IEEE* 2004; Vol. 1, p 2662.
(307) di Tomaso, E.; Capen, D.; Haskell, A.; Hart, J.; Logie, J. J.; Jain, R. K.; McDonald, D. M.; Jones, R.; Munn, L. L. *Cancer Research* **2005**, *65*, 5740.
(308) Weller, G. E. R.; Wong, M. K. K.; Modzelewski, R. A.; Lu, E.; Klibanov, A. L.; Wagner, W. R.; Villanueva, F. S. *Cancer Research* **2005**, *65*, 533.
(309) Dunehoo, A. L.; Anderson, M.; Majumdar, S.; Kobayashi, N.; Berkland, C.; Siahaan, T. J. *Journal of Pharmaceutical Sciences* **2006**, *95*, 1856.
(310) Brown, C. K.; Modzelewski, R. A.; Johnson, C. S.; Wong, M. K. *Annals of Surgical Oncology* **2000**, *7*, 743.
(311) Ruoslahti, E. *Drug Discov. Today* **2002**, *7*, 1138.
(312) Ruoslahti, E.; Bhatia, S. N.; Sailor, M. J. *Journal of Cell Biology* **2010**, *188*, 759.
(313) Rosenzweig, Z.; Kopelman, R. *Anal. Chem.* **1995**, *67*, 2650.
(314) Wolfbels, O. S. *Anal. Chem.* **2008**, *80*, 4269.
(315) Janata, J.; Josowicz, M.; Vanysek, P.; DeVaney, D. M. *Anal. Chem.* **1998**, *70*, 179R.
(316) Madou, M. J.; Morrison, S. R. *Chemical Sensing with Solid State Devices*; Academic Press, 1989.
(317) Ramamoorthy, R.; Dutta, P. K.; Akbar, S. A. *J. Mater. Sci.* **2003**, *38*, 4271.
(318) Neri, G.; Bonavita, A.; Micali, G.; Rizzo, G.; Galvagno, S.; Niederberger, M.; Pinna, N. *Chem. Commun.* **2005**, 6032.
(319) Wang, D. S.; Hao, C. H.; Zheng, W.; Peng, Q.; Wang, T. H.; Liao, Z. M.; Yu, D. P.; Li, Y. D. *Adv. Mater.* **2008**, *20*, 2628.
(320) Avouris, P.; Chen, Z. H.; Perebeinos, V. *Nat. Nanotechnol.* **2007**, *2*, 605.
(321) Tans, S. J.; Verschueren, A. R. M.; Dekker, C. *Nature* **1998**, *393*, 49.

(322) Snow, E. S.; Perkins, F. K.; Houser, E. J.; Badescu, S. C.; Reinecke, T. L. *Science* **2005**, *307*, 1942.
(323) Kauffman, D. R.; Star, A. *Angewandte Chemie-International Edition* **2008**, *47*, 6550.
(324) Kong, J.; Franklin, N. R.; Zhou, C. W.; Chapline, M. G.; Peng, S.; Cho, K. J.; Dai, H. J. *Science* **2000**, *287*, 622.
(325) Collins, P. G.; Bradley, K.; Ishigami, M.; Zettl, A. *Science* **2000**, *287*, 1801.
(326) Valentini, L.; Armentano, I.; Kenny, J. M.; Bidali, S.; Mariani, A. *Thin Solid Films* **2005**, *476*, 162.
(327) McDonagh, C.; Burke, C. S.; MacCraith, B. D. *Chem. Rev.* **2008**, *108*, 400.
(328) Wu, Z. C.; Chen, Z. H.; Du, X.; Logan, J. M.; Sippel, J.; Nikolou, M.; Kamaras, K.; Reynolds, J. R.; Tanner, D. B.; Hebard, A. F.; Rinzler, A. G. *Science* **2004**, *305*, 1273.
(329) Bekyarova, E.; Kalinina, I.; Itkis, M. E.; Beer, L.; Cabrera, N.; Haddon, R. C. *J. Am. Chem. Soc.* **2007**, *129*, 10700.
(330) Kauffman, D. R.; Star, A. *J. Phys. Chem. C* **2008**, *112*, 4430.
(331) Heller, D. A.; Jeng, E. S.; Yeung, T. K.; Martinez, B. M.; Moll, A. E.; Gastala, J. B.; Strano, M. S. *Science* **2006**, *311*, 508.
(332) O'Connell, M. J.; Eibergen, E. E.; Doorn, S. K. *Nat. Mater.* **2005**, *4*, 412.
(333) Bekyarova, E.; Itkis, M. E.; Cabrera, N.; Zhao, B.; Yu, A. P.; Gao, J. B.; Haddon, R. C. *J. Am. Chem. Soc.* **2005**, *127*, 5990.
(334) Hu, L.; Hecht, D. S.; Gruner, G. *Nano Lett.* **2004**, *4*, 2513.
(335) Lide, D. R. *CRC Handbook of Chemistry and Physics*; 85th ed.; CRC, 2005.
(336) Savvate'ev, V.; Chen-Esterlit, Z.; Aylott, J. W.; Choudhury, B.; Kim, C. H.; Zou, L.; Friedl, J. H.; Shinar, R.; Shinar, J.; Kopelman, R. *Appl. Phys. Lett.* **2002**, *81*, 4652.
(337) Heller, I.; Janssens, A. M.; Mannik, J.; Minot, E. D.; Lemay, S. G.; Dekker, C. *Nano Lett.* **2008**, *8*, 591.
(338) Kataura, H.; Kumazawa, Y.; Maniwa, Y.; Umezu, I.; Suzuki, S.; Ohtsuka, Y.; Achiba, Y. *Synth. Met.* **1999**, *103*, 2555.
(339) Saito, R.; Fujita, M.; Dresselhaus, G.; Dresselhaus, M. S. *Appl. Phys. Lett.* **1992**, *60*, 2204.
(340) Chen, R. J.; Franklin, N. R.; Kong, J.; Cao, J.; Tombler, T. W.; Zhang, Y. G.; Dai, H. J. *Appl. Phys. Lett.* **2001**, *79*, 2258.
(341) Shim, M.; Back, J. H.; Ozel, T.; Kwon, K. W. *Phys. Rev. B* **2005**, *71*, 9.
(342) Derycke, V.; Martel, R.; Appenzeller, J.; Avouris, P. *Appl. Phys. Lett.* **2002**, *80*, 2773.
(343) Hersam, M. C. *Nat. Nanotechnol.* **2008**, *3*, 387.
(344) Lee, C. Y.; Baik, S.; Zhang, J. Q.; Masel, R. I.; Strano, M. S. *J. Phys. Chem. B* **2006**, *110*, 11055.
(345) Hecht, D. S.; Ramirez, R. J. A.; Briman, M.; Artukovic, E.; Chichak, K. S.; Stoddart, J. F.; Gruner, G. *Nano Lett.* **2006**, *6*, 2031.
(346) Borghetti, J.; Derycke, V.; Lenfant, S.; Chenevier, P.; Filoramo, A.; Goffman, M.; Vuillaume, D.; Bourgoin, J. P. *Adv. Mater.* **2006**, *18*, 2535.
(347) Star, A.; Lu, Y.; Bradley, K.; Gruner, G. *Nano Lett.* **2004**, *4*, 1587.
(348) Chua, L. L.; Zaumseil, J.; Chang, J. F.; Ou, E. C. W.; Ho, P. K. H.; Sirringhaus, H.; Friend, R. H. *Nature* **2005**, *434*, 194.
(349) Hartstein, A.; Young, D. R. *Appl. Phys. Lett.* **1981**, *38*, 631.
(350) Kim, W.; Javey, A.; Vermesh, O.; Wang, O.; Li, Y. M.; Dai, H. J. *Nano Lett.* **2003**, *3*, 193.

(351) Giordano, L.; Sushko, P. V.; Pacchioni, G.; Shluger, A. L. *Phys. Rev. Lett.* **2007**, *99*, 4.
(352) Pantelides, S. T. *Thin Solid Films* **1982**, *89*, 103.
(353) Anghel, C.; Derycke, V.; Filoramo, A.; Lenfant, S.; Giffard, B.; Vuillaume, D.; Bourgoin, J. P. *Nano Lett.* **2008**, *8*, 3619.
(354) Queisser, H. J. *Phys. Rev. Lett.* **1985**, *54*, 234.
(355) Bünzli, J.-C. G.; Piguet, C. *Chem. Soc. Rev.* **2005**, *34*, 1048.
(356) Hangleiter, A. *Phys. Rev. B* **1993**, *48*, 9146.
(357) Kajihara, K.; Kamioka, H.; Hirano, M.; Miura, T.; Skuja, L.; Hosono, H. *J. Appl. Phys.* **2005**, *98*, 5.
(358) Aroutiounian, V. *Int. J. Hydrog. Energy* **2007**, *32*, 1145.
(359) Sorescu, D. C.; Jordan, K. D.; Avouris, P. *J. Phys. Chem. B* **2001**, *105*, 11227.
(360) Bonnet, C. S.; Pellegatti, L.; Buron, F.; Shade, C. M.; Villette, S.; Kubicek, V.; Guillaumet, G.; Suzenet, F.; Petoud, S.; Toth, E. *Chem. Commun.*, *46*, 124.
(361) Castelli, D. D.; Gianolio, E.; Crich, S. G.; Terreno, E.; Aime, S. *Coord. Chem. Rev.* **2008**, *252*, 2424.
(362) Mulder, W. J. M.; Strijkers, G. J.; van Tilborg, G. A. F.; Griffioen, A. W.; Nicolay, K. *NMR Biomed.* **2006**, *19*, 142.
(363) Torchilin, V. P. *Nat. Rev. Drug Discov.* **2005**, *4*, 145.
(364) Uchiyama, S.; McClean, G. D.; Iwai, K.; de Silva, A. P. *J. Am. Chem. Soc.* **2005**, *127*, 8920.
(365) Grandini, P.; Mancin, F.; Tecilla, P.; Scrimin, P.; Tonellato, U. *Angewandte Chemie-International Edition* **1999**, *38*, 3061.
(366) Diaz-Fernandez, Y.; Foti, F.; Mangano, C.; Pallavicini, P.; Patroni, S.; Perez-Gramatges, A.; Rodriguez-Calvo, S. *Chem.-Eur. J.* **2006**, *12*, 921.
(367) dos Santos, C. M. G.; Harte, A. J.; Quinn, S. J.; Gunnlaugsson, T. *Coord. Chem. Rev.* **2008**, *252*, 2512.
(368) Kalyanasundaram, K.; Thomas, J. K. *J. Am. Chem. Soc.* **1977**, *99*, 2039.
(369) Hong, Y. N.; Lam, J. W. Y.; Tang, B. Z. *Chem. Commun.* **2009**, 4332.
(370) Hemmila, I. *In High Throughput Screening*; Marcel Dekker: New York, 1997.
(371) Pellegatti, L.; Zhang, J.; Drahos, B.; Villette, S.; Suzenet, F.; Guillaumet, G.; Petoud, S.; Toth, E. *Chem. Commun.* **2008**, 6591.
(372) Nicolle, G. M.; Toth, E.; Eisenwiener, K. P.; Macke, H. R.; Merbach, A. E. *J. Biol. Inorg. Chem.* **2002**, *7*, 757.
(373) Junquera, E.; Pena, L.; Aicart, E. *Langmuir* **1997**, *13*, 219.